Defect Engineering of Spin-Correlated Luminescent Dopants in Ferromagnetic van der Waals Materials

Kimo Pressler

A dissertation
submitted in partial fulfillment of the
requirements for the degree of

Doctor of Philosophy

University of Washington
2025

Reading Committee:
Daniel R. Gamelin, Chair
Douglas A. Reed
Stefan Stoll

Program Authorized to Offer Degree:
Chemistry

University of Washington

Abstract

Defect Engineering of Spin-Correlated Luminescent Dopants in Ferromagnetic van der Waals Materials

Kimo Pressler

Chair of the Supervisory Committee:

Daniel R. Gamelin

Department of Chemistry

The controlled introduction of impurities into crystals provides a powerful means of tailoring material properties and imparting new functionalities not inherent to the native lattice. Recently, magnetically ordered van der Waals (vdW) materials have emerged as a leading platform for next-generation two-dimensional (2D) spin-based electronics, however, deliberate incorporation of optical impurities in these materials remains largely untapped. This dissertation presents the use of spin-bearing Yb^{3+} as a substitutional point defect in the archetypical vdW magnet CrX_3, marking the first report of *any* extrinsic dopant serving as an optically active point defect across all magnetically ordered vdW compounds. This work demonstrates the transformation of the featureless broadband *d-d* photoluminescence (PL) of the CrX_3 host lattice into narrow-line, spin-polarized *f-f* emission originating from isolated Yb^{3+} impurity centers, without any degradation of the host lattice magnetic integrity. Via strong superexchange coupling, the Yb^{3+} magnetization is pinned to the host CrX_3 magnetization, allowing for the controllable spin manipulation of the paramagnetic Yb^{3+} impurities by the lattice. This work highlights the use of Yb^{3+} as an optical probe to investigate local spin correlations and excited-state dynamics, emphasizing the potential of dopants to introduce novel spin-correlated optical functionalities into 2D magnetic materials.

DEDICATION

To those who were willing to cross over that small footbridge to me, thank you for your endless support

Table of Contents

Chapter 1. Optical Point Defects in Magnetic van der Waals Materials

1.1 Overview

The class of layered van der Waals (vdW) ferromagnets (FM) has gained significant attention as a promising platform for investigating topological spin phases, magnetic proximity effects, and spin dynamics in the two-dimensional (2D) limit.[1-3] The integration of magnetic monolayers into stacked heterostructures has driven significant progress in low-dimensional spintronic devices, as evidenced by advancements in electrical and thermal spin current generation, spin-orbit torque devices, and the development of spin filters.[4-7] Concurrently, there is growing interest in 2D FM vdW compounds for use in spin-photonics, enabling the optical generation and manipulation of spin states.[8-11] Such applications require materials with well-defined spin-correlated optically active transitions. However many 2D FM significantly lack this quality in their native form, as exemplified by the unresolved, featureless d-d luminescence and limited spin coherence of CrX_3.[12-14] These limitations can be addressed via the introduction of optical dopants, which impart new photonic functionalities into 2D FM vdW compounds as recently demonstrated via Yb^{3+} doped CrX_3.[15-17] Via the substitutional doping of the spin-bearing defect Yb^{3+} for Cr^{3+}, the lattice photoluminescence (PL) can be completely quenched and replaced with spin polarized sharp-line *f-f* emission with features as narrow as ~0.1 meV, without any degradation of the host lattice magnetic integrity. Through strong superexchange coupling, the paramagnetic dopant exhibits strong coupling to the lattice magnetization, providing an optical handle to both probe and control the local lattice magnetization. Despite these promising results, the use of optical dopants in 2D FM vdW compounds remains largely untapped. This work aims to demonstrate the potential of optical point defects in 2D FM vdW materials, highlighting the ability of impurities to introduce new spin-correlated photonic functionalities into these magnetic materials and inspire further exploration in this emerging area of research.

This chapter provides an overview of defect engineering in the development of magnetic vdW compounds with spin-correlated, optically addressable states. We begin with a discussion on the

power of defect engineering to introduce desirable functionality into host lattices. This is followed by an examination of the early approach of using spin-bearing transition metal (TM) dopants to induce magnetic order in nonmagnetic semiconducting vdW materials, a strategy employed before the first publications demonstrating intrinsic magnetic order at the few-layer limit in CrI_3 and $CrGeTe_3$.[18, 19] Next, we explore the potential of *intrinsic* point defects, such as vacancy centers, as optically active sites in FM lattices. We then introduce the first reported class of *extrinsic* dopants serving as optical point defects in a 2D ferromagnet; Yb^{3+}:CrX_3, with focus on the strong covalent bonding found within this system, as further discussed in Chapter 2. Additionally, we discuss the dynamics of dopant sensitization via the lattice exciton, a topic explored further in Chapter 5. In the subsequent section, we delve into the use of these dopants as optical probes to both identify and manipulate lattice magnetization, with deeper analysis provided in Chapters 3 and 4. These findings underscores the unique nature of Yb^{3+}:CrX_3, and demonstrate the potential of lanthanide doping in magnetic vdW compounds, offering new avenues for tailored material design and spin-photonic functionality in this new material class.

1.2 Introduction of Defect Engineering

Point defects, such as site vacancies, interstitial inclusions, antisite substitutions, or extrinsic dopants are common in inorganic crystals with typical concentrations in the ppm range.[20] Despite their low abundance, these defects can profoundly influence the electronic, optical, and mechanical properties of the bulk lattice**.** Defect engineering—the controlled introduction and manipulation of such defects—provides a powerful tool for tuning material properties and unlocking new functionalities.[21] One of the most notable examples of defect engineering is the *sub-*/*super*-valent doping of silicon with boron/phosphorus, which was instrumental in the development of the first p-n junctions in the 1950's.[22] This breakthrough led to the creation of transistors, laying the foundation of all modern electronics. In the 1960's Cr^{3+} dopants in synthetic ruby enabled the first functional laser,[23] revolutionizing high-bandwidth optical communication. This breakthrough not only facilitated long-distance, high-speed data transmission but also

enabled the commercialization of optically written/read data, offering significant increases in data storage density over magnetic tape memory of the time.[24]

However, as the demands for information storage, processing, and transfer continually increase while traditional semiconductor scaling is reaching its limit,[25] new technological paradigms and the materials advancements enabling them are required to meet these challenges. In this context, the development of spin-based electronics/photonics and 2D vdW compounds have emerged as critical research avenues. By exploiting spin instead of only charge as a state variable, spintronics could provide a lower-energy pathway for information processing and storage compared with conventional digital electronics. Just as defect engineering enabled transformative advancements in electronic and photonic applications in the mid 20th century, it is now poised to play a critical role in the development of the next generation of spintronic and spin-photonic devices, particularly in the rapidly expanding realm of 2D vdW compounds.

The field of 2D vdW materials has seen immense evolution since Geim and Novoselov's demonstration of graphite's exfoliability down to monolayer graphene in 2004.[26] In just two decades, the 2D vdW material landscape has expanded to include over 100 compositions, encompassing a vast regime of fascinating physical properties such as topological insulation,[27, 28] valley polarization,[29, 30] piezoelectricity,[31, 32] superconductivity,[33, 34] ferroelectricity,[32, 35] and more,[36] all within materials just a few nanometers thick. The weak interlayer van der Waal interaction and net charge neutrality of the covalently bonded monolayers allows for the near unconstrained stacking of heterogenous layers into devices,[37] free from lattice matching constraints typically found in bilayer crystalline systems. This layer stacking methodology may result in new emergent phenomena that are not present in the individual layers, as demonstrated by creation of moiré superlattices,[38-40] proximity induced effects,[2, 41] and interlayer exciton confinement[42, 43] showcasing the depth of possible physical properties within the vdW material landscape.

In this framework, defect engineering of individual layers in tandem with this flexible stacking offers unprecedented control over material behavior and allows for tailoring of desirable properties. Unlike stacking-induced proximity effects, layer-embedded defects are strongly

coupled to the lattice via direct bonding, while preserving the layer geometry and compatibility with heterostructure integration. This contrasts with defect *intercalation* schemes, which, by functionalizing interlayer surfaces, may complicate stacking and exfoliation.[44] The next section explores the use of defect engineering to impart magnetic functionality into emissive vdW semiconductors.

1.3 Defect Engineering of Nonmagnetic vdW Compounds

Prior to 2017 and the discovery of stable intrinsic ferromagnetic order in few-layer Cr^{3+}-based CrI_3[18] and $Cr_2Ge_2Te_6$[19], there was no clear route to developing vdW materials displaying both magnetic order and coupled optical transitions. Taking inspiration from the field of diluted magnetic semiconductors (DMS)[45, 46], synthetic efforts have revolved around doping spin-bearing transition metals (TM) into vdW semiconductors such as Mn^{2+} and Fe^{2+} doping in MoS_2.[47-50] The unpaired spins in the dopant *d* orbitals can impart magnetic order in the host lattice via multiple magnetic exchange pathways, including short range superexchange interactions between the dopant and neighboring host atoms, and longer range indirect exchange interactions between the isolated local TM magnetic moments with free carriers of the conduction/valence band.[51] These magnetic interactions are maximized at high TM doping concentrations, at which an associated high density of state dopant "band" is introduced. Ideally, this defect band is shallow and positioned near the conduction or valence band, enhancing the indirect exchange coupling between TM spins and free carrier spins.[52] However, these optimal factors for magnetic order hinder strong excitonic emission, as such shallow bands can quench photo-excited charge carriers and lower the probability of radiative recombination of the exciton electron-hole pair.[53] Figure 1.1 demonstrates this trade-off in magnetic integrity and strong PL.

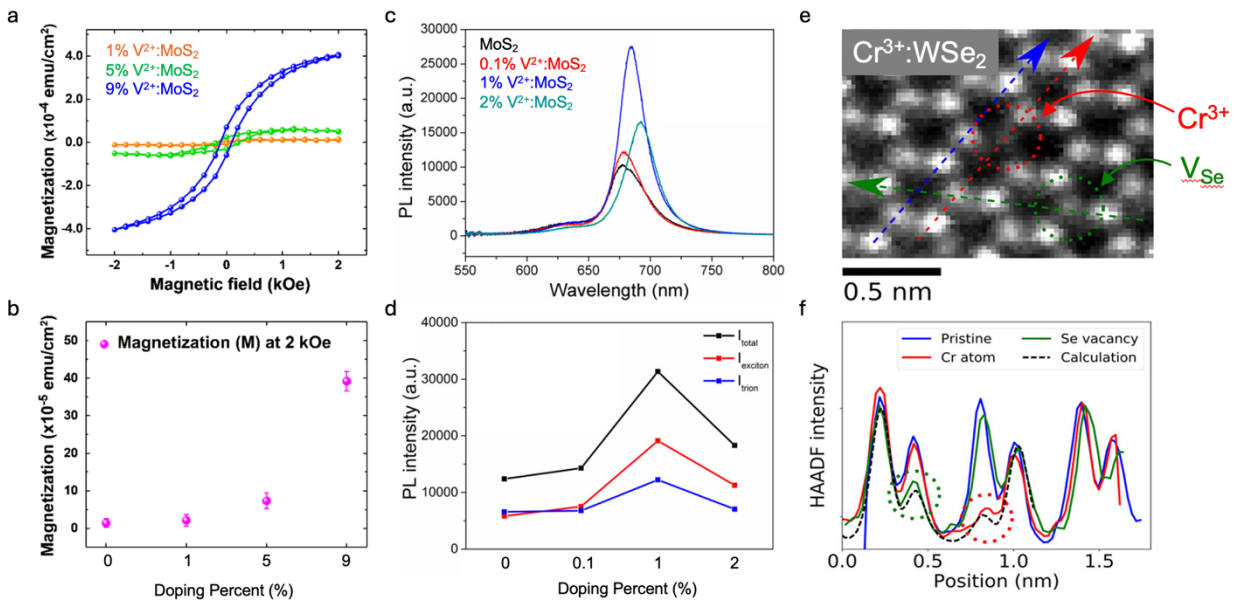

Figure 1.1 (a) Plot of magnetization vs field of 1%, 5%, and 9% V^{2+} doped MoS_2 measured at 300 K. **(b)** Plot of saturation magnetization measured at 2 kOe of the same samples shown in panel a. **(c)** Plot of 300 K PL intensity of undoped, 0.1%, 1%, and 2% V^{2+} doped MoS_2 measured under the same excitation conditions. **(d)** Plot of integrated exciton (red), trion (blue), and total (black) emission for the samples shown in panel c. **(e)** STEM-HAADF image of Cr^{3+}:WSe_2, showing a single Cr atom (red circle) with a Se-vacancy (green circle) as a third nearest neighbor. The Cr atom and Se-vacancy are confirmed via the profiles shown in panel f corresponding to the dashed colored arrows. **(f)** STEM-HAADF profiles corresponding to the dashed lines in panel e. The results are compared to simulated profiles containing a Cr dopant and Se-vacancy. Panel a,b adapted with permission from ref [54]. Panel c,d adapted with permission from ref [55]. Panel e,f adapted with permission from ref [56].

As shown in Figure 1.1a,b, work by Sahoo et al. demonstrates the development of ferromagnetic order in MoS_2 with increasing concentrations of V^{2+} doping.[54] At low doping levels (1% and 5%), the lattice exhibits weak ferromagnetic order at 300 K. However, at 9% V^{2+} doping, a five-fold increase in the saturation magnetization is observed, as has been previously computationally predicted to result from an increase in nearest-neighbor V-V superexchange interactions which promote ferromagnetic order.[57] Unfortunately, at these high doping percentages, there is a significant reduction in excitonic PL, as shown in Figure 1.1c,d. Work by Zhang et al.[55] indicates that at low levels of V^{2+} (0.1% and 1%), excitonic PL intensity initially

increases, however, considerable nonradiative quenching occurs at 2% doping, well below the ideal >8% doping for strong ferromagnetic order. These additional nonradiative pathways likely arise due to dopant induced structural defects. In vdW transition metal dichalcogenides (TMDC) semiconductors, achieving isovalent magnetic doping is challenging as many high-spin dopants (e.g., Cr^{3+}, Ni^{2+}, $Mn^{2+/3+}$, Fe^{2+}, Co^{2+}, V^{2+}) do not match the formal 4+ oxidation state of the host cation (eg. Mo^{4+}, W^{4+}). As a result, doping inherently introduces charge-compensating structural defects, as can be seen via scanning transmission electron microscopy high-angle annular dark-field imaging (STEM-HAADF) of Cr^{3+}:WSe_2, which reveals charge compensating Se vacancies positioned near the Cr^{3+} dopants (Figure 1.1e,f).[56] This inherent competition between stable magnetic order and strong photoluminescence found in TM doped vdW semiconductors presents a significant challenge in developing strongly coupled magneto-optical 2D materials based on traditional semiconducting TMDC's.

The introduction of stable intrinsically magnetic materials like CrI_3 and $Cr_2Ge_2Te_6$ marks a paradigm shift in coupling magnetic and photonic properties within the dopant-lattice framework. Rather than inducing magnetic order through introducing spin-bearing TM dopants in a semiconducting lattice, dopants can now be employed to introduce optically active electronic states directly into these magnetic vdW compounds. However, before delving into the exploration of *extrinsic* optical dopants in magnetic vdW compounds, it is valuable to first examine the natively occurring *intrinsic* point defects within these crystals, as they may offer key insights for the rational design of intentionally doped magneto-optical materials.

1.4 Native Defects as Optically Active Sites in Intrinsically Magnetic vdW Materials

Intrinsic defects (those formed solely from the constituent atoms of the lattice) arise as thermodynamic products during the growth of crystalline materials and can take various forms, including interstitial inclusions, antisite substitutions, and in their simplest form, vacancy centers. In semiconducting or insulating materials with bandgaps, these point defects may introduce electronic states within the bandgap spatially localized about the point defect itself. Vacancy

center defects, typically denoted as V_X^n (where x represents the identity of the missing atom and n indicates the charge of the defect state), are the most common type of intrinsic point defect studied as optically active sites, as in many cases they feature well-defined atom-like electronic states with discrete energy levels that are governed by the local crystal symmetry and coupled to local lattice distortions.

Emission from such vacancy center defects can offer unique functional optical properties over pure excitonic emission, exemplified by the V_{Si} defect in 4H-SiC. Exhibiting an exceptionally sharp zero-phonon line (FWHM ~ 0.1 meV),[58, 59] single-photon emission,[60] and optically addressable spin states with long spin-coherence times (~160 μs),[61] this defect has shown promise in application such as quantum photonics[62] and magnetic field sensing.[63] Moreover, since these defects can be generated post synthetically through electron-beam irradiation,[62] they offer the potential for precise spatial patterning, enabling their integration into advanced devices, such as those that rely on cavity coupling.[64]

These exciting and intriguing properties displayed by emissive defects in 3D bulk semiconductors have sparked analogous research in the domain of 2D vdW semiconductors. Such emissive intrinsic point defects have been reported for various 2D semiconductors such as the TMDC's MX_2 (M=Mo, W; X = S, Se),[65] and hexagonal boron nitride (hBN)[66]. A recent 2023 computational study investigated 5000 such point defects across 10 wide-gap semiconducting 2D materials to identify defects exhibiting sharp line emission.[67] However, this study was limited to non-magnetic vdW materials, underscoring the overall lack of exploration in the domain of 2D magnetic materials.

The most well studied 2D FM material featuring magnetically sensitive PL originating from intrinsic vacancy defects is CrSBr, as first reported on in 2022 by Klein et al.[68] CrSBr is an air-stable semiconductor with a direct electronic band gap of ~1.5 eV, featuring layered A-Type AFM ordering (T_N = 132 K). Within each vdW layer Cr^{3+} spins align FM along the *b*-axis, while adjacent layers couple in an AFM configuration, as depicted in Figure 1.2a. With the application of an external field applied along the *b*-axis, CrSBr undergoes a spin-flip transition at ~0.35 T resulting in complete *inter*- and *intra*-layer FM order. Temperature-dependent magnetic measurements,

including muon spin spectroscopy and neutron scattering, have also revealed a dynamic secondary low-temperature magnetic phase transition within the antiferromagnetically (AFM) ordered layers.[69-71] This transition is associated with a gradual reduction in magnetic fluctuations within a secondary spin sublattice, not originating from the dominant Cr^{3+} spin lattice, and has been proposed to arise from spin-bearing point defects within the lattice. This process begins at T_S = 100 K, whereby the spins in the secondary sublattice becoming completely frozen and FM coupled to the Cr^{3+} spin lattice by T_D = 40 K. This rich magnetic structure, featuring magnetically active point defects, underscores the potential for rich magneto-optical coupling of intrinsic point defects in CrSBr.

Indeed, the presence of multiple point defects are readily found in CrSBr. As shown in Figure 1.2b, scanning tunneling microscopy (STM) of an exfoliated sheet of CrSBr reveals the presence of bromide vacancies (V_{Br}) at concentrations of 10^{13} cm^{-2}, as well as a secondary indeterminant point defect present at lower concentrations of 10^{11} cm^{-2}, speculated to correspond to sulfur vacancies (V_S). Such point defects are shown to be optically active. As illustrated in Figure 1.2c, upon excitation above the band gap (2.384 eV), CrSBr exhibits a rich optical spectrum with multiple distinct emissive features. These include excitonic emission (labeled X) at 1.37 eV and a defect-related sharp-line doublet emission (labeled X^D) centered at 1.264 eV. Power-dependent PL confirms X^D arises from point defects present at low concentrations. The excitonic PL intensity is found to scale linearly with increasing power, while X^D emission saturates at 100 μW (Figure 1.2d), indicating this PL arises from sensitization of a limited concentration of point defects within the excitation radius.

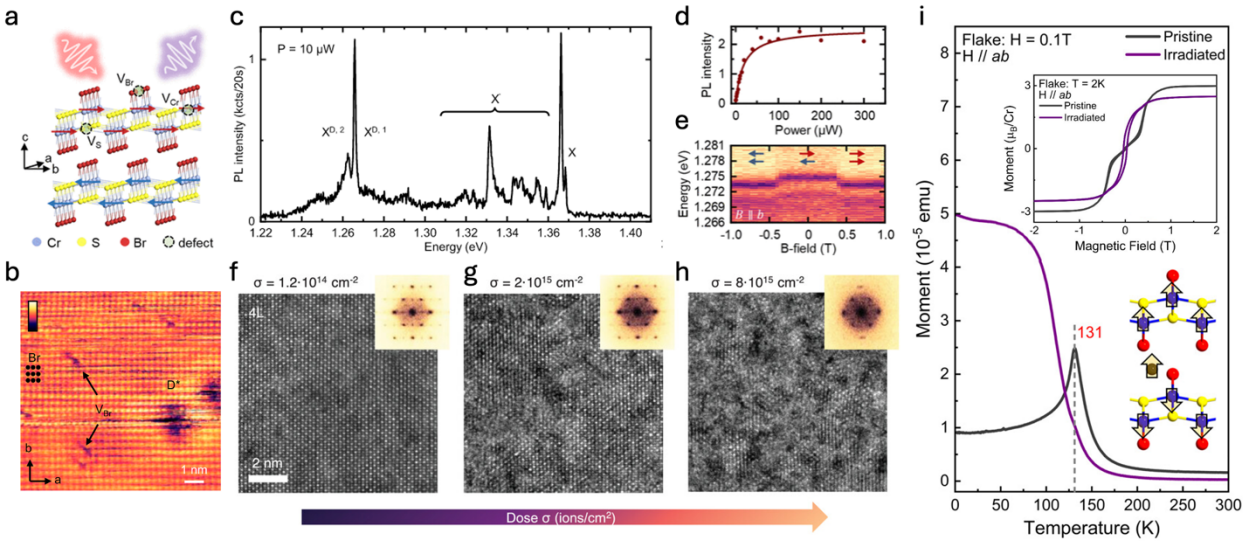

Figure 1.2 (a) Schematic illustration of multilayer CrSBr featuring A-Type FM order, with possible intrinsic defects (V_S, V_{Br}, V_{Cr}) depicted. **(b)** STM topographic image showing bromide vacancies (V_{Br}) with a surface density of ~5 x 10^{12} cm^{-2}, as well as an unknown defect (D*) situated within the layers, most likely associated with S and Cr vacancies, present at lower densities of ~3 x 10^{11} cm^{-2}. **(c)** 4.2 K PL of multilayer CrSBr, excited above the bandgap at 2.384 eV. The spectrum includes the excitonic emission (X) and its associated vibronic structure (X'), along with a defect related doublet ($X^{D,1}$, $X^{D,2}$). **(d)** Power-dependent PL intensity of the defect emission, demonstrating saturation at high power density due to sensitization of all available defects within the excitation radius. **(e)** PL of the defect doublet as a function of magnetic field. The PL undergoes a sudden shift of 1.35 meV at the coercive field of the bulk CrSBr at ~0.35 T. **(f-h)** STEM-HAADF images of 4 L CrSBr irradiated at increasing He^+ doses. **(i)** Field-cooled magnetization curves a < 1 um exfoliated flake of CrSBr, under an applied field of 0.1 T, for both a pristine flake (black) and flake irradiated with He^+ at a fluence of 8 x 10^{15} cm^{-2} (purple). After irradiation the magnetization transforms from AFM to FM. inset: Plot of magnetization vs field of the same samples. Panel a-e adapted with permission from ref [68]. Panel f-h adapted with permission from ref [71]. Panel i adapted with permission from ref [72].

As spin-bearing point defects are suspected as the origin for the low-temperature magnetic phase transition found in CrSBr, these defect PL features may exhibit magnetic correlation with the host lattice magnetization. Below T_D, upon application of an external field along the *b*-axis, the defect emission (X^D) peak energy shows an abrupt shift of 1.35 meV at the spin flip field B_{flip} = ~0.35 T, demonstrating magnetic coupling of the spin-bearing defects to the host lattice.

However, this energy shift is significantly smaller than the 20 meV shift observed in the excitonic PL (X), suggesting that the magnetic coupling of the defect electronic states to the dominant Cr^{3+} spin sublattice is weaker than that of the exciton. First-principles Green's function–Bethe–Salpeter equation (GW-BSE) calculations indicate the large shift of the exciton energy during the change from AFM to FM order is attributed to a dramatic increase in the delocalization of the excited state electron wavefunction.[73] In the AFM configuration, the exciton electron wavefunction is essentially confined to a single layer, while under the field-induced FM order, spin-allowed interlayer hybridization of the electron and hole wavefunction across adjacent layers expands the spatial distribution of the electron to both layers, resulting in the observed red shift of the exciton peak. As such, the comparably small energy shift of defect peak suggests that the wave function of the defect is significantly more confined within a single layer, as is expected a confined point defect, yet it still extends to some degree into the adjacent layer when the magnetic order changes from AFM to FM. Although the magnetic sensitivity of the defect emission is less than that of the exciton, these results underscore the potential to engineer magnetically correlated optical centers in vdW compounds.

For integration in spin-photonic devices, the ability to post-synthetically pattern optical sites at selected positions—rather than relying on the statistically random distribution formed in-situ—is of great interest. Compared to the patterned introduction of extrinsic dopants, post-synthetic formation of vacancy defects may be easier to implement, as their formation is a subtractive process rather than an additive one. As demonstrated in MoS_2[74] and graphene[75], irradiation by high-energy electrons (e^-) or helium ions (He^+) can selectively displace lattice atoms, generating defect vacancies. As shown in Figure 1.2f-h He^+ irradiation generates crystal defects proportional to the irradiation dose in CrSBr.[71] As evidenced by the corresponding fast Fourier transform (FFT) of the STEM images, at low irradiation doses the material retains a high degree of crystallinity, while increased dosage introduce some degree of lattice amorphization. While this method allows for spatial control of defect generation—dictated by the beam spot size— irradiation may lack precision in the specific type of defect that is generated.

In the case of CrSBr, Long et al.[72] observed that He^+ irradiation induced the formation of two

distinct types of defects: Br vacancies and Cr vacancies. Notably, the ejected Cr was found to incorporate into interlayer sites. These displaced cations result in a change of the ground state magnetic order from A-Type AFM to complete FM order, as interlayer Cr introduce new superexchange pathways resulting in enhanced interlayer coupling. Figure 1.2i depicts field-cooled magnetization of pristine and irradiated CrSBr flakes, illustrating this transformation in magnetic order. While e^-/He^+ irradiation can be used to post-synthetically introduce vacancy defects centers, the imprecise nature of the resulting defects, along with the potential formation of secondary inclusions from ejected lattice constituents with magnetic ramifications, limits the effectiveness of this technique to controllably and non-perturbatively create luminescent defects.

Despite their promise, the optical vacancy defects in CrSBr are remarkably the only *intentionally* explored emissive intrinsic point defects in a 2D vdW magnets, with exceptionally few other published examples that passively address this topic. One such examples where luminescent point defects have been observed are within FM $CrPS_4$.[76,77] Although not thoroughly researched yet, these defects offer insight into the broader aspects of intrinsic defects in 2D magnetic systems and particularly highlight the potential downsides of intrinsic defects as functional optical centers due to their varying emissive nature.

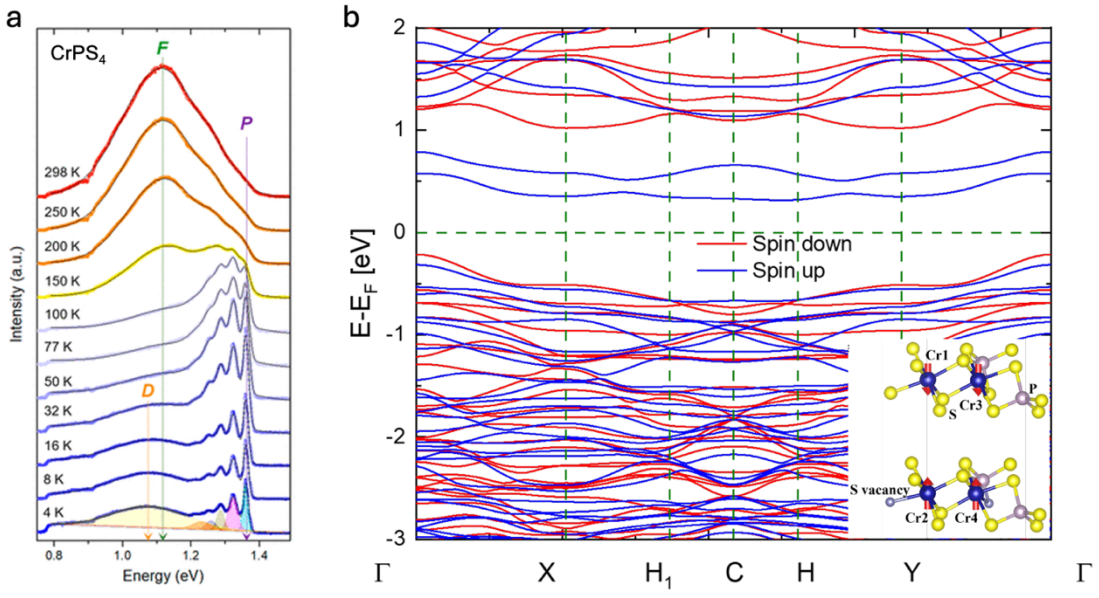

Figure 1.3 (a) Plot of variable temperature PL (VTPL) of bulk $CrPS_4$, featuring

multiple emissive features corresponding to emission originating from the Cr^{3+} ^2E_g state (labeled P), the Cr^{3+} $^4T_{2g}$ state (labeled F), and a defect feature (labeled D). **(b)** Calculated spin-polarized band structure of bilayer $CrPS_4$ featuring a single S vacancy (structure depicted in the inset). The S vacancy introduces a completely spin up polarized defect band within the bandgap. Panel a adapted with permission from ref [76]. Panel b adapted with permission from ref [77].

Figure 1.3a depicts variable temperature PL (VTPL) of bulk $CrPS_4$, which features three emissive features proposed to correspond to emission from the high spin $^4T_{2g}$ Cr^{3+} excited state (labeled P), low spin ^2E_g Cr^{3+} excited state (labeled F), as well as emission from a proposed S vacancy defect (labeled D). In contrast to the sharp-line defect emission in CrSBr, the defect emission is broad at all temperatures, with no distinguishable individual transitions. This breadth is attributed to inhomogeneous broadening and strong vibronic coupling in this highly covalent lattice. The D band can be confirmed as originating from defects, as Kim et al.[76] observed that its relative intensity increases in few layer samples, which are more prone to higher surface defect concentrations, compared to the relatively pristine-like bulk crystals. Furthermore, computational work by Shi et al.[77], confirm that S vacancies introduce mid-band states at energies comparable to those seen experimentally, as shown in Figure 1.3b. Of note, this S defect band is calculated to be completely spin-polarized, with the defect spin aligned parallel to the Cr^{3+} spins in the same layer, giving indication that these defects may be magnetically pinned to the lattice, however further experimental field-dependent PL spectroscopy must be done to confirm this finding. However, due to the considerable breadth of the defect emission, small changes in peak energy position due to changes in magnetization, akin to those observed in CrSBr, may be unobservable in $CrPS_4$.

The contrast in defect emission observed between CrSBr and $CrPS_4$ sheds light on the potential challenges of relying on intrinsic defect centers for designing materials with both functional optical properties and magnetic order. Vacancy centers induce local lattice distortions, as well as charge imbalances, making it difficult to both predict the electronic structure a priori and target specific energy levels for device applications. While defect generation can be achieved post-synthetically via high-energy irradiation, the precise control of specific defect centers

without introducing secondary defects remains challenging. Furthermore, limiting material design to only intrinsic defects significantly restricts the range of possible material design, especially when considering the vast array of extrinsic dopants available across the periodic table.

The paucity of materials displaying optically active native defects in magnetic vdW materials highlights the need to expand the realm of defects beyond those intrinsically available to the lattice, and necessitate the development of rationally designed *extrinsic* designer defects. This is exemplified by the first reports of any extrinsic optical doping in any magnetic vdW material in the system of Yb^{3+}:CrX_3, the focus of the following chapters within this thesis. The next section provides a brief overview of the optical characteristics of this system, followed by demonstrative uses of the new magneto-optical functionality brought about by these dopants.

1.5 Introduction of Extrinsic Optical Dopants in FM vdW Materials

Sparked by the 2017 demonstration of intrinsic ferromagnetic order in monolayer CrI_3,[18] the CrX_3 family (X = Cl, Br, I) has emerged as a leading class of compounds for research on manipulating low-dimensional magnetic order and its potential applications in spin-based electronic devices. The intriguing magnetic properties of CrI_3, such as its layer dependent AFM magnetic order in the few layer limit, have been exploited in the development of electric field controlled spin-filters[6], critical for spintronic applications. Strain engineering of $CrBr_3$ has led to the realization of Moiré magnetism, facilitating the controllable patterning of both AFM and FM order across a bilayer.[78] Pressure induced switching of interlayer FM to AFM order in $CrCl_3$ has been demonstrated, highlighting an additional external parameter for magnetic tunability.[79]

These few examples represent just a small portion of the ongoing *modern* research in leveraging and manipulating magnetic order in CrX_3. However this material has been known for decades, with fundamental investigation of the bulk form of this material class began in the 60's, with initial reports focused on the material magnetization,[80] and the optical response of the Cr^{3+} *d-d* crystal-field transitions to the lattice magnetization state.[81-83] Despite decades of investigation into this lattice family, the PL of these materials remained largely overlooked throughout their

history, as exemplified the first reported PL spectra of CrI_3 only being publish in 2018 and of the monolayer.[12] This oversight is likely due to the featureless broadband PL of the native lattice, which limits fundamental investigations into the material optical properties. However, as will be shown, the introduction of the luminescent dopant Yb^{3+} completely transforms the emissive nature of the CrX_3, while preserving the remarkable magnetic properties of the lattice.

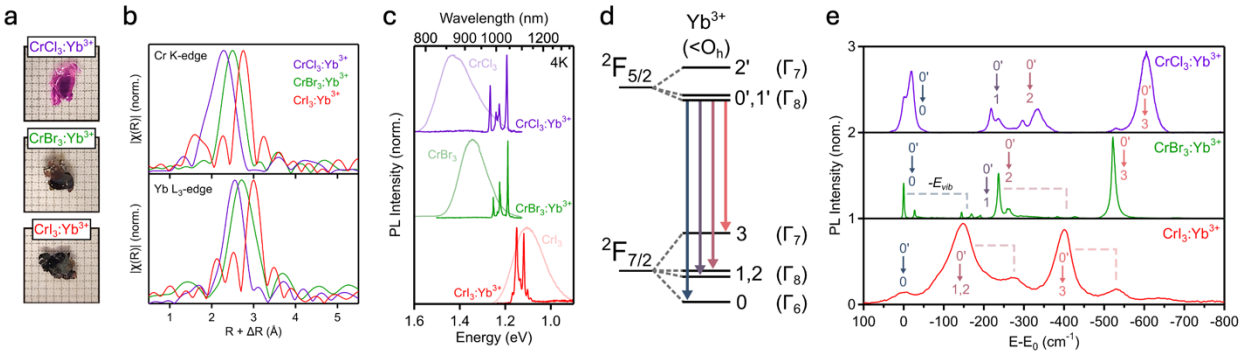

Figure 1.4 (a) Photograph of as-grown single-crystal flakes of Yb^{3+}:CrX_3 (X = Cl, Br, I). The minor grid size is 1 x 1 mm^2. **(b)** Fourier-transformed EXAFS data for Yb^{3+}:CrX_3 (X = Cl, Br, I) measured at the Cr K-edge (top) and Yb L_3-edge (bottom) corresponding to the metal-ligand bond lengths. There is a consistent increase of ~0.25 Å for the Yb-X bond lengths as compared to the corresponding Cr-X bond length. **(c)** 4 K PL spectra of undoped and doped Yb^{3+}:CrX_3 (X = Cl, Br, I) measured via excitation of the lattice. Yb^{3+} doping concentrations are 2.0, 0.4, and 4.9% for X = Cl, Br, and I, respectively. The broad featureless PL corresponds to Cr^{3+} $^4T_{2g} \rightarrow {}^4A_{2g}$ luminescence. Upon doping, this emission is quenched and replaced by sharp Yb^{3+} $^2F_{5/2} \rightarrow {}^2F_{7/2}$ luminescence. **(d)** Energy diagram of the relevant Yb^{3+} electronic states, featuring splitting due to the pseudo-O_h crystal field. The colored arrows correspond to the transitions shown in panel f. **(e)** 4 K PL spectra of Yb^{3+}:CrX_3 (X = Cl, Br, I), with assigned transitions. The data are shifted energetically such that 0′ → 0 transition are aligned for easy comparison of the spectra across the halide series. Panel a,b,c adapted with permission from ref [16]. Panel d adapted with permission from ref [17].

Yb^{3+} doped CrX_3 crystal flakes can be prepared via chemical vapor transport (CVT) using elemental Yb in addition to the corresponding lattice precursors (Cr + I_2, $CrCl_3$, $CrBr_3$). Figure 1.4a depicts crystal flakes of as prepared Yb^{3+}:CrX_3 (X = Cl, Br, I) photographed on a grid paper with a minor grid size of 1 mm. The change in color of the flakes from pink to green to black is

attributed to the shift of the Cr^{3+} spin allowed *d-d* crystal field bands to lower energies as the halide changes from Cl to I. Via Extended X-ray Absorption Fine Structure (EXAFS) measurements, it is found that Yb^{3+} substitutionally incorporates for Cr^{3+}, forming local $[YbX_6]^{3-}$ units. Figure 1.4b shows Fourier-transformed (real-space) EXAFS spectra measured at both the Cr K-edge and Yb L_3-edge; these data are well fit to a single-scattering path of a nearest-neighbor halide in octahedral coordination. The Cr K-edge spectra displays a prominent peak in the range R + ΔR = 2–3 Å, associated with the Cr-X bond length.[84-86] The Yb L_3-edge spectra also shows a similar feature, but shifted by ~0.25 Å relative to the Cr-X bond length, indicating an increase in the Yb-X bond length, associated with the larger ionic radius of Yb^{3+} *vs* Cr^{3+} (87 *vs* 62 pm).[87]

With this evidence for substitutional incorporation of Yb^{3+} we now look at the transformation of the compounds PL. Figure 1.4c shows normalized 4K PL spectra of undoped and Yb^{3+} doped CrX_3 (X = Cl, Br, I). The undoped compounds exhibit broad featureless Cr^{3+} *d-d* emission, associated with the Cr^{3+} $^4T_{2g} \rightarrow {}^4A_{2g}$ transition, which upon doping is replaced by a series of sharp line Yb^{3+} *f-f* emission features. Figure 1.4d depicts the electronic structure of Yb^{3+} in CrX_3 corresponding to the observed transitions. Spin-orbit coupling acts to split the Yb^{3+} free ion term into the $^2F_{5/2}$ (excited) and $^2F_{7/2}$ (ground) state. These states are further split by the crystal field, which in CrX_3 is pseudo-octahedral, with a minor low-symmetry splitting of the Γ_8 origin in both the ground and excited state as compared to idealized O_h symmetry. The observed low temperature PL transitions originating from the lowest excited state energy level (0′) to the ground state crystal field split energy levels (0,1,2,3) are indicated with arrows. These transitions are labeled in Figure 1.4e which compares the Yb^{3+} emission of the three halide compositions, with the spectra offset in energy such that $0' \rightarrow 0$ transition are aligned for ease of comparison. The dashed lines indicate vibronic progressions built upon the electronic origins associated with local distortions of the $[YbX_6]^{3-}$ unit.

When comparing across the halide series, the doped iodide features two notable distinctions in comparison to the bromide and chloride; namely the Yb^{3+} PL occurs at considerably lower energies and exhibits much broader and less resolved spectral features. These effects are attributed to exceptionally high Yb-I covalency in Yb^{3+}:CrI_3. High covalency acts to expand the *f-*

electron wavefunction, resulting in reduced interelectronic repulsion. This, in turn, results in a reduction of spin-orbit coupling as compared to that of the free ion, reducing the energy difference between the $^2F_{5/2}$ excited and $^2F_{7/2}$ ground state, and shifting the observed PL to lower energies. Typically, *f*-orbital covalency in trivalent lanthanides is minor, however the exceptionally low-lying ligand-to-metal charge-transfer (LMCT) band in CrI_3 acts to increase the extent of hybridization between the metal's valence orbitals and the ligand valence atomic orbitals. As a secondary effect, the integration of the relatively large Yb^{3+} ion into the smaller metal cation Cr^{3+} site acts to increase the Yb-I covalency in Yb^{3+}:CrX_3, as the lattice can be thought of as exerting an "internal pressure" on the local $[YbI_6]^{3-}$ unit, increasing the Yb^{3+} and I^- orbital overlap. These aspects, and other considerations of the covalent nature of Yb^{3+}:CrX_3, are explored in further detail in Chapter 2. We now turn to the excitation dynamics of how the excited state energy is transferred to the spatially isolated luminescent Yb^{3+} centers.

CrX_3 (X = Cl^-, Br^-, I^-) compounds feature highly localized Frenkel excitons,[88-90] with excitations essentially confined to single Cr^{3+} centers.[88, 91] These excitations may be described using the ligand-field model, which explains the absorption/emissive features as *d-d* and ligand-to-metal charge-transfer (LMCT) transitions centered at individual CrX_6^{3-} pseudo-octahedra.[83, 92, 93] As such, for the sensitization of low concentration Yb^{3+} dopants, this localized exciton must migrate throughout the lattice before encountering, and transferring energy to Yb^{3+}. This diffusion behavior can be modeled as an incoherent site-to-site hopping process.[94] Figure 1.5 schematically depicts this process in CrI_3. Due to the strong-electron phonon coupling in CrI_3, absorption of a photon results in a large distortion of the excited-state CrX_6^{3-} pseudo-octahedra, depicted by the single-configurational-coordinate diagram showing the $^4A_{2g} \rightarrow {}^4T_{2g}$ transition along the A_{1g} local nuclear coordinate (displacement along the Jahn-Teller coordinate (E_g) is also expected[95] but not shown for simplicity). This large excited-state distortion stabilizes the excited state by a reorganization energy, E_R, which may be estimated from the PL Stokes shift of CrI_3 via $E_{Stokes} = 2E_R$, giving $E_R \approx 200$ meV for CrI_3.[12] Such a large E_R requires a large nuclear reorganization for the exciton to hop from one Cr^{3+} site to a neighboring site.

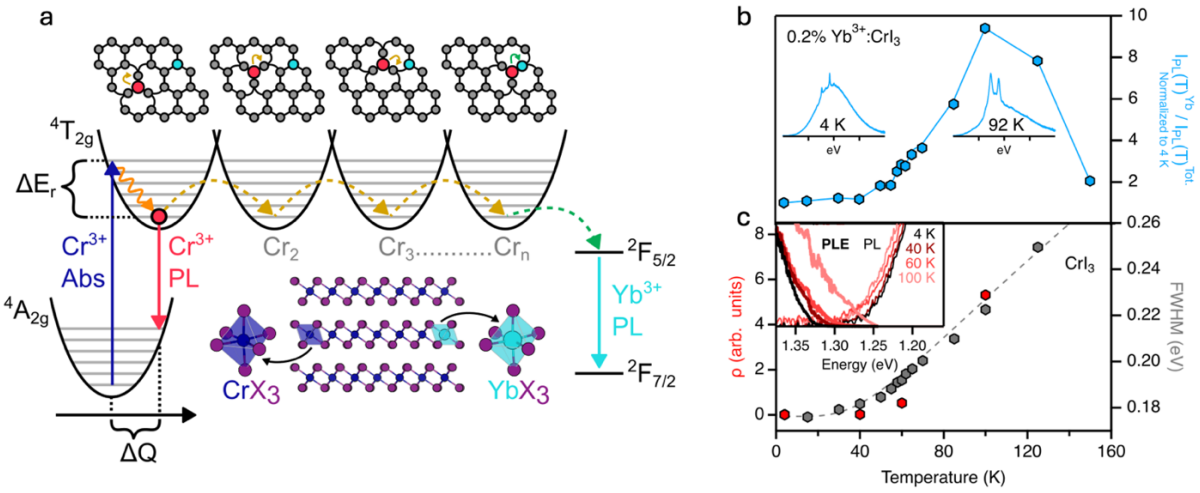

Figure 1.5 (a) Schematic depiction of excited state energy dynamics in Yb^{3+}:CrX_3. The exciton is stabilized at individual Cr^{3+} sites due to the large nuclear reorganization energy (E_R) associated with vibrational distortions along multiple nuclear coordinates such as the A_{1g} mode and E_g mode (not pictured). The exciton migrates about individual layers via site-to-site hopping involving short-range Dexter energy transfer between neighboring Cr^{3+} ions, with final step transfer to Yb^{3+}.**(b)** Plot of integrated Yb^{3+} as a portion of the total luminescence intensity normalized to their 4 K value for 0.2% Yb^{3+}:CrI_3. Also shown are the PL spectra at 4 K and 92 K. **(c)** Plot of the FWHM of CrI_3 (grey) overlayed with the calculated spectral overlap (ρ) of the Cr^{3+} $^4T_{2g} \rightarrow {}^4A_{2g}$ PL and $^4T_{2g} \leftarrow {}^4A_{2g}$ absorption, as measured via PLE. Inset: Plot of PLE (bold) and PL spectra for CrI_3 at 4, 40, 60, and 100 K. The PL spectra are normalized to a unit area.

Given such an energy barrier, the diffusion of the exciton in CrI_3 is expected to be highly temperature dependent. Figure 1.5b highlights this temperature dependance for lightly doped 0.2% Yb^{3+}:CrI_3 and depicts the ratio of the integrated Yb^{3+} ($I_{PL}{}^{Yb}$) PL intensity divided by the total integrated PL intensity, normalized to the 4 K value, with additional demonstrative spectra shown at 4 K and 92 K. At low temperatures the PL intensity is dominated by Cr^{3+} emission, as at such low doping concentrations the exciton must travel large distances before encountering the dilute Yb^{3+}, and this diffusive process is limited by the lifetime of the Cr^{3+} excited state. However, at ~50 K, there is a rapid increase in the intensity of Yb^{3+} emission, corresponding to an increase in the exciton diffusion length and increased proportional energy harvesting by Yb^{3+}. This increase in diffusion length is attributed to an increase in the site to site hopping rate between

adjacent Cr^{3+} centers (k_{Cr}^{hop}(T)), which may be described within the framework of Fermi's golden rule, as shown in eq 1.

$$k_{Cr}^{hop}(T) = \frac{2\pi}{\hbar}|M_{DA}|^2\rho(T) \quad (1)$$

Where M_{DA} describes the donor-acceptor electronic coupling and $\rho(T)$ is the temperature-dependent spectral-overlap factor, corresponding to the overlap of the Cr^{3+} $^4T_{2g} \rightarrow {}^4A_{2g}$ PL and $^4T_{2g} \leftarrow {}^4A_{2g}$ absorption. Figure 1.5b,c plots this spectral overlap factor, calculated from the experimental temperature dependent PL and PLE measurements shown in the panel inset. The spectral overlap displays the same temperature trend as the PL FWHM as with increasing temperature, higher vibrational excited states in the $^4A_{2g}$ ground and $^4T_{2g}$ excited electronic states of Cr^{3+} are thermally populated, leading to new absorption and PL intensities that increase the spectral overlap. These data show a marked similarity to the temperature dependent Yb^{3+} PL intensity shown in Figure 1.5b, with the exception of the drop in intensity at ~100 K. This drop is attributed to an increase in thermally activated non-radiative relaxation at each Cr^{3+} center, which dominates at higher temperatures, and acts to limit Yb^{3+} energy harvesting at high temperatures. Through the synthesis of a series of Yb^{3+}:CrI_3 samples with Yb^{3+} concentrations (0 to 30%) bolstered by Monte Carlo simulation, it is found that this nonradiative relaxation acts to limit the exciton diffusion length (L_D) below ~ 3 nm at all temperatures. A more detailed exploration of the excited state dynamics in Yb^{3+}:CrI_3 is explored in further detail in Chapter 5.

Prior to considering the magnetic aspects of Yb^{3+}:CrX_3, explored in the next section, it is worth noting the current literature that also investigates extrinsic optical dopants in vdW magnetic compounds. Currently, Ln^{3+}:CrX_3 represents the most well-researched example of optical extrinsic dopants in any magnetic vdW lattices, with extremely limited reports of any other optically active doped magnetic vdW compound. Recently, work by Xing et al.[96] has examined Cr^{3+} doping in AFM $MnPS_3$. It is valuable to briefly compare this transition metal dopant system to the Ln^{3+}:CrX_3 archetype in order to establish design principles for optical doping and to emphasize the advantages offered by isovalent Ln^{3+} doping.

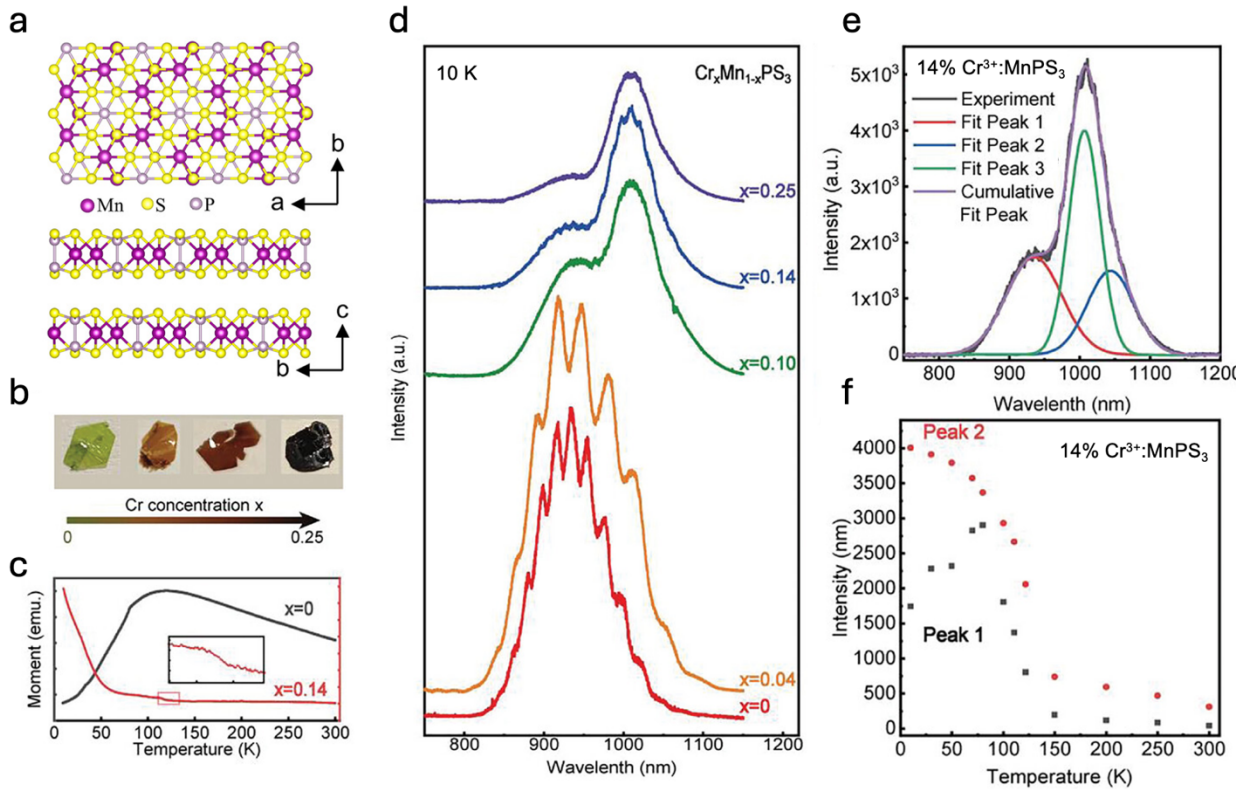

Figure 1.6 (a) Depiction of top and side views of layered $MnPS_3$, featuring the monoclinic $C/2m$ space group. **(b)** Photograph of as prepared flakes of $Cr_XMn_{1-x}PS_3$ with various Cr concentrations. **(c)** Temperature-dependent magnetic moment of undoped $MnPS_3$ (black), and $Cr_{0.14}Mn_{0.86}PS_3$ (red) measured under a 100 mT field applied parallel to the crystal *c*-axis. **(d)** 10 K PL of $Cr_XMn_{1-x}PS_3$ at various doping concentrations (x = 0, 0.04, 0.10, 0.14, 0.25). The feature at ~925 nm corresponds to the Cr^{3+} PL, while upon increased doping of Mn^{2+} a feature centered at ~1000 nm grows in intensity. The prominent periodic oscillation in the x = 0 and x = 0.04 dataset are instrumental artefacts due to the etaloning effect of the detector. **(e)** Peak fitting of the $Cr_{0.14}Mn_{0.86}PS_3$ 10 K PL shown in panel b, peak 1 is attributed to the host Mn^{2+} PL while peak 2 and 3 are both attributed to Cr^{3+} PL. **(f)** Temperature-dependent PL intensity of the lattice Mn^{2+} emission (peak 1) and the Cr^{3+} dopant emission (peak 2). Panel a adapted with permission from ref [97]. Panel b-f adapted with permission from ref [96].

Figure 1.6a depicts the crystal structure of $MnPS_3$, which crystallizes in the $C2/m$ space group, and features octahedrally coordinated Mn^{2+} bound to S with bridging P_2S_6 bipyramidal units. The family of transition metal phosphorus trichalcogenides (MPX_3, X = S, Se) is broad and has been successfully synthesized for most of the first row transition metals, including V, Mn, Fe, Co, Ni.[98] However, although Cr is stable in the 2+ oxidation state, there are no published reports for the

synthesis of $CrPS_3$, instead the trivalent chromium compound $CrPS_4$ is formed. This has been proposed to occur due to weaker M-S covalency of Cr when compared to the later first row transition metals (i.e. Mn, Fe, Co, Ni). This reduced Cr-S covalency acts to destabilize the P-P dimerization, causing a change in valence of the P_2S_6 unit from 4- to 6-, accommodating the trivalent Cr^{3+} and formation of $CrPS_4$.[99, 100] As such, Cr^{3+} doping in MPS_3 results in inherent instability of the host lattice, in contrast to Ln^{3+} doping in MX_3, whereby the complete LnX_3 analogues is isostructural with CrX_3. However, Xing et al.[96] report the successful formation of Cr^{3+}:$MnPS_3$ with up to 25% Cr doping (Figure 1.6b). X-ray diffraction (XRD) confirms the *C*2/*m* $MnPS_3$ crystal structure is retained. At high doping concentrations several XRD peaks are observed to shift to higher diffraction angles, indicating a reduction in the lattice parameter upon incorporation of the smaller Cr^{3+} cation for Mn^{2+} (0.62 Å for Cr^{3+} *vs* 0.83 Å for Mn^{2+}). As well, X-ray photoelectron spectroscopy (XPS) confirms the trivalent nature of Cr^{3+} in Cr^{3+}:$MnPS_3$. However, the introduction of Cr^{3+} greatly disrupts the long-range AFM order observed in the undoped lattice, rendering the doped lattice paramagnetic, as evidenced by temperature-dependent magnetization of undoped $MnPS_3$ and 14% Cr^{3+}:$MnPS_3$ (Figure 1.6c). Even the lowest doped sample (4% Cr^{3+}:$MnPS_3$) shows no signature of AFM order. Such reduction of long-range magnetic order upon doping highlights the need for careful choice of extrinsic dopants which do not disturb lattice crystallinity. Furthermore, the optical features introduced by Cr^{3+} doping are significantly broad, and lack the optimal signatures required for use in functional spin-photonic applications.

As shown in Figure 1.6d, at 10 K, undoped $MnPS_3$ exhibits a broad luminescent feature centered at 925 nm corresponding to emission from the Mn^{2+} (note: the periodic resonance over this feature is attributed to instrument artefacts and is not present in other publications containing $MnPS_3$ PL).[97] With increasing amounts of Cr^{3+} doping, a second feature centered at 1000 nm grows in intensity, corresponding to Cr^{3+} emission. Via peak deconvolution, it is shown that the emission feature that occurs with Cr^{3+} doping is comprised of two different features, labeled peak 2 and peak 3 (Figure 1.6e). The authors claim these two features behave identically and correspond to Cr^{3+}, but the presence of these features may indicate multiple Cr^{3+} species

occupying different site geometries, potentially a factor driven by the aliovalent nature of the doping. Figure 1.6f shows the temperature-dependent peak intensity of the Mn^{2+} emission (labeled peak 1) and the Cr^{3+} emission (labeled peak 2) for 14% Cr^{3+}:$MnPS_3$. Despite the absence of long-range AFM order (Figure 1.6c), the Mn^{2+} emission intensity is correlated with short-range AFM magnetic order and displays identical behavior to the temperature-dependent Mn^{2+} PL intensity of undoped $MnPS_3$, each showing a distinct reduction in intensity at T_N. However, no such signature of magnetic correlation is seen in the dopant Cr^{3+} PL intensity, indicating the distinct lack of magnetic integration of the TM dopant into the lattice.

This example demonstrates that while extrinsic dopants may introduce additional luminescent features to the host magnetic lattice, the magnetic integrity of the lattice may not always be preserved. In the next section, we will explore the strong magneto-optical coupling observed in Yb^{3+}:CrX_3, and highlight this dopant's potential as an optical handle for both probing and controlling the local magnetic order of the lattice.

1.6 Optical Dopants as Probes of Magnetic Order

Figure 1.7a shows magnetic circularly polarized luminescence (MCPL) of Yb^{3+}:CrI_3, at 5K measured under a small applied field used to align the ferromagnetic domains of the bulk crystal. All features show a degree of polarization, with the $\Gamma_8 \rightarrow \Gamma_7$ origin showing the highest polarization ratio ($\rho = (\sigma^- - \sigma^+)/(\sigma^- + \sigma^+) = 19\%$). Figure 1.7b plots ρ for the $\Gamma_8 \rightarrow \Gamma_7$ peak as a function of applied field. ρ exhibits a rapid increase in intensity, saturating at ~0.2 T, and demonstrates hysteretic behavior, with a coercive field of ~0.55 mT. This behavior is quite distinct from the expected magnetization of a pseudo-spin ½ paramagnetic Yb^{3+} ion, shown in purple, in which gradual rise in magnetization with complete saturation occurring at ~ 20 T would be expected. This behavior indicates the complete magnetic integration of Yb^{3+} in CrI_3, such that the Yb^{3+} magnetization is pinned to the magnetic order of the lattice, attributed to strong Yb^{3+}-Cr^{3+} superexchange coupling. The magnetic integrity of the lattice is found to be undisturbed by the incorporation of Yb^{3+}, as both traditional bulk magnetic characterization techniques, such as

Vibrating Sample Magnetometry (VSM), and optical detection of Yb^{3+} polarization indicate a T_C of 61 K (Figure 1.7c), identical to T_C of undoped CrI_3.

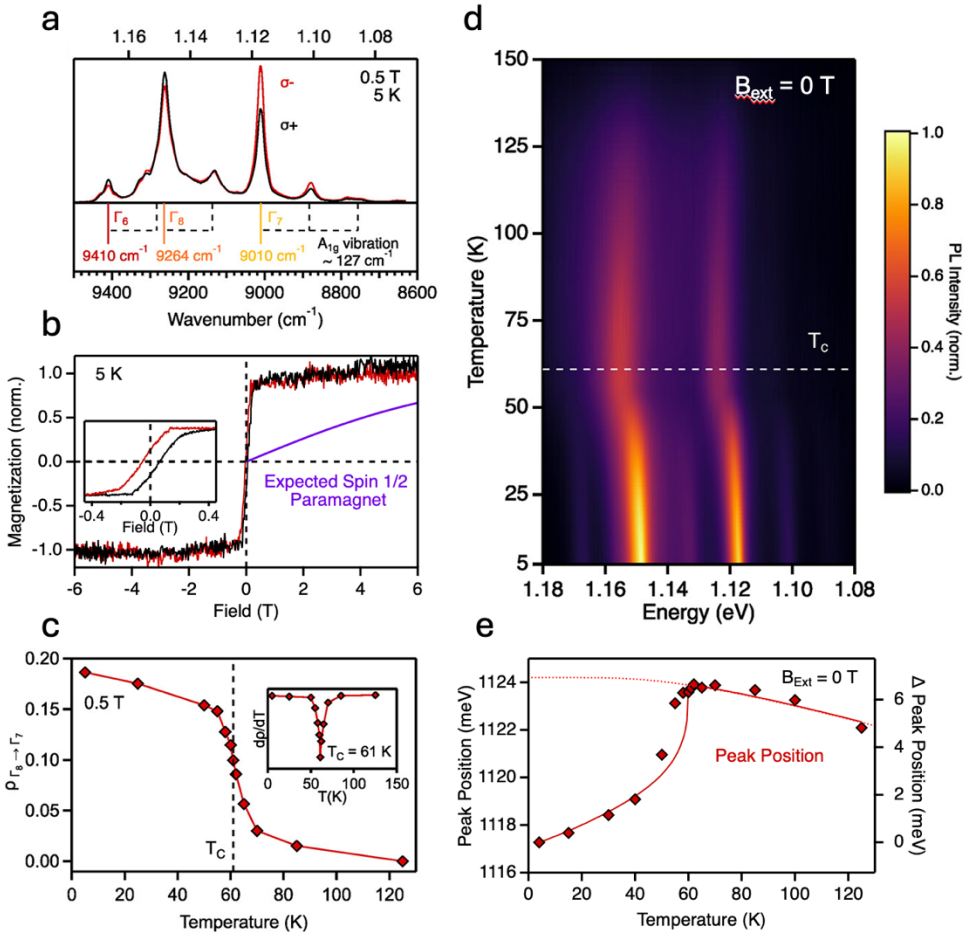

Figure 1.7 (a) Magnetic circularly polarized luminescence (MCPL) spectra of 4.9% Yb^{3+}:CrI_3 measured at 5 K with an applied magnetic field of 0.5 T. The σ^- (red) and σ^+ (black) spectra were collected using unpolarized 1.88 eV CW excitation at 40 mW/cm² and have different amplitudes. The three electronic origins in idealized O_h symmetry are indicated below the spectra, assigned to the $\Gamma_8 \rightarrow \Gamma_6$, Γ_8, and Γ_7 transitions illustrated in Figure 1.4d. The dashed black lines indicate vibronic sidebands with a characteristic energy spacing of ~127 cm–1 (15.7 meV), consistent with the A_{1g} lattice mode of CrI_3. **(b)** Polarization ratio of the $\Gamma_8 \rightarrow \Gamma_7$ electronic origin (1.117 eV) plotted as a function of magnetic field from −6 to 6 T. The black (red) trace corresponds to the positive (negative) field sweep direction. Inset: expanded plot of ρ between −0.4 and +0.4 T, showing a coercive field of ~55 mT. **(c)** Plot of the $\Gamma_8 \rightarrow \Gamma_7$ polarization ratio at the peak maximum measured at 0.5 T as a function of temperature. The red curve is a guide to the eye. Inset: derivative of ρ as a function of temperature. The extracted T_C is 61 K, indistinguishable from that of the undoped crystal. **(d)** False-color plot of the

Yb^{3+} PL intensities vs temperature measured for 4.9% Yb^{3+}:CrI_3 from 4 to 150 K at zero external magnetic field. The horizontal dashed line indicates T_C = 61 K. **(e)** Peak position of the $\Gamma_8 \rightarrow \Gamma_7$ transition plotted vs temperature. The dashed red curve shows the behavior expected from purely resonant phonon interactions, while the solid red curve shows behavior predicted with the addition of a spontaneous magnetization interaction, detailed in Chapter 3. Panel abcde adapted with permission from ref [15].

Remarkably, this magnetic sensitivity of Yb^{3+} can be seen in the absence of any external field. Below T_C and without an applied field, CrI_3 spontaneously orders ferromagnetically. However, the bulk crystal exhibits a zero net magnetization, owing to the presence of multiple magnetic domains with magnetization vectors randomly oriented in different directions. As a result, MCPL measurements show no detectable polarization. Nevertheless, the Yb^{3+} PL peak energy shifts in response to local magnetic ordering, as shown in Figure 1.7d,e. While lanthanide peak positions are expected to shift to higher energies when cooled due to changes in phonon population[101] (dashed line in Figure 7e), Yb^{3+}:CrI_3 deviates from this expected behavior. The abrupt decrease in peak energy is consistent with a second-order phase transition, reflecting the effects of spontaneous ferromagnetic ordering on Yb^{3+}. As such, Yb^{3+} acts as a local optical probe of the magnetic order in CrI_3 without the application of an external field. Such optical addressability of spin-states is ideal for magnetic sensing applications. These effects are explored in further depth in Chapter 3.

As previously described, the Yb^{3+} PL features in Yb^{3+}:CrI_3 are significantly broader than those observed in the either the bromide or chloride, owing to the unusually high degree of covalency in the iodide, which hinders a detailed analysis of the underlying electronic fine structure. Therefore, a more thorough examination of the Yb^{3+}:$CrBr_3$ is warranted. Via variable-temperature and variable-field PL measurements, it is found that the exchange coupling between Yb^{3+} and the surrounding magnetic $CrBr_3$ lattice acts to lift the degeneracy of the Yb^{3+} spin states, enabling the assignment of transitions between individual spin states. Figure 1.8a plots the Yb^{3+}:$CrBr_3$ PL corresponding to the $0' \rightarrow 0$ transition, both above and below T_C = 37 K. At 5 K, two peaks (A_1 and A_2) are observed, corresponding to transitions from the lowest spin split $0'$ excited state to

both spin components of the 0 ground state (labeled in Figure 1.8e). These peaks are split by 27 cm^{-1}, corresponding to the exchange splitting of the ground state (ΔE_{exch}^{GS}). At 10 K, thermal occupation of the higher lying 0′ spin state is accessed, resulting in the appearance of two new peaks (B_1 and B_2), also split by 27 cm^{-1}. From these transitions, the exchange splitting of the excited state(ΔE_{exch}^{ES}) can be found ($B_1 - A_1$ or $B_2 - A_2$), yielding a value of 16 cm^{-1}. Both ΔE_{exch}^{GS} and ΔE_{exch}^{ES} decrease with increasing temperature reflecting a reduction in lattice magnetization as T_C is approached. As explored further in Chapter 4, under the Curie-Weiss molecule field model, these exchange splittings correlate to an effective exchange field of ~30 T as experienced by the Yb^{3+} at the low temperature limit, due to the spontaneous magnetization of $CrBr_3$.

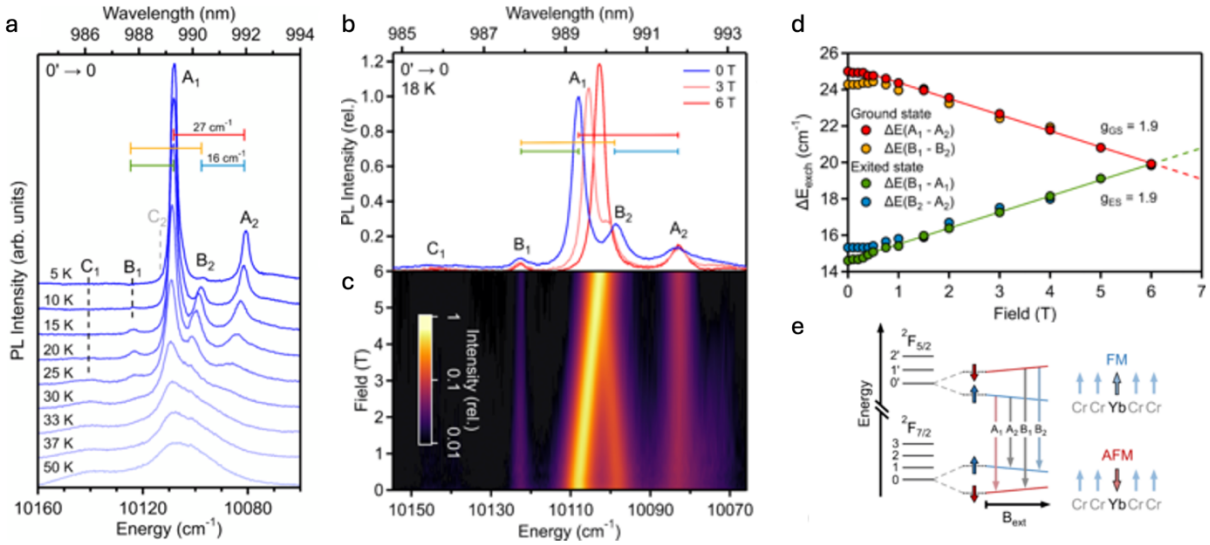

Figure 1.8 (a) VTPL of Yb^{3+}:$CrBr_3$ measured over the 0′→ 0 transition region. Peaks are labeled according to the transitions shown in panel e. (C_1 and C_2 correspond to small contributions of the thermally activated 1′→ 0 transitions. The colored bars correspond to the exchange splitting of the Yb^{3+} ground state (0) and excited state (0′) Kramers doublets. These splittings are plotted as a function of field in panel d. **(b)** 18K PL of Yb^{3+}:$CrBr_3$ measured at 0, 3 and 6 T. **(c)** False-color plot of the same PL shown in panel b. **(d)** Exchange splitting of the Yb^{3+} ground state (0) and excited state (0′) Kramers doublets plotted as a function of B_{ext}, including linear fits to the data above 0.5 T. **(e)** Energy diagram showing the effects of B_{ext} on Yb^{3+} energy states, depicting Yb^{3+} coupled AFM to the surrounding Cr^{3+} lattice in the ground state and FM in the excited state. Panel abcde adapted with permission from ref [17].

Via monitoring the field dependence of these spectral features, the nature of the coupling of the Yb^{3+} spin states to the surrounding lattice can be determined. Figure 1.8b and c depict the 18 K Yb^{3+} PL under the application of an external field from 0 to 6 T. Features B_1 and A_2 show no dependence on field, while features A_1 and B_2 display a redshift and blueshift respectively. Figure 1.8d plots ΔE_{exch}^{GS} and ΔE_{exch}^{ES} as a function of field. ΔE_{exch}^{GS} decreases while ΔE_{exch}^{ES} increases, with slopes corresponding to g values of similar magnitude, but opposite sign (~1.9). These observations indicate that Yb^{3+} exhibits AFM coupling to the surrounding Cr^{3+} lattice in the ground state, and upon excitations undergoes a spin flip, necessitated by the difference in total angular momentum between the Yb^{3+} $^2F_{7/2}$ and $^2F_{5/2}$ parent terms, leading to FM coupling in the excited state, as summarized in the energy diagram of Figure 1.8e. These well-resolved exchange-split levels of Yb^{3+} in $CrBr_3$ allow for selective optical manipulation of spin states, critically, in the absence of any external magnetic field, providing new avenues for precise spin preparation and readout in 2D vdW spin-photonic applications.

1.7 Summary

In summary, even at low concentrations, point defects can significantly modify the material properties of individual layers in atomically thin vdW compounds. While research into point defects as optical centers in magnetic vdW materials remains underexplored, the promising findings of spin-correlated intrinsic vacancy centers in CrSBr provide a compelling motivation for further investigation. However, the synthetic flexibility of *intrinsic* defects is inherently constrained by the atomic composition of the host lattice, limiting the ability to fine-tune defect characteristics. Excitingly, the promising results of Yb^{3+}:CrX_3 exemplify how *extrinsic* doping can impart new spin-correlated optical functionality into 2D magnetic materials. These findings pave the way for the exploration of a broader range of optical dopants from across the periodic table in magnetic vdW materials.

1.8 References

(1) Grebenchuk, S.; McKeever, C.; Grzeszczyk, M.; Chen, Z.; Šiškins, M.; McCray, A. R. C.; Li, Y.; Petford-Long, A. K.; Phatak, C. M.; Ruihuan, D.; et al. Topological Spin Textures in an Insulating van der Waals Ferromagnet. *J. Adv. Mater.* **2024**, *36* (24), 2311949.

(2) Huang, B.; McGuire, M. A.; May, A. F.; Xiao, D.; Jarillo-Herrero, P.; Xu, X. Emergent Phenomena and Proximity Effects in Two-Dimensional Magnets and Heterostructures. *Nat. Mater.* **2020**, *19* (12), 1276-1289.

(3) Tang, C.; Alahmed, L.; Mahdi, M.; Xiong, Y.; Inman, J.; McLaughlin, N. J.; Zollitsch, C.; Kim, T. H.; Du, C. R.; Kurebayashi, H.; et al. Spin dynamics in van der Waals magnetic systems. *Phys. Rep.* **2023**, *1032*, 1-36.

(4) Ghiasi, T. S.; Kaverzin, A. A.; Dismukes, A. H.; de Wal, D. K.; Roy, X.; van Wees, B. J. Electrical and thermal generation of spin currents by magnetic bilayer graphene. *Nat. Nanotechnol.* **2021**, *16* (7), 788-794.

(5) Marfoua, B.; Hong, J. Highly efficient spin-orbit torque generation in bilayer WTe_2/Fe_3GaTe_2 heterostructure. *Mater. Today Phys.* **2024**, *42*, 101378.

(6) Song, T.; Cai, X.; Tu, M. W.-Y.; Zhang, X.; Huang, B.; Wilson, N. P.; Seyler, K. L.; Zhu, L.; Taniguchi, T.; Watanabe, K.; et al. Giant Tunneling Magnetoresistance in Spin-Filter van der Waals Heterostructures. *Science* **2018**, *360* (6394), 1214-1218.

(7) Li, X.; Lü, J.-T.; Zhang, J.; You, L.; Su, Y.; Tsymbal, E. Y. Spin-Dependent Transport in van der Waals Magnetic Tunnel Junctions with Fe_3GeTe_2 Electrodes. *Nano Lett.* **2019**, *19* (8), 5133-5139.

(8) Lalieu, M. L. M.; Lavrijsen, R.; Koopmans, B. Integrating all-optical switching with spintronics. *Nat. Commun.* **2019**, *10* (1), 110.

(9) Žutić, I.; Xu, G.; Lindemann, M.; Faria Junior, P. E.; Lee, J.; Labinac, V.; Stojšić, K.; Sipahi, G. M.; Hofmann, M. R.; Gerhardt, N. C. Spin-lasers: spintronics beyond magnetoresistance. *Solid State Commun.* **2020**, *316-317*, 113949.

(10) Sierra, J. F.; Fabian, J.; Kawakami, R. K.; Roche, S.; Valenzuela, S. O. Van der Waals heterostructures for spintronics and opto-spintronics. *Nat. Nanotechnol.* **2021**, *16* (8), 856-868.

(11) Gish, J. T.; Lebedev, D.; Song, T. W.; Sangwan, V. K.; Hersam, M. C. Van der Waals opto-spintronics. *Nat. Electron.* **2024**, *7* (5), 336-347.

(12) Seyler, K. L.; Zhong, D.; Klein, D. R.; Gao, S.; Zhang, X.; Huang, B.; Navarro-Moratalla, E.; Yang, L.; Cobden, D. H.; McGuire, M. A.; et al. Ligand-field helical luminescence in a 2D ferromagnetic insulator. *Nat. Physics* **2018**, *14* (3), 277-281.

(13) Zhang, Z.; Shang, J.; Jiang, C.; Rasmita, A.; Gao, W.; Yu, T. Direct Photoluminescence Probing of Ferromagnetism in Monolayer Two-Dimensional $CrBr_3$. *Nano Lett.* **2019**, *19* (5), 3138-3142.

(14) Cai, X.; Song, T.; Wilson, N. P.; Clark, G.; He, M.; Zhang, X.; Taniguchi, T.; Watanabe, K.; Yao, W.; Xiao, D.; et al. Atomically Thin $CrCl_3$: An In-Plane Layered Antiferromagnetic Insulator. *Nano Lett.* **2019**, *19* (6), 3993-3998.

(15) Pressler, K.; Snoeren, T. J.; Walsh, K. M.; Gamelin, D. R. Magnetic Amplification at Yb^{3+} "Designer Defects" in the van der Waals Ferromagnet CrI_3. *Nano Lett.* **2023**, *23* (4), 1320-

1326.
(16) Snoeren, T. J.; Pressler, K.; Kluherz, K. T.; Walsh, K. M.; De Yoreo, J. J.; Gamelin, D. R. Luminescence and Covalency in Ytterbium-Doped CrX_3 (X = Cl, Br, I) van der Waals Compounds. *J. Am. Chem. Soc.* **2023**, *145* (31), 17427-17434.
(17) Snoeren, T. J.; Pressler, K.; Gamelin, D. R. Optically resolved exchange splittings in the doped van der Waals ferromagnet $CrBr_3$:Yb^{3+}. *Phys. Rev. Mater.* **2024**, *8* (10), 104410.
(18) Huang, B.; Clark, G.; Navarro-Moratalla, E.; Klein, D. R.; Cheng, R.; Seyler, K. L.; Zhong, D.; Schmidgall, E.; McGuire, M. A.; Cobden, D. H.; et al. Layer-Dependent Ferromagnetism in a van der Waals Crystal Down to the Monolayer Limit. *Nature* **2017**, *546* (7657), 270-273.
(19) Gong, C.; Li, L.; Li, Z.; Ji, H.; Stern, A.; Xia, Y.; Cao, T.; Bao, W.; Wang, C.; Wang, Y.; et al. Discovery of intrinsic ferromagnetism in two-dimensional van der Waals crystals. *Nature* **2017**, *546* (7657), 265-269.
(20) Spitaler, J.; Estreicher, S. K. Perspectives on the theory of defects. *Front. Mater.* **2018**, *5*, 70.
(21) Jiang, J.; Xu, T.; Lu, J.; Sun, L.; Ni, Z. Defect Engineering in 2D Materials: Precise Manipulation and Improved Functionalities. *Research* **2019**, *2019*.
(22) Brinkman, W. F.; Haggan, D. E.; Troutman, W. W. A history of the invention of the transistor and where it will lead us. *IEEE J. Solid-State Circuits* **1997**, *32* (12), 1858-1865.
(23) Maiman, T. H. Stimulated Optical Radiation in Ruby. *Nature* **1960**, *187* (4736), 493-494.
(24) Day, D.; Gu, M.; Smallridge, A. Review of Optical Data Storage. In *Infrared Holography for Optical Communications: Techniques, Materials, and Devices*, Boffi, P., Piccinin, D., Ubaldi, M. C. Eds.; Springer Berlin Heidelberg, 2003; pp 1-22.
(25) Waldrop, M. M. The chips are down for Moore's law. *Nature News* **2016**, *530* (7589), 144.
(26) Novoselov, K. S.; Geim, A. K.; Morozov, S. V.; Jiang, D.; Zhang, Y.; Dubonos, S. V.; Grigorieva, I. V.; Firsov, A. A. Electric Field Effect in Atomically Thin Carbon Films. *Science* **2004**, *306* (5696), 666-669.
(27) Zhang, G.; Wu, H.; Zhang, L.; Yang, L.; Xie, Y.; Guo, F.; Li, H.; Tao, B.; Wang, G.; Zhang, W.; et al. Two-Dimensional van Der Waals Topological Materials: Preparation, Properties, and Device Applications. *Small* **2022**, *18* (47), 2204380.
(28) Walsh, L. A.; Hinkle, C. L. van der Waals epitaxy: 2D materials and topological insulators. *Appl. Mater. Today* **2017**, *9*, 504-515.
(29) Rivera, P.; Seyler, K. L.; Yu, H.; Schaibley, J. R.; Yan, J.; Mandrus, D. G.; Yao, W.; Xu, X. Valley-polarized exciton dynamics in a 2D semiconductor heterostructure. *Science* **2016**, *351* (6274), 688-691.
(30) Chen, Y.-J.; Cain, J. D.; Stanev, T. K.; Dravid, V. P.; Stern, N. P. Valley-polarized exciton–polaritons in a monolayer semiconductor. *Nat. Photonics* **2017**, *11* (7), 431-435.
(31) Dai, M.; Wang, Z.; Wang, F.; Qiu, Y.; Zhang, J.; Xu, C.-Y.; Zhai, T.; Cao, W.; Fu, Y.; Jia, D.; et al. Two-Dimensional van der Waals Materials with Aligned In-Plane Polarization and Large Piezoelectric Effect for Self-Powered Piezoelectric Sensors. *Nano Lett.* **2019**, *19* (8), 5410-5416.
(32) Cui, C.; Xue, F.; Hu, W.-J.; Li, L.-J. Two-dimensional materials with piezoelectric and ferroelectric functionalities. *npj 2D Mater. Appl.* **2018**, *2* (1), 18.
(33) Navarro-Moratalla, E.; Island, J. O.; Mañas-Valero, S.; Pinilla-Cienfuegos, E.; Castellanos-Gomez, A.; Quereda, J.; Rubio-Bollinger, G.; Chirolli, L.; Silva-Guillén, J. A.; Agraït, N.; et

al. Enhanced superconductivity in atomically thin TaS_2. *Nat. Commun.* **2016**, *7* (1), 11043.
(34) Dvir, T.; Massee, F.; Attias, L.; Khodas, M.; Aprili, M.; Quay, C. H. L.; Steinberg, H. Spectroscopy of bulk and few-layer superconducting $NbSe_2$ with van der Waals tunnel junctions. *Nat. Commun.* **2018**, *9* (1), 598.
(35) Li, S.; Wang, F.; Wang, Y.; Yang, J.; Wang, X.; Zhan, X.; He, J.; Wang, Z. Van der Waals Ferroelectrics: Theories, Materials, and Device Applications. *J. Adv. Mater.* **2024**, *36* (22), 2301472.
(36) Butler, S. Z.; Hollen, S. M.; Cao, L.; Cui, Y.; Gupta, J. A.; Gutiérrez, H. R.; Heinz, T. F.; Hong, S. S.; Huang, J.; Ismach, A. F.; et al. Progress, Challenges, and Opportunities in Two-Dimensional Materials Beyond Graphene. *ACS Nano* **2013**, *7* (4), 2898-2926.
(37) Novoselov, K. S.; Mishchenko, A.; Carvalho, A.; Castro Neto, A. H. 2D materials and van der Waals heterostructures. *Science* **2016**, *353* (6298), aac9439.
(38) Wu, F.; Lovorn, T.; MacDonald, A. H. Topological Exciton Bands in Moiré Heterojunctions. *Phys. Rev. Lett.* **2017**, *118* (14), 147401.
(39) Jin, C.; Regan, E. C.; Yan, A.; Iqbal Bakti Utama, M.; Wang, D.; Zhao, S.; Qin, Y.; Yang, S.; Zheng, Z.; Shi, S.; et al. Observation of moiré excitons in WSe_2/WS_2 heterostructure superlattices. *Nature* **2019**, *567* (7746), 76-80.
(40) He, F.; Zhou, Y.; Ye, Z.; Cho, S.-H.; Jeong, J.; Meng, X.; Wang, Y. Moiré Patterns in 2D Materials: A Review. *ACS Nano* **2021**, *15* (4), 5944-5958.
(41) Huang, C.; Narayan, A.; Zhang, E.; Liu, Y.; Yan, X.; Wang, J.; Zhang, C.; Wang, W.; Zhou, T.; Yi, C.; et al. Inducing Strong Superconductivity in WTe_2 by a Proximity Effect. *ACS Nano* **2018**, *12* (7), 7185-7196.
(42) Jiang, Y.; Chen, S.; Zheng, W.; Zheng, B.; Pan, A. Interlayer exciton formation, relaxation, and transport in TMD van der Waals heterostructures. *Light Sci. Appl.* **2021**, *10* (1), 72.
(43) Regan, E. C.; Wang, D.; Paik, E. Y.; Zeng, Y.; Zhang, L.; Zhu, J.; MacDonald, A. H.; Deng, H.; Wang, F. Emerging exciton physics in transition metal dichalcogenide heterobilayers. *Nat. Rev. Mater.* **2022**, *7* (10), 778-795.
(44) Rajapakse, M.; Karki, B.; Abu, U. O.; Pishgar, S.; Musa, M. R. K.; Riyadh, S. M. S.; Yu, M.; Sumanasekera, G.; Jasinski, J. B. Intercalation as a versatile tool for fabrication, property tuning, and phase transitions in 2D materials. *npj 2D Mater. Appl.* **2021**, *5* (1), 30.
(45) Furdyna, J. K.; Kossut, J. *Diluted Magnetic Semiconductors*; Academic, 1988.
(46) Gaj, J. A.; Kossut, J. *Introduction to the physics of diluted magnetic semiconductors*; Springer Science & Business Media, 2011.
(47) Zhang, K.; Feng, S.; Wang, J.; Azcatl, A.; Lu, N.; Addou, R.; Wang, N.; Zhou, C.; Lerach, J.; Bojan, V.; et al. Manganese Doping of Monolayer MoS_2: The Substrate Is Critical. *Nano Lett.* **2015**, *15* (10), 6586-6591.
(48) Wang, S. Y.; Ko, T. S.; Huang, C. C.; Lin, D. Y.; Huang, Y. S. Optical and electrical properties of MoS_2 and Fe-doped MoS_2. *Japanese Journal of Applied Physics* **2014**, *53* (4S), 04EH07.
(49) Zhao, X.; Xia, C.; Wang, T.; Dai, X. Effect of structural defects on electronic and magnetic properties of pristine and Mn-doped MoS_2 monolayer. *Solid State Commun.* **2015**, *220*, 31-35.
(50) Tedstone, A. A.; Lewis, D. J.; O'Brien, P. Synthesis, Properties, and Applications of Transition Metal-Doped Layered Transition Metal Dichalcogenides. *Chem. Mater.* **2016**, *28* (7), 1965-

1974.
(51) Shinn-Sheng, Y.; Ven-Chung, L. Indirect exchange interaction in diluted magnetic semiconductors. *J. Phys. Condens. Matter* **1992**, *4* (11), 2961.
(52) Duan, H.; Guo, P.; Wang, C.; Tan, H.; Hu, W.; Yan, W.; Ma, C.; Cai, L.; Song, L.; Zhang, W.; et al. Beating the exclusion rule against the coexistence of robust luminescence and ferromagnetism in chalcogenide monolayers. *Nat. Commun.* **2019**, *10* (1), 1584.
(53) Wang, H.; Zhang, C.; Rana, F. Ultrafast Dynamics of Defect-Assisted Electron–Hole Recombination in Monolayer MoS_2. *Nano Lett.* **2015**, *15* (1), 339-345.
(54) Sahoo, K. R.; Talluri, M.; Maity, D.; Mundlia, S.; Lal, A.; Devapriya, M.; Haldar, A.; Murapaka, C.; Narayanan, T. N. Vanadium Doped Magnetic MoS_2 Monolayers of Improved Electrical Conductivity as Spin-Orbit Torque Layer. *arXiv preprint arXiv:2411.09277* **2024**.
(55) Zhang, J.; Zhu, Y.; Tebyetekerwa, M.; Li, D.; Liu, D.; Lei, W.; Wang, L.; Zhang, Y.; Lu, Y. Vanadium-Doped Monolayer MoS_2 with Tunable Optical Properties for Field-Effect Transistors. *ACS Appl. Nano Mater.* **2021**, *4* (1), 769-777.
(56) Ho, C.-H.; Chen, W.-H.; Tiong, K. K.; Lee, K.-Y.; Gloter, A.; Zobelli, A.; Stephan, O.; Tizei, L. H. G. Interplay Between Cr Dopants and Vacancy Clustering in the Structural and Optical Properties of WSe_2. *ACS Nano* **2017**, *11* (11), 11162-11168.
(57) Fan, X.-L.; An, Y.-R.; Guo, W.-J. Ferromagnetism in Transitional Metal-Doped MoS_2 Monolayer. *Nanoscale Res. Lett.* **2016**, *11* (1), 154.
(58) Baranov, P. G.; Bundakova, A. P.; Soltamova, A. A.; Orlinskii, S. B.; Borovykh, I. V.; Zondervan, R.; Verberk, R.; Schmidt, J. Silicon vacancy in SiC as a promising quantum system for single-defect and single-photon spectroscopy. *Phys. Rev. B* **2011**, *83* (12), 125203.
(59) Bathen, M. E.; Galeckas, A.; Müting, J.; Ayedh, H. M.; Grossner, U.; Coutinho, J.; Frodason, Y. K.; Vines, L. Electrical charge state identification and control for the silicon vacancy in 4H-SiC. *Npj Quantum Inf.* **2019**, *5* (1), 111.
(60) Lohrmann, A.; Iwamoto, N.; Bodrog, Z.; Castelletto, S.; Ohshima, T.; Karle, T. J.; Gali, A.; Prawer, S.; McCallum, J. C.; Johnson, B. C. Single-photon emitting diode in silicon carbide. *Nat. Commun.* **2015**, *6* (1), 7783.
(61) Christle, D. J.; Falk, A. L.; Andrich, P.; Klimov, P. V.; Hassan, J. U.; Son, Nguyen T.; Janzén, E.; Ohshima, T.; Awschalom, D. D. Isolated electron spins in silicon carbide with millisecond coherence times. *Nat. Mater.* **2015**, *14* (2), 160-163.
(62) Radulaski, M.; Widmann, M.; Niethammer, M.; Zhang, J. L.; Lee, S.-Y.; Rendler, T.; Lagoudakis, K. G.; Son, N. T.; Janzén, E.; Ohshima, T.; et al. Scalable Quantum Photonics with Single Color Centers in Silicon Carbide. *Nano Lett.* **2017**, *17* (3), 1782-1786.
(63) Simin, D.; Fuchs, F.; Kraus, H.; Sperlich, A.; Baranov, P. G.; Astakhov, G. V.; Dyakonov, V. High-Precision Angle-Resolved Magnetometry with Uniaxial Quantum Centers in Silicon Carbide. *Phys. Rev. Appl.* **2015**, *4* (1), 014009.
(64) Bracher, D. O.; Zhang, X.; Hu, E. L. Selective Purcell enhancement of two closely linked zero-phonon transitions of a silicon carbide color center. *PNAS* **2017**, *114* (16), 4060-4065.
(65) Mitterreiter, E.; Schuler, B.; Micevic, A.; Hernangómez-Pérez, D.; Barthelmi, K.; Cochrane, K. A.; Kiemle, J.; Sigger, F.; Klein, J.; Wong, E.; et al. The role of chalcogen vacancies for atomic defect emission in MoS_2. *Nat. Commun.* **2021**, *12* (1), 3822.
(66) Whitefield, B.; Toth, M.; Aharonovich, I.; Tetienne, J.-P.; Kianinia, M. Magnetic Field

Sensitivity Optimization of Negatively Charged Boron Vacancy Defects in hBN. *Adv. Quantum Technol.*, 2300118.

(67) Ali, S.; Nilsson, F. A.; Manti, S.; Bertoldo, F.; Mortensen, J. J.; Thygesen, K. S. High-Throughput Search for Triplet Point Defects with Narrow Emission Lines in 2D Materials. *ACS Nano* **2023**, *17* (21), 21105-21115.

(68) Klein, J.; Song, Z.; Pingault, B.; Dirnberger, F.; Chi, H.; Curtis, J. B.; Dana, R.; Bushati, R.; Quan, J.; Dekanovsky, L.; et al. Sensing the Local Magnetic Environment Through Optically Active Defects in a Layered Magnetic Semiconductor. *ACS Nano* **2023**, *17* (1), 288-299.

(69) Telford, E. J.; Dismukes, A. H.; Dudley, R. L.; Wiscons, R. A.; Lee, K.; Chica, D. G.; Ziebel, M. E.; Han, M.-G.; Yu, J.; Shabani, S.; et al. Coupling between magnetic order and charge transport in a two-dimensional magnetic semiconductor. *Nat. Mater.* **2022**, *21* (7), 754-760.

(70) López-Paz, S. A.; Guguchia, Z.; Pomjakushin, V. Y.; Witteveen, C.; Cervellino, A.; Luetkens, H.; Casati, N.; Morpurgo, A. F.; von Rohr, F. O. Dynamic magnetic crossover at the origin of the hidden-order in van der Waals antiferromagnet CrSBr. *Nat. Commun.* **2022**, *13* (1), 4745.

(71) Torres, K.; Kuc, A.; Maschio, L.; Pham, T.; Reidy, K.; Dekanovsky, L.; Sofer, Z.; Ross, F. M.; Klein, J. Probing Defects and Spin-Phonon Coupling in CrSBr via Resonant Raman Scattering. *Adv. Funct. Mater.* **2023**, *33* (12), 2211366.

(72) Long, F.; Ghorbani-Asl, M.; Mosina, K.; Li, Y.; Lin, K.; Ganss, F.; Hübner, R.; Sofer, Z.; Dirnberger, F.; Kamra, A.; et al. Ferromagnetic Interlayer Coupling in CrSBr Crystals Irradiated by Ions. *Nano Lett.* **2023**, *23* (18), 8468-8473.

(73) Wilson, N. P.; Lee, K.; Cenker, J.; Xie, K.; Dismukes, A. H.; Telford, E. J.; Fonseca, J.; Sivakumar, S.; Dean, C.; Cao, T.; et al. Interlayer electronic coupling on demand in a 2D magnetic semiconductor. *Nat. Mater.* **2021**, *20* (12), 1657-1662.

(74) Klein, J.; Lorke, M.; Florian, M.; Sigger, F.; Sigl, L.; Rey, S.; Wierzbowski, J.; Cerne, J.; Müller, K.; Mitterreiter, E.; et al. Site-selectively generated photon emitters in monolayer MoS_2 via local helium ion irradiation. *Nat. Commun.* **2019**, *10* (1), 2755.

(75) Melchioni, N.; Fabbri, F.; Tredicucci, A.; Bianco, F. Periodic Structural Defects in Graphene Sheets Engineered via Electron Irradiation. *Micromachines (Basel)* **2022**, *13* (10). From NLM.

(76) Kim, S.; Yoon, S.; Ahn, H.; Jin, G.; Kim, H.; Jo, M.-H.; Lee, C.; Kim, J.; Ryu, S. Photoluminescence Path Bifurcations by Spin Flip in Two-Dimensional $CrPS_4$. *ACS Nano* **2022**, *16* (10), 16385-16393.

(77) Shi, P.; Wang, X.; Zhang, L.; Song, W.; Yang, K.; Wang, S.; Zhang, R.; Zhang, L.; Taniguchi, T.; Watanabe, K.; et al. Magnetoresistance Oscillations in Vertical Junctions of 2D Antiferromagnetic Semiconductor $CrPS_4$. *Phys. Rev. X* **2024**, *14* (4), 041065.

(78) Yao, F.; Rossi, D.; Gabrovski, I. A.; Multian, V.; Hua, N.; Watanabe, K.; Taniguchi, T.; Gibertini, M.; Gutiérrez-Lezama, I.; Rademaker, L.; et al. Moiré magnetism in CrBr3 multilayers emerging from differential strain. *Nat. Commun.* **2024**, *15* (1), 10377.

(79) Ahmad, A. S.; Liang, Y.; Dong, M.; Zhou, X.; Fang, L.; Xia, Y.; Dai, J.; Yan, X.; Yu, X.; Dai, J.; et al. Pressure-driven switching of magnetism in layered CrCl3. *Nanoscale* **2020**, *12* (45), 22935-22944, 10.1039/D0NR04325G.

(80) Hansen, W. N. Some Magnetic Properties of the Chromium (III) Halides at 4.2°K. *J. Appl. Phys.* **1959**, *30* (4), S304-S305.
(81) Dillon, J. F., Jr.; Olson, C. E. Magnetization, Resonance, and Optical Properties of the Ferromagnet CrI_3. *J. Appl. Phys.* **1965**, *36* (3), 1259-1260.
(82) Bermudez, V. M.; McClure, D. S. Spectroscopic studies of the two-dimensional magnetic insulators chromium trichloride and chromium tribromide—II. *J. Phys. Chem. Solids* **1979**, *40*, 149-173.
(83) Bermudez, V. M.; McClure, D. S. Spectroscopic studies of the two-dimensional magnetic insulators chromium trichloride and chromium tribromide—I. *J. Phys. Chem. Solids.* **1979**, *40* (2), 129-147.
(84) McGuire, M. A.; Dixit, H.; Cooper, V. R.; Sales, B. C. Coupling of Crystal Structure and Magnetism in the Layered, Ferromagnetic Insulator CrI_3. *Chem. Mater.* **2015**, *27* (2), 612-620.
(85) Morosin, B.; Narath, A. X-Ray Diffraction and Nuclear Quadrupole Resonance Studies of Chromium Trichloride. *J. Chem. Phys.* **1964**, *40* (7), 1958-1967.
(86) Braekken, H. The Crystal Structure of Chromium Tribromide (Eng. Transl.). *K. Nor. Vidensk. Selsk.* **1932**, *5* (42).
(87) Shannon, R. Revised Effective Ionic Radii and Systematic Study of Inter Atomic Distances in Halides and Chalcogenides. *Acta Crystallogr. A.* **1976**, *32*, 751-767.
(88) Acharya, S.; Pashov, D.; Rudenko, A. N.; Rösner, M.; Schilfgaarde, M. v.; Katsnelson, M. I. Real- and momentum-space description of the excitons in bulk and monolayer chromium tri-halides. *npj 2D Mater. Appl.* **2022**, *6* (1), 33.
(89) Grzeszczyk, M.; Acharya, S.; Pashov, D.; Chen, Z.; Vaklinova, K.; van Schilfgaarde, M.; Watanabe, K.; Taniguchi, T.; Novoselov, K. S.; Katsnelson, M. I.; et al. Strongly Correlated Exciton-Magnetization System for Optical Spin Pumping in $CrBr_3$ and CrI_3. *J. Adv. Mater.* **2023**, *35* (17), 2209513.
(90) Brennan, N. J.; Noble, C. A.; Tang, J.; Ziebel, M. E.; Bae, Y. J. Important Elements of Spin-Exciton and Magnon-Exciton Coupling. *ACS Phys. Chem. Au.* **2024**, *4* (4), 322-327.
(91) Wu, M.; Li, Z.; Cao, T.; Louie, S. G. Physical origin of giant excitonic and magneto-optical responses in two-dimensional ferromagnetic insulators. *Nat. Commun.* **2019**, *10* (1), 2371.
(92) Dillon, J. F.; Kamimura, H.; Remeika, J. P. Magneto-optical properties of ferromagnetic chromium trihalides. *J. Phys. Chem. Solids* **1966**, *27* (9), 1531-1549.
(93) Grant, P. M.; Street, G. B. Optical properties of the chromium trihalides in the region 1-11 eV. *Bull. Am. Phys. Soc. II* **1968**, *13*.
(94) Grover, M.; Silbey, R. Exciton Migration in Molecular Crystals. *J. Chem. Phys.* **1971**, *54* (11), 4843-4851.
(95) Güdel, H. U.; Snellgrove, T. R. Jahn-Teller effect in the $^4T_{2g}$ state of chromium(III) in dicesium sodium indium(III) hexachloride. *Inorg. Chem.* **1978**, *17* (6), 1617-1620.
(96) Xing, Y.; Chen, H.; Zhang, A.; Hao, Q.; Cai, M.; Chen, W.; Li, L.; Peng, D.; Yi, A.; Huang, M.; et al. Optical Detection of Weak Magnetic Transitions via Photoluminescence in Cr-Doped Van Der Waals Antiferromagnets. *Adv. Opt. Mater. n/a* (n/a), 2402549.
(97) Zhou, Y.; He, K.; Hu, H.; Ouyang, G.; Zhu, C.; Wang, W.; Qin, S.; Tao, Y.; Chen, R.; Zhang, L.; et al. Strong Neel Ordering and Luminescence Correlation in a Two-Dimensional

Antiferromagnet. *Laser Photonics Rev.* **2022**, *16* (8), 2100431.
(98) Samal, R.; Sanyal, G.; Chakraborty, B.; Rout, C. S. Two-dimensional transition metal phosphorous trichalcogenides (MPX_3): a review on emerging trends, current state and future perspectives. *J. Mater. Chem. A* **2021**, *9* (5), 2560-2591.
(99) Sen, D.; Saha-Dasgupta, T. Pressure-tuned valence transition, insulator-metal transition in van der Waals antiferromagnet $CrPS_3$. *Phys. Rev. Mater.* **2023**, *7* (6), 064008.
(100) Basnet, R.; Upreti, D.; Patel, T.; Karki Chhetri, S.; Acharya, G.; Nabi, M. R. U.; Sharma, M. M.; Sakon, J.; Mortazavi, M.; Hu, J. Field-induced spin polarization in the lightly Cr-substituted layered antiferromagnet $NiPS_3$. *Phys. Rev. B* **2024**, *109* (18), 184405.
(101) Böttger, T.; Thiel, C. W.; Cone, R. L.; Sun, Y.; Faraon, A. Optical Spectroscopy and Decoherence Studies of Yb^{3+}:YAG at 968 nm. *Phys. Rev. B* **2016**, *94* (4), 045134.

Chapter 2. Luminescence and Covalency in Ytterbium-Doped CrX_3 (X = Cl, Br, I) van der Waals Compounds

2.1 Overview

The layered 2D van der Waals ferromagnets CrX_3 (X = Cl, Br, I) show broad *d-d* photoluminescence (PL). Here we report preparation, structural characterization, and spectroscopic studies of all three CrX_3 compounds doped with the optical impurity, Yb^{3+}. EXAFS measurements show very similar Cr K-edge and Yb L-edge data for each doped compound, and good fits of the latter are obtained for structures having Yb^{3+} occupying substitutional octahedral sites. Yb-X bond lengths are systematically ~0.25 Å larger than their Cr-X counterparts. 4 K PL measurements show efficient sensitization of Yb^{3+} luminescence upon photoexcitation into lattice absorption bands (Cr^{3+} *d-d* and ligand-to-metal charge-transfer (LMCT)) for all three compounds, converting their nondescript broadband *d-d* PL into sharp *f-f* emission. The PL of Yb^{3+}:$CrCl_3$ and Yb^{3+}:$CrBr_3$ occurs at energies typical for $[YbX_6]^{3-}$ with these halides, with PL decay times of 0.5-1.0 ms at 4 K, but Yb^{3+}:CrI_3 displays anomalously low-energy Yb^{3+} emission and an unusually short PL decay time of only 8 μs at 4 K. Data analysis and angular overlap model (AOM) calculations show that Yb^{3+} in Yb^{3+}:CrI_3 has a lower spin-orbit splitting energy than reported for any other Yb^{3+} in any other compound. We attribute these observations to exceptionally high covalency of the Yb^{3+} f orbitals in Yb^{3+}:CrI_3 stemming primarily from the shallow valence-shell ionization potentials of the iodide anions.

2.2 Introduction

The recent demonstration of single-layer ferromagnetism in CrI_3[1] has sparked renewed interest in the CrX_3 (X = Cl, Br, I) family of layered 2D van der Waals materials.[2-4] Although the absorption spectrum of CrI_3 was reported as early as 1965,[5] its photoluminescence (PL) went largely unexplored for decades, and apparently no PL spectra were reported until that of monolayer CrI_3 in 2018.[6] This spectrum shows just a broad nondescript band at the low edge of the visible range, characteristic of Cr^{3+} *d-d* luminescence in a weak ligand field.[7] Reports on the optical properties of $CrCl_3$ and $CrBr_3$ have followed a similar trajectory, with a handful of absorption[8-10] and reflectivity[11, 12] studies dating from the 1960s to 1980s, until the recent pursuit of exfoliable magnetic materials led to a resurgence of interest in their properties.[13, 14] The historical lack of attention given to CrX_3 PL likely results from their poor or non-existent emission at room temperature.

Optical doping of CrX_3 compounds has also received little or no attention. Recently, our group communicated the first such results,[15] showing that successful doping of Yb^{3+} ions into bulk CrI_3 yields sharp sensitized Yb^{3+} *f-f* emission in the near IR. Magneto-PL measurements demonstrated that the Yb^{3+} impurities are strongly magnetically coupled to the CrI_3 host lattice but do not interfere with its ferromagnetic ordering. As a consequence, Yb^{3+} magnetic saturation occurs at external magnetic fields roughly 100x smaller than necessary for Yb^{3+} in diamagnetic lattices. Such intimate magnetic integration of a lanthanide with a ferromagnet implies strong electronic coupling, but remarkably, the electronic structures of Yb^{3+}-doped iodide crystals have received essentially no prior attention, warranting a broader systematic investigation.

Here, we expand upon these initial results by demonstrating successful Yb^{3+} doping of the two magnetic congeners, $CrCl_3$ and $CrBr_3$, establishing the first complete series of lanthanide-doped CrX_3 (X = Cl, Br, I) van der Waals compounds. We show that Yb^{3+}:$CrCl_3$ and Yb^{3+}:$CrBr_3$ share many of the basic properties of Yb^{3+}:CrI_3 but both display higher energy *f-f* PL with narrower PL line widths and longer PL decay times. Systematic trends across this series of compounds are analyzed in terms of increasing Yb^{3+}-X^- covalency linked to the decreasing anion electronegativities and concomitantly decreasing energies of $X^- \rightarrow Yb^{3+}$ ligand-to-metal charge-

transfer (LMCT) excited states in the heavier halides. In addition to illustrating the use of lanthanide dopants to alter the photonic properties of CrX_3 van der Waals ferromagnets, these results highlight the uniquely strong effects of f-orbital covalency in Yb^{3+}:CrI_3 relative to other known Yb^{3+} compounds.

2.3 Results and Analysis

Figure 2.1a depicts a top-down view of a CrX_3 monolayer, showing its honeycomb network lattice structure. In this study, we aimed to replace Cr^{3+} ions with Yb^{3+} impurity ions (cyan) randomly throughout the lattice. To this end, CrX_3 and Yb^{3+}-doped CrX_3 crystals were grown (see Section 2.5 Experimental Methods) by chemical vapor transport using elemental Cr(0), I_2, and Yb(0) as precursors for CrI_3-based compositions,[15] and using $CrCl_3$, $CrBr_3$, and Yb(0) as precursors for the other halide compositions. Heating these precursors in sealed quartz tubes under a temperature gradient for several days yielded large single-crystal flakes as products. Individual flakes were selected from such samples and used for all of the experiments described here. Figure 2.1b shows a photograph of representative as-grown flakes of Yb^{3+}-doped CrX_3 (X = Cl, Br, I). Figure 2.1c shows room-temperature X-ray diffraction patterns of individual oriented CrX_3 flakes and their Yb^{3+}-doped counterparts taken on a powder diffractometer. Only (00*l*) reflections are observed, consistent with the flakes being single crystals with their out-of-plane axes aligned with the crystallographic *c*-axis. At room temperature, CrI_3 and $CrCl_3$ adopt a monoclinic C12/m1 structure, while $CrBr_3$ has an $R\bar{3}h$ space group, which differs from C12/m1 only in the offset between layers. At cryogenic temperatures, all three materials exist in the $R\bar{3}h$ phase.[16-18] The Yb^{3+}-doped materials all show small but nonzero shifts in 2θ, consistent with expansion of the unit cells along the soft *c*-axis relative to the undoped parent compound. Yb^{3+} doping concentrations for all measurements detailed in this work are 2.0, 0.4, and 4.9% for X = Cl, Br, and I, respectively, as determined by ICP−MS. EDX data on Yb^{3+}:$CrBr_3$ indicate even distribution of Yb throughout the material (Figure 5.3).

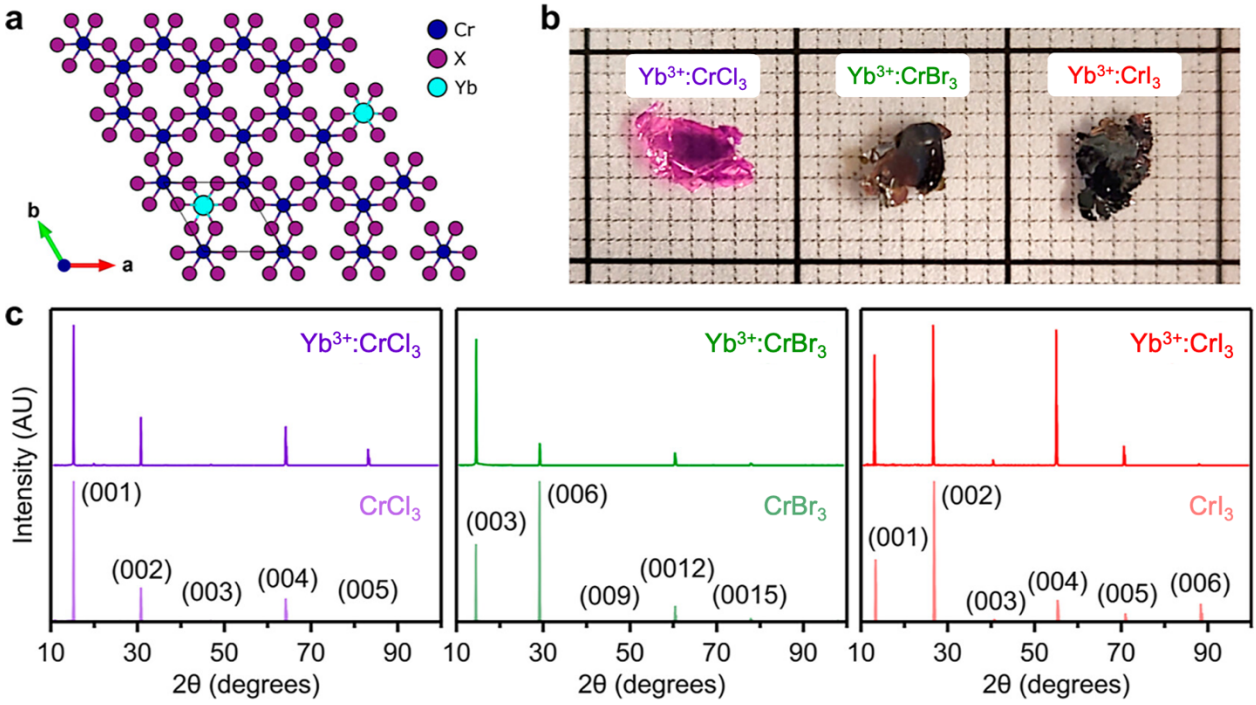

Figure 2.1 (a) Top-down view of a layer of CrX_3 (X = Cl, Br, I), with Yb^{3+} dopant ions (cyan) substitutionally replacing Cr^{3+} ions (blue) at random sites in the lattice, based on the X-ray crystal structure of Yb^{3+}:CrI_3.[15] **(b)** Photograph of representative as-grown single-crystal flakes of CrX_3 doped with Yb^{3+} on graph paper (minor grid size 1 × 1 mm^2). **(c)** Room-temperature X-ray diffraction patterns of oriented $CrCl_3$, $CrBr_3$, and CrI_3 single crystals together with their Yb^{3+}-doped counterparts, collected on a powder diffractometer. Due to sample orientation, only (00*l*) peaks are observed. For monoclinic (C12/*m*1) $CrCl_3$ and CrI_3, $l = n$, for rhombohedral ($R\bar{3}h$) $CrBr_3$ $l = 3n$. At low temperatures, all three materials adopt the $R\bar{3}h$ structure. Cation-relative Yb^{3+} doping concentrations are 2.0, 0.4, and 4.9%, respectively.

The ionic radius of Yb^{3+} with six-fold coordination is about 41% larger than that of Cr^{3+},[19] making the possibility of substitutional Yb^{3+} doping uncertain. The local structures of the Cr^{3+} and Yb^{3+} ions were therefore investigated using Extended X-ray Absorption Fine Structure (EXAFS) measurements. Figure 2.2 shows Fourier-transformed (real-space) EXAFS spectra collected at the Cr K- and Yb L_3-edges of Yb^{3+}:CrX_3, for X = Cl, Br, I. Both edges were measured for each sample at room temperature and the data were phase- corrected with their respective single-scattering paths using the Artemis package.[20] The *k*-space EXAFS data (Figure 5.1) show comparable signal-to-noise ratios for all of the samples described here, as well as a distinct

increase in low-*k* features moving from Cl to Br to I. These features are consistent with the calculated scattering paths. For all spectra, the features are fit well (Figure 5.2) by a single-scattering path of the nearest- neighbor halide and indicate octahedral coordination of the metal. Fitting parameters are summarized in Table A.1. For both edges, the Yb^{3+}:CrI_3 data show additional minority features consistent with an iodide single-scattering path. Overall, these EXAFS data strongly support the presence of $[YbX_6]^{3-}$ octahedra, likely in the form of Yb^{3+} substitution at Cr^{3+} sites. Another possibility is the vacant octahedral interstitial site within the layer,[21] which is differentiated from substitutional sites by having six Cr^{3+} nearest neighbors and threefold coordination of the bridging halides. Yb^{3+} in interstitial sites would require charge compensation, but little interstitial electron density is observed in the single-crystal X-ray structure of Yb^{3+}:CrI_3. [15] These two sites are expected to have similar geometries and hence similar EXAFS signatures.

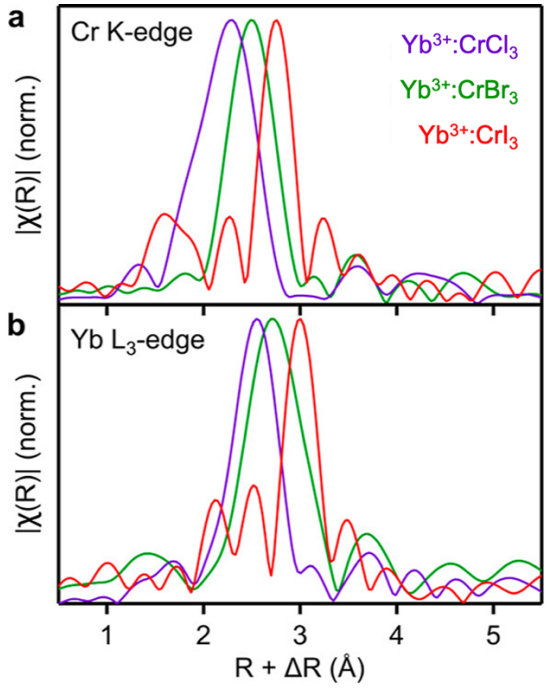

Figure 2.2 (a) Cr K-edge and **(b)** Yb L_3-edge Fourier-transformed (real-space) EXAFS data for Yb^{3+}:CrX_3 (X = Cl, Br, I) samples. Data are phase-corrected using the respective primary halide scattering paths from fits. Cr peaks are at 2.30, 2.49, and 2.76 Å for Cl, Br, and I data, respectively. Yb peaks are at 2.55, 2.70, and 3.01 Å for Cl, Br, and I data, respectively. Smaller features in the data are consistent with their respective calculated single-scattering paths.

Looking closer at these results, each spectrum in the Cr K-edge data (Figure 2.2a) shows a pronounced peak in the range of R+ΔR = 2-3 Å that can be associated with the Cr-X interatomic spacing. Analysis yields Cr-Cl, Cr-Br, and Cr-I bond lengths of 2.30, 2.49, and 2.76 Å, respectively. These values agree well with crystallographic data, which provide bond lengths of 2.34, 2.52, and 2.72 Å for the same series.[16, 18, 22] For each sample, the peak in the Yb L_3-edge data (Figure 2.2b) exhibits a very similar shape to the peak in the corresponding Cr K-edge data but is shifted to higher *R* values, indicating that all Yb-X bond lengths are elongated by *ca*. 0.25 Å relative to the corresponding Cr-X bond lengths (Yb-Cl, Yb-Br, and Yb-I bond lengths of 2.55, 2.70, and 3.01 Å, respectively). The Yb-X bond lengths found here agree well with those reported for other Yb^{3+} compounds of the same halides.[23-26]

Having clarified their structures, we now turn to the luminescence of these compounds. Figure 2.3a summarizes overview aspects of the relevant anticipated electronic states of Yb^{3+}-doped CrX_3, including the manifold of Cr^{3+} *d-d* excited states, the narrow set of Yb^{3+} *f-f* excited states just below the first Cr^{3+} *d-d* excited state, and the approximate positions of anticipated Cr^{3+} and Yb^{3+} ligand-to-metal charge-transfer (LMCT) excited states. Figure 2.3b shows normalized 4 K PL spectra of undoped and Yb^{3+}-doped CrX_3 (X = Cl, Br, I) single-crystal flakes. The undoped materials all show similarly broad Cr^{3+} *d-d* PL, with peak maxima at 1.43, 1.35, and 1.10 eV, that are consistent with the ligand-field luminescence of other weak-field Cr^{3+} ions. For example, $[CrCl_6]^{3-}$ in Cr^{3+}-doped Cs_2NaYCl_6 shows vibronically broadened PL centered at ~1.38 eV.[7] Figure 2.3b shows that the broad Cr^{3+} *d-d* PL is effectively quenched in each of the Yb^{3+}-doped CrX_3 compounds and is replaced by narrow Yb^{3+} *f-f* emission. The Yb^{3+} PL sensitization scheme is summarized by the arrows in Figure 2.3a: photoexcitation into the Cr^{3+}-based *d-d* or LMCT bands is followed by energy transfer to Yb^{3+}, from which *f-f* emission is observed. Particularly remarkable is the spectrum of 0.4% Yb^{3+}-doped $CrBr_3$, which shows little or no Cr^{3+} luminescence in its CW spectrum despite its relatively low Yb^{3+} concentration. The mean in-plane separation between Yb^{3+} ions in this material is roughly 11 cation sites, indicating that energy migration over these length scales within the Cr^{3+} lattice must be rapid even at 4 K, precluding substantial impedance from traps. CrX_3 compounds can host several native defects[21, 27] and energy trapping

is likely to affect their native PL in some way, although it is unclear whether any of the observed CrX_3 PL is actually associated with traps. Were this PL from traps, we estimate an upper limit of ~100 meV trapping depth in CrI_3 from comparison of PL and absorption spectra, and even smaller upper limits in $CrBr_3$ and $CrCl_3$, consistent with retention of $[CrX_6]^{3-}$ coordination in each case. As such, trapping is not expected to alter the present analysis or conclusions in any significant way, but may have interesting consequences in energy-migration dynamics. Current work is investigating the energy-migration dynamics that precede energy capture by Yb^{3+} dopants, and these findings will be described in a subsequent report; the present study focuses on characterizing the electronic structures of the Yb^{3+} ions themselves.

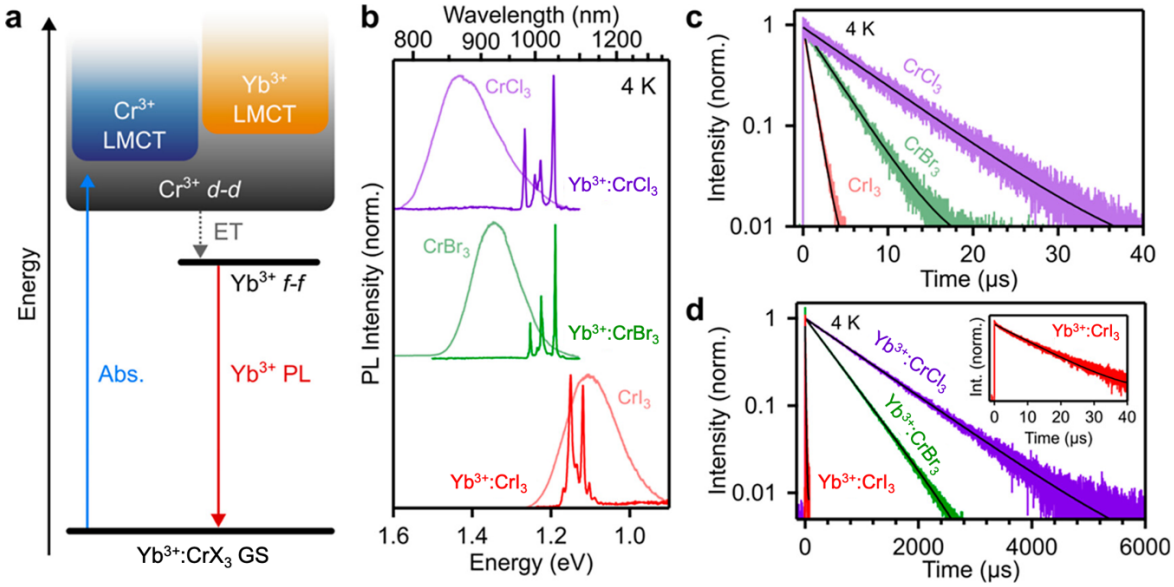

Figure 2.3 (a) State diagram illustrating absorption and subsequent energy transfer (ET) from excited-state Cr^{3+} to Yb^{3+}, resulting in Yb^{3+} PL. **(b)** Low-temperature PL spectra of CrX_3 (X = Cl, Br, I) (semi-transparent curves) showing broad $^4T_{2g} \rightarrow {}^4A_{2g}$ luminescence and of their Yb^{3+}-doped counterparts (dark curves) showing sharp $^2F_{5/2} \rightarrow {}^2F_{7/2}$ luminescence. The absence of lattice PL in the latter indicates efficient energy transfer from Cr^{3+} to Yb^{3+}. **(c)** 4 K time-resolved PL (TRPL) data for CrX_3 compounds. Decay times found from single-exponential fits (black) are 7.42(2), 3.38(4), and 0.84(1) μs for X = Cl, Br, and I, respectively. **(d)** 4 K TRPL data for Yb^{3+}:CrX_3 compounds. Decay times found from single exponential fits (black) are 971.5(6), 501.2(1), and 8.63(1) μs for X = Cl, Br, I, respectively. Inset: enlarged view of the Yb^{3+}:CrI_3 decay curve. Yb^{3+} doping concentrations are 2.0, 0.4, and 4.9% for X = Cl, Br, and I, respectively.

Figure 2.3c shows time-resolved PL (TRPL) data collected for the series of undoped CrX_3 samples measured at 4 K. The PL decay accelerates systematically down the halide series, and each decay curve is fit well to a single exponential function. We hypothesize that this acceleration is primarily due to increased radiative transition probabilities of the emissive *d*-*d* excited state associated with that state's increased charge-transfer character, as anticipated from the correspondingly decreasing energies of LMCT transitions down this series. The first LMCT absorption band in CrI_3 has been identified at ECT ≈ 1.9 eV and in $CrBr_3$ it occurs at ECT ≈ 2.9 eV,[28] but the one in $CrCl_3$ has not yet been reported. Using Jørgensen's optical electronegativity model[29] and E_{CT} ≈ 2.9 eV for $CrBr_3$, we estimate that the first LMCT band of $CrCl_3$ will occur at ~3.6 eV.

Covalency in a metal−ligand complex can be described perturbatively within the molecular-orbital (MO) model in terms of hybridization between the metal's valence orbitals ($|M\rangle$, *e.g.*, 3*d* or 4*f*) and symmetry-adapted linear combinations of ligand valence atomic orbitals ($|L_{SALC}\rangle$), as in eq (2.1).

$$\psi = N(|M\rangle - c|L_{SALC}\rangle) \tag{2.1}$$

N is a normalization constant. The covalency coefficient (*c*) is given by eq (2.2)

$$c = \frac{H_{ML}}{\Delta E_{ML}} \approx \frac{H_{ML}}{E_{CT}} \tag{2.2}$$

where ΔE_{ML} is the energy difference between metal and L_{SALC} orbitals in the absence of mixing, and H_{ML} is the off-diagonal matrix element describing the resonance energy associated with *M*-L_{SALC} mixing. The covalent admixture of ligand valence orbitals into the metal valence orbitals is given by c^2. H_{ML} is proportional to the *M*-L_{SALC} orbital overlap integral, *S*. The energy difference ΔE_{ML} relates to the difference between metal and ligand valence-shell ionization energies and is approximated by the energy of the complex's lowest-energy LMCT transition ($\Delta E_{ML} \approx E_{CT}$).

The radiative rate constant ($k_{rad} = \frac{1}{\tau_{rad}}$) controlling emission from the metal's valence-shell excited state (e.g., *d*-*d*, *f*-*f*) is proportional to the corresponding excitation's oscillator strength and is given by[30]

$$k_{rad} = \frac{e^2 n\omega^2}{2\pi\varepsilon_0 m_0 c^3} f_M \tag{2.3}$$

where n is the refractive index of the material, ω is the intra-shell transition's angular frequency, f_M is its oscillator strength, and the other parameters are fundamental constants. The refractive indices are 1.8, 2.6, and 2.0 for $CrCl_3$, $CrBr_3$, and CrI_3, respectively.[31, 32]

Because the $^4T_{2g} \rightarrow {}^4A_{2g}$ *d-d* intra-shell transitions of pseudo-octahedral Cr^{3+} are formally electric-dipole forbidden due to parity, their radiative lifetimes are to first order determined by "intensity borrowing" from parity-allowed LMCT excited states. Microscopically, this process involves mixing of *d-d* and LMCT configurations and is therefore closely related to covalency. In this scenario, the anticipated trend in *d-d* oscillator strengths is described to first order as in eq (2.4),[33, 34] where f_{CT} is the allowed LMCT transition's oscillator strength and the bracketed term is very similar to the covalency coefficient, c, of eq (2.2), with H_{MLu} representing only the odd-parity matrix elements (static or dynamic). Because of energetic proximity, intensity borrowing is dominated by contributions from the metal's intra-shell excited state (at energy E_{ES}) rather than its ground state (at energy $E_{GS} = 0$), and hence the energy denominator in eq (2.4) is reduced by E_{ES}.

$$f_M \approx \frac{E_{ES}}{E_{CT}} \left[\frac{H_{MLu}}{E_{CT} - E_{ES}}\right]^2 f_{CT} \tag{2.4}$$

Neglecting changes in f_{CT} and H_{MLu} across the CrX_3 series, eq (2.3) and eq (2.4), predict relative radiative lifetimes of (1.00):(0.32): (0.10) for Cl:Br:I, in reasonable agreement with the experimental lifetime trend of (1.00):(0.46):(0.11) at 4 K. This simple analysis thus shows that the short PL decay time of the $^4T_{2g} \rightarrow {}^4A_{2g}$ transition observed in Figure 2.3c primarily results from the relatively low LMCT energy of CrI_3, which in turn favors high *d*-orbital covalency.

Figure 2.3d shows the 4 K decay dynamics of the narrow Yb^{3+} *f-f* luminescence in each of the doped CrX_3 compounds. Again, the PL decay accelerates systematically going down the halide series, and each curve fits well to a single-exponential function. The inset shows an enlarged view of the Yb^{3+}:CrI_3 PL decay curve. The absence of noticeable rise times in these PL decay curves is consistent with the conclusion of rapid energy migration within the CrX_3 lattices. Whereas the Yb^{3+} PL decay times of ~970 and 500 μs for Yb^{3+}:$CrCl_3$ and Yb^{3+}:$CrBr_3$ are comparable to those

reported for Yb^{3+} in other chloride and bromide lattices,[35, 36] the 8.6 μs Yb^{3+} decay time of Yb^{3+}:CrI_3 is extraordinarily short. Although some of this reduction may be due to nonradiative contributions even at 4 K, low-energy LMCT transitions in $[YbI_6]^{3-}$ are also expected to relax intrashell parity forbiddenness and accelerate radiative decay, as discussed for Cr^{3+} above. The Yb^{3+} LMCT transition energies in these compounds are unknown, but the first LMCT excited states of $[YbX_6]^{3-}$ centers in other chloride, bromide, and iodide compounds have been reported at ~4.46,[29, 37, 38] ~3.60, [29, 37, 39] and ~2.21 eV, [29, 40] respectively, in each case formally generating $Yb^{2+}(4f^{14})X(np^5)[X^-(np^6)]_5$ final-state configurations.[38] The shifts in these transition energies are consistent with the differences in halide optical electronegativities. From these data, the LMCT energy for Yb^{3+} in CrI_3 is placed ~0.3 eV higher in energy than the first LMCT transitions of CrI_3 itself (Figure 2.3a). Direct spectroscopic determination of E_{CT} for Yb^{3+} in Yb^{3+}:CrX_3 is thus complicated by the low concentration of Yb^{3+} and the overlapping Cr^{3+} LMCT bands in the same spectral region.

Applying the same analysis described above using these LMCT energies, and taking the highest *f-f* emission energy in each compound at 4 K as E_{ES}, eq (2.3) and eq (2.4) predict relative Yb^{3+} radiative lifetimes across this CrX_3:Yb^{3+} series to be (1.00):(0.31):(0.06) for Cl:Br:I, compared to the experimental results of (1.00):(0.52):(0.01) from Figure 2.3d. Again, we find reasonable agreement (Figure 5.4) between experiment and expectations from the simple perturbation model of eq (2.4). Importantly, this analysis also indicates that *f*-orbital Yb^{3+}-X^- covalency (c^2) increases markedly across the Yb^{3+}:CrX_3 series in a ratio of roughly 1:2:10 for Cl:Br:I. The short lifetime of Yb^{3+} in CrI_3 is thus consistent with unusually high *f*-orbital covalency in this lattice. Although 4*f* covalency in lanthanides is often considered negligible, $[LnCl_6]^{3-}$ compounds typically have 4*f* covalencies approaching ~1%,[41, 42] suggesting that *f*-orbital covalency may reach as high as several percent in Yb^{3+}:CrI_3.

Figure 2.4a shows an enlarged view of the Yb^{3+}-doped CrX_3 PL spectra shown in Figure 2.3b. Yb^{3+}:$CrCl_3$ and Yb^{3+}:$CrBr_3$ show sharp multi-line spectra at energies that are typical for Cl and Br lattices. Although the spectra are dominated by only a few prominent peaks, careful inspection shows a multitude of nearby lines. We assign the most prominent peaks to electronic origins, as

indicated by the colored lines in Figure 2.4a. The Yb^{3+}:CrI_3 spectrum occurs at much lower energy than the other two, and its main peaks are more obviously broadened by distinct shoulders. Sideband intensities are also relatively more intense in this spectrum. We again associate the three maxima in this spectrum with electronic origins. Note that the highest-energy maximum in the Yb^{3+}:CrI_3 PL spectrum has a higher energy shoulder, making precise identification of the true electronic origin uncertain to within ~2.5 meV.

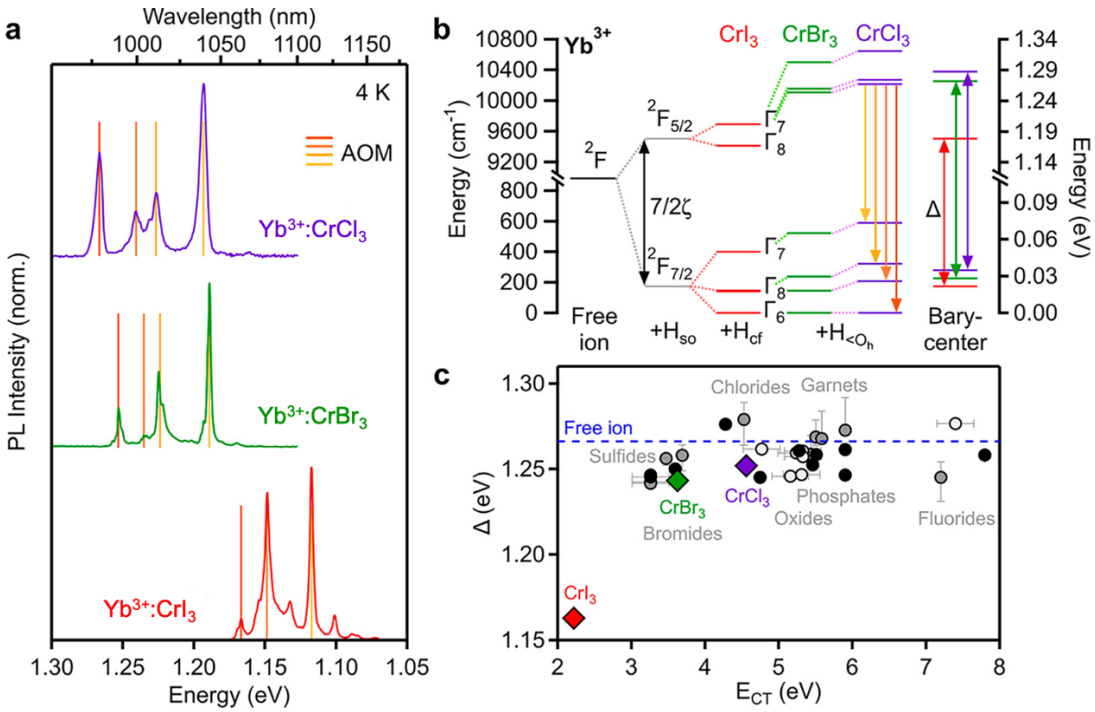

Figure 2.4 (a) Low-temperature PL data for Yb^{3+}-doped CrX_3 (X = Cl, Br, I). The colored vertical sticks indicate the electronic origin assignments used in angular overlap model (AOM) calculations. **(b)** *f*-shell spin-orbit and crystal-field splittings for Yb^{3+} ions in CrX_3 lattices, from panel (a) and calculated by AOM. The splitting of the ground- and excited-state Γ_8 levels indicates deviation from O_h Yb^{3+} site symmetry. This deviation is more pronounced for the smaller halides. The colored down arrows represent the transitions observed in panel (a). The energy difference between $^2F_{5/2}$ and $^2F_{7/2}$ barycenters is denoted Δ. **(c)** Plot of the ligand-to-metal charge-transfer (LMCT) energies vs Δ for Yb^{3+} ions doped into a variety of lattices. Δ values for Yb^{3+}:CrX_3 are obtained from panel (a) and AOM calculations, and E_{CT} is taken from literature for other $[YbX_6]^{3-}$ compounds.[29] The black data points represent experimental values for E_{CT} and Δ, the gray data points use experimental values for E_{CT} and semi- experimental values for Δ, and the white data points use experimental values for Δ and values for E_{CT} calculated from Eu^{3+} charge-transfer energies in the same lattice, following the method of Li *et al.*[43] Uncertainties

estimated from consideration of multiple literature sources are approximately the size of the CrX_3 data points.

Figure 2.4b illustrates the splitting of the Yb^{3+} ^2F free-ion term upon introduction of spin-orbit and crystal-field terms of the molecular Hamiltonian. Using the angular overlap model (AOM)[44] for analysis of these spectra, spin-orbit coupling and crystal-field parameters (Table A.2) were adjusted to reproduce the experimental $^2F_{5/2} \rightarrow {}^2F_{7/2}$ transition energies of each compound (colored lines in Figure 2.4a), from which the energies of the remaining $^2F_{5/2}$ crystal-field levels were extracted. These energies are plotted in Figure 2.4b for each compound. Barycenters of the $^2F_{5/2}$ and $^2F_{7/2}$ states were then calculated from the crystal-field levels for each compound. The energy difference between $^2F_{5/2}$ and $^2F_{7/2}$ barycenters is denoted by Δ. From Figure 2.4b, these values of Δ primarily reflect the magnitude of the spin-orbit coupling parameter, $\Delta \approx 7/2\zeta$. For example, the above AOM analysis yields Δ values that differ from $7/2\zeta$ by only 0.81, 0.59, and 0.31 meV (<0.1%) for Yb^{3+} in $CrCl_3$, $CrBr_3$, and CrI_3, respectively. Note that although the $^2F_{5/2}$ crystal-field energies in the Yb^{3+}:CrX_3 compounds are not obtained experimentally, they have relatively little influence on Δ, and essentially indistinguishable results are obtained from simply considering the mean PL energy of each spectrum in Figure 2.4a.

Inspired by the relationship between covalency and E_{CT} in eq (2.2), Figure 2.4c plots Δ vs E_{CT} for the three Yb^{3+}:CrX_3 compounds reported here. This plot also includes additional data points from a wide variety of literature sources for other Yb^{3+}-doped compounds (see Table A.3). Select compound classes are labeled in the figure. Previous studies have demonstrated that Δ is generally independent of ligand class,[45, 46] consistent with the high shielding and low covalency that typifies the 4*f* valence shell of trivalent lanthanide ions. This typical behavior is highlighted in Figure 2.4c, which shows Δ values nearly the same as the free-ion spin-orbit splitting energy for all but one notable exception: Yb^{3+}:CrI_3. Δ in this compound is substantially smaller than in any other known Yb^{3+} compound. From its value, ζ is reduced by 9% in Yb^{3+}:CrI_3 (330 meV) relative to the Yb^{3+} free ion (362 meV). Not coincidentally, Yb^{3+}:CrI_3 also has the smallest value of E_{CT}, ~1 eV smaller than for the next closest compounds in Figure 2.4c. Per eq (2.2), the data in Figure 2.4c thus support the conclusion that the anomalously small value of Δ in Yb^{3+}:CrI_3 is attributable to exceptionally high f-orbital covalency in this compound, which in turn arises from

the shallow valence-shell ionization energy of the iodide ligands relative to other ligands in this figure. This interpretation supports the conclusion drawn from analysis of the PL decay times in Figure 2.3d.

In addition to the low LMCT energies (E_{CT} in eq (2.2)), the large size discrepancy between Yb^{3+} and Cr^{3+} ($r_{Yb}/r_{Cr} = 1.41$) may also contribute to high covalency by effectively forcing the X^- ligands toward the Yb^{3+} dopant, thereby increasing orbital overlap (and hence increasing H_{ML} in eq (2.2)). To assess the importance of this kind of "internal pressure", it is interesting to compare Δ in Yb^{3+}:$CrBr_3$ with that found in Yb^{3+}:$NaYS_2$.[47] Both lattices have octahedral coordination of Yb^{3+} and show similar values of E_{CT} (~3.26 eV). The ionic radii of Br^- (196 pm) and S^{2-} (184 pm) are also similar, but in the latter Yb^{3+} substitutes for Y^{3+}, which has a substantially larger ionic radius than Cr^{3+} (90 vs 62 pm). Nevertheless, Δ in Yb^{3+}:$NaYS_2$ is very similar to that in Yb^{3+}:$CrBr_3$ (Figure 2.4c, Table A.3). This comparison suggests that E_{CT} is the dominant factor differentiating covalency in these compounds, not H_{ML}.

An additional consideration is the effect of anion spin-orbit coupling on Δ. The spin-orbit coupling constant of iodine, 581 meV (4690 cm^{-1}),[48] greatly exceeds even that of Yb^{3+} (362 meV (2918 cm^{-1}) in the Yb^{3+} free ion). Anion SOC is thus no longer negligible in Yb^{3+}:CrI_3, in contrast with most of the compounds in Figure 2.4c, and given the relatively high covalency in Yb^{3+}:CrI_3 this factor may influence the spectroscopic splitting, Δ. For example, sulfides have much smaller ligand SOC constants (36 meV (288 cm^{-1})). We note that a few examples of Yb^{3+}-doped tellurides have been reported,[49] which should have similar values for both E_{CT} and ligand SOC compared to Yb^{3+}:CrI_3. Direct comparison with Yb^{3+}:CrI_3 is precluded by the fact that these tellurides all have tetrahedral coordination of Yb^{3+}, however. This low coordination number is expected to reduce the total *f*-orbital covalency, and indeed their Δ values are again similar to the free ion. Further investigation will be required to elucidate the impact of two-center SOC in such compounds.

Overall, these data contribute to the more general discussion of f-orbital covalency in lanthanides and actinides that has recently drawn broad attention, primarily in molecular contexts.[41, 50-53] The present data provide strong evidence for so-called "degeneracy-driven"

covalency in the $[YbX_6]^{3-}$ units of Yb^{3+}:CrX_3 compounds across the Cl → Br → I composition series, based on systematic trends correlated with anion electronegativity and comparison to other lattices. Indeed, the entire Yb^{3+} data set in Figure 2.4c appears to follow a trend of the form $\Delta = 7/2\zeta_{\text{free ion}} - (\text{const.}/E_{CT})^2$, albeit with some scatter. We also note that the Yb^{3+} barycenter trend in Figure 2.4 upon going from Cl → I is far more pronounced than those typically observed for other lanthanide compounds of the same halides. For example, whereas $\Delta(I)/\Delta(Cl) \sim 92.8\%$ in Yb^{3+}:CrX_3, the average ratio of visible and near-IR Δ values in $Cs_3Er_2X_9$ compounds[54] is $\Delta_{avg}(I)/\Delta_{avg}(Cl) \sim 99.9\%$. For the Er^{3+} multiplet closest in energy to the Yb^{3+} $^2F_{5/2}$ state ($^4I_{11/2}$), this ratio is $\Delta(I)/\Delta(Cl) \sim 100.0\%$. Yb^{3+} is the second most easily reduced trivalent lanthanide behind only Eu^{3+}, and hence it has comparatively low charge-transfer energies. Er^{3+} CT states are expected ~1.8 eV higher in energy than those of Yb^{3+} with the same coordination,[37, 55] which translates to a reduction in ground-state covalency c^2 by a factor of ~3.3 in $[ErI_6]^{3-}$ relative to $[YbI_6]^{3-}$. This comparison thus supports the conclusion that ΔE_{ML} (or E_{CT}, eq (2.2)) dominates over H_{ML} in enhancing the *f*-orbital covalency of Yb^{3+} in CrI_3.

Finally, and remarkably, we note that Yb^{3+} *f-f* PL has apparently not been reported for Yb^{3+} in any other iodide lattice. In fact, surprisingly few compounds involving $[YbI_6]^{3-}$ octahedra have been reported at all,[25, 40, 56, 57] and no *f-f* spectra have been reported for those compounds. Thus, at this moment, no conclusions can be drawn about whether Yb^{3+}:CrI_3 typifies iodides or is in some way also distinct within this class. The scarcity of $[YbI_6]^{3-}$ *f-f* data is likely related to the same relative ease of Yb^{3+} reduction that leads to its enhanced covalency; $[EuI_6]^{3-}$ compounds appear to be even more rare, but both Yb^{2+} and Eu^{2+} iodides are well known.[58-60] Experiments are under way to develop other Yb^{3+}- doped iodides for deeper exploration of this rare motif, from which our preliminary results show that other iodides also fall well below the distribution represented by the other compounds in Figure 2.4c; these findings support the above analyses and will be reported separately.

2.4 Conclusion

In conclusion, we have demonstrated successful incorporation of Yb^{3+} dopants into $CrCl_3$,

$CrBr_3$, and CrI_3 van der Waals lattices. EXAFS data show Yb-X bond lengths that are ~0.25 Å larger than their Cr-X counterparts, and data fitting shows structures consistent with Yb^{3+} substituting for Cr^{3+} (or occupying the comparable antisite) despite its ~1.4x larger ionic radius. PL measurements demonstrate efficient energy transfer from Cr^{3+} to Yb^{3+}, resulting in complete quenching of the broad Cr^{3+} *d-d* luminescence and appearance of sharp Yb^{3+} *f-f* luminescence at modest Yb^{3+} doping levels. TRPL measurements show an exceptionally short excited-state lifetime of only 8.6 μs for Yb^{3+} in Yb^{3+}:CrI_3 at 4 K. Energetically, the Yb^{3+}:CrI_3 PL spectrum is also significantly redshifted compared to those of Yb^{3+}:$CrBr_3$ and Yb^{3+}:$CrCl_3$. Data analysis and AOM calculations show that this shift is due to an anomalously small $^2F_{7/2}$ - $^2F_{5/2}$ spin-orbit splitting in Yb^{3+}:CrI_3. Broader comparison to Yb^{3+} in a wide variety of other lattices shows that the low PL energy of Yb^{3+}:CrI_3 is in fact an outlier across all investigated materials. We propose that the low energy and short decay time of Yb^{3+}:CrI_3 PL are both attributable to anomalously high Yb-I *f*-orbital covalency, ultimately stemming from the shallow valence-shell ionization potentials of the iodide ligands. Beyond demonstrating Yb^{3+} doping as an effective approach to narrowing the emission of the entire family of CrX_3 2D van der Waals ferromagnets, these results provide rare fundamental insights into the electronic structure and luminescence of the remarkably underexplored $[YbI_6]^{3-}$ motif, revealing it to be an outlier among known Yb^{3+} compounds because of its exceptionally high *f*-orbital covalency. In addition to the above manifestations, this high covalency has important physical consequences for the promotion of strong Yb^{3+} - Cr^{3+} magnetic superexchange in Yb^{3+}:CrI_3.[15]

2.5 Experimental Methods

General considerations. All sample preparation and manipulation was performed in a glovebox under an atmosphere of purified dinitrogen.

Chemicals. A chromium chip (99.995%, lot MKCH4484) was purchased from Sigma Aldrich as a high-purity Cr source. The Cr chip was ground to a powder using a mortar and pestle and used as the powder precursor for CrI_3. I_2 (≥99.99%) was purchased from Sigma Aldrich. Ytterbium metal powder 40 mesh (99.9%) was purchased from BeanTown chemical. Anhydrous

chromium(III) bromide (99%, lot 28644600) was purchased from Strem Chemicals. Anhydrous chromium(III) chloride (99.9%, lot U02D017) was purchased from Alfa Aesar. All chemicals were used as received without further purification.

Synthesis of CrX_3 (X = Cl, Br, I) and Yb^{3+}-doped CrX_3 single crystals. The synthesis of single crystals of CrI_3 and Yb^{3+}:CrI_3 grown through chemical vapor transport is detailed in Pressler *et al*.[15] This procedure was slightly modified for undoped $CrBr_3$ and $CrCl_3$, for which as-bought chromium(III) bromide and chromium(III) chloride precursors were used instead of elemental precursors. For Yb^{3+}-doped CrX_3, additional Yb(0) metal was loaded along with the other starting materials. Evacuated and sealed quartz tubes loaded with precursor materials were placed in an open-ended horizontal tube furnace, with the precursors placed in the center of the furnace at 650 ℃ (CrI_3) or 750 ℃ ($CrBr_3$, $CrCl_3$). The other end of the quartz tubes was placed in the cold zone, at a temperature *ca*. 150 ℃ colder than the center of the furnace. The samples were kept at temperature for approximately 3 days and then slowly cooled to room temperature, yielding thin flakes up to 1 cm in length.

pXRD measurements. As-synthesized flakes were characterized by X-ray diffraction using a Bruker D8 Discover powder diffractometer with IμS microfocus X-ray source for Cu Kα radiation (50 kV, 1 mA). Samples were placed onto crystalline silicon substrates and packed in Kapton film under an air-free environment to avoid sample degradation in air.

ICP-MS measurements. Yb^{3+} doping was confirmed using inductively coupled plasma mass spectrometry (ICP-MS) using a PerkinElmer NexION 2000B. ICP-MS samples were digested in high-purity concentrated nitric acid, followed by dilution in ultrapure H_2O. Yb^{3+} doping levels are reported as a percentage relative to the total cation contents, $[Yb^{3+}]/([Cr^{3+}]+[Yb^{3+}])$. Yb^{3+} incorporation into the CrX_3 flakes was found to be inhomogeneous throughout the same synthesis batch. We estimate an uncertainty of ±0.3% in the Yb^{3+} concentration to account for flake-to-flake inhomogeneity.

XAS measurements. X-ray absorption near edge structure (XANES) and extended X-ray absorption fine structure (EXAFS) spectra were collected at beamline 20-BM at the Advanced Photon Source at Argonne National Laboratory. Yb L_3-edge (8944 eV) and Cr K-edge (5989 eV)

data were collected in fluorescence mode for single crystals of each sample at room temperature under helium atmosphere with active purging. Samples were sealed in Kapton tape under inert atmosphere to prevent air exposure prior to loading in the beamline holder. A Si(111) double-crystal monochromator was used to select the incident energy with He/N_2 filled ion chambers to monitor the flux. The monochromator was calibrated using Cr foil. The pre-edge region was collected from 150 to 20 eV below the edge with a step size of 10 eV and a collection time of 0.4 s at each step. From 20 eV below the edge to 30 eV above the edge, data were collected in 0.50 eV steps for 0.4 s at each step. Post-edge data were collected to 9.6 keV (for Yb) or 7 keV (for Cr) and obtained with a 0.05 keV step size and a collection time of 0.4 s per step. Data normalization and energy calibration were performed using Athena software. [20] Data were normalized to low energy regions of interest. Fits to the EXAFS data from proposed defect structures were performed with Artemis software.[20] A window from 3 $Å^{-1}$ to 12 $Å^{-1}$ with a d*k* value of 1 $Å^{-1}$ was used for shell- by-shell fitting. R-space EXAFS data were corrected in Artemis using an X (X = Cl, Br, I, depending on lattice) single scattering path from the CrX_3 host lattice structure. For the sake of clarity, we use $R + \Delta R$ to denote the corrected radial distance axis in the EXAFS data.

Photoluminescence measurements. A single crystal of the material was placed between two quartz disks and loaded into a closed-cycle helium cryostat. Measurements were performed under high vacuum (10^{-6} Pa) at a sample temperature of approximately 4 K. Samples were excited using a continuous-wave 660 nm (1.88 eV) diode in the case of X = Br, I, and a 405 nm (3.06 eV) diode for X = Cl at an excitation power of approximately 4 mW/cm^2. Sample emission was focused into a monochromator with a spectral bandwidth of 0.627 nm ($(Yb^{3+}:)CrI_3$), 1.617 nm ($CrBr_3$, $(Yb^{3+}:)CrCl_3$) and 0.259 nm ($Yb^{3+}:CrBr_3$). Spectra were collected using a LN_2-cooled silicon CCD camera ($CrCl_3$, $CrBr_3$) and a Hamamatsu InGaAs/InP NIR photomultiplier tube ($Yb^{3+}:CrCl_3$, $Yb^{3+}:CrBr_3$, $(Yb^{3+}:)CrI_3$), with signal recorded using a photon counter. All spectra were corrected for instrument response.

Time-resolved photoluminescence measurements. Measurements were done under the same conditions as used for PL measurements. Samples were excited using an EKSPLA PL2230 532 nm Nd:YAG/YVO_4 pulsed laser excitation source at a pulse frequency of 50 Hz, a pulse

duration of 20 ps and an excitation energy of ~7 nJ/cm^2 per pulse. Data was collected using a LN_2-cooled Hamamatsu InGaAs/InP NIR photomultiplier tube. Monitor wavelengths of 910, 920 and 1100 nm were used for $CrCl_3$, $CrBr_3$ and CrI_3 respectively. Monitor wavelengths of 1039, 1042.5 and 1080 nm were used for Yb^{3+}:$CrCl_3$, Yb^{3+}:$CrBr_3$ and Yb^{3+}:CrI_3, respectively. Undoped CrX_3 measurements were performed using a 5 ns bin width. Bin widths of 640, 320, and 5 ns were used for Yb^{3+}:$CrCl_3$, Yb^{3+}:$CrBr_3$ and Yb^{3+}:CrI_3, respectively.

Angular Overlap Model. Energy values for the Yb^{3+} crystal field energies were calculated using the BonnMag software package.[44] Atomic coordinates were determined from crystallographic data on CrX_3 (X = Cl, Br, I), which were used to create distorted $[YbX_6]^{3-}$ octahedra of C_2 symmetry. Size differences between Cr^{3+} and Yb^{3+} were not considered in these calculations. A Stevens orbital reduction factor k of 1.0 was used and Slater-Condon-Shortley (SCS) parameters were set to 0 for Yb^{3+} ($^4f_{13}$). The spin-orbit coupling parameter ζ was adjusted along with orbital overlap parameters e_σ and e_π to reproduce experimentally assigned electronic origin transition energies in the photoluminescence spectra. Experimental data could be reproduced well with an isotropic value for e_π in Yb^{3+}:CrI_3, but Yb^{3+}:$CrBr_3$ and Yb^{3+}:$CrCl_3$ required anisotropic values of $e_{\pi,x}$ and $e_{\pi,y}$ to accurately reproduce the spectra. Increasing (decreasing) ζ while keeping all other parameters constant results in an increase (decrease) in all transition energies while retaining peak splitting energies. Adjusting e_σ or e_π alters the relative energies of the peaks but maintains the barycenters.

2.6 References

(1) Huang, B.; Clark, G.; Navarro-Moratalla, E.; Klein, D. R.; Cheng, R.; Seyler, K. L.; Zhong, D.; Schmidgall, E.; McGuire, M. A.; Cobden, D. H.; et al. Layer-Dependent Ferromagnetism in a van der Waals Crystal Down to the Monolayer Limit. *Nature* **2017**, *546* (7657), 270-273.

(2) Burch, K. S.; Mandrus, D.; Park, J. G. Magnetism in two-dimensional van der Waals materials. *Nature* **2018**, *563* (7729), 47-52. From NLM.

(3) Duong, D. L.; Yun, S. J.; Lee, Y. H. van der Waals Layered Materials: Opportunities and Challenges. *ACS Nano* **2017**, *11* (12), 11803-11830. From NLM.

(4) Liu, Y.; Huang, Y.; Duan, X. van der Waals integration before and beyond two-dimensional materials. *Nature* **2019**, *567* (7748), 323-333. From NLM.

(5) Dillon, J. F., Jr.; Olson, C. E. Magnetization, Resonance, and Optical Properties of the Ferromagnet CrI_3. *J. Appl. Phys.* **1965**, *36* (3), 1259-1260.

(6) Seyler, K. L.; Zhong, D.; Klein, D. R.; Gao, S.; Zhang, X.; Huang, B.; Navarro-Moratalla, E.; Yang, L.; Cobden, D. H.; McGuire, M. A.; et al. Ligand-field helical luminescence in a 2D ferromagnetic insulator. *Nat. Physics* **2018**, *14* (3), 277-281.
(7) Güdel, H. U.; Snellgrove, T. R. Jahn-Teller Effect in the $^4T_{2g}$ State of Chromium(III) in Dicesium Sodium Indium(III) Hexachloride. *Inorg. Chem.* **1978**, *17* (6), 1617-1620.
(8) Dillon, J. F.; Kamimura, H.; Remeika, J. P. Magnetic Rotation of Visible Light by Ferromagnetic $CrBr_3$. *Phys. Rev. Lett.* **1962**, *9* (4), 161-163.
(9) Dillon, J. F.; Kamimura, H.; Remeika, J. P. Magneto-Optical Properties of Ferromagnetic Chromium Trihalides. *J. Phys. Chem. Solids* **1966**, *27* (9), 1531-1549.
(10) Limido, C.; Pedroli, G.; Spinolo, G. Specific magnetic rotation in the crystal field bands of $CrCl_3$. *Solid State Commun.* **1972**, *11* (10), 1385-1388.
(11) Nosenzo, L.; Samoggia, G.; Pollini, I. Effect of magnetic ordering on the optical properties of transition-metal halides: $NiCl_2$, $NiBr_2$, $CrCl_3$, and $CrBr_3$. *Phys. Rev. B* **1984**, *29* (6), 3607-3616.
(12) Borghesi, A.; Guizzetti, G.; Samoggia, G.; Reguzzoni, E. Magneto-Optical Effects in the Paramagnetic and Ferromagnetic Phases of $CrBr_3$. *Phys. Rev. Lett.* **1981**, *47* (7), 538-541.
(13) Zhang, Z.; Shang, J.; Jiang, C.; Rasmita, A.; Gao, W.; Yu, T. Direct Photoluminescence Probing of Ferromagnetism in Monolayer Two-Dimensional $CrBr_3$. *Nano Lett.* **2019**, *19* (5), 3138-3142.
(14) Cai, X.; Song, T.; Wilson, N. P.; Clark, G.; He, M.; Zhang, X.; Taniguchi, T.; Watanabe, K.; Yao, W.; Xiao, D.; et al. Atomically Thin $CrCl_3$: An In-Plane Layered Antiferromagnetic Insulator. *Nano Lett.* **2019**, *19* (6), 3993-3998.
(15) Pressler, K.; Snoeren, T. J.; Walsh, K. M.; Gamelin, D. R. Magnetic Amplification at Yb^{3+} "Designer Defects" in the van der Waals Ferromagnet CrI_3. *Nano Lett.* **2023**, *23* (4), 1320-1326.
(16) Morosin, B.; Narath, A. X-Ray Diffraction and Nuclear Quadrupole Resonance Studies of Chromium Trichloride. *J. Chem. Phys.* **1964**, *40* (7), 1958-1967.
(17) Kozlenko, D. P.; Lis, O. N.; Kichanov, S. E.; Lukin, E. V.; Belozerova, N. M.; Savenko, B. N. Spin-Induced Negative Thermal Expansion and Spin–Phonon Coupling in van der Waals Material $CrBr_3$. *npj Quantum Mater.* **2021**, *6* (1), 19.
(18) McGuire, M. A.; Dixit, H.; Cooper, V. R.; Sales, B. C. Coupling of Crystal Structure and Magnetism in the Layered, Ferromagnetic Insulator CrI_3. *Chem. Mater.* **2015**, *27* (2), 612-620.
(19) Shannon, R. Revised Effective Ionic Radii and Systematic Study of Inter Atomic Distances in Halides and Chalcogenides. *Acta Crystallogr. A.* **1976**, *32*, 751-767.
(20) Ravel, B.; Newville, M. ATHENA, ARTEMIS, HEPHAESTUS: data analysis for X-ray absorption spectroscopy using IFEFFIT. *J. Synchrotron Radiat.* **2005**, *12* (4), 537-541.
(21) Pizzochero, M. Atomic-scale defects in the two-dimensional ferromagnet CrI_3 from first principles. *J. Phys. D: Appl. Phys.* **2020**, *53*.
(22) Braekken, H. The Crystal Structure of Chromium Tribromide (Eng. Transl.). *K. Nor. Vidensk. Selsk.* **1932**, *5* (42).
(23) Templeton, D. H.; Carter, G. F. The Crystal Structures of Yttrium Trichloride and Similar Compounds. *J. Phys. Chem.* **1954**, *58* (11), 940-944.
(24) Brenner, M. *Kinetic Studies of Phase Transformations between Polymorphic Forms of Ytterbium(II)*

Bromide and Determination of the Crystal Structure of Ytterbium(III) Bromide Considering the Stacking Disorder of the Crystals Used (Eng. Transl.); Universitaẗ Karlsruhe, 1997.
(25) Asprey, L. B.; Keenan, T. K.; Kruse, F. H. Preparation and Crystal Data for Lanthanide and Actinide Triiodides. *Inorg. Chem.* **1964**, *3* (8), 1137-1141.
(26) Emge, T. J.; Kornienko, A.; Brennan, J. G. *Trans* influence in a *mer*-octahedral triiodidolanthanide: triiodidotris(tetrahydrofuran-κO)ytterbium(III). *Acta Crystallogr. C.* **2009**, *65* (11), m422-m425.
(27) Zhang, J.; Guo, Y.; Li, P.; Wang, J.; Zhou, S.; Zhao, J.; Guo, D.; Zhong, D. Imaging Vacancy Defects in Single-Layer Chromium Triiodide. *J. Phys. Chem. Lett.* **2021**, *12* (9), 2199-2205.
(28) De Siena, M. C.; Creutz, S. E.; Regan, A.; Malinowski, P.; Jiang, Q.; Kluherz, K. T.; Zhu, G.; Lin, Z.; De Yoreo, J. J.; Xu, X.; et al. Two-Dimensional van der Waals Nanoplatelets with Robust Ferromagnetism. *Nano Lett.* **2020**, *20* (3), 2100-2106.
(29) Jørgensen, C. K. *Electron Transfer Spectra.* ; John Wiley & Sons, Inc., 1970.
(30) 't Hooft, G. W.; van der Poel, W. A. J. A.; Molenkamp, L. W.; Foxon, C. T. Giant oscillator strength of free excitons in GaAs. *Phys. Rev. B* **1987**, *35* (15), 8281-8284.
(31) Bermudez, V. M.; McClure, D. S. Spectroscopic studies of the two-dimensional magnetic insulators chromium trichloride and chromium tribromide—I. *J. Phys. Chem. Solids.* **1979**, *40* (2), 129-147.
(32) Tomarchio, L.; Macis, S.; Mosesso, L.; Nguyen, L. T.; Grilli, A.; Guidi, M. C.; Cava, R. J.; Lupi, S. Low energy electrodynamics of CrI_3 layered ferromagnet. *Sci. Rep.* **2021**, *11* (1), 23405.
(33) Ballhausen, C. J. *Introduction to Ligand Field Theory*; McGraw-Hill Book Company, Inc., 1962.
(34) Solomon, E. Inorganic spectroscopy: an overview. *Comments Inorg. Chem.* **1984**, *3* (5), 225-320.
(35) Mir, W. J.; Mahor, Y.; Lohar, A.; Jagadeeswararao, M.; Das, S.; Mahamuni, S.; Nag, A. Postsynthesis Doping of Mn and Yb into $CsPbX_3$ (X = Cl, Br, or I) Perovskite Nanocrystals for Downconversion Emission. *Chem. Mater.* **2018**, *30* (22), 8170-8178.
(36) Chen, N.; Cai, T.; Li, W.; Hills-Kimball, K.; Yang, H.; Que, M.; Nagaoka, Y.; Liu, Z.; Yang, D.; Dong, A.; et al. Yb- and Mn-Doped Lead-Free Double Perovskite Cs_2AgBiX_6 ($X = Cl^-, Br^-$) Nanocrystals. *ACS Appl. Mater. Interfaces.* **2019**, *11* (18), 16855-16863.
(37) Dorenbos, P.; Josef, A.; de Haas, J. T. M.; Krämer, K. W. Vacuum referred binding energies of the lanthanides in chloride, bromide, and iodide compounds. *J. Lumin.* **2019**, *208*, 463-467.
(38) Ryan, J. L.; Jørgensen, C. K. Absorption Spectra of Octahedral Lanthanide Hexahalides. *J. Phys. Chem.* **1966**, *70* (9), 2845-2857.
(39) Gafurov, M.; Iskhakova, A.; Kurkin, I.; Kurzin, S.; Malkin, B. Z.; Nikitin, S. I.; Orlinskii, S.; Rakhmatullin, R.; Gil'man, S. S.; Tarasov, V. F. Spectra and relaxation of electronic excitations in $CsCdBr_3$: Yb^{3+} and $CsCdBr_3$: Nd^{3+} monocrystals. In *XI Feofilov Symposium on Spectroscopy of Crystals Activated by Rare-Earth and Transition Metal Ions*, 2002; SPIE: Vol. 4766, pp 279-291.
(40) Ryan, J. L. Weak or unstable iodo complexes. I. Hexaiodo complexes of the lanthanides. *Inorg. Chem.* **1969**, *8* (10), 2053-2058.
(41) Löble, M. W.; Keith, J. M.; Altman, A. B.; Stieber, S. C. E.; Batista, E. R.; Boland, K. S.; Conradson, S. D.; Clark, D. L.; Lezama Pacheco, J.; Kozimor, S. A.; et al. Covalency in Lanthanides. An X-ray Absorption Spectroscopy and Density Functional Theory Study of $LnCl_6^{x-}$ (x = 3, 2). *J. Am. Chem. Soc.* **2015**, *137* (7), 2506-2523.

(42) Atanasov, M.; Daul, C.; Güdel, H. U.; Wesolowski, T. A.; Zbiri, M. Ground States, Excited States, and Metal−Ligand Bonding in Rare Earth Hexachloro Complexes: A DFT-Based Ligand Field Study. *Inorg. Chem.* **2005**, *44* (8), 2954-2963.
(43) Li, L.; Zhou, S.; Zhang, S. Relationship between charge transfer energies of Yb^{3+} and Sm^{3+} and crystal environmental factor. *J. Lumin.* **2009**, *129* (3), 187-191.
(44) Bronova, A.; Bredow, T.; Glaum, R.; Riley, M. J.; Urland, W. BonnMag: Computer Program for Ligand-Field Analysis of f^n Systems Within the Angular Overlap Model. *J. Comp. Chem.* **2018**, *39* (3), 176-186, https://doi.org/10.1002/jcc.25096.
(45) Antic-Fidancev, E. Simple way to test the validity of $^{2S+1}L_J$ barycenters of rare earth ions (e.g. $4f^2$, $4f^3$ and $4f^6$ configurations). *J. Alloys Compd.* **2000**, *300-301*, 2-10.
(46) Haumesser, P.-H.; Gaumé, R.; Viana, B.; Antic-Fidancev, E.; Vivien, D. Spectroscopic and Crystal-Field Analysis of New Yb-doped Laser Materials. *J. Phys.: Cond. Mat.* **2001**, *13* (23), 5427-5447.
(47) Hansen, P.-A.; Kumar, S.; Meijerink, A. Strong self-sensitized green and NIR emission in $NaYS_2$ doped with Pr^{3+} and Yb^{3+} by inducing Laporte allowed and charge transfer transitions. *J. Lumin.* **2021**, *235*, 118012.
(48) Martin, W. Table of spin-orbit energies for p-electrons in neutral atomic (core) np configurations. *J. Res. Natl. Bur. Stand. Sec. A* **1971**, *75* (2), 109.
(49) Bryant, F. J. Ion implanation in group II–VI compounds. *Prog. Cryst. Growth Charact. Mater.* **1983**, *6* (2), 191-263.
(50) Neidig, M. L.; Clark, D. L.; Martin, R. L. Covalency in f-element complexes. *Coord. Chem. Rev.* **2013**, *257* (2), 394-406.
(51) Kerridge, A. Quantification of f-element covalency through analysis of the electron density: insights from simulation. *Chem. Commun.* **2017**, *53* (50), 6685-6695, 10.1039/C7CC00962C.
(52) Vitova, T.; Pidchenko, I.; Fellhauer, D.; Bagus, P. S.; Joly, Y.; Pruessmann, T.; Bahl, S.; Gonzalez-Robles, E.; Rothe, J.; Altmaier, M.; et al. The role of the 5f valence orbitals of early actinides in chemical bonding. *Nat. Commun.* **2017**, *8* (1), 16053.
(53) Vitova, T.; Roesky, P. W.; Dehnen, S. Open questions on bonding involving lanthanide atoms. *Commun. Chem.* **2022**, *5* (1), 12.
(54) Hehlen, M. P.; Krämer, K.; Güdel, H. U.; McFarlane, R. A.; Schwartz, R. N. Upconversion in Er^{3+}-dimer systems: Trends within the series $Cs_3Er_2X_9$ (X=Cl,Br,I). *Phys. Rev. B* **1994**, *49* (18), 12475-12484.
(55) Dorenbos, P. Systematic behaviour in trivalent lanthanide charge transfer energies. *J. Phys. Condens. Matter* **2003**, *15* (49), 8417.
(56) Arumugam, G. M.; Xu, C.; Karunakaran, S. K.; Shi, Z.; Zhu, C.; Wei, M.; Feifei, Q. Efficient red up-conversion emission from Er^{3+}-Yb^{3+} co-doped rubidium lead iodide perovskite nanowires with surface plasmons. *Appl. Phys. Lett.* **2018**, *112* (5).
(57) Shi, J.; Li, F.; Yuan, J.; Ling, X.; Zhou, S.; Qian, Y.; Ma, W. Efficient and stable $CsPbI_3$ perovskite quantum dots enabled by *in situ* ytterbium doping for photovoltaic applications. *J. Mater. Chem. A* **2019**, *7* (36), 20936-20944, 10.1039/C9TA07143A.
(58) Rubio, O. J. Doubly-valent rare-earth ions in halide crystals. *J. Phys. Chem. Solids.* **1991**, *52* (1), 101-174.
(59) Dorenbos, P. Energy of the first $4f^7 \rightarrow 4f^6 5d$ transition of Eu^{2+} in inorganic compounds. *J. Lumin.*

2003, *104* (4), 239-260.
(60) Meyer, G. H.; Halides, T. The Divalent State in Solid Rare Earth Metal Halides. 2012.

Chapter 3. Magnetic Amplification at Yb^{3+} "Designer Defects" in the van der Waals Ferromagnet CrI_3

3.1 Overview

The two-dimensional (2D) van der Waals ferromagnet CrI_3 has been doped with the magnetic optical impurity Yb^{3+} to yield materials that display sharp multi-line Yb^{3+} photoluminescence (PL) controlled by the magnetism of CrI_3. Magneto-PL shows that Yb^{3+} magnetization is pinned to the magnetization of CrI_3. An effective internal field of ~10 T at Yb^{3+} is estimated, attributed to strong in-plane Yb^{3+}-Cr^{3+} superexchange coupling. The anomalously low energy of Yb^{3+} PL in CrI_3 reflects relatively high Yb^{3+}-I^- covalency, contributing to Yb^{3+}-Cr^{3+} superexchange coupling. The Yb^{3+} PL energy and linewidth both reveal the effects of spontaneous zero-field CrI_3 magnetic ordering *within* 2D layers below T_C, despite the absence of net magnetization in multilayer samples. These results illustrate the use of optical impurities as "designer defects" to introduce unique functionality to 2D magnets.

3.2 Introduction

Defects have the power to transform the physical properties of crystals, imparting new and potentially useful functionalities from conductivity to quantum photon emission.[1-6] In magnetic materials, defects can strongly affect spin-wave propagation, magnetic domain-wall propagation, skyrmion dynamics, and magnetic vortex pinning.[7-9] Recently, the layered van der Waals ferromagnet CrI_3 has emerged as a promising platform for exploring strongly correlated spin physics, magnetic proximity effects, and next-generation spin-based device architectures in the

two-dimensional (2D) limit,[10-14] but the potential to expand CrI_3 functionality through introduction of defects remains untapped. Here, we report that doping CrI_3 with Yb^{3+} as a "designer point defect" transforms its normally broad and featureless *d-d* photoluminescence (PL) into narrow-line sensitized *f-f* emission, without compromising its attractive magnetic properties. We further show that Yb^{3+} in CrI_3 experiences a large internal effective field that makes it extremely sensitive to small external magnetic fields. Using this property, we demonstrate magnetically saturated circular polarization of Yb^{3+} emission at anomalously small applied fields. Strikingly, the internal effective field also transmits magnetic information to Yb^{3+} even in the absence of any applied field, making Yb^{3+} a unique embedded luminescent probe of spontaneous zero-field magnetic ordering within the 2D monolayers of bulk CrI_3. These discoveries establish optical impurity doping as an effective strategy for expanding the functionality of 2D magnets, with potential ramifications for both basic science and future spin-photonic technologies.

CrI_3 has become a model system for exploring magnetic exchange in 2D van der Waals structures,[10-14] stimulated by recent discoveries of Ising-like hard ferromagnetism in exfoliated monolayer CrI_3 and layer- and stacking-dependent magnetism in multi-layer CrI_3.[15, 16] Layering CrI_3 with non-magnetic 2D materials introduces magnetic functionality to the non-magnetic material *via* inter-layer exchange coupling, allowing magnetic manipulation of properties such as WSe_2 valley polarization and valley Zeeman splittings.[17] Extension from few to many (bulk) layers preserves the strong Ising-like intralayer ferromagnetic ordering, but facile motion of domain walls unblocks demagnetization.[18] Despite its rich magnetic properties, CrI_3 itself has not garnered much attention as an optical material. Bulk CrI_3 has been investigated for its very large Kerr and Faraday rotation strengths in relation to optical isolators and associated technologies.[19, 20] PL of bulk CrI_3 has apparently not been reported, and few-layer CrI_3 shows[17] only the very broad *d-d* PL characteristic of weak-field pseudo-octahedral Cr^{3+}.[21] Circular polarization of this *d-d* PL was used to probe the magnetism of few-layer CrI_3,[17] but the emission's breadth limits its further utility for fundamental studies or in spin-photonics, stimulating efforts to narrow the band *via* cavity coupling.[22] Doping CrI_3 with optically active impurities has also not been reported, either in bulk or exfoliated samples.

To investigate *intra*layer "proximity" effects resulting from magnetic exchange coupling, we have prepared CrI_3 doped with luminescent and spin-bearing Yb^{3+} ions. Large-diameter single-crystal flakes of CrI_3 were prepared by chemical vapor transport. Yb^{3+} was introduced by adding Yb(0) to the precursor mix. The Yb^{3+} concentration in the resulting Yb^{3+}:CrI_3 crystals is controllable, and samples with up to ~5% Yb^{3+} (cation mole fraction, $[Yb^{3+}]/([Cr^{3+}]+[Yb^{3+}])$) are described here. Further experimental details are provided in Section 3.5 Experimental Methods.

3.3 Results and Analysis

Figure 3.1a shows a photograph of representative Yb^{3+}:CrI_3 flakes in their growth tube. The flakes are between 5 and 10 mm across, with typical thicknesses of 5-20 μm (see Figure 5.5). Figure 3.1b plots XRD data collected on undoped and 4.9% Yb^{3+}-doped CrI_3 single-crystal flakes using a powder diffractometer. Only (00*l*) peaks are observed, corresponding to the interlayer lattice spacing and reflecting the flake's alignment. Figure 3.1c highlights the shifts to smaller angles of the 001 peak upon doping. From fitting the XRD peak positions of the undoped and doped samples, the interlayer lattice parameter was found to increase 0.24% from 6.996 ± 0.002 to 7.013 ± 0.002 Å, attributed to the larger ionic radius of Yb^{3+} than Cr^{3+} (87 *vs* 62 pm, respectively) (see Figure 5.6). These data suggest that the local strain of doping is relieved by distorting the lattice along its softest dimension, as expected. Substitutional incorporation of Yb^{3+} at the Cr^{3+} site is verified by single-crystal XRD measurements (see Table B.1), which also show the increased interlayer spacing. The single-crystal data show no detectable electron density between layers, ruling out Yb^{3+} intercalation.

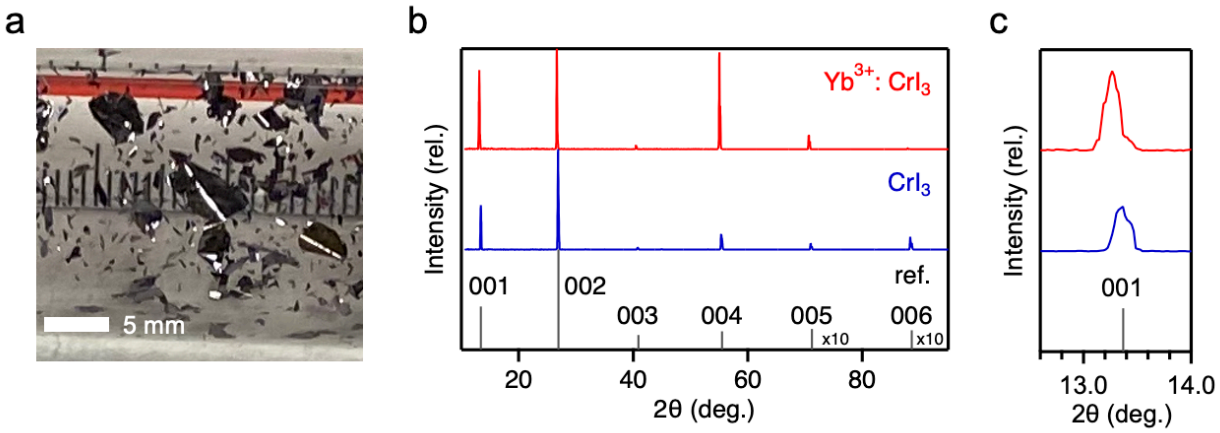

Figure 3.1 (a) Photograph of 4.9% Yb^{3+}:CrI_3 crystals prepared by chemical vapor transport. The scale bar shows 5 mm. All experiments were performed on individual single-crystal flakes from such a reaction tube. **(b)** XRD data collected on undoped and Yb^{3+}-doped CrI_3 single crystals using a powder diffractometer. Only (00*l*) peaks are observed, indicating an oriented sample. Reference peaks for *c*-oriented CrI_3 diffraction are included (black, ICSD Coll. Code 251654). **(c)** Magnified view of the 001 reflection for the same samples, displaying an increase in the interlayer lattice spacing upon Yb^{3+} doping. The displayed XRD data was corrected for instrumental error due to sample height and x-ray alignment (see Figure 5.6).

Figure 3.2a plots the PL spectra of CrI_3 and Yb^{3+}:CrI_3 single flakes measured at several temperatures between 4 and 200 K. The CrI_3 spectrum broadens and decreases in intensity with increasing temperature, eventually reaching only 7.5% of its 4 K intensity at 200 K (see Figure 5.18). Although the broadening to higher energies is expected from thermal hot bands, the broadening to lower energies is abnormal and suggests an additional feature. Upon introduction of Yb^{3+}, the broad featureless *d-d* emission of Cr^{3+} disappears and is replaced by a series of sharp *f-f* transitions of Yb^{3+} around 1.15 eV. Assignment of the PL fine structure is discussed later. In some samples, Yb^{3+} doping also reveals another broad emission band centered at ~0.95 eV, which is responsible for the red tail of the CrI_3 PL here and in some literature spectra. This feature has been traced to Ni^{2+} impurities (<0.4%) found in some Cr(0) precursors, and it can be mostly eliminated by using 5N Cr(0) precursors (Figure 3.2a, bottom panel). The Yb^{3+} PL is not influenced by this Ni^{2+} impurity (see Figure 5.18).

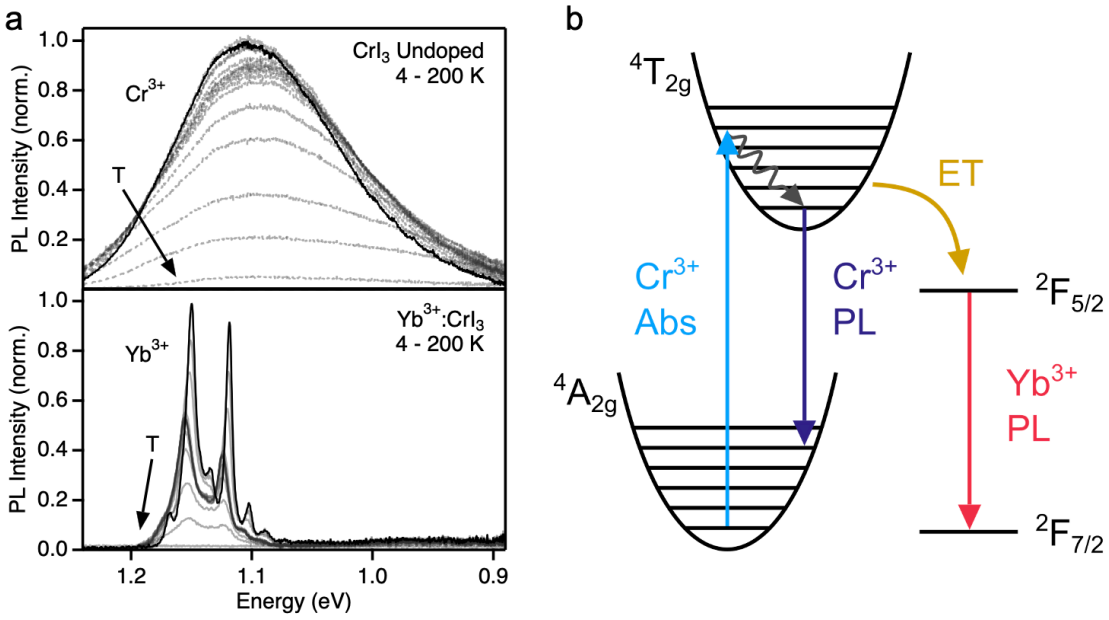

Figure 3.2 (a) Variable-temperature PL spectra of CrI_3 (top) and 4.9% Yb^{3+}:CrI_3 (bottom), measured from 4 to 200 K under 1.88 eV CW excitation at 4 mW/cm^2. **(b)** Single-configurational-coordinate diagram (A_{1g} coordinate) describing vibronic broadening of the absorption and luminescence bands associated with transitions between the $^4A_{2g}$ and $^4T_{2g}$ ligand-field states of pseudo-octahedral Cr^{3+}. In Yb^{3+}-doped CrI_3, energy transfer from the Cr^{3+} $^4T_{2g}$ excited state to Yb^{3+} yields sensitized $^2F_{5/2} \rightarrow {}^2F_{7/2}$ *f-f* luminescence.

Figure 3.2b illustrates the photophysics of Yb^{3+}:CrI_3 schematically. The lowest-energy excited state of CrI_3 is the Cr^{3+} $^4T_{2g}$ ligand-field state, involving excitation of a t_{2g} electron into a σ-antibonding e_g orbital (in idealized O_h symmetry). The resulting change in equilibrium geometry is described by the single-configurational-coordinate (SCC) diagram of Figure 3.2b, which illustrates the totally symmetric distortion coordinate. This $^4T_{2g}$ excited state also distorts along a symmetry-breaking Jahn-Teller coordinate (not illustrated).[21] These distortions lead to extensive vibronic progressions in the absorption and PL spectra associated with this transition, and cause a large PL Stokes shift. Doping CrI_3 with Yb^{3+} introduces a set of $^2F_{5/2}$ states just below the Cr^{3+} $^4T_{2g}$ excited state, favorably positioned for efficient $Cr^{3+} \rightarrow Yb^{3+}$ energy transfer. At 4.9% Yb^{3+} doping, the Cr^{3+} $^4T_{2g}$ PL is entirely quenched and strong Yb^{3+} $^2F_{5/2}$ emission is observed in its place (Figure 3.2a). Because both Cr^{3+} and Yb^{3+} states are localized at single ions, energy migration

within the CrI_3 lattice is required for this complete quenching. In undoped CrI_3, energy migration among equivalent Cr^{3+} sites may occur but is not readily apparent. In Yb^{3+}:CrI_3, this energy migration is interrupted when energy is captured by Yb^{3+} dopants. In 4.9% Yb^{3+}:CrI_3, the average Cr^{3+} ion has only ~14% probability of having a neighboring Yb^{3+}, and ~50% probability of having at least one Yb^{3+} within its first two cation shells. Energy must therefore migrate over at least a few lattice sites within the $^4T_{2g}$ lifetime to fully quench the Cr^{3+} emission as observed in Figure 3.2a.

Figure 3.3a shows the anticipated electronic structure of Yb^{3+} in CrI_3. In the free ion, spin-orbit coupling splits the ^2F term into $^2F_{5/2}$ (excited) and $^2F_{7/2}$ (ground) states by an amount $\Delta E = 7/2\zeta$, where $\zeta = 361.8$ meV is the free-ion spin-orbit coupling constant.[23] In crystals, each of these states is further split by the crystal field. Figure 3.3b shows circularly polarized PL spectra of 4.9% Yb^{3+}:CrI_3 measured in a 0.5 T field applied parallel to the crystal's *c* axis (*vide infra*). Three zero-phonon electronic origins are observed and assigned to the $\Gamma_8 \rightarrow \Gamma_6$, Γ_8, and Γ_7 transitions anticipated from Figure 3.3a using idealized O_h notation. The actual cation site symmetry in CrI_3 is lower (Figure 3.3a, right),[24] but the expected low-symmetry splitting of the Γ_8 origin is not clearly identifiable. Analysis of these PL energies within the Angular Overlap Model (AOM)[25] reproduces the $^2F_{7/2}$ splittings well, predicting a $^2F_{5/2}$ splitting of ~34 meV and splittings of the two Γ_8 levels by <0.5 meV each (see Figure 5.8). Additional satellite features are observed ~127 cm^{-1} (15.7 meV) below the Γ_8 and Γ_7 electronic origins and assigned as phonon sidebands. Raman spectra show a totally symmetric lattice breathing mode of CrI_3 at this energy ($\nu = 127$ cm^{-1}).[26]

A striking aspect of this Yb^{3+}:CrI_3 PL is its very low energy relative to other Yb^{3+} PL. This energy is primarily determined by spin-orbit coupling (Figure 3.3a). Yb^{3+} spin-orbit coupling can be reduced from that in the free ion by covalent expansion of the *f*-electron wavefunctions (nephelauxetic effect),[27, 28] but *f*-orbital covalency in trivalent lanthanides is typically very small and this effect is usually considered negligible at ambient pressure. A survey of Yb^{3+}-doped crystals shows that the energy gap between Yb^{3+} $^2F_{5/2}$ and $^2F_{7/2}$ barycenters remains very near the free-ion value of ΔE ~ 1.266 eV across doped oxide, fluoride, chloride, bromide, sulfide, and phosphide lattices (see Figure 5.10).[29-33] We note that we have been unable to find *any* reports of

PL from other Yb^{3+}-doped iodide crystals, perhaps because Yb^{3+} is easily reduced to Yb^{2+} under common iodide crystal-growth conditions. Yb^{3+}:CrI_3 deviates from this typical behavior substantially: ΔE is only ~1.163 eV, or ~9% smaller than in the free ion, representing the smallest spin-orbit coupling yet reported for Yb^{3+}. Covalency in Yb^{3+}:CrI_3 is certainly enhanced by the large ionic radius and polarizability of the iodides, but this consideration alone likely cannot explain the anomaly. The atomic spin-orbit coupling of I is also much greater than those of other common ligands for Yb^{3+}, and should contribute to the spectroscopic spin-orbit splitting *via* covalency. Furthermore, the large ionic radius of Yb^{3+} compared to Cr^{3+} means that Yb^{3+} experiences an internal pressure imposed by the surrounding lattice, which may also increase covalency. Importantly, Yb^{3+}-I^- covalency is essential for strong Yb^{3+}-Cr^{3+} superexchange coupling.

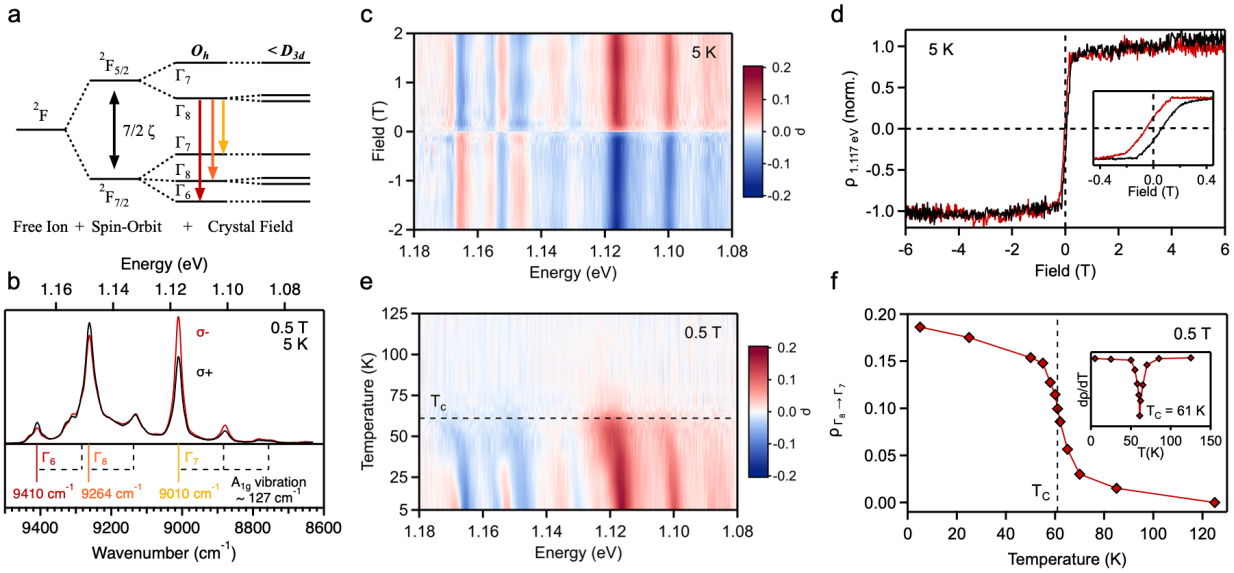

Figure 3.3 (a) Splitting of the Yb^{3+} free-ion ^2F term due to spin-orbit (ζ) and crystal-field (O_h, $<D_{3d}$) interactions. The colored down arrows indicate the three crystal-field transitions anticipated in the low-temperature PL spectrum in the idealized O_h site symmetry. The actual site symmetry is reduced to $<D_{3d}$, *e.g.*, to C_2, splitting each Γ_8 level into two Kramers doublets. **(b)** Magnetic circularly polarized luminescence (MCPL) spectra of 4.9% Yb^{3+}:CrI_3 measured at 5 K with an applied magnetic field of 0.5 T. The σ^- (red) and σ^+ (black) spectra were collected using unpolarized 1.88 eV CW excitation at 40 mW/cm^2 and have different amplitudes. The three electronic origins in idealized O_h symmetry are indicated below the spectra, assigned to the $\Gamma_8 \rightarrow \Gamma_6$, Γ_8, and Γ_7 transitions illustrated in panel (a). The dashed black lines indicate vibronic sidebands with a characteristic energy spacing of ~127 cm^{-1} (15.7 meV), consistent with the A_{1g} lattice mode of CrI_3. **(c)** False-color plot of the MCPL polarization ratio, $\rho = (\sigma^- - \sigma^+)/(\sigma^- + \sigma^+)$, for the full Yb^{3+} PL spectrum, measured from -2 to +2 T at 5 K. **(d)** ρ of the $\Gamma_8 \rightarrow \Gamma_7$ electronic origin (1.117 eV) plotted as a function of magnetic field from -6 to 6 T. The black (red) trace corresponds to the positive (negative) field sweep direction. Inset: Expanded plot of ρ between -0.4 and +0.4 T, showing a coercive field of ~55 mT. For both field-sweep measurements, the sample was excited with linearly polarized 1.96 eV excitation, but with different powers (see Section 3.5 Experimental Methods). **(e)** False-color plot of the polarization ratio *vs* temperature, measured at 0.5 T. The dashed black line indicates the Curie temperature of bulk CrI_3 (T_C = 61 K). **(f)** Plot of the $\Gamma_8 \rightarrow \Gamma_7$ polarization ratio at the peak maximum measured at 0.5 T as a function of temperature. The red curve is a guide to the eye. Inset: Derivative of ρ as a function of temperature. The extracted Curie temperature is 61 K, indistinguishable from that of the undoped crystal.

From Figure 3.3a, all features show circularly polarized PL, with the $\Gamma_8 \rightarrow \Gamma_7$ origin showing

the greatest polarization ratio ($\rho = (\sigma^- - \sigma^+)/(\sigma^- + \sigma^+) = 19\%$). ρ is independent of excitation power but its maximum value varies somewhat between samples (see Figure 5.11, Figure 5.12). Figure 3.3c plots ρ across the entire PL spectrum as a function of magnetic field. All Yb^{3+} transitions are influenced by the applied field in the same way, consistent with all PL arising from the same excited state (Γ_8). Figure 3.3d plots ρ for the $\Gamma_8 \rightarrow \Gamma_7$ peak as a function of applied field. ρ increases rapidly at very low fields and saturates at only ~0.2 T. Increasing the field from 0.2 to 6.0 T does not change ρ further, consistent with complete magnetization of Yb^{3+} by 0.2 T. On an expanded scale, these data show a hysteresis with coercivity of ~55 mT, comparable to that found in magnetic measurements of bulk CrI_3.[18, 34] We note that these ρ values are generally small compared to those in cubic Yb^{3+}:InP (~70% at 10 T, 4.2 K),[33] possibly suggesting an in-plane or canted Yb^{3+} anisotropy. Figure 3.3e summarizes the temperature dependence of ρ, measured at 0.5 T, and Figure 3.3f highlights the temperature dependence for $\Gamma_8 \rightarrow \Gamma_7$ individually. All spectral features behave similarly, showing a pronounced drop in polarization at the Curie temperature of bulk CrI_3 (~61 K, see Figure 3.3f, inset). These magneto-optical data agree well with magnetic susceptibility data (see Figure 5.13), and both indicate that Yb^{3+} doping causes no significant change in the magnetic characteristics of CrI_3 in these samples. This MCPL field and temperature dependence is highly unusual for Yb^{3+}, which generally shows simple paramagnetism of a pseudo-spin 1/2. For example, our AOM crystal-field analysis (see Figure 5.8) predicts $g_{avg} \sim 2.7$ for the lowest $^2F_{7/2}$ Kramers doublet. Overall, the anomalous magnetism seen in the Yb^{3+} MCPL reflects *magnetic* integration of Yb^{3+} with ferromagnetic CrI_3.

Magnetic ordering was originally explained by Weiss in terms of a huge internal "molecular field"[35] exerted upon individual ions by their surrounding magnetic matrix, and this model provides a useful heuristic for estimating the effective field experienced by Yb^{3+} within CrI_3. In this model, the effective field is given by the sum of external and molecular fields, as in eq (3.1)

$$H_{eff} = H_{ext} + H_{mol} \tag{3.1}$$

In Figure 3.3c,d, CrI_3 reaches magnetic saturation at very small H_{ext} (<0.2 T). At such low fields, $H_{ext} << H_{mol}$, and hence $H_{eff} \sim H_{mol}$. In the molecular-field model, H_{mol} in CrI_3 is given by eq (3.2),

$$H_{mol} = \frac{2zJ\langle S\rangle}{g\mu_B} \tag{3.2}$$

where, J is the nearest-neighbor exchange coupling constant, z = 3 in CrI_3, g is the Landé g factor (2.00 for Cr^{3+} in CrI_3), μ_B is the Bohr magneton, and $\langle S\rangle$ is the spin expectation value for Cr^{3+} in CrI_3, whose absolute value equals $3/2$ at saturation. T_C in this model is determined by J according to eq (3.3),

$$T_C = \frac{2zJS(S+1)}{3k_B} \tag{3.3}$$

where $S = 3/2$ for Cr^{3+}, and k_B is the Boltzmann constant. From T_C = 61 K, eq (3.3) yields a value of J = 0.70 meV in CrI_3. Entering this J value into eq (3.2) yields H_{mol} = ~54 T in CrI_3. H_{mol} is dominated by superexchange coupling, since dipolar contributions cannot account for the high T_C of CrI_3.[36] For Yb^{3+} in CrI_3, J is reduced by the shielding of the 4*f* orbitals. Cr^{3+}(*d*)-Yb^{3+}(*f*) superexchange coupling has received relatively little experimental or theoretical attention,[37-39] but relevant experimental data are found in inelastic neutron scattering analyses of $Cs_3Yb_{1.8}Cr_{0.2}Br_9$, where Yb^{3+}-Cr^{3+} exchange splittings are ~1/4 those for Cr^{3+}-Cr^{3+}.[37] This scaling factor is approximate because of the different lattice structure, but $Cs_3Yb_{1.8}Cr_{0.2}Br_9$ is the most similar halide-bridged Yb^{3+}-Cr^{3+} system for which reliable exchange-coupling strengths could be found. This rough scaling reduces H_{mol} to ~14 T. Accounting for the larger g value of Yb^{3+} (~2.7, see Figure 5.8), our best estimate is H_{mol} ~ 10 T for Yb^{3+} ions within CrI_3. Future spectroscopic measurements (*e.g.*, inelastic neutron scattering, Mössbauer, *etc.*) and calculations will be needed to refine this estimate, but the central conclusion drawn from both the experimental data and this analysis is clear: Yb^{3+} magnetization in Yb^{3+}:CrI_3 is effectively pinned to the magnetic ordering of the CrI_3 lattice through strong Yb^{3+}-Cr^{3+} superexchange coupling. The large H_{mol} in Yb^{3+}:CrI_3 is attributable in large part to the Yb^{3+}-I^- covalency discussed above. For comparison, exchange fields of 1.7 and ~1.1 T are reported for Yb^{3+} in ferrimagnetic hexagonal $YbFeO_3$[40] and distorted orthorhombic $YbCrO_3$.[41] At these values, Yb^{3+} magnetization is not pinned to the ordered TM^{3+} spin sublattices.

A further remarkable aspect of Yb^{3+}:CrI_3 is that the effects of H_{mol} are evident even at zero magnetic field (H_{ext} = 0). Figure 3.4a plots zero-field Yb^{3+} PL spectra as a function of temperature

from 4 to 200 K. Viewing the data starting from high temperature, the peak positions appear nearly constant until roughly T_C. Below T_C, the peaks all shift to lower energy together. This redshift is also evident in Figure 3.3e. Figure 3.4b highlights the temperature dependence of the $\Gamma_8 \rightarrow \Gamma_7$ transition energy. From 120 K to ~T_C, the transition energy increases gradually by only ~2 meV. Such temperature dependence has been variously modeled in terms of Raman scattering of non-resonant phonons or direct absorption/emission of phonons resonant with a crystal-field splitting.[42, 43] For example, both models reproduce the $^2F_{7/2} \rightarrow {}^2F_{5/2}$ transition energies of Yb^{3+}:YAG well, whereas the resonant phonon model reproduces absorption linewidths marginally better.[43] As such, we apply the resonant phonon model here. The PL energies above T_C are thus described by eq (3.4),[42, 43]

$$E(T) = E_0 + \frac{\alpha_s}{e^{\Delta/k_B T} - 1} \qquad T > T_C \tag{3.4}$$

where E_0 is the energy at 0 K, a_s describes the electron-phonon interaction strength, and Δ is the energy of the activating phonon mode, fixed at $\Delta = 127$ cm^{-1} (15.7 meV, Figure 3.3b).

The solid curve in the high-temperature portion of Figure 3.4b (>T_C) shows a fit to the high-temperature data using eq (3.4), floating E_0 and a_s and yielding best-fit values of 1.1242 eV and -6.3 meV, respectively. Eq (3.4) plateaus at E_0 in the limit of 0 K (dashed line < T_C in Figure 3.4b), but the experimental peak energy shows a discontinuity at T_C, dropping sharply and decreasing with decreasing temperature until reaching ~7 meV below E_0 in the low-temperature limit. With its link to T_C and its characteristic curvature, this trend in Yb^{3+} PL energy is associated with the spontaneous magnetization of individual CrI_3 monolayers, even though there is no net magnetization in these samples.

Spontaneous ferromagnetic ordering is classified as a second-order phase transition and, within the theory of universal scaling laws, is characterized by the order parameter β shown in eq (3.5) describing the magnetization temperature dependence.[44]

$$M(T) = M_0 \left(-\frac{T - T_c}{T_c}\right)^{\beta} \tag{3.5}$$

M_0 is the saturation moment per magnetic ion and equals 3.1 μ_B for CrI_3.[18] The precise value of β depends on the underlying spin physics, but it is commonly around 1/3.[12] Previous

examination of bulk CrI_3 found a critical exponent of β = 0.284, between that expected from the 3D Ising model (β = 0.325) and that of the tri-critical mean-field model (β = 0.250).[34] Accordingly, the data in Figure 3.4b below T_C were simulated using eq (3.6) (sum of eq (3.4) and eq (3.5), with eq (3.4) parameters fixed by the high-temperature data). The scaling parameter (γ) in eq (3.6) relates magnetization to PL energy shift. The data are reproduced well using fixed values of β = 1/3, T_C = 60 K, and Δ = 127 cm^{-1} (15.7 meV), with γ as the only adjustable parameter. Relating eq (3.5) and eq (3.6), these results indicate an Yb^{3+} PL energy shift of -2.2 meV/μ_B during spontaneous CrI_3 intralayer magnetization. We stress that the zero-field PL data in Figure 3.4 are not magnetic data, but highlight the strong influence of CrI_3 spontaneous magnetization on the Yb^{3+} PL. Because T_C in these samples is indistinguishable from that of bulk CrI_3 (Figure 3.3f, Figure 5.13), we tentatively attribute the small apparent broadening of the PL energy discontinuity around T_C in Figure 3.4b to additional PL hot bands that are not spectrally resolved.

$$E(T) = E_0 + \frac{\alpha_s}{e^{\Delta/k_B T} - 1} + \gamma\left(-\frac{T - T_c}{T_c}\right)^{\beta} \qquad \mathrm{T} < \mathrm{T}_C \tag{3.6}$$

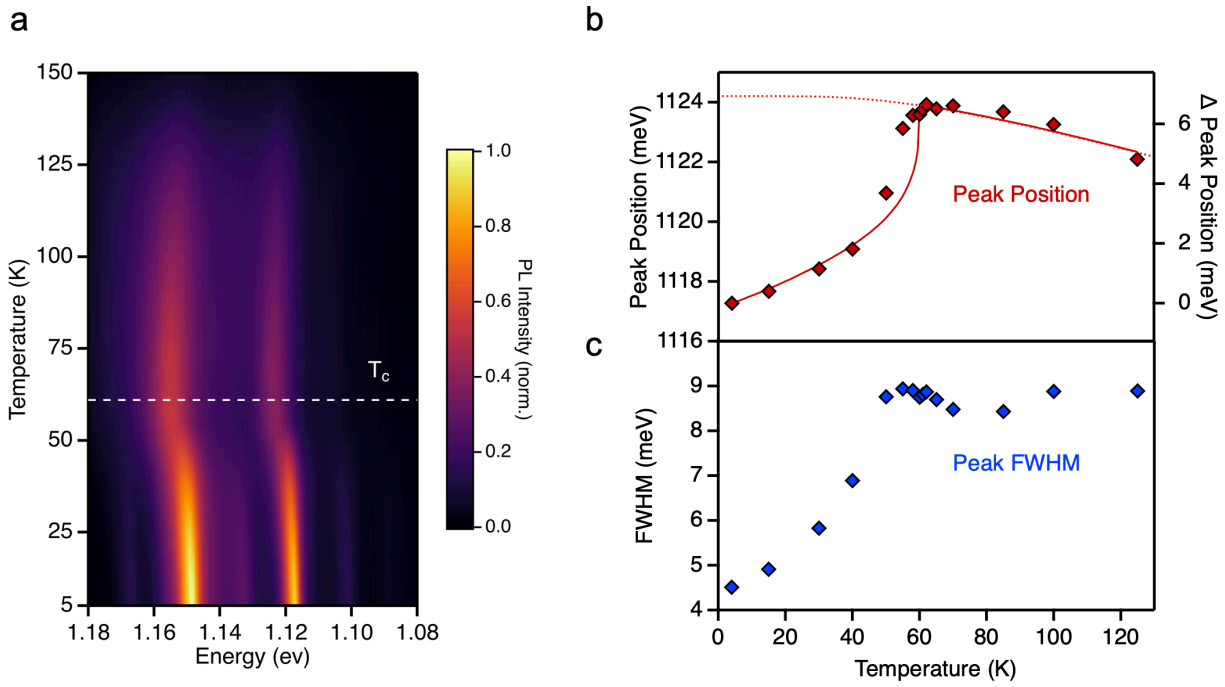

Figure 3.4 (a) False-color plot of the Yb^{3+} PL intensities vs temperature measured for 4.9% Yb^{3+}:CrI_3 from 4 to 150 K at zero external magnetic field. The horizontal dashed line indicates T_C = 61 K. **(b)** Peak position of the $\Gamma_8 \rightarrow \Gamma_7$ transition plotted vs temperature. The solid red curve shows the behavior predicted from the combination of resonant phonon interactions (eq (3.4)) and spontaneous magnetization (below T_C, eq (3.6)). The dashed red curve shows the behavior predicted from eq (3.4) alone below T_C. The solid curve was obtained using eq (3.4) and eq (3.6) with fixed parameters of Δ = 127 cm^{-1} (15.7 meV), T_C = 60 K, and β = 1/3, adjusting only the amplitude scaling. **(c)** Plot of the $\Gamma_8 \rightarrow \Gamma_7$ PL linewidth vs temperature, from the same VTPL measurements.

Figure 3.4c plots the temperature dependence of the $\Gamma_8 \rightarrow \Gamma_7$ linewidth (full-width-at-half-maximum, FWHM). These data show similar trends as observed in the peak energies of Figure 3.4b. Below T_C, the FWHM decreases from ~9 meV to ~4.5 meV in the low-temperature limit, attributed to the reduction in spin disorder around Yb^{3+}. These data thus also reflect spontaneous magnetic ordering in monolayers of CrI_3. Although distinct low-energy shoulders are not resolved in these data, we hypothesize that the energy and linewidth changes below T_C both ultimately stem from loss of hot-magnon sideband intensity as CrI_3 monolayers order magnetically.[45] It will be an interesting future direction to explore magnon coupling to *f-f* transitions in these and related doped 2D magnetic materials.

3.4 Conclusion

In summary, doping Yb^{3+} into the 2D van der Waals ferromagnet CrI_3 transforms this material's PL from broad-band to sharp multi-line, while retaining its key magnetic functionality. The *f-f* PL of Yb^{3+}:CrI_3 is anomalously low in energy, reflecting relatively covalent Yb^{3+}-I^- bonding. Yb^{3+} magnetization is pinned to CrI_3 by strong superexchange interactions, which contribute an effective internal field of ~10 T that is greater than the field required for magnetic saturation of paramagnetic Yb^{3+} and much greater than the field required for full CrI_3 magnetization at low temperature (~0.2 T). Flipping the magnetization of CrI_3 with a small external field thus also flips the Yb^{3+} magnetization and inverts its PL circular polarization. Magnetic pinning is maintained up to the T_C of CrI_3, but is rapidly lost above T_C. We further showed that the Yb^{3+} PL energy and linewidth both sense this internal field even at zero applied field, mapping spontaneous *intra*layer magnetic ordering below T_C despite the absence of net magnetization. Because each Yb^{3+} ion is a local lattice defect within an individual CrI_3 monolayer, we expect these induced functionalities to persist down to the monolayer, prompting future studies on exfoliated Yb^{3+}:CrI_3 and associated stacked van der Waals heterostructures and layered devices. These results demonstrate the power of designer defects to add functionality to 2D magnetic materials, enrich their fundamental physics, and create new materials of potential utility for future spin-photonics applications.

3.5 Experimental Methods

General Considerations. All sample preparation and manipulation was performed in a glovebox under an atmosphere of purified dinitrogen.

Chemicals. Chromium metal powder (200 mesh, 99.94%, lot X15E028) was purchased from Alfa Aesar. According to the manufacturer's certificate of analysis, the majority of the impurity in this sample lot was Ni at 343 ppm. A chromium chip (99.995%, lot MKCH4484) was also purchased from Sigma Aldrich as a higher-purity Cr source. The Cr chip was ground to a powder using a mortar and pestle and used in an analogous manner as the powder precursor. I_2 (≥99.99%)

was purchased from Sigma Aldrich. Ytterbium metal powder 40 mesh (99.9%) was purchased from BeanTown chemical. All chemicals were used as received without further purification.

Synthesis of CrI_3 and Yb^{3+}-Doped CrI_3 Single Crystals. Single crystals of the doped and undoped CrI_3 were grown by chemical vapor transport in a manner similar to that described in previous literature reports.[46] For undoped CrI_3, Cr(0) metal and I_2 were loaded as a 1:3 stochiometric ratio into a quartz tube and sealed under an evacuated atmosphere. For Yb^{3+}-doped CrI_3, additional Yb(0) metal was loaded along with the other starting materials. The quartz tubes were 15 cm long with inner and outer diameters of 14 and 16 mm, respectively. Sealed tubes were placed in an open-ended horizontal tube furnace with the starting materials in the hot zone set at 650 ˚C and the other end at a temperature of ca. 500 ˚C. Samples were heated for 5 days and then allowed to slowly cool to room temperature. Once cooled, the tubes were brought into a glove box and cracked open to yield shiny dark plate-like crystals that had formed at the cold end of the quartz tube. Elemental analysis of the Yb^{3+}-doped samples was performed by inductively coupled plasma mass spectrometry (ICP-MS) using a PerkinElmer NexION 2000B. Samples were prepared by digesting single crystals in concentrated nitric acid with sonication and then further diluted in ultrapure H_2O. Yb^{3+} doping levels are reported as cation mole fraction, $[Yb^{3+}]/([Cr^{3+}]+[Yb^{3+}])$, in percentage, with an estimated uncertainty of ±0.1%. Crystal thickness was measured by mounting a representative flake to a glass slide using double-sided tape and imaging the flake with an optical microscope in a glovebox at various magnifications. The edge length was calculated in ImageJ[47] using known pixel resolutions.

X-ray Diffraction (XRD) Characterization. Samples were prepared for XRD on the powder diffractometer by placing single crystals onto silicon substrates and sealing under Kapton films to reduce exposure to air. Data were collected using a Bruker D8 Discover powder diffractometer with a high-efficiency IμS microfocus x-ray source for Cu Kα radiation (50 kV, 1 mA). For single-crystal XRD, a crystal measuring 0.10 x 0.05 x 0.01 mm^3 was mounted on a loop with oil. Data were collected at 263 K on a Bruker APEX II single-crystal X-ray diffractometer using Mo-radiation, equipped with a Miracol X-ray optical collimator. The data were integrated and scaled using SAINT, SADABS within the APEX2 software package by Bruker.[48] Solution by direct

methods (SHELXT[49, 50] or SIR97[51, 52]) produced a complete heavy-atom phasing model consistent with the proposed structure. The structure was completed by difference Fourier synthesis with SHELXL.[53, 54] Scattering factors are from Waasmair and Kirfel.[55] All atoms were refined anisotropically by full-matrix least-squares.

Including intrinsic disorder, a least squares refinement optimization of the data yields the lattice structure that we report. From the 983 reflections collected covering the indices, $-8 \leq h \leq 8$, $-14 \leq k \leq 14$, $-8 \leq l \leq 8$, 518 reflections were found that were symmetry independent and an R_1 value of 0.0521 was obtained, indicating a good fit. R_1 is calculated as:

$$R_1 = \frac{\sum\big||F_{obs}| - |F_{calc}|\big|}{\sum|F_{obs}|}$$

There is no detectable electron density between layers, indicating that Yb^{3+} does not intercalate between layers in CrI_3.

Variable-Temperature Photoluminescence (VTPL). Samples for VTPL measurements were prepared by placing a single crystal between two quartz disks and loading into a closed-cycle helium cryostat. PL spectra were collected by exciting the sample with a continuous-wave 660 nm (1.88 eV) diode at 4 mW/cm^2. Emission was collected and focused into a monochromator with a spectral bandwidth of 0.627 nm and detected by a Hamamatsu InGaAs/InP NIR photomultiplier tube, with signal recorded using a photon counter. Temperature was varied from 4 to 300 K, starting at low temperature. All spectra were corrected for instrument response.

Magnetic Circularly Polarized Luminescence (MCPL). Samples for MCPL measurements were prepared as single crystals placed between two quartz disks and loaded into a superconducting magneto-optical cryostat (Cryo-Industries SMC-1659 OVT) oriented in the Faraday configuration. For full-spectrum measurements at static fields, samples were excited with a 660 nm (1.88 eV) diode at approximately 40 mW/cm^2. For field-sweep measurements, samples were excited with a linearly polarized HeNe laser (632.8 nm/1.96 eV, 27 mW/cm^2 for -6 to +6 T scans, 55 mW/cm^2 for -0.4 to +0.4 T scans). No distinguishable difference was found in the either the PL spectra or variable-field data between the two excitation sources. For field-sweep measurements, the monochromator was centered at 1.117 eV with a 6 nm spectral bandwidth,

and the signal was continuously monitored as the field was swept at a rate of 0.10 T/min and 0.45 T/min for the 0.4 T and 6 T scans, respectively. PL was collected along the magnetic-field axis and passed through a liquid-crystal variable retardation plate set at $\lambda/4$, followed by a linear polarizer to separate the left- and right-circularly polarized components. The PL was then focused into a fiber-optic cable and fed into a monochromator with a spectral bandwidth of 0.627 nm and detected by a Hamamatsu InGaAs/InP NIR photomultiplier, with signals recorded using a photon counter. Polarization ratios are defined as $\rho = (\sigma^- - \sigma^+)/(\sigma^- + \sigma^+) = (I_L - I_R)/(I_L + I_R) = \Delta I/I$, following the sign conventions outlined in Piepho and Schatz.[56]

Magnetic Measurements. Magnetic data on individual single-crystal flakes were collected using a Quantum Design PPMS DynaCool vibrating sample magnetometer (VSM). A flake was affixed to the end of a quartz paddle with varnish (VGE 7031). The paddle was then snapped into the VSM brass sample holder with another quartz paddle placed symmetrically above the sample. The weak background signal from the sample holder was removed in the data analysis. The sample was probed with the external field aligned perpendicular to the face of the crystal, and magnetization data were collected as a function of applied field and temperature. The masses of individual flakes are below 0.1 mg and could not be accurately measured, so the magnetic data are reported in units of emu.

Ligand-field calculations within the Angular Overlap Model (AOM). Yb^{3+} ligand(crystal)-field energies and *g* factors were calculated using the BonnMag package.[25] Crystallographic data[18] on CrI_3 were used to create an $[YbI_6]^{3-}$ unit with reduced symmetry (point group C_2). Crystallographic parameters were not adjusted for size differences between Cr^{3+} and Yb^{3+}. The electronic structure of Yb^{3+} was calculated using the spin-orbit coupling parameter ζ as well as AOM parameters e_σ and e_π to describe σ and π interactions with the I^- ligands, respectively. The value for e_π was taken to be isotropic. The Slater-Condon-Shortley (SCS) parameters F_2, F_4, and F_6 were taken to be 0, as is typically the case for Yb^{3+} ($4f^{13}$ configuration). The Stevens orbital reduction factor *k* was taken to be equal to 1.0. Increasing (decreasing) ζ while keeping all other parameters constant results in an increase (decrease) in all transition energies while retaining peak splitting energies. Adjusting e_σ or e_π alters the relative energies of the peaks but maintains

the barycenters.

3.6 References

(1) Cox, P. A. *Electronic Structure and Chemistry of Solids*; Oxford University Press, 1987.

(2) Henderson, B.; Imbusch, G. F. *Optical Spectroscopy of Inorganic Solids*; Oxford University Press, 1989.

(3) Kittel, C. *Introduction to Solid State Physics*; Wiley, 2004.

(4) Bassett, L. C.; Alkauskas, A.; Exarhos, A. L.; Fu, K.-M. C. Quantum defects by design. *Nanophotonics* **2019**, *8* (11), 1867-1888.

(5) Tran, T. T.; Elbadawi, C.; Totonjian, D.; Lobo, C. J.; Grosso, G.; Moon, H.; Englund, D. R.; Ford, M. J.; Aharonovich, I.; Toth, M. Robust Multicolor Single Photon Emission from Point Defects in Hexagonal Boron Nitride. *ACS Nano* **2016**, *10* (8), 7331-7338.

(6) Hong, J.; Jin, C.; Yuan, J.; Zhang, Z. Atomic Defects in Two-Dimensional Materials: From Single-Atom Spectroscopy to Functionalities in Opto-/Electronics, Nanomagnetism, and Catalysis. *Adv. Mater.* **2017**, *29* (14), 1606434.

(7) Cowley, R. A.; Buyers, W. J. L. The Properties of Defects in Magnetic Insulators. *Rev. Mod. Phys.* **1972**, *44* (2), 406-450.

(8) Wiesendanger, R. Nanoscale Magnetic Skyrmions in Metallic Films and Multilayers: A New Twist for Spintronics. *Nat. Rev. Mater.* **2016**, *1* (7), 16044.

(9) Lima Fernandes, I.; Bouaziz, J.; Blügel, S.; Lounis, S. Universality of Defect-Skyrmion Interaction Profiles. *Nat. Commun.* **2018**, *9* (1), 4395.

(10) Song, T.; Cai, X.; Tu, M. W.-Y.; Zhang, X.; Huang, B.; Wilson, N. P.; Seyler, K. L.; Zhu, L.; Taniguchi, T.; Watanabe, K.; et al. Giant Tunneling Magnetoresistance in Spin-Filter van der Waals Heterostructures. *Science* **2018**, *360* (6394), 1214-1218.

(11) Huang, B.; McGuire, M. A.; May, A. F.; Xiao, D.; Jarillo-Herrero, P.; Xu, X. Emergent Phenomena and Proximity Effects in Two-Dimensional Magnets and Heterostructures. *Nat. Mater.* **2020**, *19* (12), 1276-1289.

(12) Gibertini, M.; Koperski, M.; Morpurgo, A. F.; Novoselov, K. S. Magnetic 2D materials and heterostructures. *Nat. Nanotech.* **2019**, *14* (5), 408-419.

(13) Gong, C.; Zhang, X. Two-dimensional magnetic crystals and emergent heterostructure devices. *Science* **2019**, *363* (6428), eaav4450.

(14) Wang, Q. H.; Bedoya-Pinto, A.; Blei, M.; Dismukes, A. H.; Hamo, A.; Jenkins, S.; Koperski, M.; Liu, Y.; Sun, Q.-C.; Telford, E. J.; et al. The Magnetic Genome of Two-Dimensional van der Waals Materials. *ACS Nano* **2022**, *16* (5), 6960-7079.

(15) Huang, B.; Clark, G.; Navarro-Moratalla, E.; Klein, D. R.; Cheng, R.; Seyler, K. L.; Zhong, D.; Schmidgall, E.; McGuire, M. A.; Cobden, D. H.; et al. Layer-Dependent Ferromagnetism in a van der Waals Crystal Down to the Monolayer Limit. *Nature* **2017**, *546* (7657), 270-273.

(16) Sivadas, N.; Okamoto, S.; Xu, X.; Fennie, C. J.; Xiao, D. Stacking-Dependent Magnetism in Bilayer CrI_3. *Nano Lett.* **2018**, *18* (12), 7658-7664.

(17) Seyler, K. L.; Zhong, D.; Huang, B.; Linpeng, X.; Wilson, N. P.; Taniguchi, T.; Watanabe, K.; Yao, W.; Xiao, D.; McGuire, M. A.; et al. Valley Manipulation by Optically Tuning the

Magnetic Proximity Effect in WSe_2/CrI_3 Heterostructures. *Nano Lett.* **2018**, *18* (6), 3823-3828.
(18) McGuire, M. A.; Dixit, H.; Cooper, V. R.; Sales, B. C. Coupling of Crystal Structure and Magnetism in the Layered, Ferromagnetic Insulator CrI_3. *Chem. Mater.* **2015**, *27* (2), 612-620.
(19) Dillon, J. F.; Kamimura, H.; Remeika, J. P. Magneto-Optical Properties of Ferromagnetic Chromium Trihalides. *J. Phys. Chem. Solids* **1966**, *27* (9), 1531-1549.
(20) Suits, J. Faraday and Kerr Effects in Magnetic Compounds. *IEEE Trans. Mag.* **1972**, *8* (1), 95-105.
(21) Güdel, H. U.; Snellgrove, T. R. Jahn-Teller Effect in the $^4T_{2g}$ State of Chromium(III) in Dicesium Sodium Indium(III) Hexachloride. *Inorg. Chem.* **1978**, *17* (6), 1617-1620.
(22) Peng, B.; Chen, Z.; Li, Y.; Liu, Z.; Liang, D.; Deng, L. Multiwavelength Magnetic Coding of Helical Luminescence in Ferromagnetic 2D Layered CrI_3. *iScience* **2022**, *25* (1), 103623.
(23) Wyart, J.-F.; Tchang-Brillet, W.-Ü. L.; Spector, N.; Palmeri, P.; Quinet, P.; Biémont, E. Extended Analysis of the Spectrum of Triply-ionized Ytterbium (Yb IV) and Transition Probabilities. *Phys. Scripta* **2001**, *63* (2), 113-121.
(24) Georgescu, A. B.; Millis, A. J.; Rondinelli, J. M. Trigonal Symmetry Breaking and Its Electronic Effects in the Two-Dimensional Dihalides MX_2 and Trihalides MX_3. *Phys. Rev. B* **2022**, *105* (24), 245153.
(25) Bronova, A.; Bredow, T.; Glaum, R.; Riley, M. J.; Urland, W. BonnMag: Computer program for ligand-field analysis of f^n systems within the angular overlap model. *J. Comp. Chem.* **2018**, *39* (3), 176-186.
(26) Zhang, Y.; Wu, X.; Lyu, B.; Wu, M.; Zhao, S.; Chen, J.; Jia, M.; Zhang, C.; Wang, L.; Wang, X.; et al. Magnetic Order-Induced Polarization Anomaly of Raman Scattering in 2D Magnet CrI_3. *Nano Lett.* **2020**, *20* (1), 729-734.
(27) Al-Mobarak, R.; Warren, K. D. The Effect of Covalency on the Spin—Orbit Coupling Constant. *Chem. Phys. Lett.* **1973**, *21* (3), 513-516.
(28) Bungenstock, C.; Tröster, T.; Holzapfel, W. B. Effect of Pressure on Free-Ion and Crystal-Field Parameters of Pr^{3+} in LOCl (L = La, Pr, Gd). *Phys. Rev. B* **2000**, *62* (12), 7945-7955.
(29) Schwartz, R. W. Electronic Structure of the Octahedral Hexachloroytterbate Ion. *Inorg. Chem.* **1977**, *16* (7), 1694-1698.
(30) Kanellakopulos, B.; Amberger, H. D.; Rosenbauer, G. G.; Fischer, R. D. Zur Elektronenstruktur hochsymmetrischer Verbindungen der Lanthanoiden und Actinoiden—V: Paramagnetische Suszeptibilität und elektronisches Raman-Spektrum von $Cs_2NaYb(III)Cl_6$. *J. Inorg. Nuc. Chem.* **1977**, *39* (4), 607-611.
(31) Tsujii, N.; Imanaka, Y.; Takamasu, T.; Kitazawa, H.; Kido, G. Photoluminescence of Yb^{3+}-Doped $CuInS_2$ Crystals in Magnetic Fields. *J. Appl. Phys.* **2001**, *89* (5), 2706-2710.
(32) Haumesser, P.-H.; Gaumé, R.; Viana, B.; Antic-Fidancev, E.; Vivien, D. Spectroscopic and Crystal-Field Analysis of New Yb-doped Laser Materials. *J. Phys.: Cond. Mat.* **2001**, *13* (23), 5427-5447.
(33) de Maat-Gersdorf, I. Spectroscopic Analysis of Erbium-Doped Silicon and Ytterbium Doped Indium Phosphide. University of Amsterdam, 2001.
(34) Liu, Y.; Petrovic, C. Three-Dimensional Magnetic Critical Behavior in CrI_3. *Phys. Rev. B* **2018**,

97 (1), 014420.
(35) Coey, J. M. D. *Magnetism and Magnetic Materials*; Cambridge University Press 2010.
(36) Lado, J. L.; Fernández-Rossier, J. On the Origin of Magnetic Anisotropy in Two Dimensional CrI_3. *2D Mater.* **2017**, *4* (3), 035002.
(37) Aebersold, M. A.; Güdel, H. U.; Hauser, A.; Furrer, A.; Blank, H.; Kahn, R. Exchange Interactions in Mixed Yb^{3+}-Cr^{3+} and Yb^{3+}-Ho^{3+} Dimers: An Inelastic-Neutron-Scattering Investigation of $Cs_3Yb_{1.8}Cr_{0.2}Br_9$ and $Cs_3Yb_{1.8}Ho_{0.2}Br_9$. *Phys. Rev. B* **1993**, *48* (17), 12723-12731.
(38) Mironov, V. S.; Chibotaru, L. F.; Ceulemans, A. Exchange Interaction in the $YbCrBr_9^{3-}$ Mixed Dimer: The Origin of a Strong Yb^{3+}-Cr^{3+} Exchange Anisotropy. *Phys. Rev. B* **2003**, *67* (1), 014424.
(39) Atanasov, M.; Daul, C.; Güdel, H. U. Modelling of Anisotropic Exchange Coupling in Rare-Earth -Transition-Metal Pairs: Applications to Yb^{3+}-Mn^{2+} and Yb^{3+}-Cr^{3+} Halide Clusters and Implications to the Light Up-Conversion. In *Comp. Chem.: Rev. Current Trends*, Computational Chemistry: Reviews of Current Trends, Vol. 9; World Scientific, 2005; pp 153-194.
(40) Cao, S.; Sinha, K.; Zhang, X.; Zhang, X.; Wang, X.; Yin, Y.; N'Diaye, A. T.; Wang, J.; Keavney, D. J.; Paudel, T. R.; et al. Electronic Structure and Direct Observation of Ferrimagnetism in Multiferroic Hexagonal $YbFeO_3$. *Phys. Rev. B* **2017**, *95* (22), 224428.
(41) Dalal, B.; Sarkar, B.; Dev Ashok, V.; De, S. K. Evolution of Magnetic Properties and Exchange Interactions in Ru Doped $YbCrO_3$. *J. Phys.: Cond. Mat.* **2016**, *28* (42), 426001.
(42) Imbusch, G. F.; Yen, W. M.; Schawlow, A. L.; McCumber, D. E.; Sturge, M. D. Temperature Dependence of the Width and Position of the $^2E \rightarrow {}^4A_2$ Fluorescence Lines of Cr^{3+} and V^{2+} in MgO. *Phys. Rev.* **1964**, *133* (4A), A1029-A1034.
(43) Böttger, T.; Thiel, C. W.; Cone, R. L.; Sun, Y.; Faraon, A. Optical Spectroscopy and Decoherence Studies of Yb^{3+}:YAG at 968 nm. *Phys. Rev. B* **2016**, *94* (4), 045134.
(44) Fisher, M. E. The Theory of Equilibrium Critical Phenomena. *Rep. Prog. Phys.* **1967**, *30* (2), 615-730.
(45) Bermudez, V. M.; McClure, D. S. Spectroscopic studies of the two-dimensional magnetic insulators chromium trichloride and chromium tribromide—II. *J. Phys. Chem. Solids* **1979**, *40*, 149-173.
(46) Seyler, K. L.; Zhong, D.; Klein, D. R.; Gao, S.; Zhang, X.; Huang, B.; Navarro-Moratalla, E.; Yang, L.; Cobden, D. H.; McGuire, M. A.; et al. Ligand-field helical luminescence in a 2D ferromagnetic insulator. *Nat. Physics* **2018**, *14* (3), 277-281.
(47) Abramoff, M. D.; Magalhaes, P. J.; Ram, S. J. Image Processing with ImageJ. *Biophot. Int.* **2004**, *11* (7), 35-42.
(48) Bruker. APEX2 (Version 2.1-4), SAINT (version 7.34A), SADABS (version 2007/4),. **2007**.
(49) Sheldrick, G. M. A short history of SHELX. *Acta Cryst.* **2007**, *A64*, 112-122.
(50) Sheldrick, G. M. SHELXT - Integrated space-group and crystal-structure determination. *Acta Cryst.* **2015**, *A71*, 3-8.
(51) Altomare, A.; Cascarano, G. L.; Giacovazzo, C.; Guagliardi, A. Completion and refinement of crystal structures with *SIR*92. *J. Appl. Cryst.* **1993**, *26*, 343-350.
(52) Altomare, A.; Burla, C.; Camalli, M.; Cascarano, G. L.; Giacovazzo, C.; Guagliardi, A.;

Moliterni, A. G. G.; Polidori, G.; Spagna, R.; Burla, C.; et al. SIR97: a new tool for crystal structure determination and refinement. *J. Appl. Crystallogr.* **1999**, (32), 115-119.
(53) Sheldrick, G. M. SHELXL-97, Program for the Refinement of Crystal Structures. **1997**.
(54) Sheldrick, G. M. Crystal structure refinement with SHELXL. *Acta Cryst.* **2015**, *C71*, 3-8.
(55) Waasmaier, D.; Kirfel, A. New Analytical Scattering Factor Functions for Free Atoms and Ions. *Acta Crysta.* **1995**, *A51* (416-430).
(56) Piepho, S. B.; Schatz, P. N. *Group theory in spectroscopy with applications to magnetic circular dichroism*; John Wiley & Sons, 1983.

Chapter 4. Optically Resolved Exchange Splittings from Strong Impurity-Lattice Magnetic Coupling in the van der Waals Ferromagnet $Yb^{3+}:CrBr_3$

4.1 Overview

The chromium-trihalides (CrX_3; X = Cl, Br, I) have long served as model systems for understanding magnetism and magneto-optics in ionic crystals and they have recently also emerged as archetypes of magnetic two-dimensional (2D) van der Waals materials. Although the physical properties of CrX_3 compounds have now been explored in great depth, the use of impurity doping to generate new properties remains surprisingly underexplored. Here we report on the magnetic and magneto-optical properties of lanthanide-doped $CrBr_3$, in which Yb^{3+} is introduced as a spin-bearing optical point defect. Narrow-line near-infrared dopant photoluminescence is efficiently sensitized by $CrBr_3$-to-Yb^{3+} energy transfer. Magneto-optical measurements show facile spin manipulation of the paramagnetic Yb^{3+} impurities by the surrounding $CrBr_3$ lattice. Photoluminescence data reveal that the Kramers spin degeneracies of the ground- and excited-state Yb^{3+} doublets are spontaneously lifted by strong magnetic exchange with neighboring Cr^{3+} ions, such that individual Yb^{3+} spin transitions are easily resolved even at zero external magnetic field. The temperature and field dependence of these splittings can be used to probe both local and long-range spin correlations. These results highlight the use of extrinsic optical impurities to add new spin-photonic functionality to this classic 2D van der Waals magnet.

4.2 Introduction

The intriguing optical and magneto-optical properties of the layered chromium-trihalide (CrX_3; X = Cl, Br, I) magnetic insulators have been studied for several decades. As relatively simple ionic crystals, early studies of CrX_3 compounds sought to unravel the fundamental origins of their large magnetic rotations of linearly polarized light[1] and the modification of excited energy levels by magnetic states, particularly exchange-related phenomena in the crystal-field transitions of Cr^{3+}.[2-4] The recent demonstration[5] of ferromagnetism in monolayer CrI_3 triggered a rapid resurgence in interest in the chromium trihalides (CrX_3).[6-8] Since then, discoveries involving CrX_3 compounds have ranged from topological spin textures[9-11] to spin-filtering magnetic tunnel junctions constructed from stacked van der Waals heterostructures.[12, 13] The broad, featureless *d-d* luminescence and poor spin coherence of CrX_3[14-17] do not lend themselves to applications in quantum or classical spin-photonic technologies, however, and they obscure any interplay between magnetic ordering and optical transition energies or electronic structure. Harnessing optical defects in crystals, whether intrinsic or extrinsic, offers a pathway for achieving unique and powerful new functionalities, as demonstrated by the examples of nitrogen-doped diamond, diluted magnetic semiconductors, and the ruby laser.[18-20] In magnetic two-dimensional (2D) van der Waals materials, recent reports have investigated the (magneto-)optical properties of vacancies in CrSBr,[21, 22] but deliberate incorporation of optical impurities remains almost entirely unexplored.

Recently, our group reported on the magneto-optical properties of impurity-doped CrI_3.[23] Paramagnetic Yb^{3+} ions added to this lattice are tightly coupled to the surrounding spins and their photoluminescence (PL) allows optical sensing of spontaneous or induced magnetization in bulk CrI_3. The specifics of the Yb-Cr coupling remain unclear, however, because anomalously high Yb_{3+} *f*-orbital covalency in Yb^{3+}:CrI_3 broadens the *f-f* PL, impeding in-depth analysis of the underlying electronic structure.[17]

Here, we report a detailed investigation of the PL of $CrBr_3$ crystals doped with Yb^{3+}. Yb^{3+} *f*-orbital covalency in this material is substantially smaller than in Yb^{3+}:CrI_3.[17] As a consequence, the PL of Yb^{3+}:$CrBr_3$ is dramatically narrower and reveals extensive fine structure that has not

been resolvable in Yb^{3+}:CrI_3. Variable-temperature and variable-field measurements allow assignment of the fine structure to specific Yb^{3+} electronic transitions between states whose Kramers spin degeneracies are lifted via exchange coupling with the surrounding magnetic $CrBr_3$ lattice. Analysis of these data allows the microscopic Yb^{3+}-Cr^{3+} exchange-coupling strength to be quantified and indicates an effective exchange field of ~30 T experienced by Yb^{3+} in the low-temperature limit. The observation of well-resolved exchange-split impurity spin levels at zero magnetic field in Yb^{3+}:$CrBr_3$ may have interesting ramifications for optical spin preparation and readout, inverse Faraday effect, or other spin-photonic functionalities in this modified magnetic van der Waals material.

4.3 Results and Analysis

4.3.1 Optical Spectroscopy

Figure 4.1a shows the room-temperature absorption spectrum of a single-crystal flake of Yb^{3+}-doped $CrBr_3$. The absorption spectrum shows two main bands that are assigned to the spin-allowed Cr^{3+} $^4A_{2g} \rightarrow {}^4T_{2g}$ and $^4T_{1g}$ ligand-field transitions, two shoulders assigned to the spin-forbidden $^4A_{2g} \rightarrow {}^2T_{1g}$ and $^2T_{2g}$ ligand-field transitions, and a broad band at high energy assigned as a ligand-to-metal charge-transfer (LMCT) transition. All transitions are in good agreement with those previously reported for $CrBr_3$.[3] The weak, parity-forbidden Yb^{3+} *f-f* transitions are not observed due to the low Yb^{3+} doping concentration of ~0.4% relative to the total cation concentration. Figure 4.1a also shows the 5 K photoluminescence excitation (PLE) spectrum of Yb^{3+}:$CrBr_3$, collected by monitoring the Yb^{3+} emission at 1043 nm (*vide infra*). The PLE spectrum shows the same features as the absorption spectrum, with narrower peaks due to the lower temperature, demonstrating efficient sensitization of Yb^{3+} PL by $CrBr_3$.

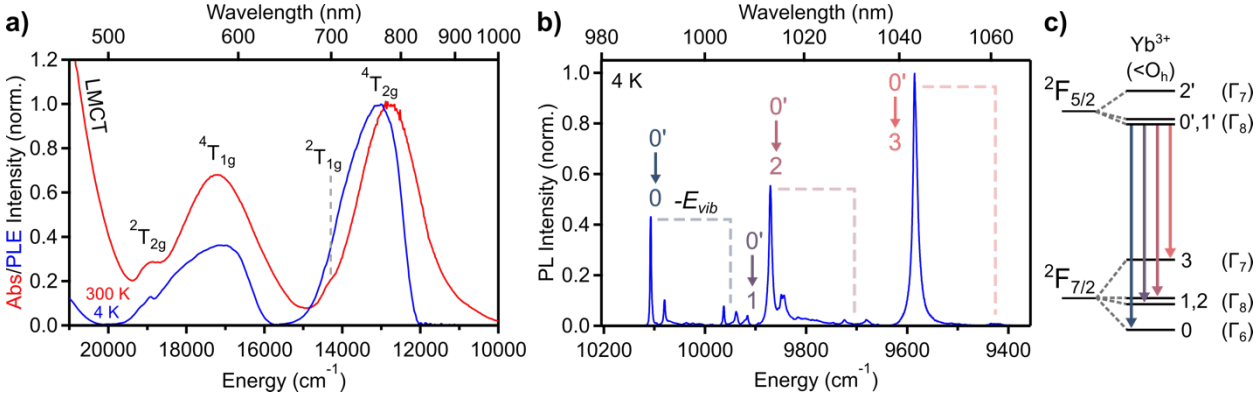

Figure 4.1 (a) 300 K absorption spectrum (red) of a Yb^{3+}:$CrBr_3$ (0.4%) single crystal. Several Cr^{3+} $^4A_{2g} \rightarrow {}^{2S+1}\Gamma$ transitions are labeled. The same transitions are observed in the 5 K Yb^{3+} PLE spectrum (λ_{em} = 1043 nm; see panel (b)), indicating energy transfer between Cr^{3+} and Yb^{3+}. The shifts in PLE peak positions relative to the absorption measurement are due to the measurement temperature. **(b)** 5 K PL spectrum (λ_{ex} = 405 nm) of Yb^{3+}:$CrBr_3$ (0.4%), showing sharp near-IR Yb^{3+} emission peaks. The electronic origins are labeled, and vibronic features are indicated with dashed lines. **(c)** Schematic overview of the observed transitions in the Yb^{3+} PL spectrum. A slightly distorted octahedral crystal field splits the orbital degeneracies of the Γ_8 levels.

Figure 4.1b shows the sensitized Yb^{3+} PL spectrum measured at 5 K. The spectrum is characterized by very narrow linewidths; the highest energy peak has a full width at half maximum (FWHM) of ~1.1 cm^{-1} (0.14 meV; see Figure 5.21). This is in contrast to the PL spectrum of Yb^{3+}:CrI_3 , where the FWHM of the narrowest feature is about 30x larger, even at liquid helium temperatures.[23] Aside from the assigned electronic origins, separate sets of peaks (indicated by dashed lines) are found at fixed energy spacings of ~145 cm^{-1} from the origins. This spacing does not exactly match an A_{1g} vibration in either $CrBr_3$[24] or $YbBr_3$[25]; these peaks are assigned to coupling of the electronic transitions with local $[YbBr_6]^{3-}$ cluster vibrations. The main Yb^{3+} transitions are schematically indicated in Figure 4.1c, where the orbital degeneracies of the 8 spin-orbit states in both the $^2F_{7/2}$ and $^2F_{5/2}$ multiplets are lifted as a result of a small reduction in site symmetry from O_h.

4.3.2 Magneto-optical Properties

The top part of Figure 4.2a shows low-temperature magnetic circularly polarized luminescence (MCPL) spectra of Yb^{3+}:$CrBr_3$ (0.4%) measured for σ^- and σ^+ circular polarizations at an external magnetic field of 6.0 T. At this field, the lattice is fully magnetized and the polarization ratio, defined as $\rho = (\sigma^- - \sigma^+)/(\sigma^- + \sigma^+)$[26],is maximized. The bottom half of Figure 4.2a plots the temperature dependence of ρ for the full spectrum measured at 0.5 T. It is evident that ρ decreases in magnitude as the temperature increases and almost vanishes at temperatures above T_C. Simultaneously, most peaks show a blueshift in the center of gravity, in part due to the appearance of hot bands.

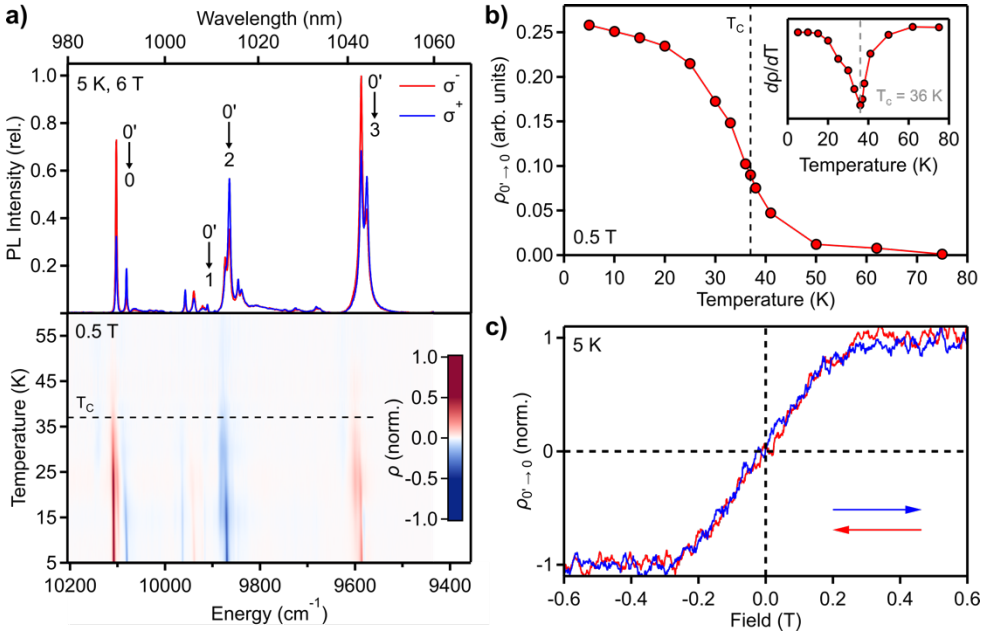

Figure 4.2 (a) Top: MCPL spectra of Yb^{3+}:$CrBr_3$ (0.4%) showing left- and right-circularly polarized emission, denoted σ^- and σ^+, respectively. Spectra were collected at B_{ext} = 6.0 T Bottom: temperature dependence of the polarization ratio (ρ) of the full Yb^{3+} PL spectrum collected at B_{ext} = 0.5 T, where $\rho = (\sigma^- - \sigma^+)/(\sigma^- + \sigma^+)$. **(b)** Polarization ratio of the highest-energy Yb^{3+} $0' \rightarrow 0$ PL peak (A_1 see Section 4.3.3) plotted as a function of temperature. The derivative of these data shows a minimum at 36 K, in close agreement with the reported $CrBr_3$ Curie temperature of 37 K. **(c)** Normalized polarization ratio of the Yb^{3+} $0' \rightarrow 0$ PL plotted as a function of external magnetic field, B_{ext}. The saturation field of ~0.3 T agrees well with reported $CrBr_3$ magnetic data.

Figure 4.2b plots the polarization ratio of the highest energy transition (~10,110 cm^{-1}) as a

function of temperature, highlighting the rapid drop in ρ as the temperature approaches the $CrBr_3$ Curie temperature. Some polarization is observed above T_C, up to a temperature of around 50 K. The inset shows the derivative of ρ with respect to temperature, which has a minimum at 36 K, in good agreement with the reported $CrBr_3$ Curie temperature of 37 K.[27]

Figure 4.2c shows a magnetic field-sweep hysteresis loop obtained by monitoring the polarization ratio of the 10,110 cm^{-1} Yb^{3+} emission as a function of external magnetic field. The saturation field of ~0.3 T agrees well with magnetization measurements of bulk $CrBr_3$.[28, 29] As previously shown for Yb^{3+}:CrI_3,[23] this correlation of Yb^{3+} and Cr^{3+} magnetization indicates pinning of the Yb^{3+} spins to the magnetic host lattice under these conditions. Due to the similarity in magneto-optical properties of Yb^{3+}:$CrBr_3$ and Yb^{3+}:CrI_3, we can make use of the highly resolved spectral data on Yb^{3+}:$CrBr_3$ to deepen our understanding of both materials.

4.3.3 Yb^{3+} Exchange Splittings

Figure 4.3a shows an enlarged view of the Yb^{3+} $0' \rightarrow 0$ transition, plotting spectra in this region collected at various temperatures up to slightly above T_C. Full spectra are shown in Figure 5.22 and Figure 5.23. At 5 K, only peaks A_1 and A_2 are clearly visible, separated by 27 cm^{-1}. At 10 K, two new peaks (B_1 and B_2) appear and these are also separated from one another by 27 cm^{-1}. The energy spacing between A_1 and B_1 is equal to the energy spacing between A_2 and B_2, 16 cm^{-1} at 5 K. At 15 K, A_2 and B_2 begin to shift to higher energies and the linewidths of all transitions increase. Above 25 K, another peak (C_1) starts to grow at ~32 cm^{-1} above A_1. Following the splitting patterns of the other peaks described above, a sixth peak (C_2) may also be expected 27 cm^{-1} below C_1, but this peak is not clearly observed and may be present only as a shoulder on A_1. Above 30 K, all transitions become severely broadened and individual features are poorly resolved.

The rich fine structure in the Yb^{3+}:$CrBr_3$ PL spectrum can be explained by the presence of magnetic exchange splittings in both the ground and excited crystal-field states of Yb^{3+} at zero external field. To illustrate the magnetic character of these peaks, crystals of Yb^{3+}:YBr_3 were prepared and their 5 K PL was investigated. YBr_3 is isostructural to $CrBr_3$ (space group $R\bar{3}h$), but due to the closed-shell configuration of Y^{3+}, the lattice is diamagnetic. The two spectra show the

same main features, with the Yb^{3+}:YBr_3 spectrum shifted to slightly higher energies and spaced closer together due to a reduced crystal field compared to Yb^{3+}:$CrBr_3$ (see Figure 5.25). Both observations can be attributed to the longer metal-ligand bond lengths of Yb^{3+}:YBr_3. Figure 4.3b compares the 5 K PL spectra of Yb^{3+}:$CrBr_3$ and Yb^{3+}:YBr_3 zoomed in at the first Yb^{3+} electronic origin (plotted as energy shift from the respective $0' \rightarrow 0$ origin), highlighting the fact that the Yb^{3+}:YBr_3 spectrum shows no feature analogous to the A_2 peak of Yb^{3+}:$CrBr_3$. Similar differences are identified for each of the electronic origins when comparing the full spectra (see Figure 5.25), and higher-temperature spectra show the absence of hot bands analogous to the *B* peaks in Yb^{3+}:YBr_3 (see Figure 5.26). These results support the assertion that the rich structure described in Figure 4.3a arises from magnetic exchange. Notably, the low-temperature linewidth of Yb^{3+}:$CrBr_3$ in Figure 4.3b is nearly indistinguishable from that of Yb^{3+} in the nonmagnetic YBr_3 lattice, consistent with minimal spin disorder in Yb^{3+}:$CrBr_3$ at 5 K. At higher temperatures, spin fluctuations cause the Yb^{3+}:$CrBr_3$ linewidths to increase rapidly until T_C is reached, while the linewidths of the diamagnetic Yb^{3+}:YBr_3 increase only marginally over the same temperature range (see Figure 5.26). This result highlights the sensitivity of Yb^{3+} optical transitions to spin fluctuations in $CrBr_3$.

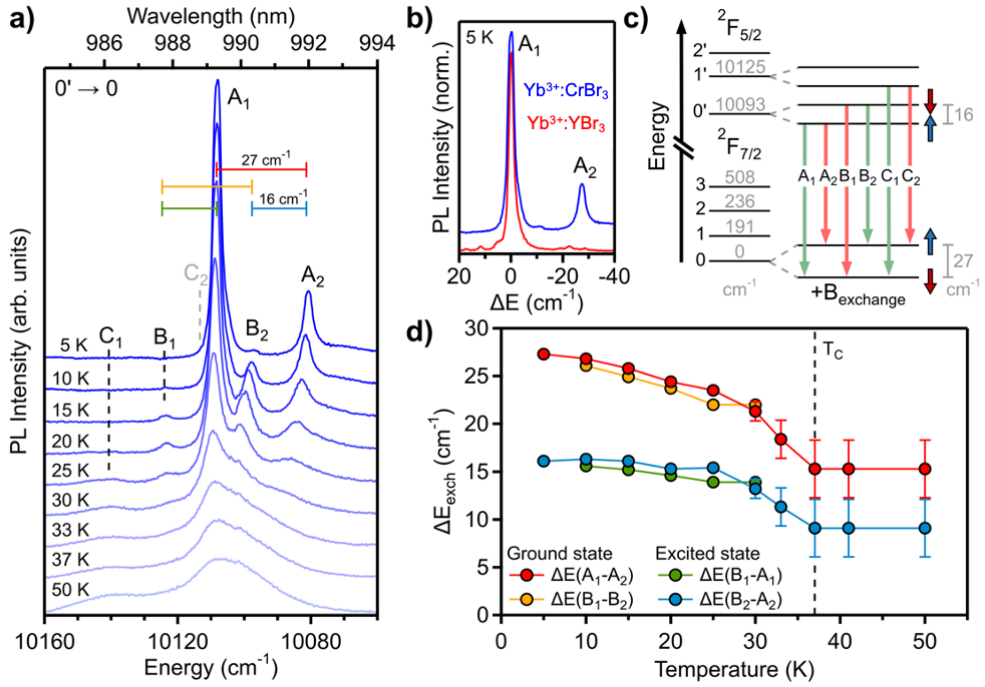

Figure 4.3 (a) Variable-temperature PL spectra of Yb^{3+}:$CrBr_3$ measured in the region of the 0′ → 0 transition. Fine-structure peaks and relevant splitting energies are labeled. The peaks shift as the temperature is increased and the fine structure largely becomes unresolved when T approaches T_C. Colored bars indicate the energy spacings tracked in panel (d). **(b)** Enlarged view of the 0′ → 0 transition in Yb^{3+}:$CrBr_3$ (blue) and a reference sample involving a nonmagnetic host lattice, Yb^{3+}:YBr_3 (red), measured at 5 K. The spectra are normalized and offset for comparison. The A_2 peak, which results from exchange splitting of the ground state (0), is absent in Yb^{3+}:YBr_3. **(c)** Energy diagram for Yb^{3+} showing the 5 K exchange splittings of ground- and excited-state Kramers doublets at zero field, based on the observations of panel (a). The corresponding PL transitions of panel (a) are indicated. The colors indicate if the transition is allowed (green) or forbidden (red), as judged from peak intensities. Individual Yb^{3+} spin states indicated, as explained in Section 4.3.4 **(d)** Ground-state (0) and first-exited-state (0′) exchange splittings (ΔE_{exch}) at zero field plotted as a function of temperature, as determined from the PL peak energies in panel (a). The decrease in ΔE_{exch} with increasing temperature is attributed to loss of lattice spin correlation at higher temperatures.

Figure 4.3c summarizes the results of Figure 4.3a, assigning each peak to a specific transition between exchange-split Yb^{3+} levels. From this diagram, it is clear that the splitting between peaks A_1 and A_2 (or B_1 and B_2) reveals the ground-state exchange splitting (ΔE_{exch}), whereas the splitting

between peaks A_1 and B_1 (or A_2 and B_2) corresponds to ΔE_{exch} of the 0′ excited state. Figure 4.3d plots the ground-state (0) and first-excited-state (0′) splittings (ΔE_{exch}) at zero external magnetic field as a function of temperature. For both states, ΔE_{exch} decreases with increasing temperature, consistent with a decrease in magnetic order of the host lattice at higher temperatures. By 37 K, the splitting is unresolved and only a broad shoulder is observed. The spectrum at 50 K (above T_C) is nearly indistinguishable from that at 37 K, indicating a discontinuity at T_C and confirming the magnetic source of these splittings. For both the ground and excited states, ΔE_{exch} above T_C is around half as large as at 4 K.

4.3.4 Yb^{3+} Spin Alignment in $CrBr_3$

Figure 4.4a shows Yb^{3+}:$CrBr_3$ 0′ → 0 PL spectra collected at different external magnetic fields, measured at 18 K, where B_1 and B_2 peaks are visible. Peaks B_1 and A_2 do not shift with field, whereas peaks A_1 and B_2 shift in opposite directions. The absence of a conventional Zeeman splitting of any of the individual peaks—which would amount to ~1 cm^{-1}/T assuming a g value of ~2.0—is consistent with the spin degeneracy of the Yb^{3+} sublevels having already been lifted at zero external field. The remaining regions of the spectrum match this interpretation (see Figure 5.27).

Using the peak assignments of Figure 4.3c, Figure 4.4b plots the ground- and excited-state splitting energies (ΔE_{exch}) as a function of external magnetic field. Up to ~0.3 T, the Yb^{3+} splittings are nearly insensitive to the external magnetic field, attributed to the presence of cancelling magnetic domains at zero field: the external field's effect on Yb^{3+} spins in domains magnetized parallel to that field is canceled out by its effect on Yb^{3+} spins in domains having the opposite magnetization. At field strengths greater than ~0.3 T, the lattice is fully magnetized (Figure 4.2c) and ΔE_{exch} of the Yb^{3+} ground state decreases while ΔE_{exch} of the excited state increases, with slopes corresponding to g values of similar magnitude (~1.9, eq (4.1)) but opposite signs. The field dependence of the Yb^{3+} energies is summarized schematically in Figure 4.4c. From ΔE_{exch} and the g value obtained from Figure 4.4b, the exchange field experienced by Yb^{3+} can be estimated to be ~ 30 T at 5 K.

$$g = \left|\frac{1}{\mu_B}\frac{\partial \Delta E_{exch}}{\partial B}\right| \tag{4.1}$$

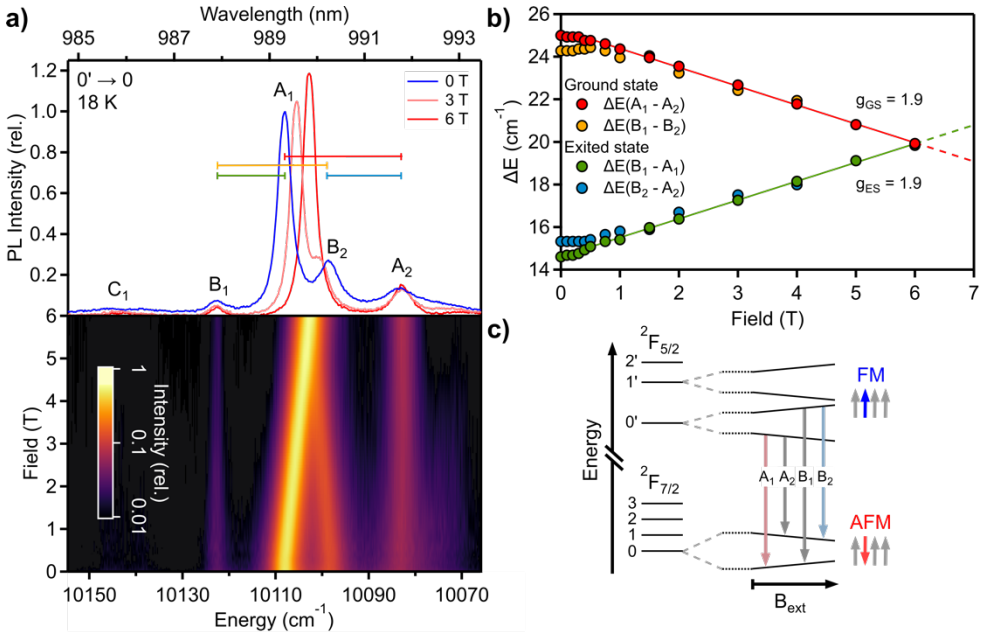

Figure 4.4 (a) Top: PL spectra of **Yb³⁺:CrBr₃** (0.4%) measured in the region of the $0' \rightarrow 0$ transition at 18 K and at various external magnetic fields (B_{ext} | | c). Colored bars indicate the energy spacings tracked in panel (b). Bottom: False-color plot of PL in the same region vs B_{ext}. **(b)** Splittings of the Yb³⁺ Kramers doublets (ΔE_{exch}) plotted as a function of B_{ext}. The solid lines represent linear fits of the data above 0.5 T. **(c)** Energy diagram summarizing the dependence of the Yb³⁺ states on B_{ext}, with Yb³⁺ spins coupled antiferromagnetically to the surrounding **Cr³⁺** lattice in the ground state and ferromagnetically in the excited state. The colors of the arrows indicate whether the transition redshifts, blueshifts, or is insensitive to the magnetic field. The splittings at B_{ext} = 0 are the exchange splittings (ΔE_{exch}) summarized in Figure 4.3.

The difference in sign between ground- and excited-state g values indicates that the Yb³⁺ spins reverse their orientation in the magnetic field between the ground and emissive excited states. This change in Yb³⁺ spin orientation is a direct consequence of the difference in total angular momentum J between the $^2F_{7/2}$ and $^2F_{5/2}$ parent terms.[30] Importantly, the magnetic field dependence of the individual spin sublevels also reveals that the Yb³⁺ spins are antiferromagnetically coupled with $CrBr_3$ in the Yb³⁺ ground state but are ferromagnetically coupled with $CrBr_3$ in the emissive Yb³⁺ excited state (Figure 4.4c). Note that this analysis does

not provide information on any possible canting of the Yb^{3+} spins relative to Cr^{3+} spins or to the $CrBr_3$ plane, and further experiments would be required to determine the full details of the Yb^{3+} spin tensor in this material.

The low-temperature value for the ground-state exchange splitting can be used to estimate the Yb-Cr pairwise exchange coupling parameter $J_{\text{Yb-Cr}}$, using the exchange Hamiltonian $H = -\sum J_{ij} S_i \cdot S_j$. In the absence of an external field, $H_{\text{eff}} = H_{\text{mol}}$, so we can rewrite the Curie-Weiss molecular field expression for H_{eff}[31] to get eq (4.2):

$$J_{Yb-Cr} = \frac{g\mu_B H_{mol}^{Yb}}{z\langle S_{Cr}\rangle} = \frac{\Delta E_{exch}}{z\langle S_{Cr}\rangle} \tag{4.2}$$

In this equation, z is the number of nearest-neighbor Cr^{3+} ions (3) surrounding a given Yb^{3+} impurity and $\langle S_{\text{Cr}}\rangle$ is the Cr^{3+} spin expectation value, which has an absolute value of $3/2$ in the fully ordered state of $CrBr_3$ (low-temperature limit). Using an extrapolated 0 K ground-state exchange splitting of 27.6 cm^{-1} (Figure 4.3d) and accounting for the antiferromagnetic alignment of Yb^{3+}, $J_{\text{Yb-Cr}}$ is calculated to equal -6.2 cm^{-1} (-0.77 meV). This value is half as large as the experimental nearest-neighbor $J_{\text{Cr-Cr}}$ found for $CrBr_3$ (+12 cm^{-1} (+1.5 meV)).[32, 33] Lanthanide *f*-orbital exchange interactions are typically weak due to high shielding, but this comparison suggests considerable overlap between Yb^{3+} 4*f* and Cr^{3+} 3*d* wave functions in Yb^{3+}:$CrBr_3$.

The data in Figure 4.3d show that, for both the 0 and 0′ states of Yb^{3+}, ΔE_{exch} at high temperature (paramagnetic) equals ~50% of its value at the lowest temperature (ferromagnetic). The persistence of a sizeable exchange splitting even above T_C can be understood by considering that the Yb-Cr interaction is short range, depending only on the immediately neighboring Cr^{3+} ions, and it is not affected by the presence or absence of long-range spin correlation. Thus, although $\langle S_{\text{Cr}}\rangle = 0$ in the high-temperature (paramagnetic) regime at zero field, the three nearest-neighbor Cr^{3+} ions exchange coupled to a given Yb^{3+} dopant may have nonzero net spin. A 2D Ising spin lattice has two phases: ferromagnetic (e.g., all Cr^{3+} spins have $S_z = +3/2$) and paramagnetic (spins disordered, e.g., S_z randomly $+3/2$ or $-3/2$ for Cr^{3+}). Considering all possible spin configurations of the cluster of three neighboring Cr^{3+} ions acting independently in the Ising paramagnetic phase, two have $S_{3\text{Cr}} = 9/2$ and six have $S_{3\text{Cr}} = 3/2$. Due to interconversion among

these configurations, the observed Yb^{3+} ΔE_{exch} will reflect the average magnitude of S_{3Cr}. Thus one predicts a ratio of $\Delta E_{exch}(PM)/\Delta E_{exch}(FM) = 1/2$ for Yb^{3+}:$CrBr_3$, agreeing well with our experimental observations. This same consideration holds even in more complicated (and realistic) descriptions of the magnetism of this extended lattice, but the fact that the value of ΔE_{exch} above T_C predicted in this simple Ising approximation is similar to the one observed experimentally (Figure 4.3d) suggests that this system remains strongly anisotropic up to at least ~50 K. The exchange splittings observed above T_C in Figure 4.3d therefore reflect noncanceling short-range coupling between Yb^{3+} and its three nearest- neighbor Cr^{3+} ions, whereas the PL line broadening in this regime reflects spin disorder among these nearest-neighbor Cr^{3+} ions.

4.4 Conclusion

We have shown that incorporation of Yb^{3+} impurities into $CrBr_3$ yields sharp Yb^{3+} *f-f* emission centered at ~10,000 cm^{-1}, sensitized through Cr^{3+} *d-d* absorption. Variable-field MCPL measurements show that Yb^{3+} spins are pinned to the $CrBr_3$ magnetization, providing unusually facile control over the dopant's magnetization. The highly resolved *f-f* PL spectra allow direct optical quantification of Yb^{3+}-Cr^{3+} exchange splittings, revealing them to vastly exceed kT at 5 K and showing that Yb^{3+}-Cr^{3+} coupling inverts from antiferromagnetic to ferromagnetic upon photoexcitation. The large spontaneous exchange splittings observed in Yb^{3+}:$CrBr_3$ present unique opportunities for optical spin manipulation of point defects in the absence of external magnetic fields or for in situ monitoring of short-range spin fluctuations and magnetic phase transitions. Such optically addressable spin defects may also have interesting ramifications for influencing spin textures and domain wall pinning in $CrBr_3$ itself, for generating localized strain effects, or for adding spin-photonic functionality to exfoliated or stacked van der Waals nanostructures.

4.5 Experimental Methods

General considerations. All sample preparation and manipulation was done in a glovebox under an atmosphere of purified dinitrogen.

Synthesis of Yb^{3+}:$CrBr_3$ **and** Yb^{3+}:YBr_3 **single crystals.** The synthesis of single crystals of

Yb^{3+}:$CrBr_3$ grown through chemical vapor transport is detailed in Snoeren et al.[17] The synthesis of Yb^{3+}:YBr_3 was carried out under similar conditions. YBr_3 (99.9%, ultra dry, ThermoFisher Scientific) and Yb metal (99.9%, 40 mesh, BeanTown Chemical) were used as precursors. The precursors were mixed at the desired stoichiometry and vacuum sealed in a quartz ampoule. The ampoule was placed in a tube furnace with the precursors at the center. The sample was kept at 800°C for 4 days.

Photoluminescence (PL) measurements. A single crystal of the material was placed between two quartz disks and loaded into a closed-cycle helium cryostat. Measurements were performed under high vacuum (10^{-6} Pa). For Yb^{3+}:$CrBr_3$ the sample was excited using a continuous-wave 405 nm (3.06 eV) diode. Yb^{3+}:YBr_3 was excited using a continuous wave 340 nm (3.64 eV) diode. The diode output was focused down to a spot size of approximately 1 mm^2 at an excitation power of approximately 4 mW/cm^2. Sample emission was focused into a monochromator with a spectral bandwidth of 0.25 nm for Yb^{3+}:$CrBr_3$ and a spectral bandwidth of 0.02 nm for Yb^{3+}:YBr_3 Spectra were collected using a LN_2-cooled silicon CCD camera and were corrected for instrument response.

Photoluminescence excitation (PLE) measurements. PLE measurements were likewise carried out in a closed-cycle helium cryostat under high vacuum. The sample was excited using a broadband tungsten-halogen lamp. The excitation wavelength was selected using a monochromator with a spectral bandwidth of 2.15 nm. Excitation light was focused onto the sample with a spot size of approximately 1 mm^2. Sample emission was focused onto a monochromator with a spectral bandwidth of 16 nm and emission counts were monitored using a Hamamatsu InGaAs/InP NIR photomultiplier tube.

Absorption measurements. Absorption measurements were carried out using a Cary 5000 UV-Vis Spectrophotometer in dual beam mode. Scan rates of 2 nm/s were used with a step size of 1 nm and a spectral bandwidth of 1 nm. Due to the air-sensitive nature of the material, special care was taken to avoid air exposure during the measurement: a single crystal of the material was placed between two quartz disks, spaced with a rubber o-ring to avoid squishing of the crystal while also excluding ambient atmosphere. The ensemble was held together by two metal plates

with a circular aperture for light transmission. To ensure all light passed through the sample, a mask with a diameter of about 1 mm was placed on the exterior of one of the quartz disks.

Magnetic circularly polarized luminescence (MCPL) measurements. A single crystal was placed between two quartz disks and loaded into a Cryo-Industries SMC-1650 OVT superconducting magneto-optical cryostat oriented in the Faraday configuration. The sample was excited with a 405 nm (3.06 eV) diode at approximately 4 mW/cm^2. Sample emission was collected along the magnetic field axis and passed through a liquid-crystal variable retardation plate set at $\lambda/4$, followed by a linear polarizer to separate the left- and right-circularly polarized components, and then focused onto a fiber-optic cable. Sample emission was then passed through a monochromator with a spectral bandwidth of 0.25 nm and was collected using a LN_2-cooled silicon CCD camera.

Field-sweep measurements were performed by continuously monitoring the sample emission using a monochromator with a spectral bandwidth of 9.9 nm. Emission counts were monitored using a Hamamatsu InGaAs/InP NIR photomultiplier tube with an integration time of 0.1 s. The field was swept at a rate of 1.5 mT/s (0.09 T/min).

Polarization ratios are defined as $\rho = (\sigma^- - \sigma^+)/(\sigma^- + \sigma^+) = (I_L - I_R)/(I_L + I_R)$, following the sign conventions outlined in Piepho and Schatz.[34]

4.6 References

(1) Dillon, J. F.; Kamimura, H.; Remeika, J. P. Magnetic Rotation of Visible Light by Ferromagnetic $CrBr_3$. *Phys. Rev. Lett.* **1962**, *9* (4), 161-163.

(2) Dillon, J. F., Jr.; Olson, C. E. Magnetization, Resonance, and Optical Properties of the Ferromagnet CrI_3. *J. Appl. Phys.* **1965**, *36* (3), 1259-1260.

(3) Bermudez, V. M.; McClure, D. S. Spectroscopic studies of the two-dimensional magnetic insulators chromium trichloride and chromium tribromide—II. *J. Phys. Chem. Solids* **1979**, *40*, 149-173.

(4) Bermudez, V. M.; McClure, D. S. Spectroscopic studies of the two-dimensional magnetic insulators chromium trichloride and chromium tribromide—I. *J. Phys. Chem. Solids.* **1979**, *40* (2), 129-147.

(5) Huang, B.; Clark, G.; Navarro-Moratalla, E.; Klein, D. R.; Cheng, R.; Seyler, K. L.; Zhong, D.; Schmidgall, E.; McGuire, M. A.; Cobden, D. H.; et al. Layer-Dependent Ferromagnetism in a van der Waals Crystal Down to the Monolayer Limit. *Nature* **2017**, *546* (7657), 270-273.

(6) McGuire, M. A.; Dixit, H.; Cooper, V. R.; Sales, B. C. Coupling of Crystal Structure and

Magnetism in the Layered, Ferromagnetic Insulator CrI_3. *Chem. Mater.* **2015**, *27* (2), 612-620.
(7) Chen, W.; Sun, Z.; Wang, Z.; Gu, L.; Xu, X.; Wu, S.; Gao, C. Direct Observation of van der Waals Stacking–Dependent Interlayer Magnetism. *Science* **2019**, *366* (6468), 983-987.
(8) McGuire, M. A.; Clark, G.; Santosh, K. C.; Chance, W. M.; Jellison, G. E.; Cooper, V. R.; Xu, X.; Sales, B. C. Magnetic Behavior and Spin-Lattice Coupling in Cleavable van der Waals Layered $CrCl_3$ Crystals. *Phys. Rev. Mater.* **2017**, *1* (1), 014001.
(9) Grebenchuk, S.; McKeever, C.; Grzeszczyk, M.; Chen, Z.; Šiškins, M.; McCray, A. R. C.; Li, Y.; Petford-Long, A. K.; Phatak, C. M.; Ruihuan, D.; et al. Topological Spin Textures in an Insulating van der Waals Ferromagnet. *J. Adv. Mater.* **2024**, *36* (24), 2311949.
(10) Augustin, M.; Jenkins, S.; Evans, R. F. L.; Novoselov, K. S.; Santos, E. J. G. Properties and Dynamics of Meron Topological Spin Textures in the Two-Dimensional Magnet $CrCl_3$. *Nat. Commun.* **2021**, *12* (1), 185.
(11) Sun, Q.-C.; Song, T.; Anderson, E.; Brunner, A.; Förster, J.; Shalomayeva, T.; Taniguchi, T.; Watanabe, K.; Gräfe, J.; Stöhr, R.; et al. Magnetic Domains and Domain Wall Pinning in Atomically Thin $CrBr_3$ Revealed by Nanoscale Imaging. *Nat. Commun.* **2021**, *12* (1), 1989.
(12) Song, T.; Cai, X.; Tu, M. W.-Y.; Zhang, X.; Huang, B.; Wilson, N. P.; Seyler, K. L.; Zhu, L.; Taniguchi, T.; Watanabe, K.; et al. Giant Tunneling Magnetoresistance in Spin-Filter van der Waals Heterostructures. *Science* **2018**, *360* (6394), 1214-1218.
(13) Wang, Z.; Gutiérrez-Lezama, I.; Ubrig, N.; Kroner, M.; Gibertini, M.; Taniguchi, T.; Watanabe, K.; Imamoğlu, A.; Giannini, E.; Morpurgo, A. F. Very large tunneling magnetoresistance in layered magnetic semiconductor CrI_3. *Nat. Commun.* **2018**, *9* (1), 2516.
(14) Seyler, K. L.; Zhong, D.; Klein, D. R.; Gao, S.; Zhang, X.; Huang, B.; Navarro-Moratalla, E.; Yang, L.; Cobden, D. H.; McGuire, M. A.; et al. Ligand-field helical luminescence in a 2D ferromagnetic insulator. *Nat. Physics* **2018**, *14* (3), 277-281.
(15) Zhang, Z.; Shang, J.; Jiang, C.; Rasmita, A.; Gao, W.; Yu, T. Direct Photoluminescence Probing of Ferromagnetism in Monolayer Two-Dimensional $CrBr_3$. *Nano Lett.* **2019**, *19* (5), 3138-3142.
(16) Cai, X.; Song, T.; Wilson, N. P.; Clark, G.; He, M.; Zhang, X.; Taniguchi, T.; Watanabe, K.; Yao, W.; Xiao, D.; et al. Atomically Thin $CrCl_3$: An In-Plane Layered Antiferromagnetic Insulator. *Nano Lett.* **2019**, *19* (6), 3993-3998.
(17) Snoeren, T. J.; Pressler, K.; Kluherz, K. T.; Walsh, K. M.; De Yoreo, J. J.; Gamelin, D. R. Luminescence and Covalency in Ytterbium-Doped CrX_3 (X = Cl, Br, I) van der Waals Compounds. *J. Am. Chem. Soc.* **2023**, *145* (31), 17427-17434.
(18) Doherty, M. W.; Manson, N. B.; Delaney, P.; Jelezko, F.; Wrachtrup, J.; Hollenberg, L. C. L. The Nitrogen-Vacancy Colour Centre in Diamond. *Phys. Rep.* **2013**, *528* (1), 1-45.
(19) Furdyna, J. K.; Kossut, J. *Diluted Magnetic Semiconductors*; Academic, 1988.
(20) Maiman, T. H. Stimulated Optical Radiation in Ruby. *Nature* **1960**, *187* (4736), 493-494.
(21) Klein, J.; Song, Z.; Pingault, B.; Dirnberger, F.; Chi, H.; Curtis, J. B.; Dana, R.; Bushati, R.; Quan, J.; Dekanovsky, L.; et al. Sensing the Local Magnetic Environment Through Optically Active Defects in a Layered Magnetic Semiconductor. *ACS Nano* **2023**, *17* (1), 288-299.
(22) Torres, K.; Kuc, A.; Maschio, L.; Pham, T.; Reidy, K.; Dekanovsky, L.; Sofer, Z.; Ross, F. M.;

Klein, J. Probing Defects and Spin-Phonon Coupling in CrSBr via Resonant Raman Scattering. *Adv. Funct. Mater.* **2023**, *33* (12), 2211366.

(23) Pressler, K.; Snoeren, T. J.; Walsh, K. M.; Gamelin, D. R. Magnetic Amplification at Yb^{3+} "Designer Defects" in the van der Waals Ferromagnet CrI_3. *Nano Lett.* **2023**, *23* (4), 1320-1326.

(24) Kozlenko, D. P.; Lis, O. N.; Kichanov, S. E.; Lukin, E. V.; Belozerova, N. M.; Savenko, B. N. Spin-Induced Negative Thermal Expansion and Spin–Phonon Coupling in van der Waals Material $CrBr_3$. *npj Quantum Mater.* **2021**, *6* (1), 19.

(25) Choca, M.; Ferraro, J. R.; Nakamoto, K. Vibrational Spectra of Lanthanide Hexahalides of the Type $(RH)_3LnX_6$. *J. Inorg. Nucl. Chem.* **1975**, *37* (6), 1425-1428.

(26) Piepho, S. B.; Schatz, P. N. *Group theory in spectroscopy with applications to magnetic circular dichroism*; John Wiley & Sons, 1983.

(27) Tsubokawa, I. On the Magnetic Properties of a $CrBr_3$ Single Crystal. *J. Phys. Soc. Jpn.* **1960**, *15* (9), 1664-1668.

(28) Shen, X.; Chen, H.; Li, Y.; Xia, H.; Zeng, F.; Xu, J.; Kwon, H. Y.; Ji, Y.; Won, C.; Zhang, W.; et al. Multi-Domain Ferromagnetic Resonance in Magnetic Van der Waals Crystals CrI_3 and $CrBr_3$. *J. Magn. Magn. Mater.* **2021**, *528*, 167772.

(29) Grzeszczyk, M.; Acharya, S.; Pashov, D.; Chen, Z.; Vaklinova, K.; van Schilfgaarde, M.; Watanabe, K.; Taniguchi, T.; Novoselov, K. S.; Katsnelson, M. I.; et al. Strongly Correlated Exciton-Magnetization System for Optical Spin Pumping in $CrBr_3$ and CrI_3. *J. Adv. Mater.* **2023**, *35* (17), 2209513.

(30) Kojima, N.; Tsushima, K.; Tsujikawa, I. Optical Investigations of $YbCrO_3$. I. Optical Absorption Spectra of Yb^{3+} Ion. *J. Phys. Soc. Jpn.* **1980**, *49* (4), 1449-1455.

(31) Smart, J. S. *Effective Field Theories of Magnetism*; Saunders, 1966.

(32) Cai, Z.; Bao, S.; Gu, Z.-L.; Gao, Y.-P.; Ma, Z.; Shangguan, Y.; Si, W.; Dong, Z.-Y.; Wang, W.; Wu, Y.; et al. Topological Magnon Insulator Spin Excitations in the Two-Dimensional Ferromagnet $CrBr_3$. *Phys. Rev. B* **2021**, *104* (2), L020402.

(33) Nikitin, S. E.; Fåk, B.; Krämer, K. W.; Fennell, T.; Normand, B.; Läuchli, A. M.; Rüegg, C. Thermal Evolution of Dirac Magnons in the Honeycomb Ferromagnet $CrBr_3$. *Phys. Rev. Lett.* **2022**, *129* (12), 127201.

(34) Piepho, S. B.; Schatz, P. N. *Group Theory in Spectroscopy: With Applications to Magnetic Circular Dichroism*; Wiley, 1983.

Chapter 5. Exciton Annihilation by Lanthanide Dopants: An Atomic Probe of Sub-Diffraction Exciton Diffusion in Ferromagnetic CrI_3

5.1 Overview

Excitons in two-dimensional (2D) magnetic van der Waals (vdW) materials offer unique windows into the properties of strongly correlated electrons. Their generation can be used to drive magnetic phase transitions, manipulate spins coherently, or access novel non-equilibrium regimes. Despite extensive investigation into the spin physics of CrI_3, exciton dynamics in this archetypal magnetic 2D material remain underexplored. Here, we report the use of Yb^{3+} impurity point defects as exciton annihilators to probe exciton diffusion in CrI_3. Variable-temperature photoluminescence (PL) measurements for a series of x% Yb^{3+}:CrI_3 samples reveals thermally activated Dexter-type site-to-site hopping of excitons, with low exciton diffusivity associated with strong electron-nuclear coupling. Using Monte Carlo modeling calibrated by the experimental data, diffusivities are found to be orders of magnitudes lower than in 2D vdW semiconductors. Exciton diffusion lengths (L_D) are below ~3 nm at all temperatures, and thus well below the optical diffraction limit. These results have basic implications for the use of excitons to probe and manipulate their surroundings in this and related magnetic CrX_3 materials.

5.2 Introduction

The recent demonstration of stable long-range magnetic order in monolayer CrI_3[1] has paved the way for new technologies based on ferromagnetic van der Waals (vdW) materials[2-5] and sparked renewed interest in the fundamental properties of CrI_3 and related compounds.[6-8] Despite its intriguing magnetic properties, one aspect of CrI_3 photophysics that has not yet been

sufficiently investigated is how photogenerated excitons propagate within the lattice in space and time. Real-space migration of excitons is central to many existing and future optoelectronic technologies. Exciton diffusion in CrI_3 is essential to proposed schemes for using exciton scattering to control topological magnetic structures using light or for generating an excitonic anomalous Hall effect.[9, 10] Likewise, exciton diffusion to surfaces is suggested to enable a surface-localized defect-assisted Auger recombination process that enhances lattice magnetization in $CrCl_3$.[11] A more complete description of exciton diffusion in CrX_3 materials may advance the basic-science understanding of such phenomena and aid efforts to harness their photophysics in future spin-based optoelectronic technologies.

Whereas spatial probes of exciton diffusion in vdW materials often employ time-resolved optical microscopy,[12-14] such methods are constrained by optical diffraction limits in both excitation and detection, with typical resolution of ~500 nm in the near-IR. Super-resolution techniques can improve upon this limitation by achieving bin sizes of 10s of nanometers or smaller, but this may still be insufficient for probing exciton dynamics in a material like CrI_3, because unlike many other workhorse vdW materials such as transition-metal dichalcogenides, CrI_3 excitons are localized around individual Cr^{3+} ions. Indeed, the optical responses of CrX_3 (X = Cl^-, Br^-, I^-) compounds have historically been described using the ligand-field model, which thoroughly accounts for their multitude of absorption features as *d-d* and ligand-to-metal charge-transfer (LMCT) transitions centered at individual CrX_6^{3-} pseudo-octahedra.[15-17] Although recent reports have variously referred to the emissive excited states of CrX_3 compounds as exciton polarons,[18-20] Frenkel excitons,[21-23] or self-trapped excitons (STEs),[24] all of these interpretations invoke strong localization. Computational studies have also suggested that CrI_3 excitons localize at individual Cr^{3+} ions.[21, 25] Direct optical probes are thus poorly suited for quantifying CrI_3 exciton diffusion.

An alternative approach to probing exciton diffusion is to monitor the annihilation of excitons under various conditions. For example, recent experiments have used variable-excitation-rate photoluminescence (PL) measurements in CrX_3 compounds to demonstrate exciton–exciton annihilation,[19, 26, 27] an Auger-like process in which two excitons combine energies to generate just

one high-energy exciton. From excitation statistics and PL data, information about the exciton diffusion preceding annihilation can be deduced, and such experiments have been used to estimate a room-temperature exciton diffusion coefficient (D) between ~10^{-6} and ~10^{-2} cm^2/s for bulk $CrCl_3$.[27] This approach necessarily requires elevated excitation densities, which may in some cases alter the apparent exciton diffusion by inducing lattice heating or secondary nonradiative effects. For example, exciton-exciton scattering in WS_2 is reported to cause a non-linear increase in D with increasing excitation power.[28] Furthermore, because the probability of exciton–exciton annihilation depends non-linearly on excitation density, experimental factors such as non-uniform (*e.g.*, gaussian) excitation profiles also complicate extraction of reliable quantitative results.

Here, we report the use of lanthanide impurity ions in CrI_3 as highly effective probes of exciton diffusion in this material. As luminescence activators, lanthanides harvest individual CrI_3 excitons *via* direct $CrI_3 \rightarrow Yb^{3+}$ energy transfer (ET), eliminating the non-linear dependence of exciton-exciton annihilation on excitation density and allowing measurements to be performed at arbitrarily low excitation densities where lattice heating and other photo-induced artifacts are eliminated. Previous work on Yb^{3+}-doped CrX_3 compounds has revealed strong dopant-lattice magnetic superexchange coupling that pins Yb^{3+} spins to those of the surrounding CrX_3 lattice.[29, 30] These superexchange interactions rely on covalency, which also promotes $CrX_3 \rightarrow Yb^{3+}$ ET through the well-known Dexter mechanism. Using a combination of continuous-wave (CW) and time-resolved PL measurements performed as a function of temperature and Yb^{3+} doping level, complemented by Monte Carlo modeling, we develop a detailed description of exciton-diffusion dynamics in CrI_3. The results demonstrate that exciton diffusion is restricted by strong electron-nuclear coupling in the emissive $^4T_{2g}$ (O_h) excited state, with a low-temperature value of D = 1.4 x 10^{-8} cm^2/s that increases to 2.2 x 10^{-7} cm^2/s by room temperature. Above ~100 K, the PL data show evidence for thermally activated nonradiative relaxation *via* phonon emission that ultimately limits exciton diffusion lengths to below ~3 nm at all temperatures, *i.e.*, well below the optical diffraction limit. These results thus provide a quantitative description of exciton diffusion in CrI_3 that will aid the interpretation of other photophysical phenomena such as exciton-exciton

annihilation and, more broadly, that enriches our fundamental understanding of exciton physics in the CrX_3 family of strongly correlated magnetic materials.

5.3 Experimental Results and Analysis

5.3.1 General Considerations

In idealized O_h symmetry, the five Cr 3*d* orbitals are split into t_{2g} and e_g sets by the crystal field, and the three unpaired spins in the degenerate t_{2g} orbital yield a $^4A_{2g}$ ground state. The lowest-energy $^4T_{2g}$ ligand-field excited state corresponds to excitation of one t_{2g} electron into a σ-antibonding e_g orbital. In actuality, this formally parity-forbidden transition in CrI_3 gains electric-dipole allowedness through static symmetry lowering (C_2 site symmetry), boosted by configuration interaction with low-energy ligand-to-metal charge-transfer excited states.[31] Figure 5.1a depicts a single-configurational-coordinate diagram describing the $^4A_{2g} \rightarrow {}^4T_{2g}$ absorption and luminescence transitions for the A_{1g} local nuclear coordinate. For simplicity, the comparably large displacement expected along the E_g (Jahn-Teller) nuclear coordinate[32] is not shown. Excited-state distortion along these two nuclear coordinates (ΔQ_i, i = A_{1g}, E_g) stabilizes that state by a reorganization energy, E_R, as described by eq (5.1):

$$E_{\mathrm{R}} = \sum_i \frac{1}{2} k_i (\Delta Q_i)^2 \tag{5.1}$$

Spectroscopically, E_R can be estimated from the PL Stokes shift through $E_{Stokes} = 2E_R$, giving $E_R \approx 200$ meV for CrI_3.[33] Importantly, when E_R is so large, exciton hopping from one Cr^{3+} site to a neighboring site also requires a large nuclear reorganization, as depicted schematically in Figure 5.1b, and this reduces the microscopic site-to-site ET rate constant, k_{Cr}^{hop}.

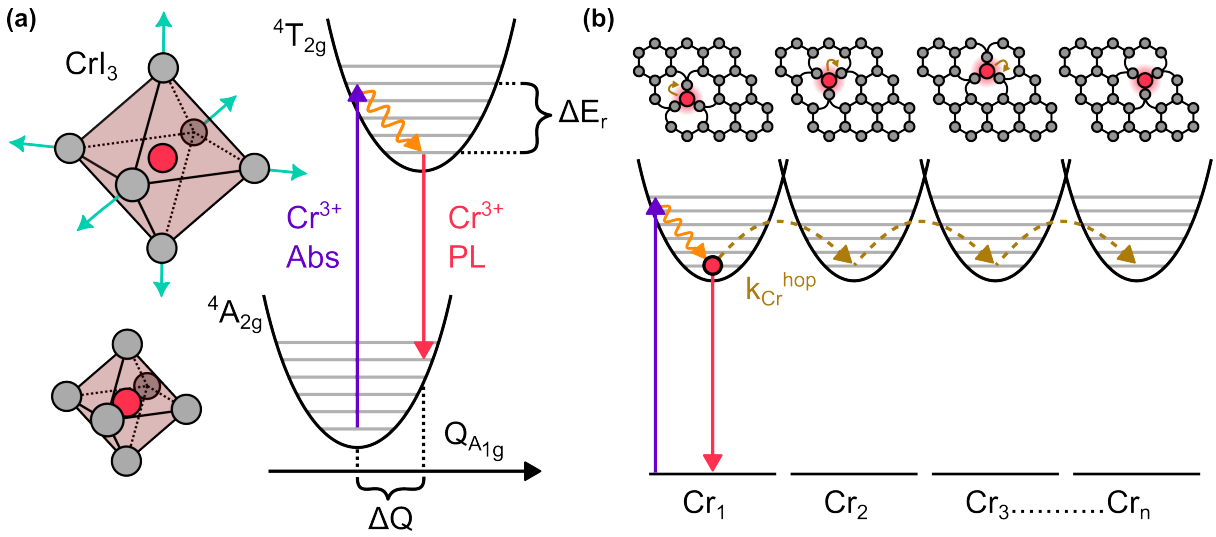

Figure 5.1 (a) Single-configurational-coordinate (SCC) diagram describing nuclear reorganization along the A_{1g} coordinate during transitions between the $^4A_{2g}$ and $^4T_{2g}$ ligand-field states of octahedral Cr^{3+} in idealized O_h symmetry. The pictures illustrate the A_{1g} distortion in the $[CrI_6]^{3-}$ excited state. Additional displacement along the E_g nuclear coordinate (not shown) is also expected. The large nuclear reorganization energy (E_R) associated with these distortions stabilizes excitons at individual Cr^{3+} sites. The actual Cr^{3+} site symmetry is lower (C_2) and lacks inversion. **(b)** Schematic depiction of site-to-site exciton hopping involving short-range Dexter energy transfer between Cr^{3+} ions.

5.3.2 Time-Resolved Photoluminescence Spectroscopy of Yb^{3+}:CrI_3

Figure 5.2a-d shows 4 K PL spectra of a series of x% Yb^{3+}:CrI_3 single crystals with x = 0.0, 0.2, 1.6, and 18.6 (see 5.6 Experimental Methods). With increasing Yb^{3+} concentration there is a corresponding increase in the relative intensity of sharp-line Yb^{3+} $^2F_{5/2} \rightarrow {}^2F_{7/2}$ PL centered ~ 1.135 eV, and a concomitant suppression of the broad Cr^{3+} $^4T_{2g} \rightarrow {}^4A_{2g}$ PL centered ~ 1.08 eV. Figure 5.2e plots 4 K PL decay curves for the samples shown in Figure 5.2a-d, all collected at 1.20 eV and therefore corresponding solely to Cr^{3+} PL. The Cr^{3+} decay time shortens from ~0.8 μs in undoped CrI_3 to ~0.2 μs at the highest Yb^{3+} concentration (18.6%), and the full dataset is summarized in Figure 5.2e(inset). Despite a small amount of scatter, the trend of decreasing τ_{Cr} with increasing concentration of Yb^{3+} is clear. We speculate that the scatter comes from sample-to-sample variations in intrinsic defects. Figure 5.2f plots 4 K PL decay dynamics for the same samples but now collected at 1.15 eV, where both Cr^{3+} and Yb^{3+} emit. In addition to the same CrI_3 decay seen

in Figure 5.2e, a new Yb^{3+} signal is observed with a concentration-independent decay time of ~10 μs but whose relative intensity increases with increased Yb^{3+} doping. These data demonstrate CrI_3 exciton annihilation by Yb^{3+} dopants. Critically, the ability to independently probe both participants involved in the annihilation (CrI_3 and Yb^{3+}) offers a rare opportunity to gain additional insight into the underlying CrI_3 photophysics.

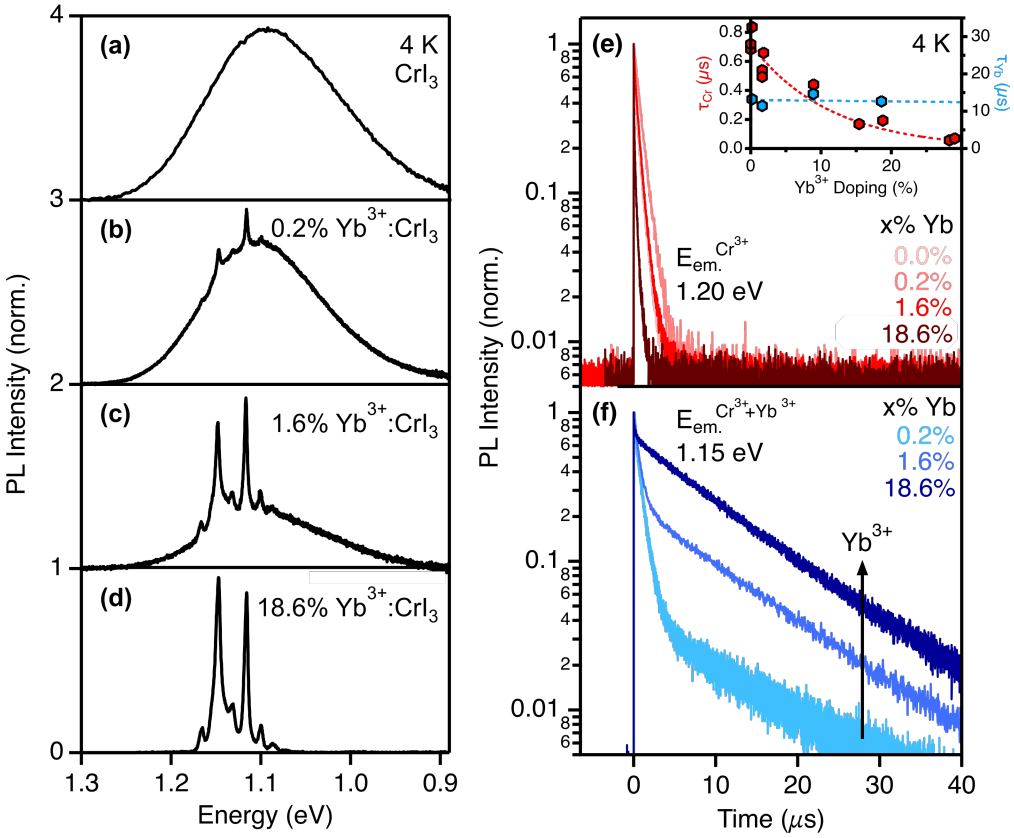

Figure 5.2 PL spectra of (**a**) 0.0% Yb^{3+}:CrI_3, (**b**) 0.2% Yb^{3+}:CrI_3, (**c**) 1.6% Yb^{3+}:CrI_3, and (**d**) 18.6% Yb^{3+}:CrI_3 measured at 4 K using CW excitation at 1.88 eV. **(e-f)** 4 K PL decay curves measured for the same samples using a 40 ps, 50 Hz pulsed laser excitation source at 532 nm (2.33 eV) and a 6.27 nm spectral bandwidth for detection. The sample PL was measured at two regions 1.20 eV (e) and 1.15 eV (f), representing CrI_3 emission (Cr^{3+}) and a superposition of CrI_3 and dopant emission (Yb^{3+} + Cr^{3+}), respectively. Inset: Cr^{3+} (red) and Yb^{3+} (blue) PL decay times plotted vs Yb^{3+} concentration, x. With increased x, the Cr^{3+} decay time shortens while the Yb^{3+} PL decay time remains relatively constant. The dashed lines are guides to the eye.

Figure 5.3a shows gated 4 K PL spectra of the 18.6% Yb^{3+} sample collected by integrating only

the first 50 ns following the excitation pulse (t_{delay} = 25 ns, Δt = 50 ns). The spectrum consists of ~8% Yb^{3+} (integrated) intensity and 92% Cr^{3+} (integrated) intensity. By 225 ns after the excitation pulse (t_{delay} = 225 ns, Δt = 50 ns), the spectrum has evolved to become 30% Yb^{3+} and 70% Cr^{3+}. The CW spectrum shows >99% Yb^{3+} PL. These data indicate that CrI_3 exciton capture by Yb^{3+} occurs on the timescale of hundreds of nanoseconds. The two independent PL signals can thus be used to quantify the exciton-annihilation dynamics. To illustrate, Figure 5.3b,c plots 4 K PL decay traces collected at 1.20 eV (only Cr^{3+} PL) and 1.15 eV (Cr^{3+} and Yb^{3+} PL) for the 0.2% and 1.6% Yb^{3+} samples shown in Figure 5.2, focusing on the early times. Subtracting the former curves from the latter isolates the time evolution of just the Yb^{3+} PL. These Yb^{3+} curves are also plotted in Figure 5.3b,c, and both show a distinct rise in Yb^{3+} PL following the laser pulse, reflecting the time required for CrI_3 excitons to be harvested by Yb^{3+} impurities. Fitting these Yb^{3+} curves to biexponential (rise + decay) functions yields rise times of τ_{rise} = 684 ± 1 ns for the 0.2% Yb^{3+} sample and 268 ± 3 ns for the 1.6% Yb^{3+} sample. These results demonstrate faster CrI_3 exciton annihilation in samples with more Yb^{3+}, as anticipated.

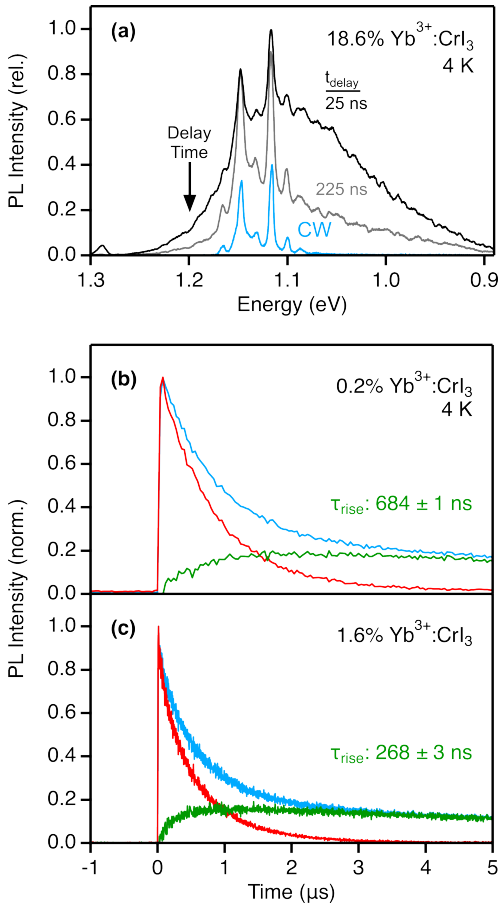

Figure 5.3 (a) PL spectrum of 18.6% Yb^{3+}:CrI_3 measured at 4 K using CW excitation and time-integrated detection (blue line), compared to gated PL spectra of the same sample collected at 4 K. The black and grey spectra correspond to center times of 25 and 225 ns, respectively, each with integration windows of 50 ns following a 40 ps laser pulse (E_{ex} = 2.33 eV). **(b, c)** PL decay curves collected at 4 K for (b) 0.2% and (c) 1.6% Yb^{3+}:CrI_3 following 40 ps excitation at 2.33 eV. The red and blue decay traces were collected at 1.20 and 1.15 eV and correspond to host-lattice emission (Cr^{3+}) and a superposition of host and dopant emission (Yb^{3+} + Cr^{3+}), respectively, shown in Figure 5.2e,f. The green curves plot the differences between these two decay traces normalized at t = 0 for each sample, showing rise times for Yb^{3+} emission of τ_{rise} = 684 ± 1 ns and 268 ± 3 ns for 0.2 and 1.6% Yb^{3+}:CrI_3, respectively.

5.3.3 Variable-Temperature Photoluminescence Spectroscopy of Yb^{3+}:CrI_3

To explore the effect of temperature on exciton diffusion and annihilation, PL measurements were performed at several temperatures. Figure 5.4a-d shows variable-temperature PL (VTPL) spectra collected from 4 to 200 K for the series of x% Yb^{3+}:CrI_3 samples shown in Figure 5.2. All

samples show a monotonic reduction in total integrated PL intensity with increasing temperature, and no PL above ~200 K. With increasing temperature, the Yb^{3+} PL features at all doping levels broaden due to thermal spin disorder[29] and growth of hot bands. At all temperatures, the 0.2% and 1.6% Yb^{3+} samples (Figure 5.4b,c) display a mixture of broad Cr^{3+} emission and narrow Yb^{3+} emission, whereas the 18.6% Yb^{3+}:CrI_3 (Figure 5.4d) displays only Yb^{3+} emission.

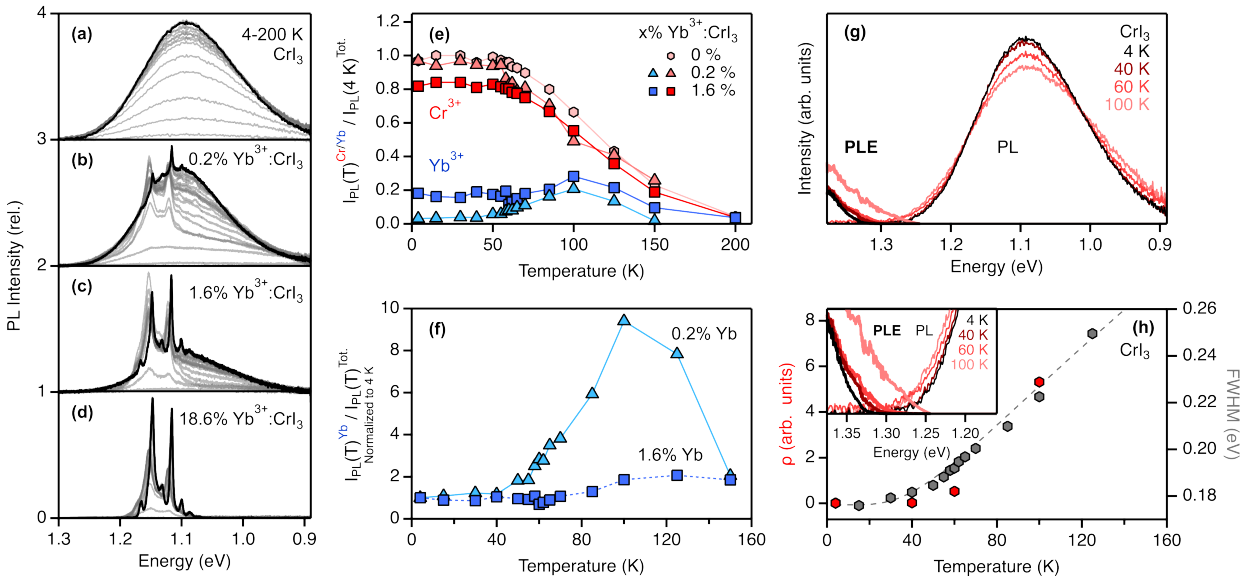

Figure 5.4 VTPL spectra of (**a**) 0.0% Yb^{3+}:CrI_3, (**b**) 0.2% Yb^{3+}:CrI_3, (**c**) 1.6% Yb^{3+}:CrI_3, and (**d**) 18.6% Yb^{3+}:CrI_3 measured from 4 to 200 K using CW excitation at 1.88 eV. **(e)** Plots of the integrated Cr^{3+} (red) and Yb^{3+} (blue) PL intensities divided by the total integrated PL intensity at 4 K for each sample in panels (a-d). See Figure 5.28 for further details. All samples show a similar temperature dependence. **(f)** Plot of integrated Yb^{3+} as a portion of the total luminescence intensity normalized to their 4 K value for the 0.2% and 1.6% sample. **(g)** Plot of PLE (bold) and PL spectra for CrI_3 at 4, 40, 60, and 100 K. The PL spectra were normalized to a unit area. **(h)** Plot of the FWHM of CrI_3 (grey) overlayed with the calculated spectral overlap derived from panel (g). Inset: expanded plot of the spectra shown in panel (g) highlighting the region of spectral overlap.

Because Yb^{3+} emission only occurs after a CrI_3 exciton is annihilated by a dopant, the integrated Yb^{3+} PL intensity directly reflects the number of excitons that have diffusively encountered a dopant. Figure 5.4e plots the temperature dependence of the integrated Cr^{3+} (I_{PL}^{Cr}) and Yb^{3+} (I_{PL}^{Yb}) PL intensities divided by the total integrated PL intensity at 4 K ($I_{PL}^{tot}(4K)$). These ratios convey the PL fraction coming from each center (Cr^{3+} or Yb^{3+}) relative to the total intensity

measured at 4 K. The fractional Cr^{3+} PL ($I_{PL}^{Cr}(T)/I_{PL}^{tot}(4K)$) is temperature-independent up to ~60 K and then steadily decreases with increasing temperature up to 200 K, independent of Yb^{3+} doping. Conversely, in 0.2% Yb^{3+}:CrI_3, the ratio $I_{PL}^{Yb}(T)/I_{PL}^{tot}(4K)$ is temperature-independent from 4 to ~60 K before *rising* from ~0.03 to a maximum of 0.20 at 100 K, and then dropping at higher temperatures. 1.6% Yb^{3+}:CrI_3 shows a larger value of $I_{PL}^{Yb}(T)/I_{PL}^{tot}(4K)$ at 4 K (0.18), which rises to 0.28 at 100 K. Figure 5.4f recasts these data as $I_{PL}^{Yb}(T)/I_{PL}^{tot}(T)$ normalized to $I_{PL}^{Yb}(4K)/I_{PL}^{tot}(4K)$. In both samples, the Yb^{3+} PL intensity remains constant from 4 K up to ~50 to 60 K and then increases with increasing temperature. Above ~100 K, the Yb^{3+} PL intensity drops steeply to zero.

These data show exciton annihilation by Yb^{3+} becoming more probable at higher temperature, indicating that CrI_3 exciton diffusion is thermally activated. This temperature dependence is distinct from that of CrI_3 spin correlation, however, as represented by the infinite spin-correlation function $(M(T)/M(0))^2$, where M is magnetization (Figure 5.31). This spin-correlation function decreases immediately starting at the lowest temperatures before dropping sharply to zero around T_C = 61 K. The PL temperature dependence in Figure 5.4 thus shows no evidence of being affected by spin ordering, consistent with expectations for Dexter energy transfer. This insensitivity to spin differs from that observed in AFM-ordered $(CH_3)_4NMnCl_3$, where exciton migration is reduced upon magnetization due to suppression of dipole-dipole Mn^{2+}-Mn^{2+} energy transfer, which requires a change of spin state ($^4T_1$ to $^6A_1$) on each ion.[34] We also observe no spin contribution to exciton diffusion in time-resolved PL measurements around T_C (Figure 5.32). Instead, we attribute the PL temperature dependence to thermal spectral broadening.

5.3.4 Temperature-Dependent Exciton Hopping

Strong electron-phonon coupling in the luminescent excited state of CrI_3 effectively confines an exciton to a single Cr^{3+} site. This exciton may still diffuse by incoherent hopping between individual lattice sites (Figure 5.1b),[35] with a temperature-dependent hopping rate constant ($k_{Cr}^{hop}(T)$) that can be described within the framework of Fermi's golden rule, as shown in eq (5.2).

$$k_{Cr}^{hop}(T) = \frac{2\pi}{\hbar}|M_{DA}|^2\rho(T) \tag{5.2}$$

Here, M_{DA} describes the donor-acceptor electronic coupling and $\rho(T)$ is the temperature-dependent spectral-overlap factor, defined in eq (5.3), where $\bar{f}_D(E)$ represents the area-normalized donor emission spectrum and $\bar{\varepsilon}_A(E)$ represents the area-normalized absorption spectrum of the acceptor, obtained experimentally by PL excitation (PLE).

$$\rho = \int_0^\infty \bar{f}_D(E)\bar{\varepsilon}_A(E)dE \tag{5.3}$$

Figure 5.4g plots PLE spectra of undoped CrI_3 measured at 4, 40, 60, and 100 K, collected by monitoring the Cr^{3+} emission at 1.0 eV and normalizing by the relative PL intensity at each temperature. The corresponding PL spectra are also shown for each temperature, also normalized to relative PL intensity. The PL spectrum is unchanged from 4 to ~50 K, but the band broadens noticeably at higher temperatures. A similar trend is observed in the PLE spectrum. The inset to Figure 5.4h plots the overlap region of Figure 5.4g on an expanded scale, showing that ρ increases with increasing temperature due to this spectral broadening. Using eq (5.3), the data in Figure 5.4g can be analyzed to quantify the temperature dependence of ρ, and the results are plotted in red in Figure 5.4h. Figure 5.4h also plots values for the full widths at half-maximum (FHWM) determined from the PL spectra of undoped CrI_3 measured between 4 and 160 K (Figure 5.4a). The FHWM and ρ values show very similar trends with temperature, both remaining constant at low temperatures before increasing above ~50 K. With increasing temperature, higher vibrational excited states in the $^4A_{2g}$ ground and $^4T_{2g}$ excited electronic states of Cr^{3+} are thermally populated, leading to new absorption and PL intensities that increase the spectral overlap (ρ). More quantitatively, the FWHM data were fit to the second-moment hyperbolic cotangent function of eq (5.4),[36] where ν_{eff} represents the energy of an effective activating vibration. The best-fit value of ν_{eff} = 97 cm^{-1} is close to the energies of the dominant vibrational modes observed in CrI_3 resonance Raman spectra[37] and consistent with expectations for the A_{1g} and E_g local modes of $[CrI_6]^{3-}$.

$$FWHM(T) = FWHM(0)\left[\coth\left(\frac{\upsilon_{eff}}{2k_BT}\right)\right]^{1/2} \tag{5.4}$$

Importantly, the temperature dependence of ρ is very similar to those of the Cr^{3+} and Yb^{3+} PL intensities (Figure 5.4e,f), confirming the importance of thermal spectral broadening in CrI_3

exciton diffusion and annihilation by Yb^{3+} and thereby confirming the critical role that nuclear reorganization plays in limiting exciton diffusion in CrI_3.

Exciton diffusion in CrI_3 can also be probed by monitoring the dependence of Cr^{3+} PL decay dynamics on Yb^{3+} doping concentration at various temperatures. Figure 5.5a summarizes the temperature dependence of the Cr^{3+} PL decay times (τ_{Cr}) for a series of x% Yb^{3+}:CrI_3 samples (x = 0.0, 0.2, 1.6, 8.9, 18.6). At a fixed temperature, increasing x shortens τ_{Cr}, *e.g.*, from ~0.80 ms in 0.2% Yb^{3+} to only ~0.15 ms in 18% Yb^{3+} at 4 K. For all samples, τ_{Cr} is independent of temperature up to ~50 K, above which it decreases with increasing temperature. When these τ_{Cr} data are normalized to their low-temperature values as shown in Figure 5.5b, it is evident that increased Yb^{3+} doping also increases the temperature dependence of τ_{Cr}: the higher-doped samples show a steeper decrease in τ_{Cr} above 50 K.

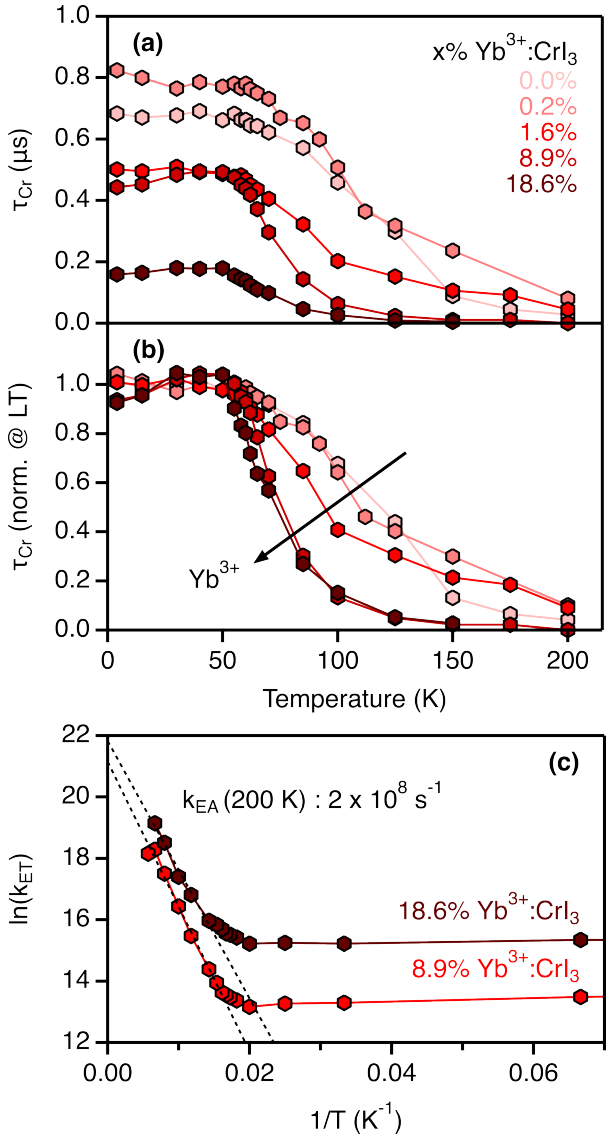

Figure 5.5 CrI_3 PL decay times plotted vs temperature for x% Yb^{3+}:CrI_3 (x = 0.0, 0.2, 1.6, 8.9, 18.6), measured following 40 ps excitation at 2.33 eV. Increased x shortens the CrI_3 decay time. The shorter decay time of the undoped CrI_3 compared to the 0.2% Yb^{3+}:CrI_3 sample is attributed to its reduced crystal quality. **(b)** The data from panel (a) normalized to the lowest temperature region. Increasing x increases the rate of PL quenching with temperature. **(c)** Plot of the effective energy-transfer rate constant (k_{ET}) vs temperature for 8.9 and 18.6% Yb^{3+}:CrI_3 samples. The dashed lines show best fits of the data to the Arrhenius model of eq (5.6).

The data in Figure 5.5a can now be used to estimate effective exciton annihilation rate constants (k_{EA}) following the approach of Kambli *et al.*,[38] summarized in eq (5.5).

$$k_{EA} = k_{Cr\_doped} - k_{Cr\_undoped} = {}^{1}/_{\tau_{Cr\_doped}} - {}^{1}/_{\tau_{Cr\_undoped}} \quad (5.5)$$

k_{EA} consists of two processes: (*i*) the multiple $Cr^{3+} \rightarrow Cr^{3+}$ hopping steps that occur as the exciton migrates through the lattice prior to capture by Yb^{3+}, individually described microscopically by k_{Cr}^{hop}, and (*ii*) the final $Cr^{3+} \rightarrow Yb^{3+}$ energy-transfer step, described by $k_{Yb}^{hop}(T)$. Because $k_{Yb}^{hop} > k_{Cr}^{hop}$ at all temperatures (*vide infra*), k_{Yb}^{hop} is effectively temperature independent in these measurements. Consequently, the experimental data in Figure 5.5a,b directly reflect the temperature dependence of k_{Cr}^{hop}. At low temperatures, $Cr^{3+} \rightarrow Cr^{3+}$ hopping is slow and thus τ_{Cr} is at its maximum. In this regime, increasing the concentration of Yb^{3+} reduces the number of hops required before exciton annihilation by Yb^{3+}, as shown by the decrease in τ_{Cr}. Above ~50 K, k_{Cr}^{hop} increases, and this accelerates exciton annihilation in all samples.

Figure 5.5c presents the 8.9 and 18.6% Yb^{3+} τ_{Cr} data from Figure 5.5a as k_{EA} values (converted using eq (5.5)) plotted in Arrhenius form, highlighting the thermal activation of exciton diffusion in CrI_3. Fitting the high-temperature slope to eq (5.6) yields $k_{EA}(\infty) \approx 2 \times 10^9$ s^{-1}, representing the hypothetical scenario in which k_{Cr}^{hop} is still rate limiting at infinite temperature. The fact that k_{EA} is always larger in 18.6% Yb^{3+} than in 8.9% Yb^{3+} indeed indicates that k_{Cr}^{hop} is rate determining at all temperatures probed experimentally. k_{EA} at our highest experimental temperature (200 K) thus provides an experimental lower bound of 2×10^8 s^{-1} for the value of k_{Yb}^{hop}. This value is comparable to, for example, the lower limit of $k_{EA} \sim 10^8$ s^{-1} reported for energy transfer in structurally well-defined cyanide-bridged Cr^{3+}-Yb^{3+} dimers at 300 K.[39]

$$k_{EA}(T) = k_{EA}(\infty) e^{-\Delta / k_B T} \tag{5.6}$$

When considered together with the preceding experimental data, it is clear that exciton diffusion in CrI_3 is slow, thermally activated, and governed by nearest-neighbor hopping kinetics, and that the final ET step to Yb^{3+} is sufficiently fast to never be rate-limiting.

5.4 Kinetic Monte Carlo Simulation Results and Analysis

5.4.1 General Considerations

To describe the real-space and -time profiles of exciton diffusion in CrI_3, kinetic Monte Carlo (KMC) simulations were performed using parameters defined by the above experiments. Exciton diffusion was modeled as sequential nearest-neighbor random hopping events within hexagonal

CrI_3 lattices containing randomly distributed Yb^{3+} impurities at various designated concentrations. For k_{Cr}^{hop}, two possible mechanisms of energy transfer may be considered: through-space multipolar Förster-type resonant energy transfer (FRET) and through-bond Dexter-type energy transfer (DET), both of which may be present. Previous work has shown that ferromagnetic order in CrI_3 arises from high Cr-I covalency, which enhances the ferromagnetic superexchange coupling.[40-43] Because of this high covalency, intra-layer DET is expected to dominate k_{Cr}^{hop}, an assumption validated below. Figure 5.6a illustrates the full set of rate constants governing specific state transitions applied in this work.

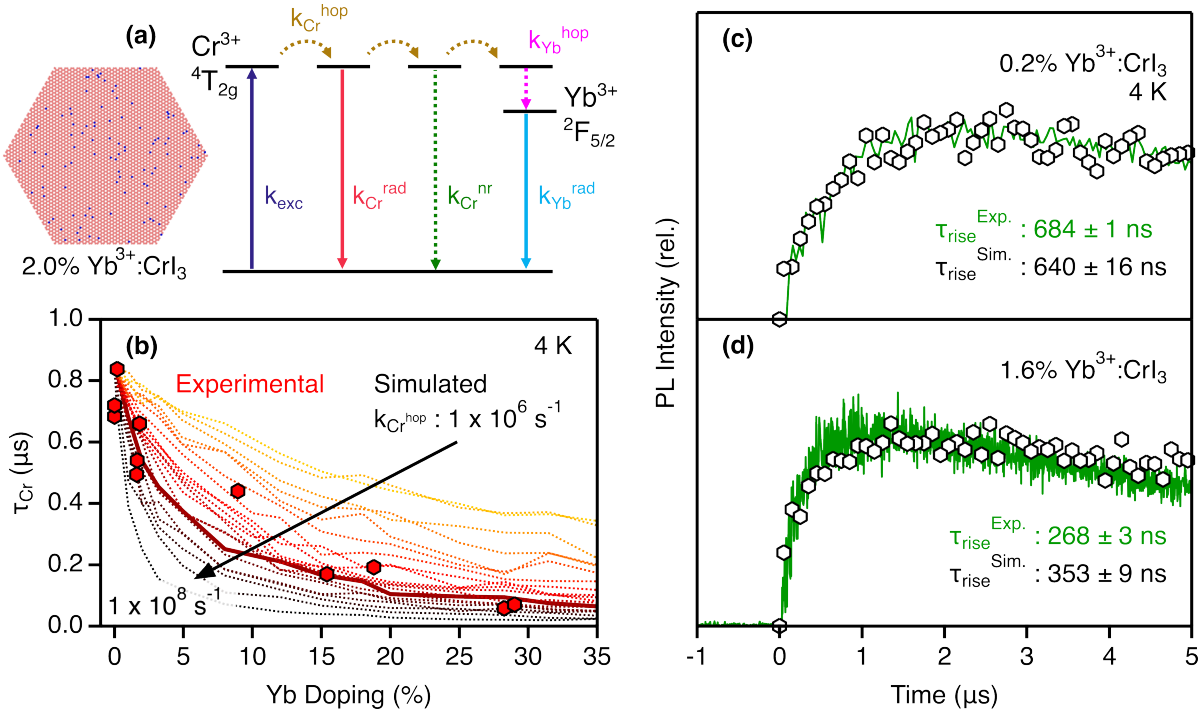

Figure 5.6 A representative trial crystal with random Yb^{3+} doping at 2% of the cation sites. Each red (blue) pixel corresponds to an octahedrally coordinated Cr^{3+} (Yb^{3+}) ion. The energy diagram illustrates the processes and rate constants addressed in the Monte Carlo simulation. Values k_{Cr}^{rad}, k_{Cr}^{nr}, k_{Yb}^{rad}, k_{Yb}^{hop} were all determined experimentally (see main text), while k_{Cr}^{hop} was determined *via* simulation as shown in panel (b). These processes compete with one another on each Cr^{3+} ion but are illustrated on different ions for ease of viewing. **(b)** Plot of experimental Cr^{3+} decay times at 4 K for various Yb^{3+} doping levels (red scatter points). The curves show simulated values of the 4 K Cr^{3+} decay times calculated over many values of k_{Cr}^{hop}. The bold red line corresponds to the best fit, yielding a value of k_{Cr}^{hop} = 1 x 10^7 s^{-1} under these conditions. **(c-d)** Plot of simulated Yb^{3+} PL dynamics (white scatter points) for (c) 0.2% and (d) 1.6% Yb^{3+}:CrI_3 at 4 K,

calculated using k_{Cr}^{hop} = 1.0 x 10^7 s^{-1}. The corresponding experimental data (green, from Figure 5.3b,c) are included for comparison.

Simulations were performed by constructing trial crystals of Yb^{3+}-doped CrI_3. Each crystal contained 5100 M^{3+} octahedra ordered into the hexagonal structure of monolayer CrI_3. For each Yb^{3+} doping level, 250 unique crystals were generated, each with a random distribution of the appropriate number of Yb^{3+} dopants. One such trial crystal with 2% Yb^{3+} doping is shown in Figure 5.6a. For each of these trial crystals, 250 excitons were simulated, and all results were aggregated across the 250 crystals, resulting in the simulation of a total 62,500 excitons for each Yb^{3+} doping level at each temperature. Each simulation was launched with an exciton at the central ion of the crystal, and the fate of this exciton was tracked over time as it migrated around the lattice stochastically and eventually decayed, as determined by the given rate constants. Exciton-exciton annihilation was not considered in the simulation because of the very low excitation densities used experimentally (2 nJ/cm^2, or one exciton per ~7×10^6 Cr^{3+} ions, see 5.7D.4 Calculation of Excitation Density). The time of emission, the identity of the emitting site (Cr^{3+} or Yb^{3+}), and the position in space of the emission event were all recorded for each excitation. See 5.6 Experimental Methods for further details about the KMC simulations.

5.4.2 Experimental Definition of KMC Parameters

To constrain the KMC simulations, several rate constants were defined based on the experimental results presented above, as described here: The observed rate constant for CrI_3 excited-state decay has radiative (k_{Cr}^{rad}) and nonradiative (k_{Cr}^{nr}) contributions, as described by eq (5.7).

$$\frac{1}{\tau_{Cr}} = k_{Cr} = k_{Cr}^{rad} + k_{Cr}^{nr} \tag{5.7}$$

As shown in Figure 5.34, the PL intensity (I_{PL}) and τ_{Cr} for undoped CrI_3 show identical temperature dependence, indicating that the decrease in each with increasing temperature stems from thermally activated nonradiative decay and that k_{Cr}^{rad} is effectively independent of temperature, as expected for Cr^{3+} with C_2 site symmetry. Substituting a thermally activated Mott-Seitz-type expression for k_{Cr}^{nr} as shown in eq (5.8),

$$k_{Cr}^{nr}(T) = k_{Cr}^{nr}(0) \cdot \exp\left(-E/k_B T\right) \tag{5.8}$$

followed by rearrangement, gives eq (5.9), which describes the temperature-dependent excited-state lifetime.

$$\tau_{Cr}(T) = \frac{1}{k_{Cr}^{rad} + \left(k_{Cr}^{nr}(0) \cdot \exp\left(-E/k_B T\right)\right)} \tag{5.9}$$

Fitting the $\tau_{Cr}(T)$ data for CrI_3 (Figure 5.34) yields k_{Cr}^{nr}(4 K) ~ 0 s^{-1} increasing to 9.9 x 10^6 s^{-1} at 200 K. A value of k_{Cr}^{rad} = 1.9 x10^6 s^{-1} was taken from the experimental τ_{Cr}(4 K) of 0.2% Yb^{3+}:CrI_3, which was the longest decay time observed in our sample set. Similarly, k_{Yb}^{rad} is taken as $1/\tau_{Yb}$ measured for the sample at 4 K, were nonradiative decay is suppressed, giving a value of k_{Yb}^{rad} = 7.1 x 10^4 s^{-1} (see 5.6 Experimental Methods).

Doping CrI_3 with Yb^{3+} makes the exciton decay dynamics sensitive to diffusion. In addition to k_{Cr}^{hop}, k_{Yb}^{hop} is introduced to account for $Cr^{3+} \rightarrow Yb^{3+}$ energy transfer. For the simulations, k_{Yb}^{hop} was set to a temperature-independent value of 2.0 x 10^8 s^{-1} based on the high-temperature lower limit determined experimentally (Figure 5.5c), although variations in the precise value of this parameter have no effect because it is never rate limiting (see Figure 5.5 and discussion). To determine $k_{Cr}^{hop}(T)$, the low-temperature experimental data from Figure 5.2e are considered. The radiative and nonradiative decay constants found for CrI_3 (k_{Cr}^{rad}, k_{Cr}^{nr}) are intrinsic and hence treated as independent of Yb^{3+} doping. Thus, only $k_{Cr}^{hop}(T)$ remains undefined by experiment. The full set of experimental parameters used in the KMC simulations is provided in Table D.1.

5.4.3 KMC Simulations to Determine kCrhop

Figure 5.6b shows simulated Cr^{3+} decay times plotted *vs* temperature, calculated for the full range of Yb^{3+} concentrations using the above fixed values for k_{Cr}^{rad}, k_{Cr}^{nr}, k_{Yb}^{hop}, with a range of values for k_{Cr}^{hop} spanning over two orders of magnitude. The experimental data are best reproduced using k_{Cr}^{hop}(4 K) ≈ 1.0 x 10^7 s^{-1} (Figure 5.6b, bold). This hopping rate constant is similar to those determined for Frenkel exciton migration in other ionic lattices such as $RbMnF_3$, $CsMnF_3$, and $GdCl_3$,[44-46] and critically, it is ~10x slower than the experimental lower limit of k_{Yb}^{hop} from Figure 5.5. At the same time, this k_{Cr}^{hop}(4 K) value is ≥10^3x larger than the calculated 4 K rate constants for intra- and inter-layer nearest-neighbor FRET (Figure 5.38), supporting the assertion

that exciton diffusion is limited to DET within the same monolayer.

As an independent cross-check, this value for k_{Cr}^{hop} was used to simulate the experimental 4 K Yb^{3+} PL dynamics of 0.2% and 1.6% Yb^{3+}:CrI_3 (Figure 5.3b,c). The simulated data are plotted in Figure 5.6c,d and reproduce the experimental results well, showing effective rise times of 640 ± 16 and 353 ± 9 ns, respectively. This comparison shows that the set of microscopic parameters used to simulate the 4 K Cr^{3+} PL dynamics in Figure 5.6b also faithfully reproduces the 4 K Yb^{3+} PL dynamics.

To simulate the full temperature range probed experimentally, the temperature dependence of k_{Cr}^{hop} was analyzed. The temperature dependence of the PL FWHM can be expressed based on eq (5.4) as shown in eq (5.10).

$$\Delta FWHM = FWHM(T) - FWHM(0) = FWHM(0)\left[\coth\left(\frac{\upsilon_{eff}}{2k_BT}\right)\right]^{\frac{1}{2}} - FWHM(0) \qquad (5.10)$$

From Figure 5.4h, ρ shows the same temperature dependence as the FWHM, and from eq (5.2), k_{Cr}^{hop} is proportional to ρ. Introducing a proportionality factor (C) into eq (5.10) thus allows substitution of k_{Cr}^{hop} for FWHM, and rearrangement then gives eq (5.11).

$$\Delta k_{Cr}^{hop} = k_{Cr}^{hop}(T) - k_{Cr}^{hop}(0) = C\left[\left[\coth\left(\frac{\upsilon_{eff}}{2k_BT}\right)\right]^{\frac{1}{2}} - 1\right] \qquad (5.11)$$

Following eq (5.11), experimental data were simulated across all temperatures and Yb^{3+} concentrations using only a single universal adjustable scaling parameter (C), and the results are summarized in Figure 5.7a-c for the value of C that best reproduces the experimental data. The best-fit value of C = 8 x 10^7 s^{-1} corresponds to a ~7-fold increase in k_{Cr}^{hop} from 1 x 10^7 s^{-1} at 4 K to 6.8 x 10^7 s^{-1} at 200 K. The influence of C on k_{Cr}^{hop} is illustrated in Figure 5.37. Using this result, Figure 5.7a plots simulated Cr^{3+} PL decay times at temperatures from 4 to 200 K for x% Yb^{3+}:CrI_3 (x = 0.0, 0.2, 1.6, 5.0, 10.0, 18.6). These simulated results compare well with the corresponding experimental data in Figure 5.5a, covering a very broad range of compositions and temperatures. Overall, the KMC simulations reproduce all experimental variable-temperature, variable doping level, and time-dependence data well using a single experimentally constrained set of parameters, lending credence to the remaining parameters (k_{Cr}^{hop} and C) determined by fitting to

the data.

5.4.4 Exciton Diffusion

With these results, we are now able to analyze exciton diffusion in CrI_3 quantitatively. Figure 5.7b plots the exciton diffusion lengths (L_D) determined from the simulated trial data. L_D is calculated as the average distance of exciton diffusion according to eq (5.12),

$$L_D = \sqrt{1/N \sum_i x_i^2} \tag{5.12}$$

where N is the total number of excitons in a trial set and x_i is the real-space difference between the initial and final positions of the i-th trial exciton. At 4 K, L_D in undoped CrI_3 is 18.4 Å, corresponding to only ~5 lattice sites from the initial excitation. As the temperature increases, faster exciton hopping increases L_D, which reaches a maximum value of ~27 Å in undoped CrI_3 at ~100 K. At even higher temperatures, L_D decreases again due to thermally activated nonradiative decay. L_D also decreases with increasing Yb^{3+} concentration at every temperature, reflecting the increasing probability of exciton annihilation by Yb^{3+}. At higher doping levels, L_D becomes less sensitive to temperature because excitons are always efficiently annihilated after just a few hops, even at 4K.

Figure 5.7c plots exciton diffusion coefficients (diffusivities) determined at each temperature for each sample following eq (5.13).

$$D = \frac{L_D^2}{\tau} \tag{5.13}$$

In undoped CrI_3, D increases from 1.4 x 10^{-8} cm^2/s at 4 K to 1.5 x 10^{-7} cm^2/s at 200 K. The temperature dependence of D is linear above ~50 K, allowing facile extrapolation to a room-temperature value of D = 2.2 x 10^{-7} cm^2/s. D is also relatively insensitive to Yb^{3+} doping level at all temperatures.

From these results, it is clear that exciton diffusivity in CrI_3 is several orders of magnitude lower than reported for other 2D materials such as $MoSe_2$, WSe_2, and the 2D perovskite PEA_2PbI_4, which all show D ~ 10^{-1} – 10^{1} cm^2/s at 300 K, as probed by spatially resolved PL spectroscopy.[13, 47-49] As semiconductors, those materials feature far more delocalized excitons with much smaller

nuclear reorganization energies, E_R. The low exciton diffusivity of CrI_3 is more similar to the exciton diffusivities reported for other ionic insulators,[44-46] for close-packed films of colloidal CdSe/CdS quantum dots,[50] and for organic materials,[51] all of which involve discrete site-to-site exciton hopping.

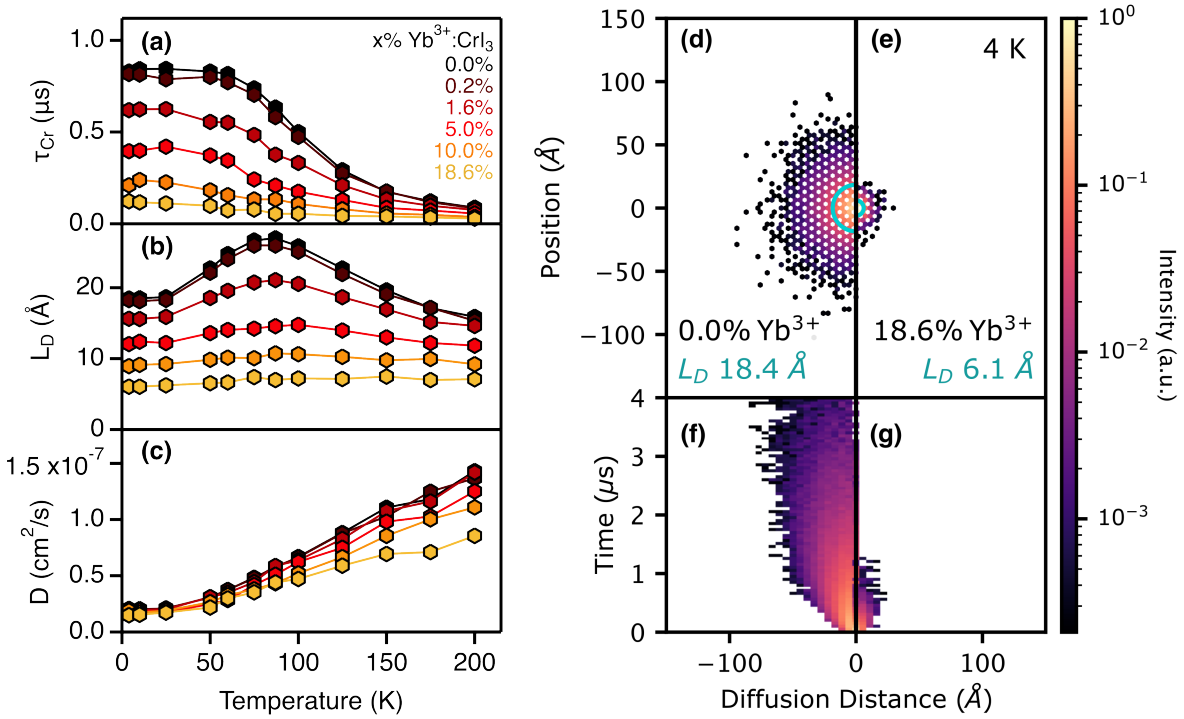

Figure 5.7 (a) Simulated Cr^{3+} PL decay times obtained from Monte Carlo modeling for x% Yb^{3+}:CrI_3 (x = 0.0, 0.2, 1.6, 5.0, 10.0, 18.6). **(b)** Simulated exciton diffusion lengths, L_D, plotted as a function of temperature. **(c)** Diffusion constant D as a function of temperature, calculated as $\boldsymbol{D = L_D^2/\tau}$. **(d-e)** False-color plots of simulated spatial PL mapping for 62,500 excitons in CrI_3 (d) and 18.6% Yb^{3+}:CrI_3 (e) at 4 K. The teal circle indicates L_D for each simulation. All excitations began in the center of the crystal. **(f-g)** False-color plots of emission intensity as it evolves in space and time for the same data from panels (d-e).

To highlight the spatial and temporal aspects of these results, Figure 5.7d,e shows false-color simulated spatial PL maps for CrI_3 and 18.6% Yb^{3+}-doped CrI_3 at 4 K, plotting the final location of each CrI_3 exciton relative to its initial position. Both profiles are gaussian, with the majority of PL occurring within the first few cation shells. The teal radii denote L_D in each case. L_D = 18.4 Å in undoped CrI_3 at 4 K, with some excitons traveling up to 100 Å, and this value decreases to 6.1

Å upon doping with 18.6% Yb^{3+}. Figure 5.7f,g plots the calculated PL intensities for these two samples as they evolve in space and time. Compared to the longer-lived excitons of undoped CrI_3, all excitons in 18.6 % Yb^{3+}-doped CrI_3 are quickly annihilated by nearby Yb^{3+} ions. Notably, all CrI_3 samples have L_D well below the optical diffraction limit at all temperatures.

5.5 Conclusion

We have demonstrated the use of emissive lanthanide impurities as atomic probes of exciton diffusion in CrI_3. These energy-harvesting dopants act as isolated atomic lattice sites for exciton annihilation, allowing exciton diffusion within the lattice to be systematically probed. We find that the highly localized excitons of CrI_3 diffuse through the lattice slowly *via* thermally activated site-to-site hopping driven by nearest neighbor Dexter energy transfer. Through a combination of time-resolved and continuous wave PL spectroscopies supported by Monte Carlo simulations, we showed that the large nuclear reorganization reduces spectral overlap and impedes hopping, leading to exciton diffusivities of 10^{-7}-10^{-8} cm^2/s that are orders of magnitude lower than in 2D vdW semiconductors. Thus, exciton diffusion lengths in CrI_3 are also small, limited to < 3 nm at all temperatures, well below the optical diffraction limit. This understanding of CrI_3 exciton diffusivity should help to inform future studies of CrI_3 and related CrX_3 materials that are under investigation as spin-photonic components in advanced optoelectronics architectures.

More generally, as well as affording the opportunity to probe these otherwise inaccessibly small length scales of exciton diffusion, the use of impurity ions as exciton annihilators allows energy transport to be monitored at arbitrarily low excitation densities. Employment of lanthanide probes is not limited to compounds featuring slow exciton diffusion, such as CrI_3, but is extendable to a variety of interesting and complex compositions, including those involving heterointerfaces, which may itself offer interesting possibilities for investigating energy transport in novel van der Waals constructs. For example, it could be intriguing to study exciton diffusion in inorganic 2D perovskites by an analogous approach, because these materials feature self-trapped excitons and are increasingly being integrated into van der Waals heterostructure

devices.[52-54] A particularly interesting material for such studies could be the 2D magnetic vdW compound NiPS3.[55, 56] Recently, resonant inelastic x-ray scattering (RIXS) data with high energy resolution have shown evidence of dispersive excitons in $NiPS_3$ based on localized Ni^{2+} $^3A_{2g} \rightarrow {}^1A_{1g}$ spin-flip excitations.[56] These excitons are proposed to propagate via a spin-conserving site-to-site hopping mechanism. Although not quantified, the weak electron-nuclear coupling in this Ni^{2+} spin-flip excitation compared to the Cr^{3+} $^4A_{2g} \rightarrow {}^4T_{2g}$ excitation of CrI_3 should enable greater diffusion lengths in the former, a hypothesis testable by the doping approach described here. Ultimately, any system in which impurity luminescence activators can be incorporated statistically at controlled and tunable concentrations offers the opportunity to probe exciton diffusion by the approach described here. Whereas highly mobile excitons with large diffusion lengths are already amenable to study by direct PL profiling, the use of impurity luminescence activators excels when diffusion lengths are too small for such methods. Luminescent impurities, and especially lanthanides with their distinctively narrow line shapes, thus offer a powerful complementary tool for exploring energy transport in a diverse array of materials, paving the way for new insights and innovations in 2D optoelectronics.

5.6 Experimental Methods

General Considerations. All sample preparation and manipulation was conducted within a glovebox environment under a purified dinitrogen atmosphere.

Chemicals. For the chromium source, high purity chromium chip (99.995%, lot MKCH4484) was purchased from Sigma Aldrich. The chromium chip was ground into a fine powder using a mortar and pestle. Iodine (≥99.99%) was purchased from Sigma Aldrich, while ytterbium metal powder 40 mesh (99.9%) was obtained from BeanTown Chemical. The Ytterbium and iodine were used in their as-received state without any further purification.

Synthesis of CrI_3 and Yb^{3+}-Doped CrI_3 Single Crystals. Doped and undoped CrI_3 single crystals were grown by chemical vapor transport as described in a previous report.[29] Undoped CrI_3 was made by placing Cr(0) metal and I_2 at a 1:3 stochiometric ratio (per I atom) in a 15 cm long quartz tube with an inner diameter of 14 mm. For the doped samples, additional Yb metal

was added alongside the other reactants. The tubes were evacuated and flame sealed. The reaction tubes were positioned within an open-ended horizontal tube furnace, with the precursors situated at the center of the furnace set at 650 ˚C and the other end of the tube near the edge of the furnace at a temperature of ca. 500 ˚C. Samples were heated for 5 days and then allowed to gradually cool down to room temperature, yielding thin shiny black crystal flakes.

Elemental Analysis. Elemental analysis of the doped samples was performed via inductively coupled plasma mass spectrometry (ICP-MS) using a PerkinElmer NexION 2000B. Samples were digested in concentrated high-purity nitric acid with the aid of sonication, followed by dilution in ultrapure H_2O. Yb^{3+} doping levels are reported as cation mole fraction; $[Yb^{3+}]/([Cr^{3+}]+[Yb^{3+}])$, with an estimated uncertainty of ±0.1%

Variable-Temperature Photoluminescence (VTPL). For VTPL measurements, single crystals were placed between two quartz disks and loaded into a closed-cycle helium cryostat, which was evacuated to pressures below 10^{-6} Pa. Samples were cooled to 4 K before measurements began. All variable-temperature series started at low temperature and progressed to higher temperatures. Samples were excited with a CW 660 nm (1.88 eV) diode at 4 mW/cm^2. Sample emission was collected, focused into a monochromator with a spectral bandwidth of 0.627 nm, and detected by a Hamamatsu InGaAs/InP liquid-nitrogen-cooled NIR photomultiplier. All spectra were corrected for instrument response. All luminescence spectra are displayed as photon counts versus energy (eV) following appropriate conversion.[57, 58]

Variable-Temperature Time-Resolved Photoluminescence (VT-TRPL). Time-resolved measurements were performed under the same conditions as used for CW PL measurements. An EKSPLA PL2230 Nd:YAG/YVO_4 laser with a pulse frequency of 50 Hz and a pulse duration of 20 ps was used to excite the samples at 532 nm (2.33 eV). Samples were excited with ~2 nJ/cm^2 per pulse. For decay traces, two emission energies were monitored: 1.2 eV and 1.15 eV for Cr^{3+} and Yb^{3+} + Cr^{3+} emission, respectively, each with a spectral bandwidth of 8 meV. Cr^{3+} signals were collected with a bin size of 5 ns, and Yb^{3+} signals were collected with a bin size of 20 ns. The decay curves collected at 1.2 eV were fit using a bi-exponential function. The reported τ_{Cr} values correspond to the weighted average of biexponential decay times. To determine τ_{Yb}, the data

collected at 1.15 eV were considered. All Cr^{3+} emission has fully decayed by ~15 μs, and the data from 15-200 μs thus corresponds solely to Yb^{3+} emission. These latter data were fit to a biexponential and the weighted average of the two exponential decay times is reported as τ_{Yb}. Gated PL measurements were performed using a gated photon counter (Stanford Research Systems SR400), where spectra were collected via only integrating over a 50 ns bin, delayed to various times following the excitation pulse.

Monte Carlo Simulations. Code for Monte Carlo random-walk-type simulations was developed in python 3.10.12; see Figure 5.35 for flowchart. Simulations were performed as follows: For each Yb^{3+} concentration, 250 independent trial crystal lattices were generated each having random distributions of the prescribed concentration of Yb^{3+} ions. The size of the simulated crystal (2600 unit cells) was large enough that no simulated excitons hit the border of any crystal. Lattice constants were taken from ICSD Coll. Code 251655.[59] On each trial lattice, 250 excitation trials were performed. Each excitation trial began on a central Cr^{3+} ion. On each Cr^{3+} ion, four potential paths are possible: hopping to a neighboring Cr^{3+} ion, emitting from the current ion, hoping to a neighboring Yb^{3+} ion if one exists in the first coordination sphere, or non-radiative relaxation. Each of these transitions from the initial state i to another state j was given a rate constant, k_{ij}, that characterizes its probability per unit time, assuming first-order exponential statistics. The rate constants for Cr-Cr hopping and non-radiative thermal relaxation are modified by temperature (see main text). Which stochastic event occurs is determined by randomly generating a number r ($0 < r \leq 1$) for each potential event, from which a dwell time of $t_{dwell} = -(1/k_{ij})\ln(r)$ describes how long state i remains before transitioning to j. The event with the minimum t_{dwell} is identified as the determined event, and the system moves to state j with the recorded time. The process then repeats from this new initial state (for more details see Voter[60]), and continues to repeat after each transition until the trial ends due to emission, non-radiative relaxation, or annihilation. The entire sequence was repeated for a total of 62,500 excitons with the results aggregated over all random lattices. The emission events were binned in 50 ns intervals. Simulated decay curves were fit to biexponential functions to determine the simulated decay times. The spatial locations of all N exciton emission events were recorded, with each

individual exciton diffusion length x_i corresponding to the distance between the starting and ending position of that exciton. The aggregate diffusion length L_D was calculated as $L_D = \sqrt{1/N \sum_i x_i^2}$.

5.7 References

(1) Huang, B.; Clark, G.; Navarro-Moratalla, E.; Klein, D. R.; Cheng, R.; Seyler, K. L.; Zhong, D.; Schmidgall, E.; McGuire, M. A.; Cobden, D. H.; et al. Layer-Dependent Ferromagnetism in a van der Waals Crystal Down to the Monolayer Limit. *Nature* **2017**, *546* (7657), 270-273.

(2) Tian, S.; Zhang, J.-F.; Li, C.; Ying, T.; Li, S.; Zhang, X.; Liu, K.; Lei, H. Ferromagnetic van der Waals Crystal VI_3. *J. Am. Chem. Soc.* **2019**, *141* (13), 5326-5333.

(3) Son, J.; Son, S.; Park, P.; Kim, M.; Tao, Z.; Oh, J.; Lee, T.; Lee, S.; Kim, J.; Zhang, K.; et al. Air-Stable and Layer-Dependent Ferromagnetism in Atomically Thin van der Waals $CrPS_4$. *ACS Nano* **2021**, *15* (10), 16904-16912.

(4) Wang, Q. H.; Bedoya-Pinto, A.; Blei, M.; Dismukes, A. H.; Hamo, A.; Jenkins, S.; Koperski, M.; Liu, Y.; Sun, Q.-C.; Telford, E. J.; et al. The Magnetic Genome of Two-Dimensional van der Waals Materials. *ACS Nano* **2022**, *16* (5), 6960-7079.

(5) Ziebel, M. E.; Feuer, M. L.; Cox, J.; Zhu, X.; Dean, C. R.; Roy, X. CrSBr: An Air-Stable, Two-Dimensional Magnetic Semiconductor. *Nano Lett.* **2024**, *24* (15), 4319-4329.

(6) Huang, B.; Clark, G.; Klein, D. R.; MacNeill, D.; Navarro-Moratalla, E.; Seyler, K. L.; Wilson, N.; McGuire, M. A.; Cobden, D. H.; Xiao, D.; et al. Electrical control of 2D magnetism in bilayer CrI_3. *Nat. Nanotechnol.* **2018**, *13* (7), 544-548.

(7) Wang, Z.; Gutiérrez-Lezama, I.; Ubrig, N.; Kroner, M.; Gibertini, M.; Taniguchi, T.; Watanabe, K.; Imamoğlu, A.; Giannini, E.; Morpurgo, A. F. Very large tunneling magnetoresistance in layered magnetic semiconductor CrI_3. *Nat. Commun.* **2018**, *9* (1), 2516.

(8) Li, T.; Jiang, S.; Sivadas, N.; Wang, Z.; Xu, Y.; Weber, D.; Goldberger, J. E.; Watanabe, K.; Taniguchi, T.; Fennie, C. J.; et al. Pressure-controlled interlayer magnetism in atomically thin CrI_3. *Nat. Mater.* **2019**, *18* (12), 1303-1308.

(9) Kazemi, M.; Shahnazaryan, V. A.; Zhumagulov, Y. V.; Bessarab, P. F.; Shelykh, I. A. Interaction of excitons with magnetic topological defects in 2D magnetic monolayers: localization and anomalous Hall effect. *2D Mater.* **2023**, *10* (1), 015003.

(10) Kazemi, M.; Kudlis, A.; Bessarab, P. F.; Shelykh, I. A. All-optical control of skyrmion configuration in CrI_3 monolayer. *Sci. Rep.* **2024**, *14* (1), 11677.

(11) Zhang, X.-Y.; Graham, T. K. M.; Bae, H.; Wang, Y.-X.; Delegan, N.; Ahn, J.; Wang, Z.-C.; Regner, J.; Watanabe, K.; Taniguchi, T.; et al. Enhanced magnetization by defect-assisted exciton recombination in atomically thin $CrCl_3$. *Phys. Rev. Mater.* **2024**, *8* (10), 104402.

(12) Akselrod, G. M.; Deotare, P. B.; Thompson, N. J.; Lee, J.; Tisdale, W. A.; Baldo, M. A.; Menon, V. M.; Bulović, V. Visualization of exciton transport in ordered and disordered molecular solids. *Nat. Commun.* **2014**, *5* (1), 3646.

(13) Kumar, N.; Cui, Q.; Ceballos, F.; He, D.; Wang, Y.; Zhao, H. Exciton diffusion in monolayer and bulk $MoSe_2$. *Nanoscale* **2014**, *6* (9), 4915-4919.

(14) Ginsberg, N. S.; Tisdale, W. A. Spatially Resolved Photogenerated Exciton and Charge Transport in Emerging Semiconductors. *Annu. Rev. Phys. Chem.* **2020**, *71* (Volume 71, 2020), 1-30.
(15) Dillon, J. F.; Kamimura, H.; Remeika, J. P. Magneto-optical properties of ferromagnetic chromium trihalides. *J. Phys. Chem. Solids* **1966**, *27* (9), 1531-1549.
(16) Grant, P. M.; Street, G. B. Optical properties of the chromium trihalides in the region 1-11 eV. *Bull. Am. Phys. Soc. II* **1968**, *13*.
(17) Bermudez, V. M.; McClure, D. S. Spectroscopic studies of the two-dimensional magnetic insulators chromium trichloride and chromium tribromide—I. *J. Phys. Chem. Solids.* **1979**, *40* (2), 129-147.
(18) Jin, W.; Kim, H. H.; Ye, Z.; Ye, G.; Rojas, L.; Luo, X.; Yang, B.; Yin, F.; Horng, J. S. A.; Tian, S.; et al. Observation of the polaronic character of excitons in a two-dimensional semiconducting magnet CrI_3. *Nat. Commun.* **2020**, *11* (1), 4780.
(19) Li, X.; Wang, A.; Chen, H.; Tao, W.; Chen, Z.; Zhang, C.; Li, Y.; Zhang, Y.; Shang, H.; Weng, Y.-X.; et al. Ultrafast Spontaneous Localization of a Jahn-Teller Exciton Polaron in Two-Dimensional Semiconducting CrI_3 by Symmetry Breaking. *Nano Lett.* **2022**, *22* (21), 8755-8762.
(20) Zhumagulov, Y.; Chiavazzo, S.; Shelykh, I. A.; Kyriienko, O. Robust polaritons in magnetic monolayers of CrI_3. *Phys. Rev. B* **2023**, *108* (16), L161402.
(21) Acharya, S.; Pashov, D.; Rudenko, A. N.; Rösner, M.; Schilfgaarde, M. v.; Katsnelson, M. I. Real- and momentum-space description of the excitons in bulk and monolayer chromium tri-halides. *npj 2D Mater. Appl.* **2022**, *6* (1), 33.
(22) Grzeszczyk, M.; Acharya, S.; Pashov, D.; Chen, Z.; Vaklinova, K.; van Schilfgaarde, M.; Watanabe, K.; Taniguchi, T.; Novoselov, K. S.; Katsnelson, M. I.; et al. Strongly Correlated Exciton-Magnetization System for Optical Spin Pumping in $CrBr_3$ and CrI_3. *J. Adv. Mater.* **2023**, *35* (17), 2209513.
(23) Brennan, N. J.; Noble, C. A.; Tang, J.; Ziebel, M. E.; Bae, Y. J. Important Elements of Spin-Exciton and Magnon-Exciton Coupling. *ACS Phys. Chem. Au.* **2024**, *4* (4), 322-327.
(24) Bai, Y.; Wang, Y.; Meng, S. Ab Initio Self-Trapped Excitons. *Phys. Rev. Lett.* **2024**, *133* (4), 046903.
(25) Wu, M.; Li, Z.; Cao, T.; Louie, S. G. Physical origin of giant excitonic and magneto-optical responses in two-dimensional ferromagnetic insulators. *Nat. Commun.* **2019**, *10* (1), 2371.
(26) Yin, T.; You, J.-Y.; Huang, Y.; Thu Do, H. T.; Prosnikov, M. A.; Zhao, W.; Serra, M.; Christianen, P. C. M.; Sofer, Z.; Sun, H.; et al. Signature of Ultrafast Formation and Annihilation of Polaronic States in a Layered Ferromagnet. *Nano Lett.* **2022**, *22* (19), 7784-7790.
(27) Sridhar, S.; Khansari, A.; O'Donnell, S.; Barth, A. T.; Danilov, E. O.; Castellano, F. N.; Maggard, P. A.; Dougherty, D. B. Ligand field exciton annihilation in bulk $CrCl_3$. *J. Chem. Phys.* **2024**, *161* (11).
(28) Kulig, M.; Zipfel, J.; Nagler, P.; Blanter, S.; Schüller, C.; Korn, T.; Paradiso, N.; Glazov, M. M.; Chernikov, A. Exciton Diffusion and Halo Effects in Monolayer Semiconductors. *Phys. Rev. Lett.* **2018**, *120* (20), 207401.
(29) Pressler, K.; Snoeren, T. J.; Walsh, K. M.; Gamelin, D. R. Magnetic Amplification at Yb^{3+} "Designer Defects" in the van der Waals Ferromagnet CrI_3. *Nano Lett.* **2023**, *23* (4), 1320-

1326.
(30) Snoeren, T. J.; Pressler, K.; Gamelin, D. R. Optically resolved exchange splittings in the doped van der Waals ferromagnet $CrBr_3$:Yb^{3+}. *Phys. Rev. Mater.* **2024**, *8* (10), 104410.
(31) Snoeren, T. J.; Pressler, K.; Kluherz, K. T.; Walsh, K. M.; De Yoreo, J. J.; Gamelin, D. R. Luminescence and Covalency in Ytterbium-Doped CrX_3 (X = Cl, Br, I) van der Waals Compounds. *J. Am. Chem. Soc.* **2023**, *145* (31), 17427-17434.
(32) Güdel, H. U.; Snellgrove, T. R. Jahn-Teller effect in the $^4T_{2g}$ state of chromium(III) in dicesium sodium indium(III) hexachloride. *Inorg. Chem.* **1978**, *17* (6), 1617-1620.
(33) Seyler, K. L.; Zhong, D.; Klein, D. R.; Gao, S.; Zhang, X.; Huang, B.; Navarro-Moratalla, E.; Yang, L.; Cobden, D. H.; McGuire, M. A.; et al. Ligand-field helical luminescence in a 2D ferromagnetic insulator. *Nat. Physics* **2018**, *14* (3), 277-281.
(34) Zhu, X.; Yan, X.; Kang, E.; Han, Y.; Yin, C.; Ye, S. Suppressing Energy Migration via Antiparallel Spin Alignment in One-Dimensional Mn^{2+} Halide Magnets with High Luminescence Efficiency. *Angew. Chem. Int. Ed.* **2024**, (e202417218).
(35) Grover, M.; Silbey, R. Exciton Migration in Molecular Crystals. *J. Chem. Phys.* **1971**, *54* (11), 4843-4851.
(36) Ballhausen, C. J. *Introduction to Ligand Field Theory*; McGraw-Hill Book Company, Inc., 1962.
(37) McCreary, A.; Mai, T. T.; Utermohlen, F. G.; Simpson, J. R.; Garrity, K. F.; Feng, X.; Shcherbakov, D.; Zhu, Y.; Hu, J.; Weber, D.; et al. Distinct magneto-Raman signatures of spin-flip phase transitions in CrI_3. *Nat. Commun.* **2020**, *11* (1), 3879.
(38) Kambli, U.; Güdel, H. U. Transfer of electronic excitation energy in the antiferromagnets rubidium trichloromanganate(II), cesium trichloromanganate(II), cesium tribromomanganate(II), and rubidium tetrachloromanganate(II). *Inorg. Chem.* **1984**, *23* (22), 3479-3486.
(39) Lazarides, T.; Davies, G. M.; Adams, H.; Sabatini, C.; Barigelletti, F.; Barbieri, A.; Pope, S. J. A.; Faulkner, S.; Ward, M. D. Ligand-field excited states of hexacyanochromate and hexacyanocobaltate as sensitisers for near-infrared luminescence from Nd(iii) and Yb(iii) in cyanide-bridged d–f assemblies. *Photochem. Photobiol. Sci.* **2007**, *6* (11), 1152-1157.
(40) Lado, J. L.; Fernández-Rossier, J. On the origin of magnetic anisotropy in two dimensional CrI_3. *2D Mater.* **2017**, *4* (3), 035002.
(41) Liu, Y.; Petrovic, C. Three-dimensional magnetic critical behavior in CrI_3. *Phys. Rev. B* **2018**, *97* (1), 014420.
(42) Frisk, A.; Duffy, L. B.; Zhang, S.; van der Laan, G.; Hesjedal, T. Magnetic X-ray spectroscopy of two-dimensional CrI_3 layers. *Mater. Lett.* **2018**, *232*, 5-7.
(43) Kim, D.-H.; Kim, K.; Ko, K.-T.; Seo, J.; Kim, J. S.; Jang, T.-H.; Kim, Y.; Kim, J.-Y.; Cheong, S.-W.; Park, J.-H. Giant Magnetic Anisotropy Induced by Ligand *LS* Coupling in Layered Cr Compounds. *Phys. Rev. Lett.* **2019**, *122* (20), 207201.
(44) Moncorgé, R.; Jacquier, B.; Madej, C.; Blanchard, M.; Brunel, L. C. Exciton dynamics and energy transfers in pure $CsMnF_3$. *J. Phys. France* **1982**, *43* (8), 1267-1281.
(45) Mahiou, R.; Jacquier, B.; Madej, C. One-dimensional energy transfer in $GdCl_3$. *J. Chem. Phys.* **1988**, *89* (9), 5931-5942.
(46) Wunsch, F. R.; Gebhardt, W. Energy transfer between Jahn-Teller systems in $RbMnF_3$. *J. Phys. Condens. Matter* **1989**, *1* (5), 855.

(47) Cui, Q.; Ceballos, F.; Kumar, N.; Zhao, H. Transient absorption microscopy of monolayer and bulk WSe_2. *ACS Nano* **2014**, *8* (3), 2970-2976. From NLM.
(48) Ziegler, J. D.; Zipfel, J.; Meisinger, B.; Menahem, M.; Zhu, X.; Taniguchi, T.; Watanabe, K.; Yaffe, O.; Egger, D. A.; Chernikov, A. Fast and Anomalous Exciton Diffusion in Two-Dimensional Hybrid Perovskites. *Nano Lett.* **2020**, *20* (9), 6674-6681.
(49) Seitz, M.; Magdaleno, A. J.; Alcázar-Cano, N.; Meléndez, M.; Lubbers, T. J.; Walraven, S. W.; Pakdel, S.; Prada, E.; Delgado-Buscalioni, R.; Prins, F. Exciton diffusion in two-dimensional metal-halide perovskites. *Nat. Commun.* **2020**, *11* (1), 2035.
(50) Lee, E. M. Y.; Tisdale, W. A. Determination of Exciton Diffusion Length by Transient Photoluminescence Quenching and Its Application to Quantum Dot Films. *J. Phys. Chem. C* **2015**, *119* (17), 9005-9015.
(51) Powell, R. C.; Soos, Z. G. Singlet exciton energy transfer in organic solids. *J. Lumin.* **1975**, *11* (1), 1-45.
(52) Li, S.; Luo, J.; Liu, J.; Tang, J. Self-Trapped Excitons in All-Inorganic Halide Perovskites: Fundamentals, Status, and Potential Applications. *J. Phys. Chem. Lett* **2019**, *10* (8), 1999-2007.
(53) Wang, H.; Ma, J.; Li, D. Two-Dimensional Hybrid Perovskite-Based van der Waals Heterostructures. *J. Phys. Chem. Lett* **2021**, *12* (34), 8178-8187.
(54) Zhang, L.; Wang, Y.; Chu, A.; Zhang, Z.; Liu, M.; Shen, X.; Li, B.; Li, X.; Yi, C.; Song, R.; et al. Facet-selective growth of halide perovskite/2D semiconductor van der Waals heterostructures for improved optical gain and lasing. *Nat. Commun.* **2024**, *15* (1), 5484.
(55) Kang, S.; Kim, K.; Kim, B. H.; Kim, J.; Sim, K. I.; Lee, J.-U.; Lee, S.; Park, K.; Yun, S.; Kim, T.; et al. Coherent many-body exciton in van der Waals antiferromagnet $NiPS_3$. *Nature* **2020**, *583* (7818), 785-789.
(56) He, W.; Shen, Y.; Wohlfeld, K.; Sears, J.; Li, J.; Pelliciari, J.; Walicki, M.; Johnston, S.; Baldini, E.; Bisogni, V.; et al. Magnetically propagating Hund's exciton in van der Waals antiferromagnet $NiPS_3$. *Nat Commun* **2024**, *15* (1), 3496.
(57) Ejder, E. Methods of Representing Emission, Excitation, and Photoconductivity Spectra. *J. Opt. Soc. Am.* **1969**, *59* (2), 223_221-224.
(58) Mooney, J.; Kambhampati, P. Get the Basics Right: Jacobian Conversion of Wavelength and Energy Scales for Quantitative Analysis of Emission Spectra. *J. Phys. Chem. Lett.* **2013**, *4* (19), 3316-3318.
(59) McGuire, M. A.; Dixit, H.; Cooper, V. R.; Sales, B. C. Coupling of Crystal Structure and Magnetism in the Layered, Ferromagnetic Insulator CrI_3. *Chem. Mater.* **2015**, *27* (2), 612-620.
(60) Voter, A. Introduction to the kinetic Monte Carlo method. Vol. book; 2007; pp 1-23.

Appendix A *Supplementary Information for Chapter 2* – Luminescence and Covalency in Ytterbium-Doped CrX_3 (X = Cl, Br, I) van der Waals Compounds

A.1 Additional EXAFS Characterization

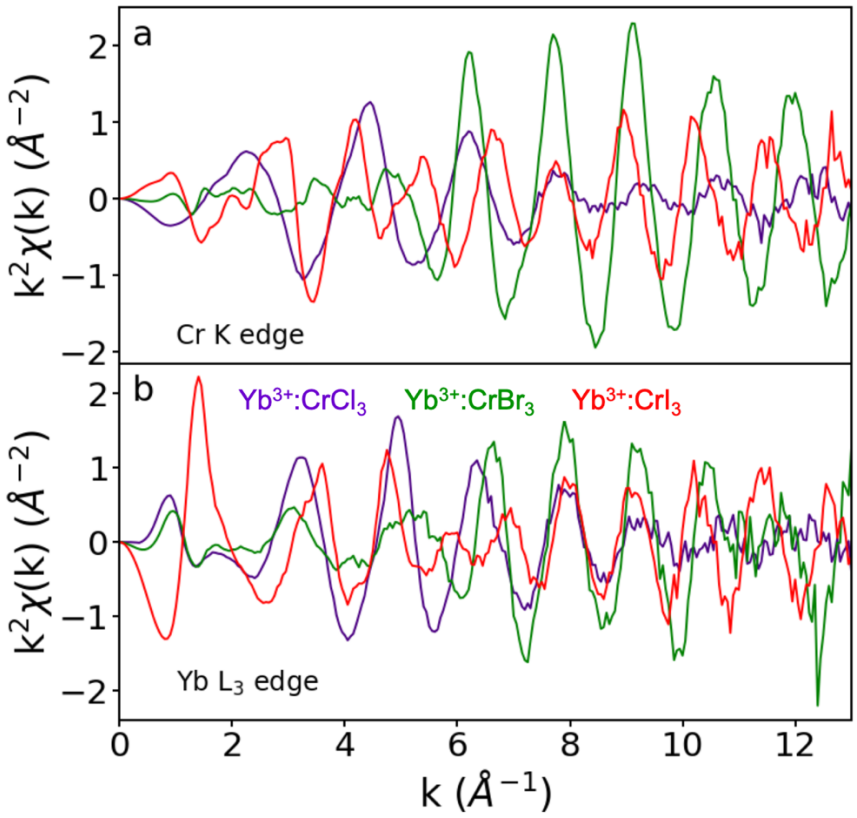

Figure 5.1 *k*-space EXAFS data from the **(a)** Cr K- and **(b)** Yb L_3-edges for Yb^{3+}:CrX_3 (X = Cl, Br, I) single crystals, plotted with a *k*-weight of 2. A window from 3 $Å^{-1}$ to 12 $Å^{-1}$ with a d*k* value of 1 $Å^{-1}$ was used for shell-by-shell fitting in Artemis.

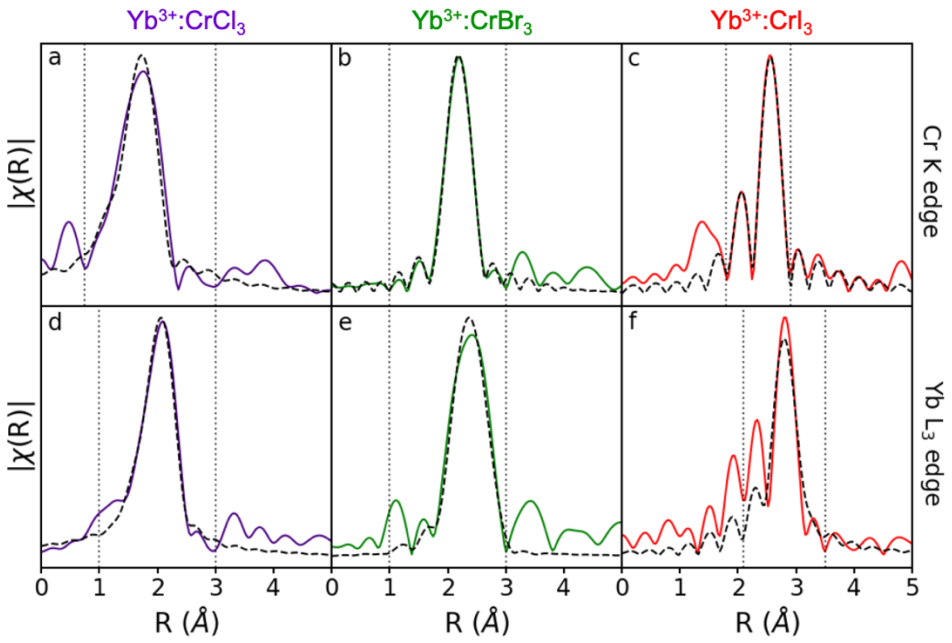

Figure 5.2 Fourier-transform (real-space) EXAFS data (colored) and fits (black dashed) using the nearest-neighbor halide scatterers for the Cr K edge (top row) and Yb L_3 edge (bottom row) for each sample. **(a,d)** Yb^{3+}:$CrCl_3$ data (purple); **(b,e)** Yb^{3+}:$CrBr_3$ data (green); **(c,f)** Yb^{3+}:CrI_3 data (red). Vertical dotted lines in each panel mark the fitting windows used, in R-space. Note that the radial distances have not been corrected for phase shift, in order to compare with the fits.

Table A.1 Fitting parameters and bond distances for optimized shell-by-shell fits of EXAFS data for Yb^{3+}:CrX_3 (X = Cl, Br, I) single-crystal samples.

	R-factor	$\chi 2$	$\chi 2_{red}$	Debye-Waller	Bond Distance (Å)
Cr K edge					
Yb^{3+}:$CrCl_3$	0.016	1380	239	0.0013	2.252 ± 0.015
Yb^{3+}:$CrBr_3$	0.001	69	7	0.0033	2.494 ± 0.002
Yb^{3+}:CrI_3	0.008	39	18	0.0036	2.715 ± 0.006
Yb L_3 edge					
Yb^{3+}:$CrCl_3$	0.017	624	88	0.0108	2.541 ± 0.013
Yb^{3+}:$CrBr_3$	0.012	42	11	0.0068	2.806 ± 0.019
Yb^{3+}:CrI_3	0.007	16	4	0.0040	2.945 ± 0.005

A.2 SEM and EDX Characterization

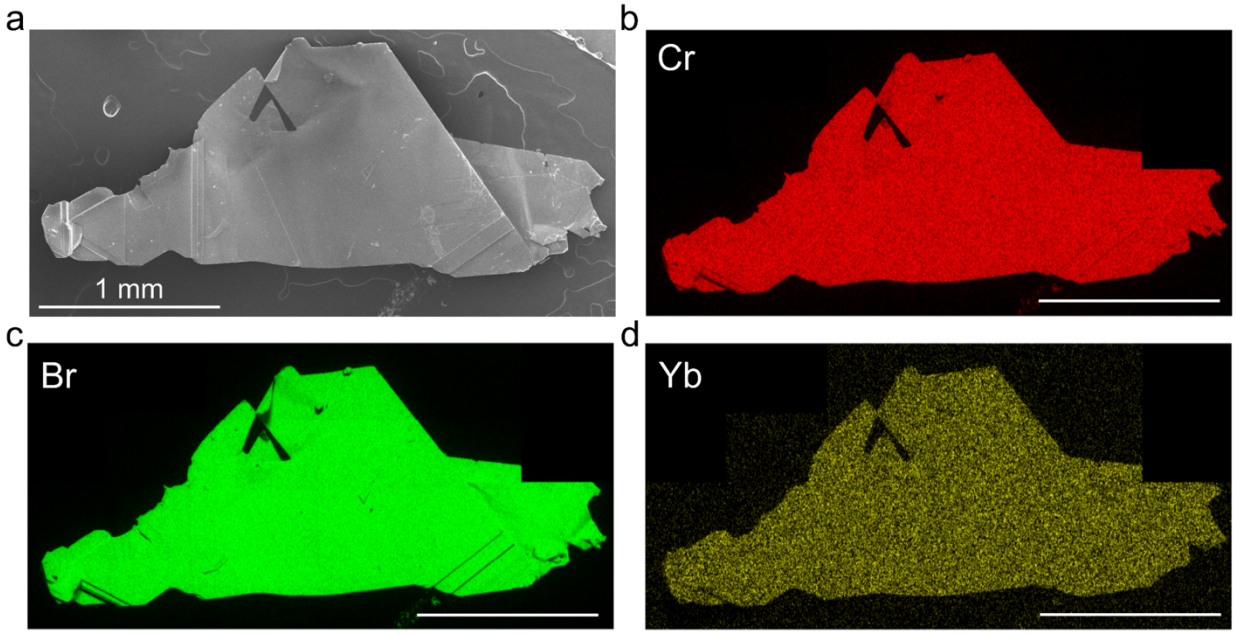

Figure 5.3 (a) SEM image of a representative $Yb^{3+}:CrBr_3$ flake. **(b-d)** EDX mapping of the same flake showing an even distribution of Cr, Br, and Yb throughout the material. The low concentration of Yb in this sample leads to worse signal to noise relative to Cr. All scale bars are 1 mm.

A.3 AOM Parameters

Table A.2 Summary of Angular Overlap Model (AOM) calculation parameters. All values are in cm^{-1}.

	ζ	e_σ	$e_{\pi,x}$	$e_{\pi,y}$
$Yb^{3+}:CrCl_3$	2883	288.5	198	100.5
$Yb^{3+}:CrBr_3$	2863.5	219.5	212.5	137.5
$Yb^{3+}:CrI_3$	2665	176.5	122.5	122.5

A.4 Survey of Yb^{3+} Energies Across Various Lattices

Table A.3 Yb^{3+} *f-f* energy levels and ligand-to-metal charge-transfer energies (E_{CT}) in different host lattices. Several of the Yb^{3+} crystal-field energies are collected in an overview paper by Haumesser *et al.*[1] Some charge-transfer energies are collected in an overview paper by Nikl *et al.*[2] Eu^{3+} charge-transfer energies, used to estimate E_{CT} for select Yb^{3+} compounds, are collected in an overview paper by Dorenbos.[3] Charge-transfer energies are rounded to the nearest hundred wavenumbers. All energies in cm^{-1}.

Host Lattice	0	1	2	3	$^2F_{7/2}$ Barycenter	0'	1'	2'	$^2F_{5/2}$ Barycenter	Δ	ref.	E_{CT}	ref.
$LiYF_4$	0	216	371	479	267	10288	10409	10547	10415	10148	[4]	62900	[5]
LaF_3	0	72	183	396	163	10268	10442	10668	10459	10296	[6]	59700[a]	[7, 8]
CaF_2	0	331	482	669	371	10116	?	?	10412[b]	10042	[9]	58100	[10]
YPO_4	0	265	265	841	343	10415	?	?	10607[c]	10264	[11]	47600	[5, 12]
$LuPO_4$	0	84	277	277	159.5	10244	10275	10480	10333	10174	[6]	47600	[5]
$Y_3Al_5O_{12}$	0	565	612	785	491	10327	10624	10679	10543	10052	[13, 14]	47600	[2, 5]
$Lu_3Al_5O_{12}$	0	127	372	601	275	10352	?	?	10500[d]	10224	[15]	45000	[2, 15, 16]
$Y_3Ga_5O_{12}$	0	132	330	540	251	10315	?	?	10483[d]	10232	[15]	44400	[15]
Sc_2O_3	0	474	634	1076	546	10250	10640	11198	10696	10150	[17]	44400	[5]
Y_2O_3	0	536	536	941	503	10235	10526	11050	10604	10101	[18]	44100	[5]
$LaPO_4$	0	135	135	551	205	10241	?	?	10356[c]	10151	[19, 20]	43900	[5, 12]
Al_2O_3	0	337	550	1020	477	10252	10476	11120	10616	10139	[21]	43000[a]	[22]
$YAl_3(BO_3)_4$	0	94	185	581	215	10194	10277	10672	10381	10166	[23]	43000[a]	[24]
$Ca_5(PO_4)_3F$	0	409	597	1099	526	10178	10496	11069	10581	10055	[6]	42800[a]	[25]
$YAlO_3$	0	209	341	590	285	10220	10410	10730	10453	10168	[4]	42600	[5, 26]
$Ca_4GdO(BO_3)_3$	0	423	668	1003	524	10246	10706	11089	10680	10156	[27]	42300[a]	[28]
$Sr_5(PO_4)_3F$	0	362	618	1190	543	10150	10512	11108	10590	10048	[29]	41600[a]	[30]
$SrLaGa_3O_7$	0	220	386	910	379	10190	10450	11025	10555	10176	[31]	38500[a]	[32]
$Cs_2NaYbCl_6$	0	362	362	701	356	10243	10243	10708	10398	10042	[33]	38300	[33]
YCl_3	0	318	506	746	393	10392	?	?	10706[b]	10314	[34]	36500	[34]
$Na_3Y(PO_4)_2$	0	188	325	722	309	10244	10515	11045	10601	10292	[35, 36]	34500	[35]
YBr_3	0	109	332	519	240	10194	?	?	10386[b]	10146	[34]	29800	[34]
$CsCdBr_3$	0	159	198	466	206	10125	10139	10598	10287	10081	[37]	29000	[38]
ZnS	0	63	108	229	100	10151	?	?	10231[b]	10131	[39]	28000	[39]
$NaYS_2$	0	229	229	522	245	10101	?	?	10297[b]	10052	[40]	26300	[40]
$CuInS_2$	0	32	87	182	75	10033	10060	?	10095[b]	10020	[41]	26300	[e]
$NaInS_2$	0	266	266	582	279	10070	?	?	10293[b]	10014	[42]	26300	[e]
$PbIn_2S_4$	0	200	200	549	237	10091	?	?	10281[b]	10044	[42]	26300	[e]
Free Ion	-	-	-	-	0	-	-	-	10213	10213	[43]	-	-
CrI_3	0	144	147	400	173	9410	9411	9689	9503	9330	[44]	17900	[f]
$CrBr_3$	0	145	237	522	226	10107	10154	10498	10253	10027	This Work	29200	[f]
$CrCl_3$	0	206	321	590	280	10214	10270	10646	10377	10097	This Work	36700	[f]

a Calculated from Eu^{3+} charge-transfer energies using the method outlined by Li *et al.*[45]

b Calculated from $^2F_{7/2}$ barycenter using $E_{F_{5/2}} = E_{0'} + \sigma E_{F_{7/2}}$ where E_F indicates the barycenter energy, $E_{0'}$ indicates the energy of the lowest-energy crystal-field state of the $^2F_{5/2}$ manifold, and $\sigma = 0.8$ (unless stated otherwise), as determined by Pressler *et al.* (SI).[44]

c Calculated as described in (b) using σ = 0.56 (from $LuPO_4$)

d Calculated as described in (b) using σ = 0.67 (from $Y_3Al_5O_{12}$)

e CT values have not been reported for these lattices, the value used here is for $NaYS_2$ as measured by Hansen *et al.*[40] Error bars are included in figures in Chapter 2 to indicate expected deviations from this value.

f CT values were not reported for these lattices. Values for $[YbX_6]^{3-}$ in solution were used from Ryan and Jørgensen.[46, 47] Estimated error bars are roughly the size of the CrX_3 data points in Figure 2.4c.

Note: Due to limited resolution of some of the reported spectra and uncertainties in assigning the electronic origins, some of the listed splitting energies may not be entirely accurate. The most important factor in determining the value of Δ is the highest energy transition in the PL spectrum, i.e., $0' \rightarrow 0$, as this value is the largest component of Δ. The $0' \rightarrow 0$ transition has a high intensity in

many lattices and can thus be determined with reasonable accuracy. The $^2F_{7/2}$ and $^2F_{5/2}$ crystal-field splittings shift the value of Δ by no more than several tens of wavenumbers (several meV). As a result, in most cases the expected error bars on the value of Δ are no larger than the size of the data points in in Figure 2.4c.

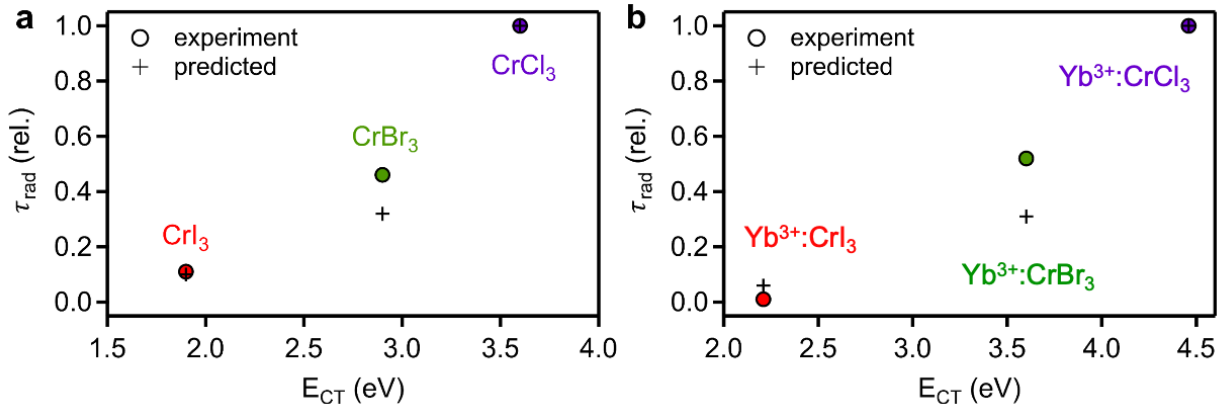

Figure 5.4 (a) Cr^{3+} PL decay times for CrX_3 compounds plotted vs the energy of the first LMCT transition (E_{CT}). Circles: Experimental data from Figure 2.3d. Crosses: Values predicted using eq (2.3) and eq (2.4) **(b)** Same as (a) but for Yb^{3+} PL decay times in Yb^{3+}:CrX_3 compounds.

A.5 References

(1) Haumesser, P.-H.; Gaumé, R.; Viana, B.; Antic-Fidancev, E.; Vivien, D. Spectroscopic and Crystal-Field Analysis of New Yb-doped Laser Materials. *J. Phys.: Cond. Mat.* **2001**, *13* (23), 5427-5447.

(2) Nikl, M.; Yoshikawa, A.; Fukuda, T. Charge transfer luminescence in Yb^{3+}-containing compounds. *Opt. Mater.* **2004**, *26* (4), 545-549.

(3) Dorenbos, P. Energy of the first $4f^7 \rightarrow 4f^6 5d$ transition of Eu^{2+} in inorganic compounds. *J. Lumin.* **2003**, *104* (4), 239-260.

(4) Morrison, C. A.; Leavitt, P. Handbook on the physics and chemistry of rare earths, ch 46. Amsterdam: Elsevier: 1982.

(5) van Pieterson, L.; Heeroma, M.; de Heer, E.; Meijerink, A. Charge transfer luminescence of Yb^{3+}. *J. Lumin.* **2000**, *91* (3), 177-193.

(6) DeLoach, L. D.; Payne, S. A.; Chase, L. L.; Smith, L. K.; Kway, W. L.; Krupke, W. F. Evaluation of absorption and emission properties of Yb^{3+} doped crystals for laser applications. *IEEE J. Quant. Elect.* **1993**, *29* (4), 1179-1191.

(7) Gérard, I.; Krupa, J. C.; Simoni, E.; Martin, P. Investigation of charge transfer $O^{2-} \rightarrow Ln^{3+}$ and $F^- \rightarrow Ln^{3+}$ in LaF_3:(Ln^{3+}, O^{2-}) and YF_3:(Ln^{3+}, O_{2-}) systems. *J. Alloys Compd.* **1994**, *207-208*, 120-127.

(8) Mayolet, A.; Krupa, J. C.; Gerard, I.; Martin, P. Luminescence of Eu^{3+} doped materials excited

by VUV synchrotron radiation. *Mater. Chem. Phys.* **1992**, *31* (1), 107-109.
(9) Kuznetsov, S. V.; Morozov, O. A.; Gorieva, V. G.; Mayakova, M. N.; Marisov, M. A.; Voronov, V. V.; Yapryntsev, A. D.; Ivanov, V. K.; Nizamutdinov, A. S.; Semashko, V. V.; et al. Synthesis and luminescence studies of CaF_2:Yb:Pr solid solutions powders for photonics. *J. Fluor. Chem.* **2018**, *211*, 70-75.
(10) Radzhabov, E. A.; Nepomnyashchikh, A. I.; Kozlovskiĭ, V. Charge-transfer bands in crystals of alkaline earth fluorides with Eu^{3+} and Yb^{3+1}. *Opt. Spectrosc.* **2008**, *105* (3), 364-368.
(11) Li, K.-Y.; Liu, L.; Wang, R.; Xiao, S.; Zhou, H.; Yan, H. Broadband sensitization of downconversion phosphor YPO_4 by optimizing TiO_2 substitution in host lattice co-doped with Pr^{3+}-Yb^{3+} ion-couple. *J. Appl. Phys.* **2014**, *115*, 123103.
(12) van Pieterson, L.; Meijerink, A. Charge transfer luminescence of Yb^{3+} in orthophosphates. *J. Alloys Compd.* **2000**, *300-301*, 426-429.
(13) Takaichi, K.; Yagi, H.; Lu, J.; Shirakawa, A.; Ueda, K.; Yanagitani, T.; Kaminskii, A. A. Yb^{3+}-doped $Y_3Al_5O_{12}$ ceramics – A new solid-state laser material. *physica status solidi (a)* **2003**, *200* (1), R5-R7.
(14) Bogomolova, G. A.; Bumagina, L. A.; Kaminskii, A. A.; Malkin, B. Z. Crystal field in laser garnets with TR^{3+} ions in the exchange charge model. *Sov. Phys. Solid State* **1977**, *19* (8), 1428-1435.
(15) Kamenskikh, I. A.; Guerassimova, N.; Dujardin, C.; Garnier, N.; Ledoux, G.; Pedrini, C.; Kirm, M.; Petrosyan, A.; Spassky, D. Charge transfer fluorescence and f–f luminescence in ytterbium compounds. *Opt. Mater.* **2003**, *24* (1), 267-274.
(16) Ogino, H.; Yoshikawa, A.; Lee, J.-H.; Nikl, M.; Solovieva, N.; Fukuda, T. Growth and Scintillation Properties of Yb-Doped $Lu_3Al_5O_{12}$ Crystals. *J. Cryst. Growth* **2003**, *253*, 314-318.
(17) Mix, E. PhD Thesis. Hamburg University, 1999.
(18) Kong, J.; Tang, D. Y.; Lu, J.; Ueda, K. Spectral characteristics of a Yb-doped Y_2O_3 ceramic laser. *Appl. Phys. B.* **2004**, *79* (4), 449-455.
(19) Shimizu, T.; Isobe, T. Relation between shell thickness and near infrared photoluminescence of $LaPO_4$:Yb^{3+}/$GdPO_4$ core/shell nanoparticles. *Mater. Lett.* **2013**, *110*, 180-183.
(20) Kaminska, A.; Duzynska, A.; Suchocki, A.; Bettinelli, M. Spectroscopy of f-f radiative transitions of Yb^{3+} ions in ytterbium doped orthophosphates at ambient and high hydrostatic pressures. *J. Condens. Matter Phys.* **2010**, *22* (22), 225902. From NLM.
(21) Krebs, J. K.; Happek, U. Yb^{3+} energy levels in α-Al_2O_3. *J. Lumin.* **2001**, *94-95*, 65-68.
(22) Mariscal, L. B.; Carmona-Téllez, S.; Alarcón-Flores, G.; Meza-Rocha, A. N.; Murrieta, H. S.; Falcony, C. Synthesis of Al_2O_3: Eu^{3+} Powder and PET Films with this Powder Incorporated: A Luminescence Study. *ECS J. Solid State Sci. Technol.* **2015**, *4* (7), R97.
(23) Wang, P.; Dawes, J. M.; Dekker, P.; Knowles, D. S.; Piper, J. A.; Lu, B. Growth and evaluation of ytterbium-doped yttrium aluminum borate as a potential self-doubling laser crystal. *J. Opt. Soc. Am. B* **1999**, *16* (1), 63-69.
(24) Blasse, G.; Bril', A. S. Study of Energy Transfer from Sb^{3+}, Bi^{3+}, Ce^{3+} to Sm^{3+}, Eu^{3+}, Tb^{3+}, Dy^{3+}. *J. Chem. Phys.* **1967**, *47*, 1920-1926.
(25) Sahoo, R.; Bhattacharya, S. K.; Debnath, R. A new type of charge compensating mechanism in $Ca_5(PO_4)_3F$:Eu^{3+} phosphor. *J. Solid State Chem.* **2003**, *175* (2), 218-225.

(26) Shim, J. B.; Yoshikawa, A.; Nikl, M.; Solovieva, N.; Pejchal, J.; Yoon, D. H.; Fukuda, T. Growth and characterization of Yb^{3+}-doped $YAlO_3$ fiber single crystals grown by the modified micro-pulling-down method. *J. Cryst. Growth* **2003**, *256* (3), 298-304.
(27) Mougel, F.; Dardenne, K.; Aka, G.; Kahn-Harari, A.; Vivien, D. Ytterbium-doped $Ca_4GdO(BO_3)_3$: an efficient infrared laser and self-frequency doubling crystal. *J. Opt. Soc. Am. B* **1999**, *16* (1), 164-172.
(28) Dirksen, G. J.; Blasse, G. Tetracalcium gadolinium oxoborate ($Ca_4GdO(BO_3)_3$) as a new host lattice for luminescent materials. *J. Alloys Compd.* **1993**, *191* (1), 121-126.
(29) Gruber, J. B.; Zandi, B.; Merkle, L. Crystal-field splitting of energy levels of rare-earth ions $Dy^{3+}(4f^9)$ and $Yb^{3+}(4f^{13})$ in M (II) sites in the fluorapatite crystal $Sr_5(PO_4)_3F$. *J. Appl. Phys.* **1998**, *83* (2), 1009-1017.
(30) Jagannathan, R.; Kutty, T. R. N. Anomalous fluorescence features of Eu^{2+} in apatite—pyromorphite type matrices. *J. Lumin.* **1997**, *71* (2), 115-121.
(31) Simondi-Teisseire, B. PhD Thesis. Paris VI University, 1996.
(32) Kubota, S.-i.; Izumi, M.; Yamane, H.; Shimada, M. Luminescence of Eu^{3+}, Tb^{3+} and Tm^{3+} in $SrLaGa_3O_7$. *J. Alloys Compd.* **1999**, *283* (1), 95-101.
(33) Schwartz, R. W. Electronic Structure of the Octahedral Hexachloroytterbate Ion. *Inorg. Chem.* **1977**, *16* (7), 1694-1698.
(34) Dorenbos, P.; Josef, A.; de Haas, J. T. M.; Krämer, K. W. Vacuum referred binding energies of the lanthanides in chloride, bromide, and iodide compounds. *J. Lumin.* **2019**, *208*, 463-467.
(35) Legendziewicz, J.; Guzik, M.; Szuszkiewicz, W. Charge transfer and f–f emission of trivalent ytterbium observed in double phosphates $M^{I}M^{III}(PO_4)_2$ (M^{I}=Na, Rb; M^{III}=Lu, Y). *J. Alloys Compd.* **2008**, *451* (1), 165-171.
(36) Godlewska, P.; Matraszek, A.; Macalik, L.; Hermanowicz, K.; Ptak, M.; Tomaszewski, P. E.; Hanuza, J.; Szczygieł, I. Spectroscopic and structural properties of $Na_3RE(PO_4)_2$:Yb orthophosphates synthesised by hydrothermal method (RE=Y, Gd). *J. Alloys Compd.* **2015**, *628*, 199-207.
(37) Malkin, B. Z.; Leushin, A. M.; Iskhakova, A. I.; Heber, J.; Altwein, M.; Moller, K.; Fazlizhanov, I. I.; Ulanov, V. A. EPR and optical spectra of Yb^{3+} in $CsCdBr_3$: Charge-transfer effects on the energy-level structure of Yb^{3+} in the symmetrical pair centers. *Phys. Rev. B* **2000**, *62* (11), 7063.
(38) Demirbilek, R.; Heber, J.; Nikitin, S. *Charge transfer and $4f^n$-$4f^{n-1}$ 5d transitions of trivalent rare-earch ions in $CsCdBr_3$*; SPIE, 2002.
(39) Przybylińska, H.; Świątek, K.; Stąpor, A.; Suchocki, A.; Godlewski, M. Recombination processes in Yb-activated ZnS. *Phys. Rev. B* **1989**, *40* (3), 1748-1755.
(40) Hansen, P.-A.; Kumar, S.; Meijerink, A. Strong self-sensitized green and NIR emission in $NaYS_2$ doped with Pr^{3+} and Yb^{3+} by inducing Laporte allowed and charge transfer transitions. *J. Lumin.* **2021**, *235*, 118012.
(41) Tsujii, N.; Imanaka, Y.; Takamasu, T.; Kitazawa, H.; Kido, G. Photoluminescence of Yb^{3+}-Doped $CuInS_2$ Crystals in Magnetic Fields. *J. Appl. Phys.* **2001**, *89* (5), 2706-2710.
(42) Creutz, S. E.; Fainblat, R.; Kim, Y.; De Siena, M. C.; Gamelin, D. R. A Selective Cation Exchange Strategy for the Synthesis of Colloidal Yb^{3+}-Doped Chalcogenide Nanocrystals with Strong Broadband Visible Absorption and Long-Lived Near-Infrared Emission. *J. Am.*

Chem. Soc. **2017**, *139* (34), 11814-11824.
(43) Wyart, J.-F.; Tchang-Brillet, W.-Ü. L.; Spector, N.; Palmeri, P.; Quinet, P.; Biémont, E. Extended Analysis of the Spectrum of Triply-ionized Ytterbium (Yb IV) and Transition Probabilities. *Phys. Scripta* **2001**, *63* (2), 113-121.
(44) Pressler, K.; Snoeren, T. J.; Walsh, K. M.; Gamelin, D. R. Magnetic Amplification at Yb^{3+} "Designer Defects" in the van der Waals Ferromagnet CrI_3. *Nano Lett.* **2023**, *23* (4), 1320-1326.
(45) Li, L.; Zhou, S.; Zhang, S. Relationship between charge transfer energies of Yb^{3+} and Sm^{3+} and crystal environmental factor. *J. Lumin.* **2009**, *129* (3), 187-191.
(46) Ryan, J. L.; Jørgensen, C. K. Absorption Spectra of Octahedral Lanthanide Hexahalides. *J. Phys. Chem.* **1966**, *70* (9), 2845-2857.
(47) Ryan, J. L. Weak or unstable iodo complexes. I. Hexaiodo complexes of the lanthanides. *Inorg. Chem.* **1969**, *8* (10), 2053-2058.

Appendix B *Supplementary Information for Chapter 3* - Magnetic Amplification at Yb^{3+} "Designer Defects" in the van der Waals Ferromagnet CrI_3

B.1 Sample Characterization

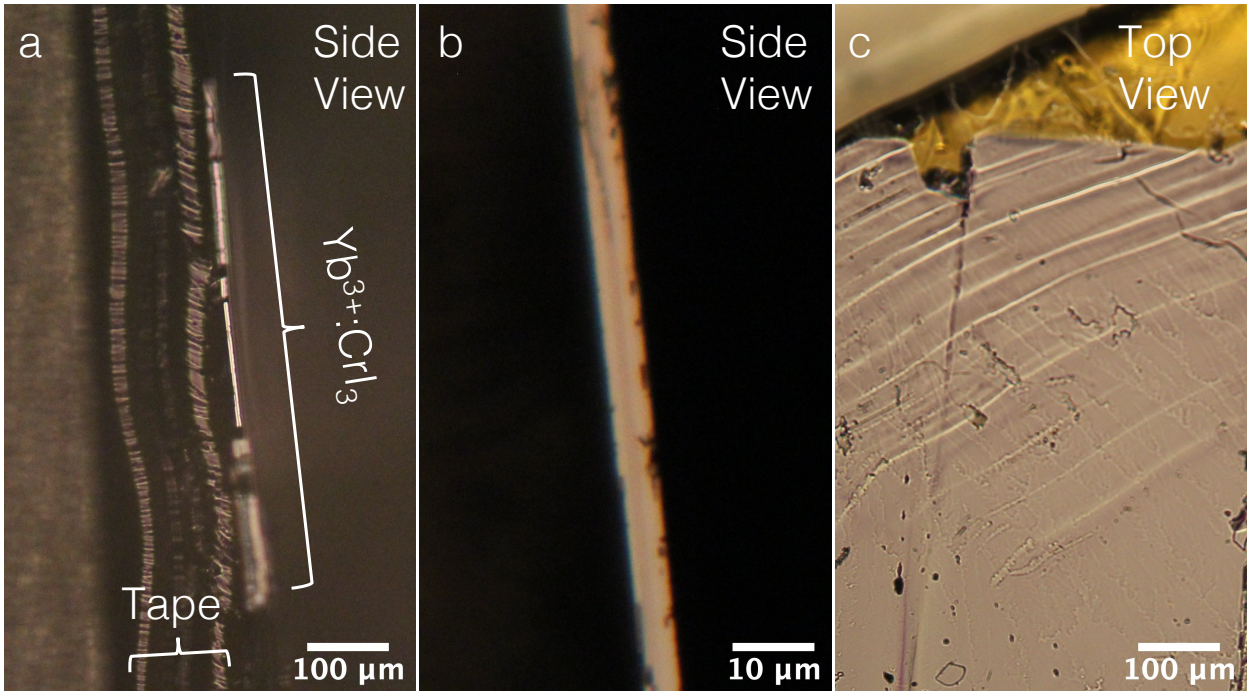

Figure 5.5 Images of an individual Yb^{3+}:CrI_3 single-crystal flake under an optical microscope at various magnification levels, viewing the flake's **(a,b)** edge, and **(c)** face. The flake thickness is estimated to be 5.1 ± 0.3 µm.

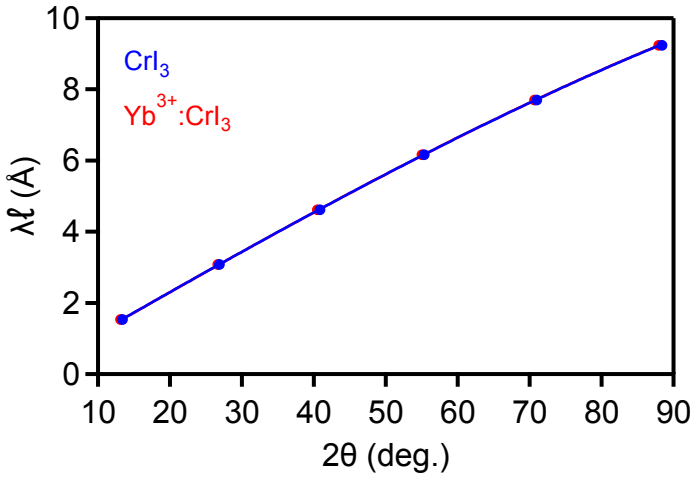

Figure 5.6 Analysis of XRD reflections collected using a powder diffractometer for 4.9% Yb^{3+}-doped and undoped CrI_3 single-crystal flakes (same data as shown in Figure 3.1bc). Using the method described by Jesche,[1] the lattice parameter *c* for oriented single crystals with a monoclinic space group can be extracted from XRD data from a powder diffractometer using the following equation:

$$2c \cdot \sin\beta \cdot \sin\left(\theta - S\frac{\cos\theta}{2}\right) = \lambda\ell \tag{B.1}$$

Here, β is the obtuse angle in the monoclinic unit cell (108.507° for CrI_3), λ is the x-ray wavelength (Cu, 1.5406 Å), ℓ is the Miller index of each reflection in the XRD spectrum and $S\frac{\cos\theta}{2}$ is a correction factor related to the displacement of the x-ray focal plane relative to the sample surface. Plotting 2θ values of the peak maxima *vs* $\lambda\ell$, the data can be fit using the equation above. For fitting, β and θ were taken in radians. By this method, the *c* lattice parameters were found to be 6.996 ± 0.002 and 7.013 ± 0.002 Å for the undoped and doped samples, respectively. From the lattice parameter *c*, the position of the (00ℓ) powder diffractometer XRD peaks for a monoclinic single crystal can be calculated using the following equation:

$$2\theta = 2\sin^{-1}\left(\frac{\lambda}{2\sin\beta}\frac{\ell}{c}\right) \tag{B.2}$$

The zero-shift in 2θ was determined by adding an offset to the experimental 2θ values and adjusting the offset to minimize the difference between experimental and calculated peak positions across all peaks in the XRD spectrum. This offset accounts for the measurement discrepancy due to the thickness of the single crystals displacing the x-ray focal plane. For CrI_3, a zero-shift of -0.015° was found, contrasted to a zero-shift of +0.164° for Yb^{3+}-doped CrI_3. The displacement-corrected XRD spectra are shown in Figure 3.1c in the chapter text.

Table B.1 Single-crystal X-ray diffraction data for 2.5% Yb^{3+}:CrI_3 measured at 263 K, compared to literature data for CrI_3.

	Yb^{3+}:CrI_3	CrI_3 (250 K, ref. [2])
Space group	C2/m	C2/m
a	6.86 Å	6.87 Å
b	11.89 Å	11.89 Å
c	6.99 Å	6.98 Å
α	90.0°	90.0°
β	108.7°	108.5°
γ	90.0°	90.0°
$[(Yb/Cr) - Cr]_{avg}$	3.96 Å	3.96 Å
$[(Yb/Cr) - I]_{avg}$	2.72 Å	2.72 Å
$[(Yb/Cr) - I - (Yb/Cr)]_{avg}$	93.3°	93.6°
$[I - (Yb/Cr) - I]_{avg}$	86.8°	86.9°

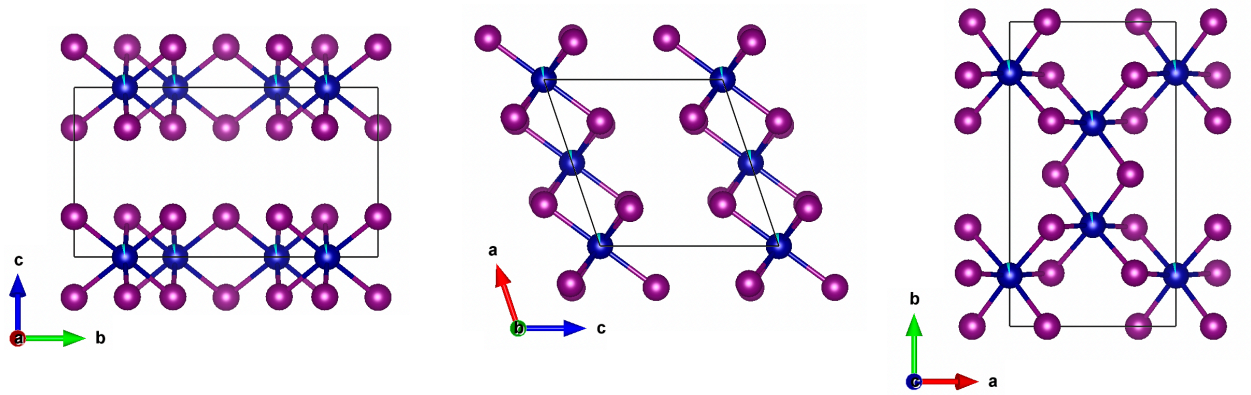

Figure 5.7 Visualization of the experimental room-temperature single-crystal XRD structure as viewed along the *a*, *b*, and *c* principal axes (left to right). Yb^{3+} (cyan) is found to substitute for Cr^{3+} (blue) in the edge-sharing octahedra formed by I^- (purple) anions. No excess electron density is observed between layers. Intralayer disorder is observed. The structure refines to the expected high-temperature *C2/m* monoclinic symmetry. Some intralayer disorder was observed (not shown).

B.2 Angular Overlap Model Calculations and Data

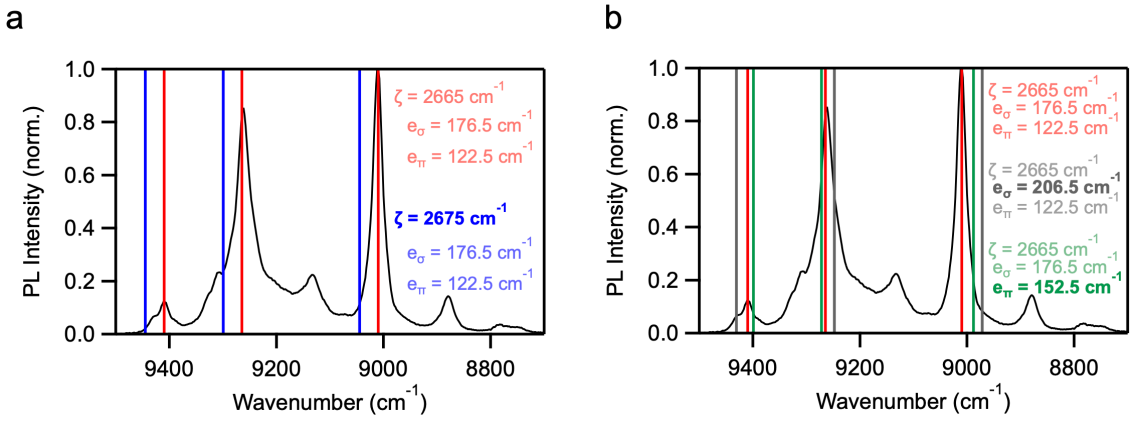

Figure 5.8 Comparison of the 5 K experimental data and calculated (AOM) *f-f* PL transition energies for 4.9% Yb^{3+}:CrI_3. A best fit to the experimental PL data resulted in the following values: ζ = 2665 cm^{-1} (330.4 meV), e_σ = 176.5 cm^{-1} (21.9 meV), e_π = 122.5 cm^{-1} (15.2 meV). The calculated transition energies using these parameters are shown as the vertical red lines in both panels. **(a)** Comparison of calculated transition energies obtained by changing from ζ = 2665 cm^{-1} (red) to ζ = 2675 cm^{-1} (blue), with all other parameters constant to the best-fit (red). **(b)** Comparison of calculated transition energies obtained by individually changing the values of e_σ and e_π. The gray traces show the effect of changing from e_σ = 176.5 cm^{-1} (red) to e_σ = 206.5 cm^{-1} with all other parameters constant to the best fit (red). The green traces show the effect of changing from e_π = 122.5 cm^{-1} (red) to e_π = 152.5 cm^{-1} with all other parameters constant to the best fit (red). From the best-fit parameters, g is anisotropic (g_1 = 2.672, g_2 = 2.686, g_3 = 2.642) and an average ground-state g value of ~2.7 is predicted.

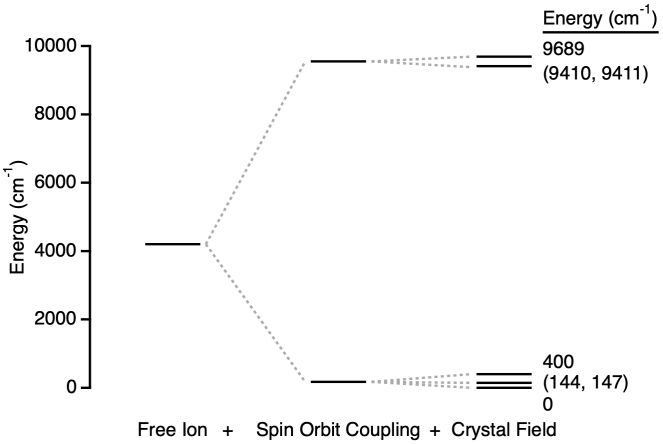

Figure 5.9 The Yb^{3+} valence energy level diagram described by the best-fit parameters of Figure 5.8. The energies of the crystal field states in eV are: 0.0000, (0.0179, 0.0182), 0.0496, (1.1667, 1.1668), 1.2013 eV.

Table B.2 Energies (cm^{-1}) of the valence electronic states, $^2F_{5/2}$ and $^2F_{7/2}$ barycenter energies,[a] and ΔE(Barycenter) for Yb^{3+} ions in several host crystals, and for the free ion. These data were used to generate Figure 5.10 (after converting to eV). Many of these entries are compiled in ref. [3].

Host Lattice	0	1	2	3	$^2F_{7/2}$ Barycenter	0'	1'	2'	$^2F_{5/2}$ Barycenter	ΔE(Bary)	ref.
$Ca_2Ga_2SiO_7$ (CGS)	0.0	300	490	970	440	10250	10570	11010	10610	10170	[4]
$SrLaGa_3O_7$ (SLG)	0.0	220	386	910	379	10190	10450	11025	10555	10176	[4]
$Ca_4GdO(BO_3)_3$ (GdCOB) (site I, Gd)	0.0	423	668	1003	524	10246	10706	11089	10680	10157	[5]
GdCOB (site II, Ca)	0.0	437	694	1003	534	10261	10737	11150	10716	10183	[5]
GdCOB (site III, Ca)	0.0	417	688	1003	527	10240	10682	11026	10649	10122	[5]
$Ca_4YO(BO_3)_3$ (YCOB)	0.0	427	556	1023	502	10242	10537	11109	10629	10128	[6]
Sc_2O_3	0.0	474	634	1076	546	10250	10640	11198	10696	10150	[7]
$Ca_5(PO_4)_3F$ (CFAP)	0.0	409	597	1099	526	10178	10496	11069	10581	10055	[8]
$Sr_5(PO_4)_3F$ (SFAP)	0.0	362	618	1190	543	10150	10512	11108	10590	10048	[9]
$Sr_5(VO_4)_3F$ (SVAP)	0.0	321	562	1078	490	10141	10740	11050	10644	10153	[10]
$Y_3Al_5O_{12}$ (YAG)	0.0	584	635	783	501	10328	10752	10917	10666	10165	[11]
$BaCaBO_3F$ (BCBF)	0.0	303	533	902	435	10204	10570	11000	10591	10157	[12]
$LiNbO_3$	0.0	352	448	788	397	10204	10471	11090	10588	10191	[13]
$KGd(WO_4)_2$ (KGW)	0.0	163	385	535	271	10188	10471	10682	10447	10176	[14]
$KY(WO_4)_2$ (KYW)	0.0	169	407	568	286	10187	10476	10695	10453	10167	[14]
$CaWO_4$	0.0	220	366	492	270	10278	10366	10665	10436	10167	[15]
$YAlO_3$	0.0	209	341	590	285	10220	10410	10730	10453	10168	[15]
$LiYF_4$	0.0	216	371	479	267	10288	10409	10547	10415	10148	[15]
$YAl_3(BO3)_4$ (YAB)	0.0	94	185	581	215	10194	10277	10672	10381	10166	[16]
$Cs_2NaYbCl_6$	0	225	225	573	256	10243	10243	10708	10398	10142	[17, 18]
$Cs_3Yb_2Br_9$	0.0	144	201	421	192	10277	10301	10578	10385	10194	[19]
$CsCdBr_3$	0.0	114	140	441	174	10119	10146	10590	10285	10111	[19]
$CuInS_2$	0.0	32	87	182	75	10033	10060	---	10095[a]	10020	[20]
InP	0	35.5	35.5	97.5	42	10018	10064	10064	10049	10007	[21]
Free ion	---	---	---	---	0.0	---	---	---	10213	10213	[22]
CrI_3	0.0	146	146	400	173	9410		---	9551[a]	9379	this work

[a]For the entire data set of complete entries, the ratio of $^2F_{5/2}$:$^2F_{7/2}$ CF splitting energies, (E($^2F_{5/2}$ Barycenter) - $E_{0'}$)/(E($^2F_{7/2}$ Barycenter)) is 0.82 ± 0.14. The $^2F_{5/2}$ barycenter energies for Yb^{3+}:CrI_3 and Yb^{3+}:$CuInS_2$ were thus set equal to the $^2F_{7/2}$ barycenter energies for the same compounds. The resulting uncertainties in ΔE(Bary) are estimated to be < ~1%, close to or smaller than the data points in Figure 5.10. For comparison, the Yb^{3+}:CrI_3 AOM calculations above yield: $^2F_{7/2}$ barycenter = 173 cm^{-1} (21 meV), $^2F_{5/2}$ barycenter = 9503 cm^{-1} (1.178 eV), ΔE (Bary) = 9330 cm^{-1} (1.157 eV), within this uncertainty range.

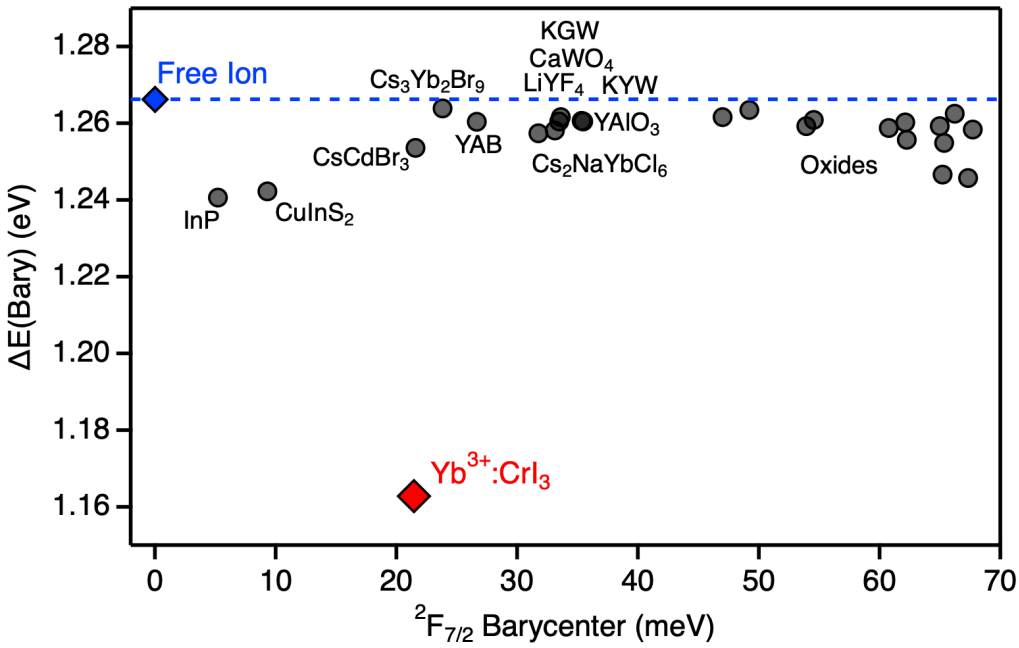

Figure 5.10 Plot of the difference between experimental Yb^{3+} $^2F_{5/2}$ and $^2F_{7/2}$ barycenter energies (ΔE(Bary)) for the compounds listed in Table B.2, and for the free ion, *vs* the barycenter energy for the $^2F_{7/2}$ ground multiplet. The compounds associated with select data points are labeled. The dashed blue line shows the value of the free ion.

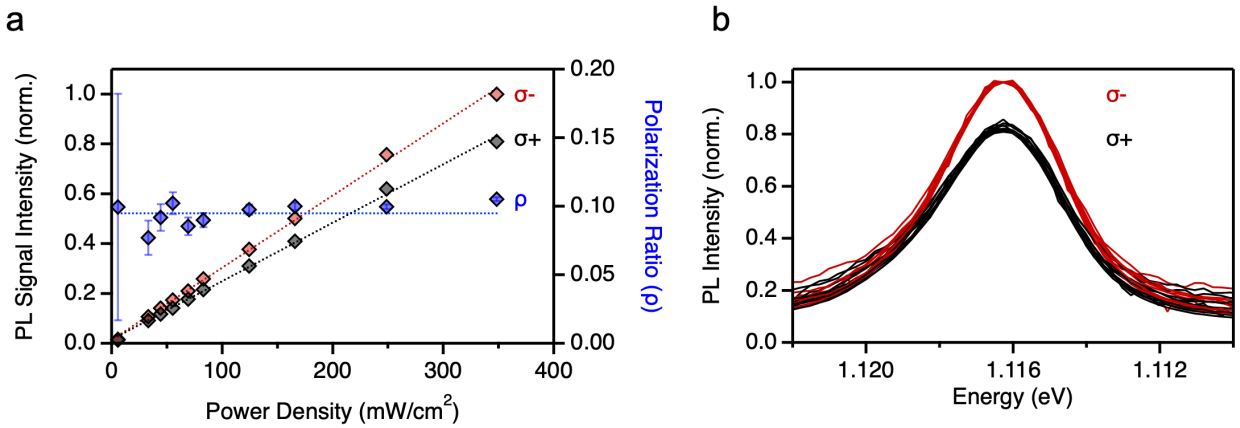

Figure 5.11 (a) Power dependence of σ^- (red) and σ^+ (black) PL peak intensities and circular polarization (ρ, blue) of the $\Gamma_8 \rightarrow \Gamma_7$ transition. The data were collected at 0.5 T and 5 K and the sample was excited with linearly polarized light at 1.96 eV. The PL intensities show a linear increase with power, resulting in a constant polarization ratio. The error bars represent uncertainty estimated from the linear fit of the polarization intensities. **(b)** The σ^- (red) and σ^+ (black) component of the $\Gamma_8 \rightarrow \Gamma_7$ transition normalized across all powers. The traces overlay each other well, showing no detectable power dependence.

B.3 Field-Dependent PL Spectroscopy and Vibrating Sample Magnetometry Data

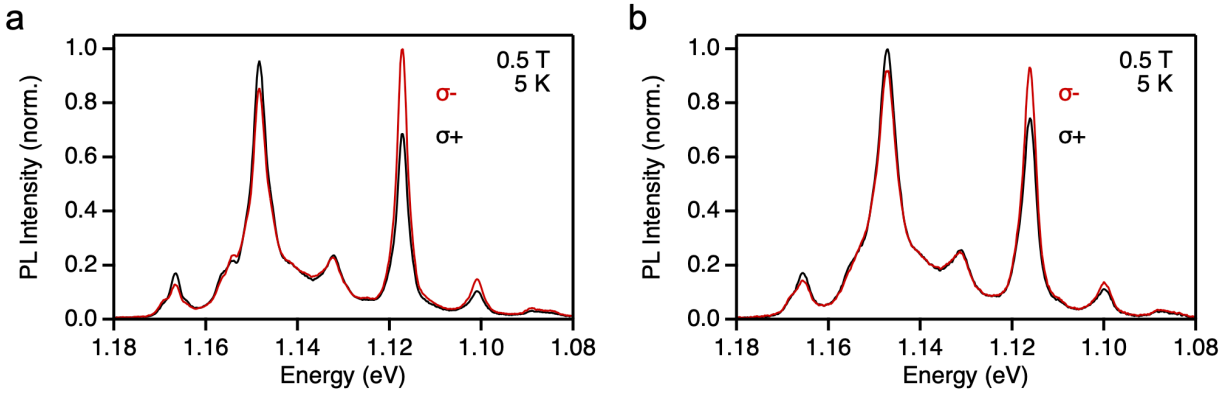

Figure 5.12 Comparison of full MCPL spectra across two different samples, measured at 0.5 T, 5 K. **(a)** The sample used in Figure 3.3b,c,e,f. **(b)** The sample used in Figure 3.3d. The two samples show very similar spectra, with slight differences in polarization magnitude.

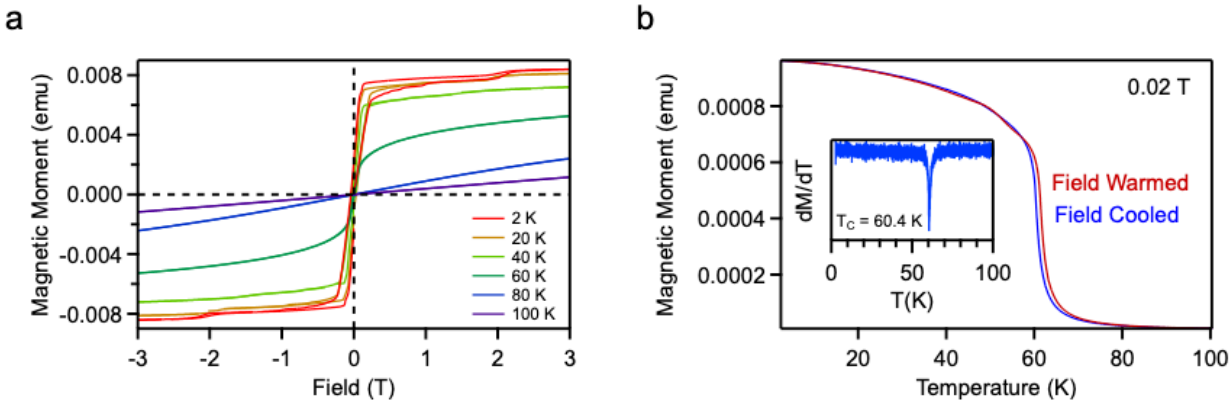

Figure 5.13 Magnetic data for a single-crystal flake of 5% Yb^{3+}:CrI_3, measured by VSM. The sample was probed with the external field aligned perpendicular to the face of the crystal. **(a)** Plots of magnetization vs external field measured at various temperatures. The data are similar to those collected on undoped CrI_3 bulk crystals (*e.g.*, Figure 5.14). At 2 K, a coercive field of ~44 mT was found. **(b)** Plot of magnetization *vs* temperature measured in the field-cooled and field-warmed directions. The inset shows the derivative of the field-cooled data as a function of temperature, where the Curie temperature is found to be 60.4 K. These data show that Yb^{3+} doping has no significant effect on the magnetism of CrI_3 in these samples.

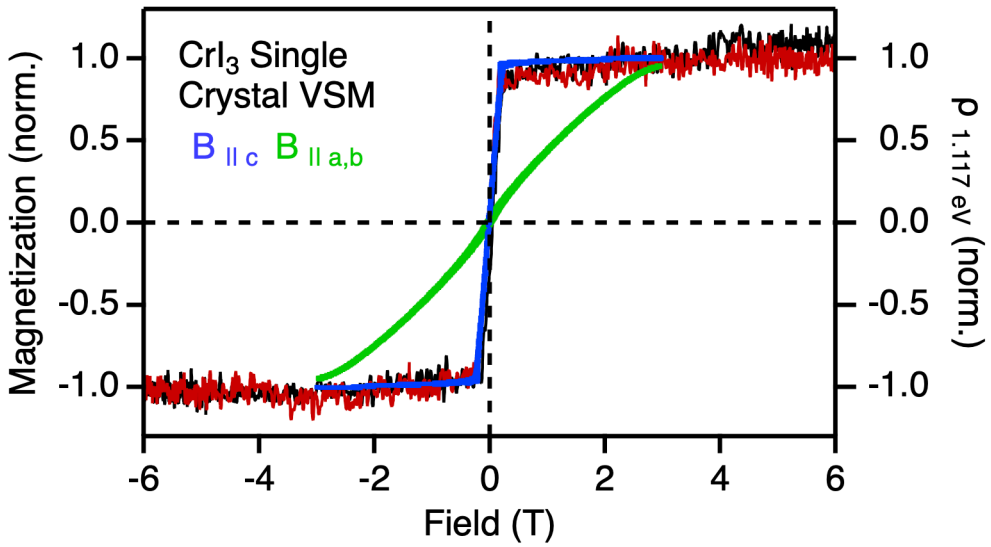

Figure 5.14 The same polarization data as featured in Figure 3.3d overlayed with CrI_3 magnetization data measured from -3 to +3 T with the field oriented parallel to the crystallographic *c* axis (blue) by single-crystal vibrating sample magnetometry (VSM).[23] For comparison, the magnetization perpendicular to *c* (green) is also shown. The Yb^{3+} MCPL polarization ρ is superimposable with the CrI_3 magnetization measured in the same configuration.

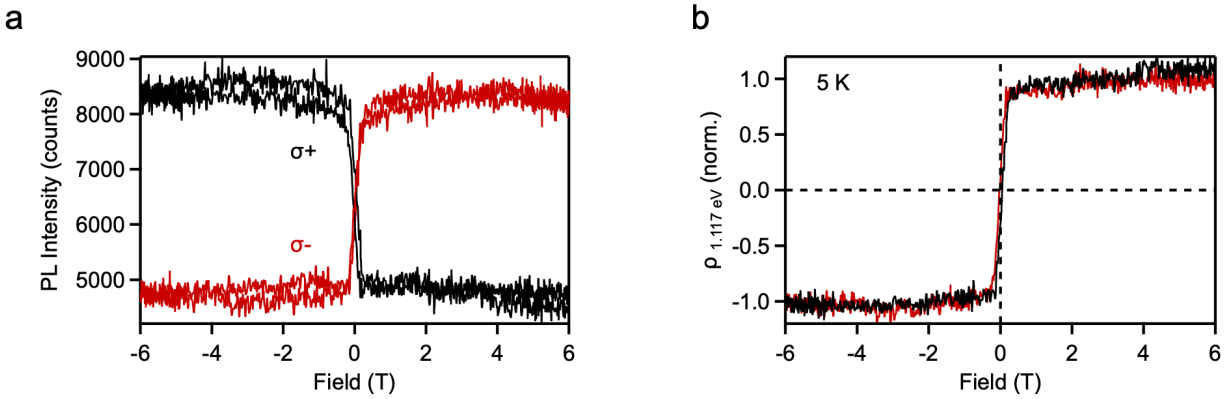

Figure 5.15 (a) Individual circularly polarized MCPL components measured during continuous field sweeps from -6 to +6 T and back at 5 K. (b) The same data, displayed as the polarization ratio (ρ, normalized). Panel (b) is shown as Figure 3.3d. Data measured using 14 mW/cm² excitation.

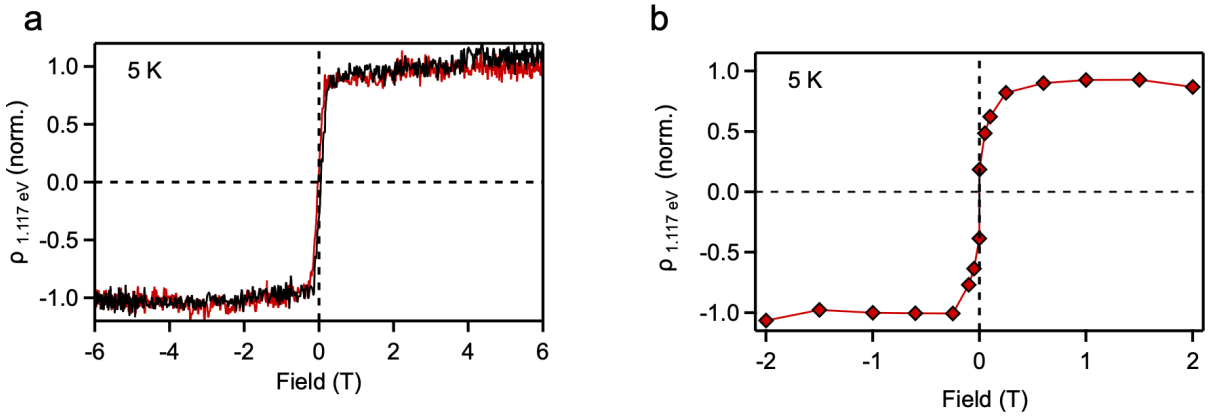

Figure 5.16 Comparison of field-dependent polarization ratios (ρ, normalized) measured with **(a)** linearly polarized and **(b)** unpolarized excitation at 5 K. In panel (b), no data were collected above 2 T. Panel (a) is shown as Figure 3.3d.

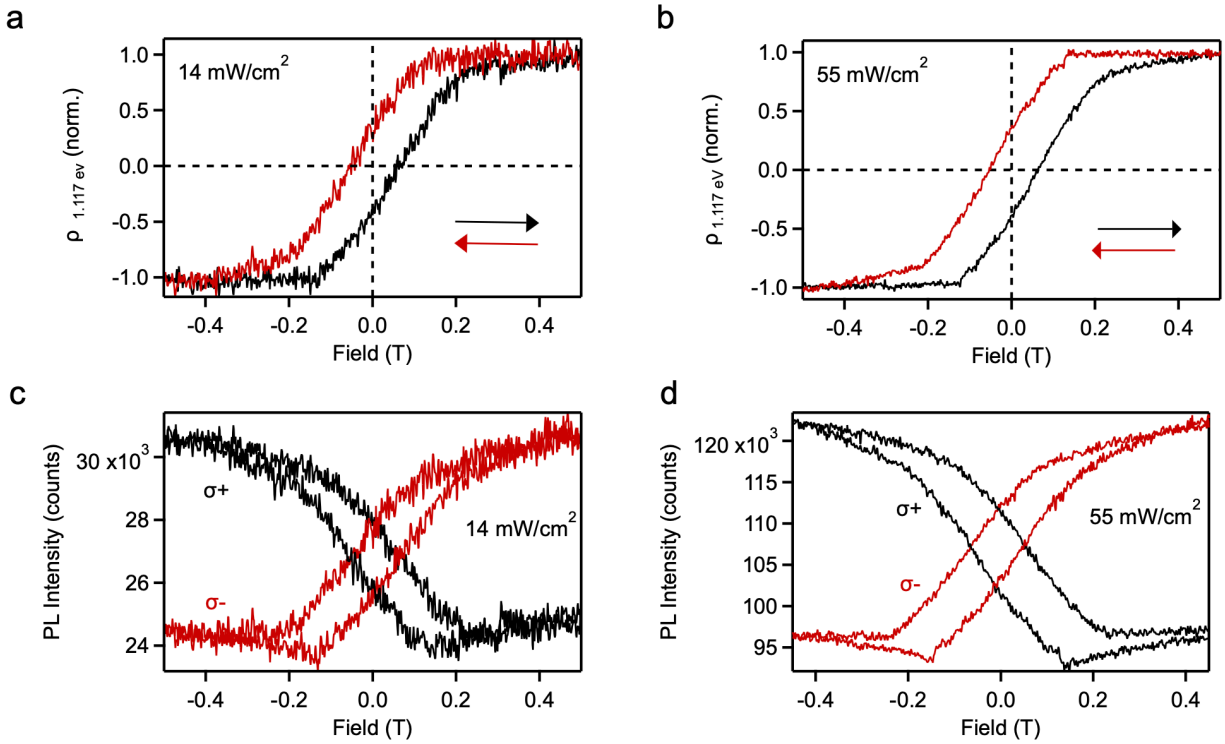

Figure 5.17 (a,b) Effect of excitation power on the polarization ratio (ρ, normalized). Magnetic hystereses measured under (a) low- and (b) higher-power excitation (14 *vs* 55 mW/cm², 5 K) show no difference. The black (red) trace corresponds to the sweep from negative (positive) to positive (negative) fields. **(c, d)** The separate circularly polarized PL components from the same (c) low- and (d) high-power measurements.

B.4 Zero-Field PL Spectroscopy

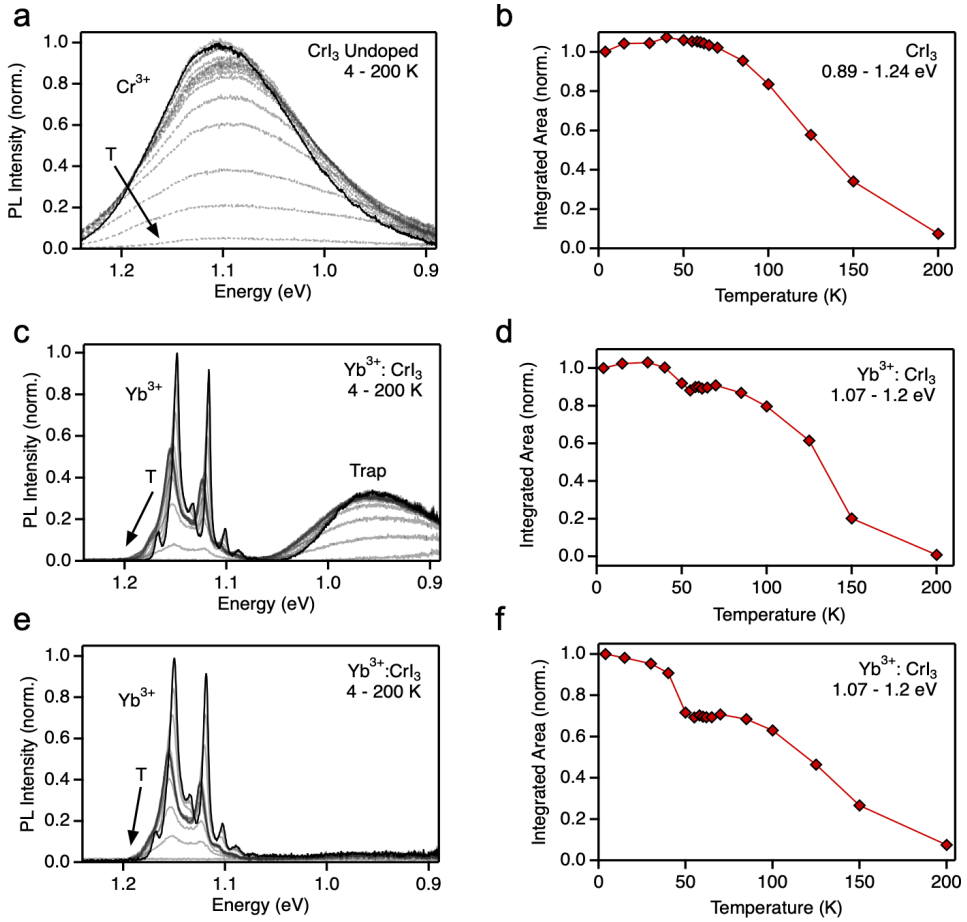

Figure 5.18 (a) Variable-temperature PL spectra of CrI_3 measured from 4 to 200 K under 1.88 eV CW excitation (from Figure 3.2). **(b)** Scatter plot depicting total integrated area of the CrI_3 PL from panel (a). The 200 K intensity is 7.5% that of the 4 K value. **(c)** Variable-temperature PL spectra of 4.9% Yb^{3+}:CrI_3 measured from 4 to 200 K under 1.88 eV CW excitation (from Figure 3.2). **(d)** Scatter plot depicting total integrated area of the Yb^{3+} PL from panel (c). The 200 K intensity is 0.8% that of the 4 K value. **(e)** Variable-temperature PL spectra of 5.0% Yb^{3+}:CrI_3 measured from 4 to 200 K under 1.88 eV CW excitation (from Figure 3.2). **(f)** Scatter plot depicting total integrated area of the Yb^{3+} PL from panel (e). The 200 K intensity is 7.5% that of the 4 K value. Note that a second, broad "trap" PL band is observed at ~0.98 eV in samples made from Cr metal powder precursor (99.94%, panel (c)) but not in samples made from Cr chip precursor (99.995%, panel (e)). Ni is the primary impurity in the powder precursor (see Section 3.5 Experimental Methods), and Ni is detected in this CrI_3 sample at 0.4% cation mole fraction. Ni^{2+} $^3A_{2g} \rightarrow {}^3T_{2g}$ absorption in NiI_2 and Ni^{2+}:CdI_2 is centered around 0.93 eV,[24] and the broad "trap" PL band in panel (c) is thus tentatively attributed to Ni^{2+} impurities in CrI_3.

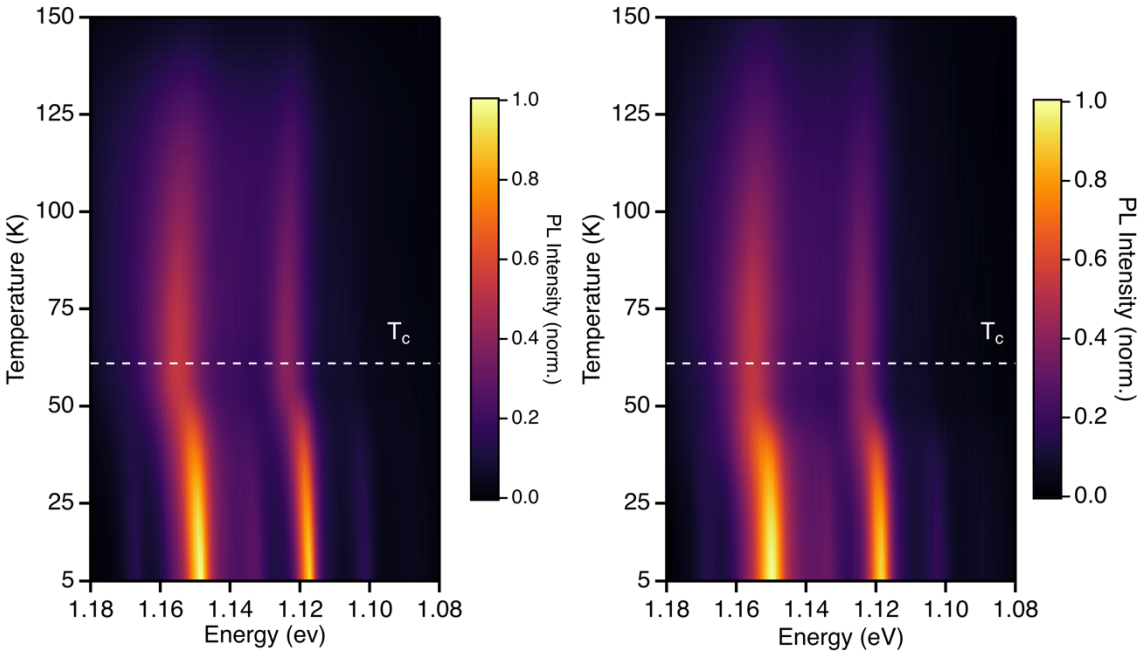

Figure 5.19 (a,b) False-color plots of the Yb^{3+} PL intensities *vs* temperature measured for the two samples shown in Figure 5.18c,e, respectively, from 4 to 150 K at zero external magnetic field. The horizontal dashed line indicates T_C = 61 K. The two samples show the same temperature dependence, but the features are slightly better resolved in panel (a). Panel (a) is shown as Figure 3.4a.

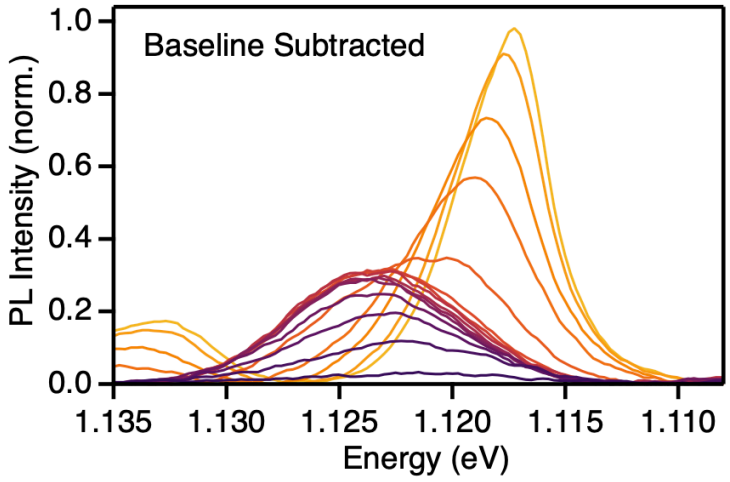

Figure 5.20 Temperature dependence of the $\Gamma_8 \rightarrow \Gamma_7$ PL feature of 4.9% Yb^{3+}:CrI_3 measured from 4 to 200 K under no external magnetic field (from Figure 3.4, T = 4, 15, 30, 40, 50, 55, 58, 60, 62, 65, 70, 85, 100, 125, 150 K). A linear baseline was subtracted from each spectrum here to facilitate viewing and determination of the peak's FWHM.

B.5 References

(1) Jesche, A. F., M.; Kreyssig, A.; Meier, W. R.; Canfield, P. C. X-Ray Diffraction on large single crystals using a powder diffractometer. *Philos, Mag. (Abingdon)* **2016**, *96* (20), 2115-2124.

(2) McGuire, M. A.; Dixit, H.; Cooper, V. R.; Sales, B. C. Coupling of Crystal Structure and Magnetism in the Layered, Ferromagnetic Insulator CrI_3. *Chem. Mater.* **2015**, *27* (2), 612-620.

(3) Haumesser, P.-H.; Gaumé, R.; Viana, B.; Antic-Fidancev, E.; Vivien, D. Spectroscopic and crystal-field analysis of new Yb-doped laser materials. *J. Phys.: Cond. Mat.* **2001**, *13* (23), 5427-5447.

(4) Simondi-Teisseire, B. PhD Thesis. Paris VI University, 1996.

(5) Mougel, F.; Dardenne, K.; Aka, G.; Kahn-Harari, A.; Vivien, D. Ytterbium-doped $Ca_4GdO(BO_3)_3$: an efficient infrared laser and self-frequency doubling crystal. *J. Opt. Soc. Am. B* **1999**, *16* (1), 164-172.

(6) Mougel, F. PhD Thesis. Paris VI University, 1999

(7) Mix, E. PhD Thesis. Hamburg University, 1999.

(8) DeLoach, L. D.; Payne, S. A.; Chase, L. L.; Smith, L. K.; Kway, W. L.; Krupke, W. F. Evaluation of absorption and emission properties of Yb^{3+} doped crystals for laser applications. *IEEE J. Quant. Elect.* **1993**, *29* (4), 1179-1191.

(9) Gruber, J. B.; Zandi, B.; Merkle, L. Crystal-field splitting of energy levels of rare-earth ions $Dy^{3+}(4f^9)$ and $Yb^{3+}(4f^{13})$ in M (II) sites in the fluorapatite crystal $Sr_5(PO_4)_3F$. *J. Appl. Phys.* **1998**, *83* (2), 1009-1017.

(10) Payne, S. A.; DeLoach, L. D.; Smith, L. K.; Kway, W. L.; Tassano, J. B.; Krupke, W. F.; Chai, B. H. T.; Loutts, G. Ytterbium-doped apatite-structure crystals: A new class of laser materials. *J. Appl. Phys.* **1994**, *76* (1), 497-503.

(11) Bogomolova, G. A.; Bumagina, L. A.; Kaminskii, A. A.; Malkin, B. Z. Crystal field in laser garnets with TR^{3+} ions in the exchange charge model. *Sov. Phys. Solid State* **1977**, *19* (8), 1428-1435.

(12) Schaffers, K. I.; DeLoach, L. D.; Payne, S. A. Crystal growth, frequency doubling, and infrared laser performance of Yb^{3+}: $BaCaBO_3F$. *IEEE J. Quant. Elect.* **1996**, *32* (5), 741-748.

(13) Montoya, E.; Sanz-Garcıa, J.; Capmany, J.; Bausá, L.; Diening, A.; Kellner, T.; Huber, G. Continuous wave infrared laser action, self-frequency doubling, and tunability of Yb^{3+}: MgO: $LiNbO_3$. *J. Appl. Phys.* **2000**, *87* (9), 4056-4062.

(14) Kuleshov, N. V.; Lagatsky, A. A.; Podlipensky, A. V.; Mikhailov, V. P.; Huber, G. Pulsed laser operation of Yb-doped $KY(WO_4)_2$ and $KGd(WO_4)_2$. *Optics lett.* **1997**, *22* (17), 1317-1319.

(15) Morrison, C. A.; Leavitt, P. Handbook on the physics and chemistry of rare earths, ch 46. Amsterdam: Elsevier: 1982.

(16) Wang, P.; Dawes, J. M.; Dekker, P.; Knowles, D. S.; Piper, J. A.; Lu, B. Growth and evaluation of ytterbium-doped yttrium aluminum borate as a potential self-doubling laser crystal. *J. Opt. Soc. Am. B* **1999**, *16* (1), 63-69.

(17) Schwartz, R. W. Electronic Structure of the Octahedral Hexachloroytterbate Ion. *Inorg. Chem.* **1977**, *16* (7), 1694-1698.

(18) Kanellakopulos, B.; Amberger, H. D.; Rosenbauer, G. G.; Fischer, R. D. Zur

Elektronenstruktur hochsymmetrischer Verbindungen der Lanthanoiden und Actinoiden—V: Paramagnetische Suszeptibilität und elektronisches Raman-Spektrum von $Cs_2NaYb(III)Cl_6$. *J. Inorg. Nuc. Chem.* **1977**, *39* (4), 607-611.

(19) Malkin, B. Z.; Leushin, A. M.; Iskhakova, A. I.; Heber, J.; Altwein, M.; Moller, K.; Fazlizhanov, I. I.; Ulanov, V. A. EPR and optical spectra of Yb^{3+} in $CsCdBr_3$: Charge-transfer effects on the energy-level structure of Yb^{3+} in the symmetrical pair centers. *Phys. Rev. B* **2000**, *62* (11), 7063.

(20) Tsujii, N.; Imanaka, Y.; Takamasu, T.; Kitazawa, H.; Kido, G. Photoluminescence of Yb^{3+}-Doped $CuInS_2$ Crystals in Magnetic Fields. *J. Appl. Phys.* **2001**, *89* (5), 2706-2710.

(21) de Maat-Gersdorf, I. Spectroscopic Analysis of Erbium-Doped Silicon and Ytterbium Doped Indium Phosphide. University of Amsterdam, 2001.

(22) Wyart, J.-F.; Tchang-Brillet, W.-Ü. L.; Spector, N.; Palmeri, P.; Quinet, P.; Biémont, E. Extended Analysis of the Spectrum of Triply-ionized Ytterbium (Yb IV) and Transition Probabilities. *Phys. Scripta* **2001**, *63* (2), 113-121.

(23) De Siena, M. C.; Creutz, S. E.; Regan, A.; Malinowski, P.; Jiang, Q.; Kluherz, K. T.; Zhu, G.; Lin, Z.; De Yoreo, J. J.; Xu, X.; et al. Two-Dimensional van der Waals Nanoplatelets with Robust Ferromagnetism. *Nano Lett.* **2020**, *20* (3), 2100-2106.

(24) Kuindersma, S. R.; Boudewijn, P. R.; Haas, C. Near-Infrared d–d Transitions of NiI_2, CdI_2:Ni^{2+}, and CoI_2. *Phys. stat. sol. (b)* **1981**, *108* (1), 187-194.

Appendix C *Supplementary Information for Chapter 4* – Optically Resolved Exchange Splittings from Strong Impurity-Lattice Magnetic Coupling in the van der Waals Ferromagnet $Yb^{3+}:CrBr_3$

C.1 Additional Zero-Field PL Spectroscopy

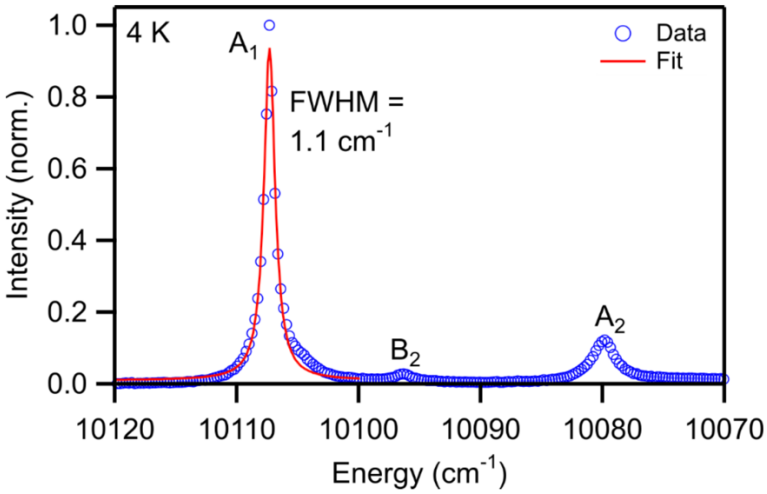

Figure 5.21 Zoom-in on the 0′ → 0 transition in the 4 K PL spectrum of $Yb^{3+}:CrBr_3$ collected at a spectral bandwidth of 0.002 nm. A Lorentzian fit of peak A_1 (red) gives a full width at half max (FWHM) of 1.1 cm^{-1} (0.14 meV).

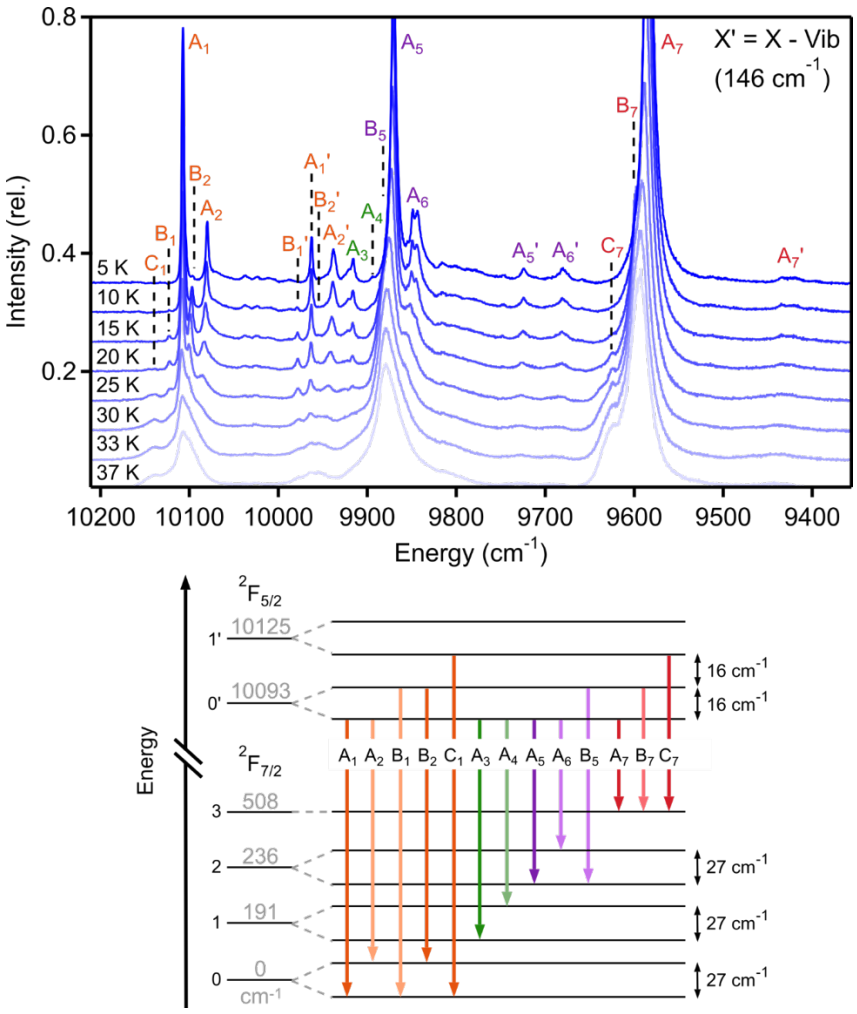

Figure 5.22 Full assignment of the Yb^{3+}:$CrBr_3$ PL spectrum. At 5 K, only the lowest-energy excited state (0′) is populated and only peaks labeled A are observed. As the temperature increases, B peaks arise from the higher-energy spin level of the exchange-split 0′ state. At even higher temperatures, C peaks appear, arising from the 1′ excited state. At a fixed energy spacing of ~145 cm^{-1} from the purely electronic transitions, vibronic transitions are observed. These peaks are labeled with a prime (′). Another set of vibronic peaks is possibly observed between the main and primed peaks. The 5 and 20 K spectra are plotted on a logarithmic y-axis in Figure 5.23 below.

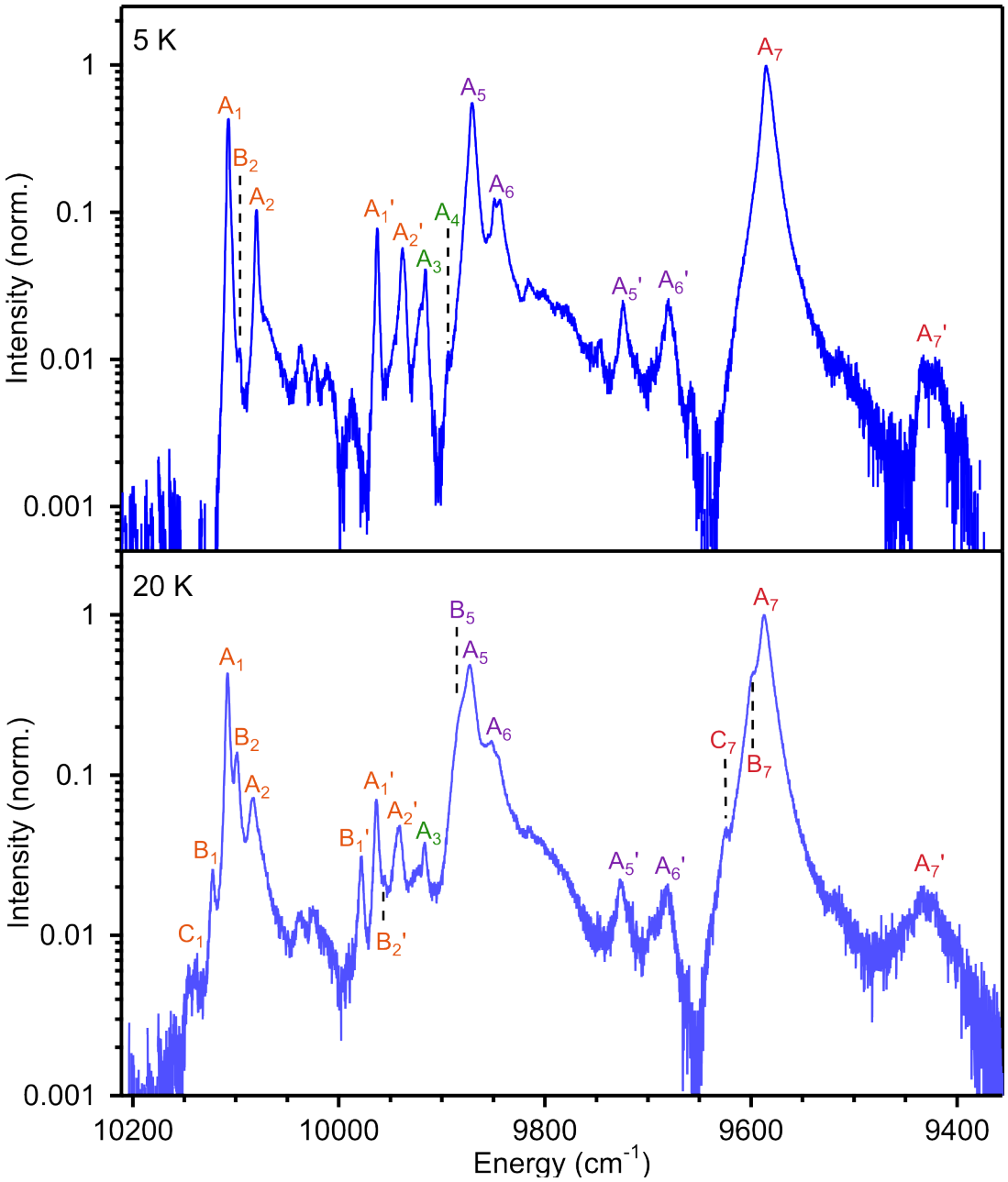

Figure 5.23 Full Yb^{3+}:$CrBr_3$ PL spectrum collected at 5 K (top) and 20 K (bottom), plotted on a logarithmic y-axis to facilitate identification of weak peaks. Peaks are labeled according to the diagram shown in Figure 5.22.

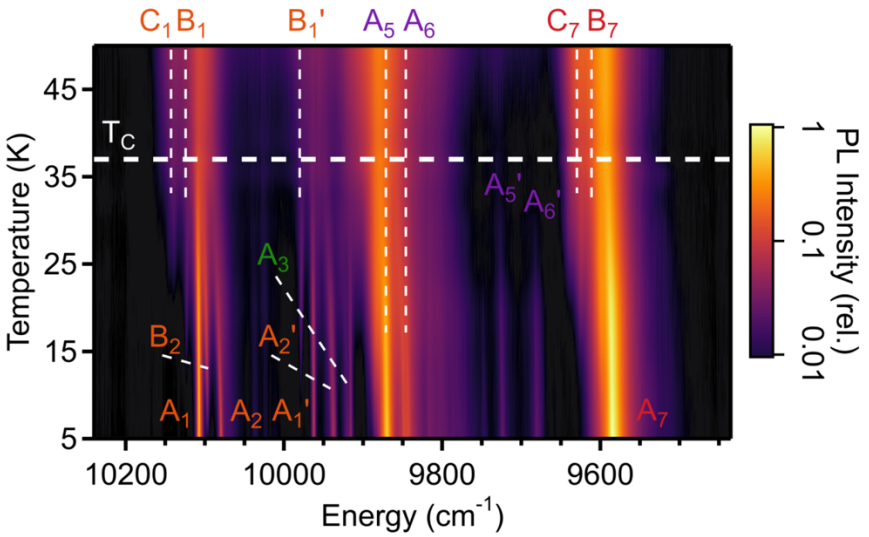

Figure 5.24 False-color plot of the $Yb^{3+}:CrBr_3$ (0.4 %) spectrum plotted versus temperature. At higher temperatures, the center of mass of the peaks blueshifts due to the appearance of hot bands.

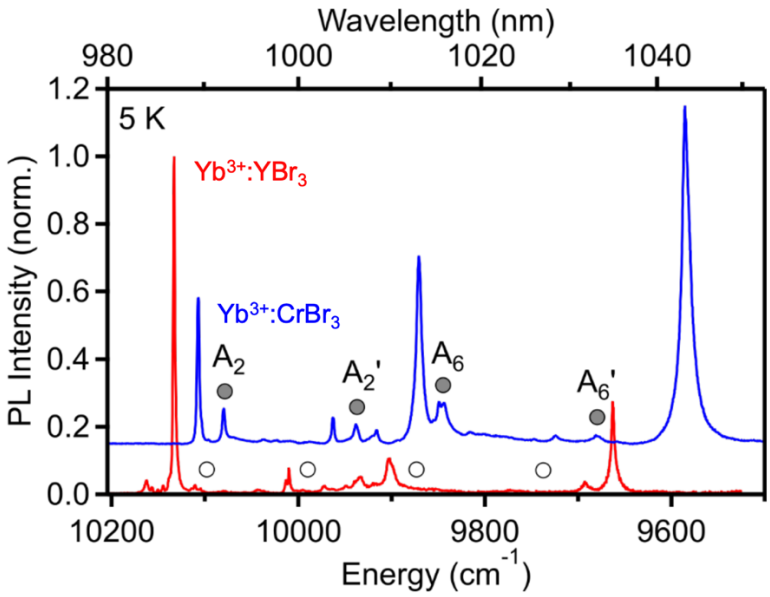

Figure 5.25 K PL spectra of $Yb^{3+}:CrBr_3$ (blue) and $Yb^{3+}:YBr_3$ (red). Several peaks associated with exchange splitting are indicated by filled circles for $Yb^{3+}:CrBr_3$. Prime symbols (′) indicate vibronic features. The absence of the corresponding peaks in the non- magnetic $Yb^{3+}:YBr_3$ is indicated by empty circles. The $Yb^{3+}:CrBr_3$ spectrum is offset vertically for easier comparison.

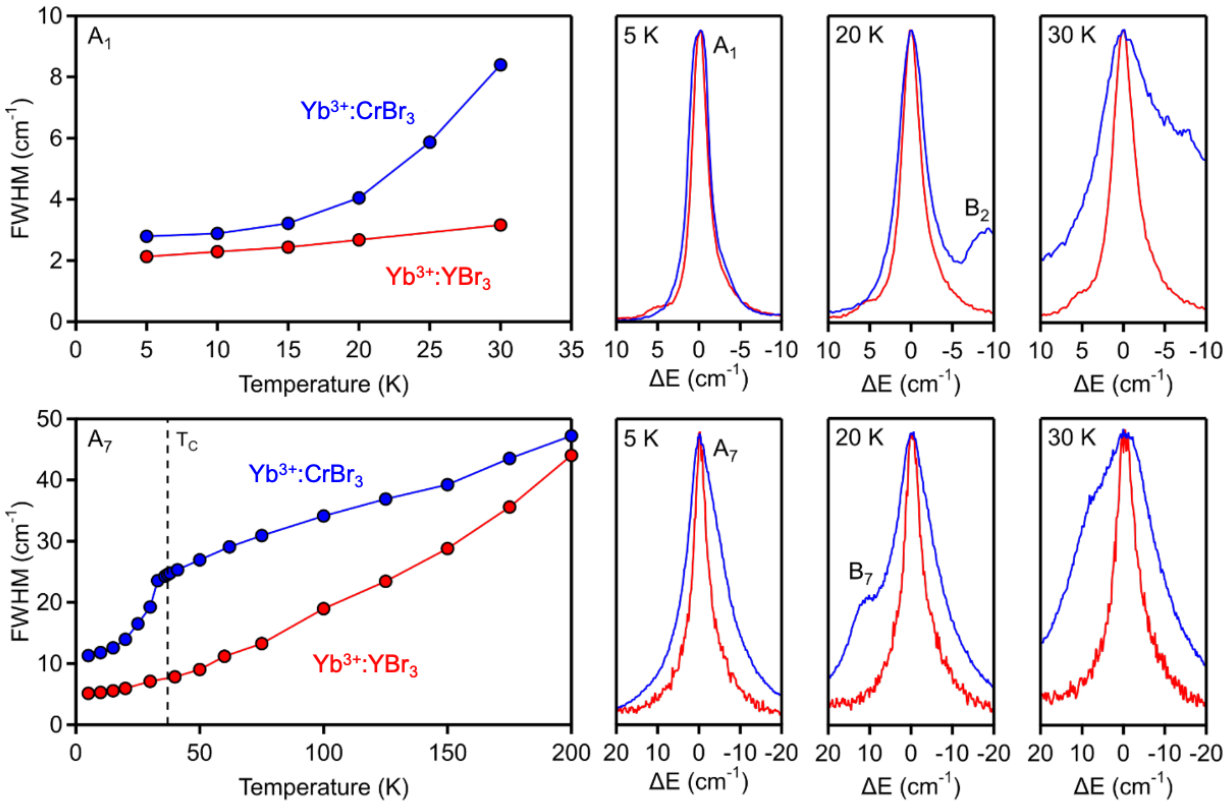

Figure 5.26 Top: Comparison of the full width at half maximum (FWHM) of the highest- energy peak (A_1) in both $Yb^{3+}:CrBr_3$ 0.4% (blue) and $Yb^{3+}:YBr_3$ (red) at various temperatures. The $Yb^{3+}:CrBr_3$ FWHM increases more rapidly than that of $Yb^{3+}:YBr_3$ due to spin fluctuations. Offset spectra of both are shown at select temperatures for visual comparison. Above ~30 K, the $Yb^{3+}:CrBr_3$ A_1 peak broadening is too large to quantify reliably. **Bottom:** FWHM of the lowest-energy peak (A_7) in both $Yb^{3+}:CrBr_3$ 0.4% (blue) and $Yb^{3+}:YBr_3$ (red) at various temperatures. A clear discontinuity is seen at T_C in the $Yb^{3+}:CrBr_3$ FWHM that is attributed to magnetic ordering of the Cr^{3+} lattice. The reduction in Cr^{3+} nearest-neighbor spin fluctuations results in a sharpening of the Yb^{3+} peaks at lower temperatures. The absence of peaks B_2 (top) and B_7 (bottom) in the $Yb^{3+}:YBr_3$ spectrum is further evidence that the $Yb^{3+}:CrBr_3$ spin states are split via exchange interactions (see Figure 5.22 for peak assignment). Note that unlike the A_1 peak, the exchange splitting of this A_7 peak in $Yb^{3+}:CrBr_3$ is not resolved and its temperature dependence is thus embedded in these linewidths.

C.2 Additional Field-Dependent PL Spectroscopy

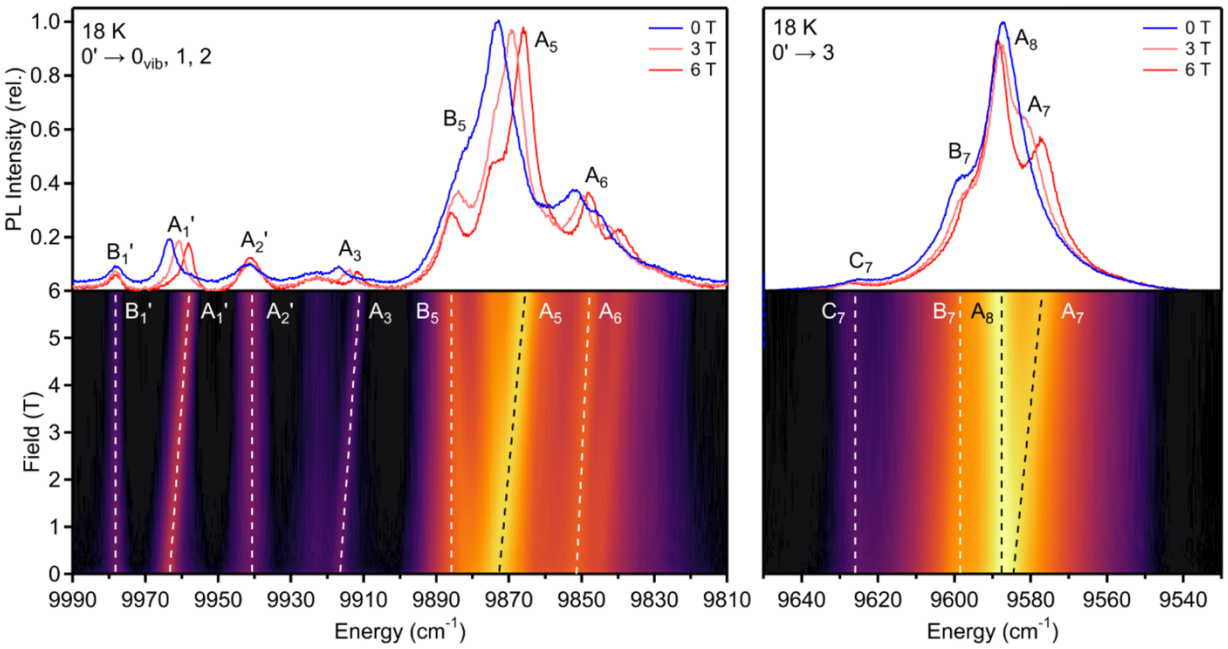

Figure 5.27 Top: PL spectra of Yb^{3+}:$CrBr_3$ 0.4% measured in the region of the 0′ → 0_{vib}, 1, 2, and 3 transitions at 18 K and at various external magnetic fields (B_{ext} | | c). **Bottom**: False- color plots of the PL in the same region vs B_{ext}. See Figure 5.22 for peak assignments. Note that peaks A_7 and A_8 are (nearly) degenerate ($\Delta E_{exch} \approx 0$ cm^{-1}) at B_{ext} = 0 T and both are labeled together as A_7 in other figures, where only a single peak is visible. At higher external magnetic field, the degeneracy is lifted and A_7 shifts to lower energies like the other odd-value A peaks, while A_8 stays in place like the even-value A peaks.

Appendix D *Supplementary Information for Chapter 5* – Exciton Annihilation by Lanthanide Dopants: An Atomic Probe of Sub-Diffraction Exciton Diffusion in Ferromagnetic CrI_3

D.1 Additional PL Spectroscopy

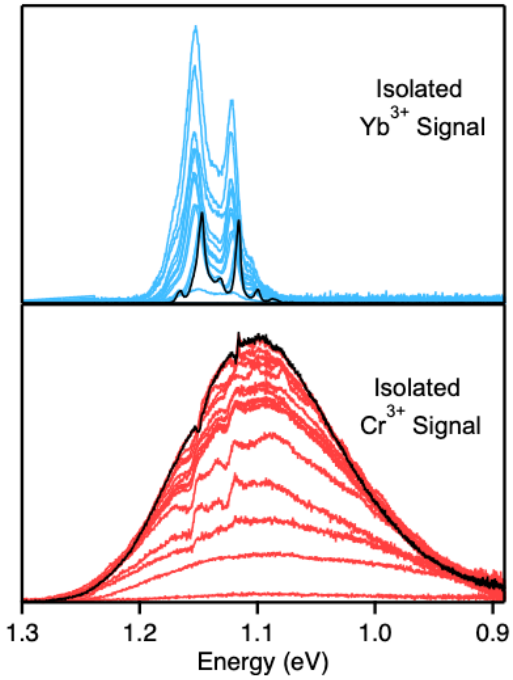

Figure 5.28 VTPL spectra of the same 0.2% Yb^{3+}:CrI_3 sample described Chapter 5, deconvoluted into Yb^{3+} (blue) and Cr^{3+} (red) components. To separate the two PL components, the 18.6% Yb^{3+}:CrI_3 PL spectrum, which features only Yb^{3+} PL, was scaled and subtracted from the 0.2% spectra, giving the two data sets plotted here. The integrated intensities of these spectra are plotted in Figure 5.4e,f. The same deconvolution procedure was performed for the 1.6% Yb^{3+}:CrI_3 sample.

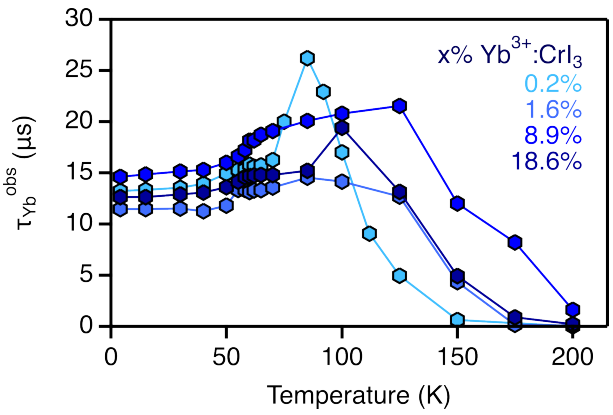

Figure 5.29 Plot of Yb^{3+} PL decay times *vs* temperature for *x*% Yb^{3+}:CrI_3 (*x* = 0.2, 1.6, 8.9, 18.6), collected with CrI_3 photoexcitation.

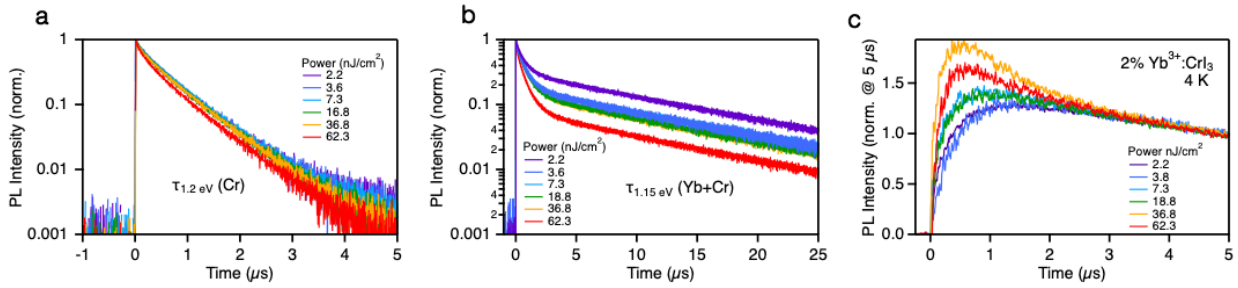

Figure 5.30 Normalized PL decay curves for 1.6% Yb^{3+}:CrI_3 measured as a function of excitation power. PL was measured at **(a)** 1.20 eV, representing CrI_3 emission (Cr^{3+}), and **(b)** 1.15 eV, representing a superposition of CrI_3 and Yb^{3+} emission (Yb^{3+} + Cr^{3+}), respectively. With increasing excitation power, the relative contribution of the Yb^{3+} emission decreases, likely due to Yb^{3+} PL saturation. **(c)** Yb^{3+}-only PL decay curves for each excitation power density, found by scaling and subtracting the data in panel (a) from the data in panel (b) at the same power (See Chapter 5). The rise time for the Yb^{3+} PL decreases with increasing excitation power, consistent with increased probabilities of Cr^{3+} exciton capture by Yb^{3+} at increased excitation densities. All time-resolved PL data reported in the main text were collected using the lowest power density of 2 nJ/cm², corresponding to one absorbed photon per ~7 × 10^6 Cr^{3+} ions (see D.4 Calculation of Excitation Density).

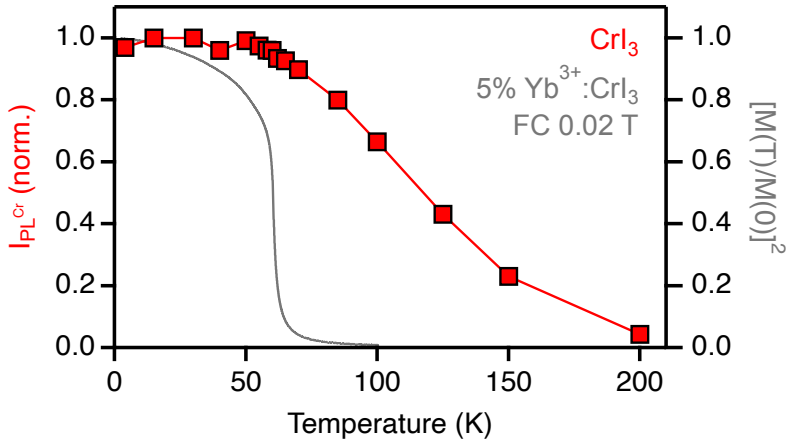

Figure 5.31 Comparison of the integrated PL intensity of undoped CrI_3 (red) with the lattice magnetization measured in using a magnetic field of 0.02 T applied parallel to the crystal's c-axis. Magnetization is plotted as the infinite spin-correlation function, represented by $[(M(T)/M(0)]^2$. The lattice magnetization decreases rapidly before reaching near zero at T_C = 61 K, whereas I_{PL} shows a different and more graduate change extending to much higher temperatures. This comparison provides no indication of correlation between PL intensity and spin order. The magnetization data are taken from Pressler *et al.*[1]

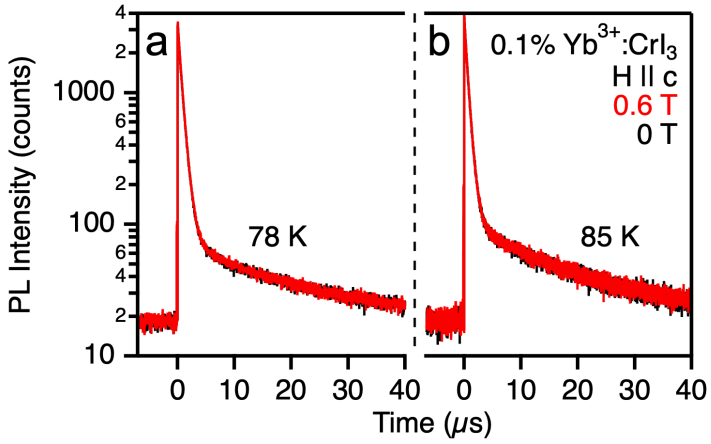

Figure 5.32 (a) 78 K and **(b)** 85 K PL decay curves of 1% Yb^{3+}:CrI_3 measured at 1.20 eV showing a superposition of Cr^{3+} and Yb^{3+} PL signals. Data were collected using a 40 ps, 50 Hz pulsed laser excitation source at 2.33 eV. The black traces correspond to no applied external field, while the red traces correspond to a 0.6 T field applied parallel to the crystal's c-axis. At 78 K (just above T_C), the change in lattice magnetization is appreciable with 0.6 T,[2] but there is no discernible difference in the decay dynamics upon application of the external field. These data show no indication of any sensitivity of exciton diffusion to lattice spin ordering. A similar result is obtained at 85 K.

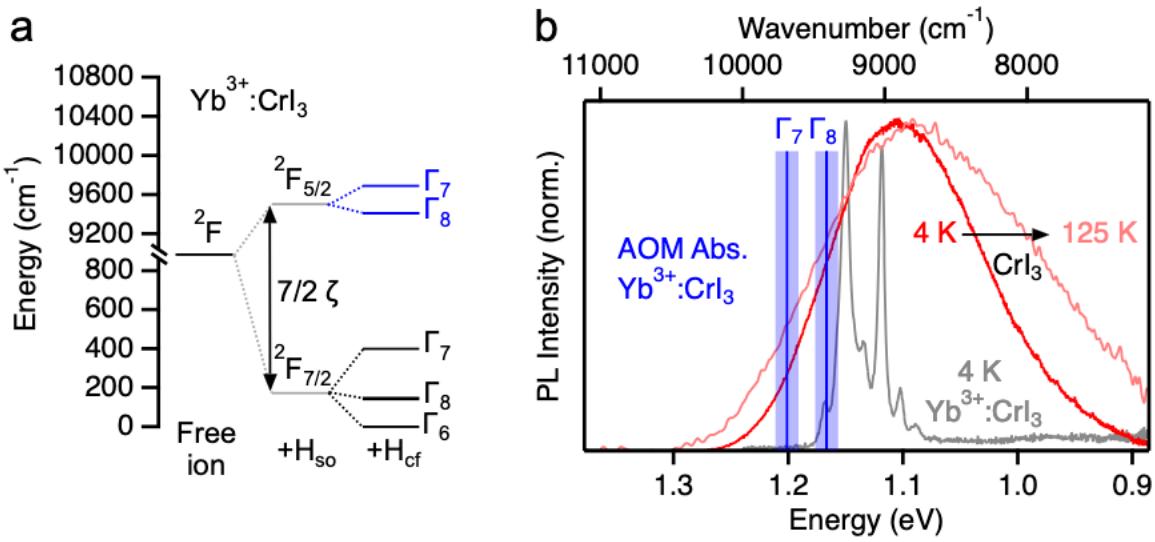

Figure 5.33 (a) *f*-shell spin-orbit and crystal-field splittings for Yb^{3+} dopants in CrI_3, calculated using the Angular Overlap Model (AOM). See Snoeren[3] for calculation details. The calculated energies of the Γ_7 and Γ_8 excited crystal-field states are shown in blue in panel b. **(b)** PL spectrum of undoped CrI_3 at 4 K (red) and 125 K (pink) and of 18.6% Yb^{3+}:CrI_3 at 4 K (grey), plotted together with the calculated energies of the Yb^{3+} Γ_7 and Γ_8 excited states (blue). The Yb^{3+} excited states lie in a region of broad donor Cr^{3+} PL at both low and high temperatures, resulting in resonant $Cr^{3+} \rightarrow Yb^{3+}$ energy transfer with a spectral overlap factor that is largely temperature-independent.

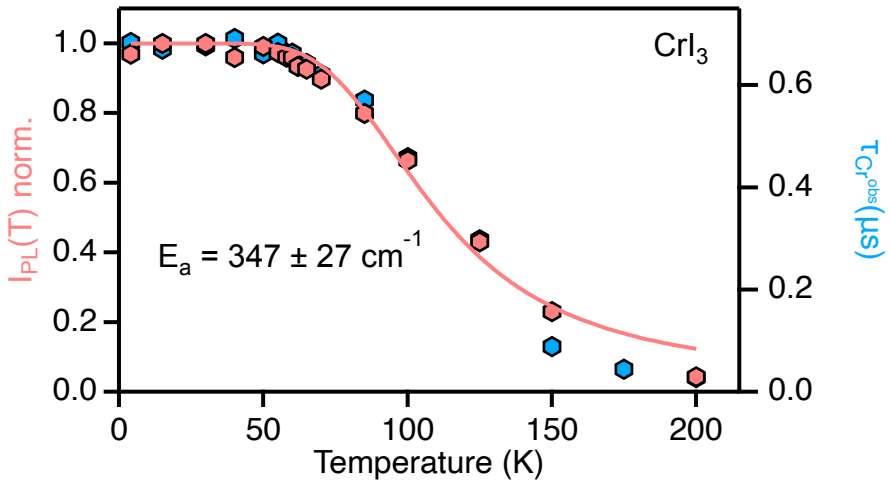

Figure 5.34 CrI_3 integrated PL intensities (red) and Cr^{3+} PL decay times (blue) plotted *vs* temperature. The solid red curve plots the best fit of the integrated PL data to an Arrhenius function: $I_{PL}(T) = (I_0/(1+a^*\exp(-E_a/(k_BT))))$, yielding E_a = 347 ± *27* cm^{-1}. The two data sets show the same temperature dependence.

D.2 Additional Monte Carlo Simulation Details

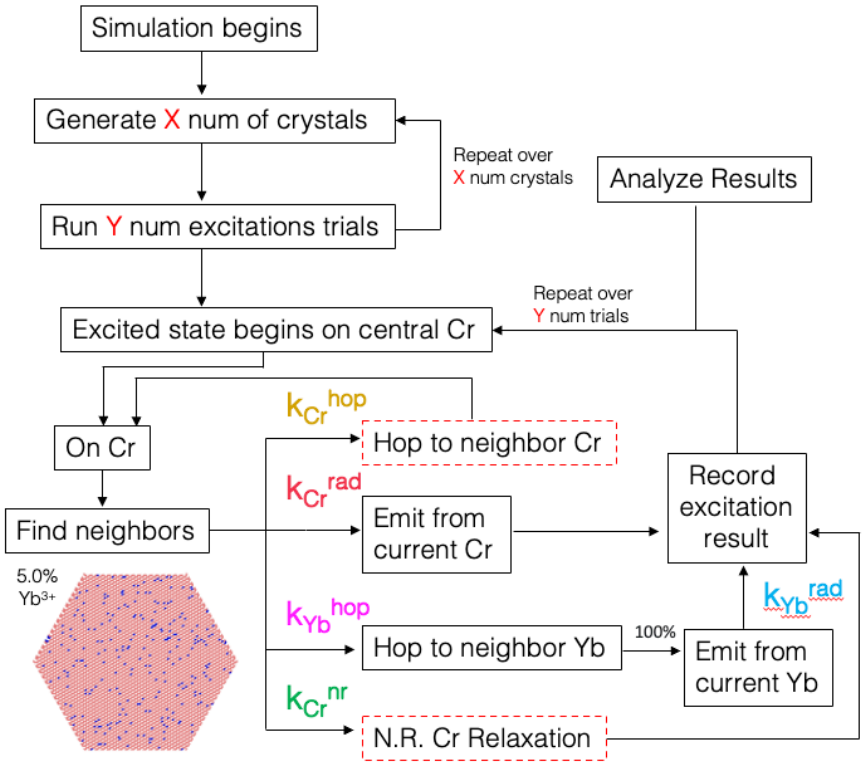

Figure 5.35 Flowchart of the Monte Carlo simulation, with a single simulated lattice depicted for reference. See 5.6 Experimental Methods for details. The processes outlined in red are temperature dependent. The data shown in Chapter 5 are from simulations of over 250 crystals at every given doping level, each with 250 excitation trials at every given temperature, for a total of 62,500 simulated excitons for each doping level at each temperature.

Table D.1 Rate constants and their values determined by Kinetic Monte Carlo simulations.

Simulation parameter	4 K rate constant (s^{-1})	200 K rate constant (s^{-1})
k_{Cr}^{rad}	1.9×10^6	temperature independent
k_{Cr}^{nr}	~0	9.9×10^6
k_{Cr}^{hop}	1.0×10^7	6.8×10^7
k_{Yb}^{rad}	1.1×10^7	temperature independent
k_{Yb}^{hop}	2.0×10^8	temperature independent

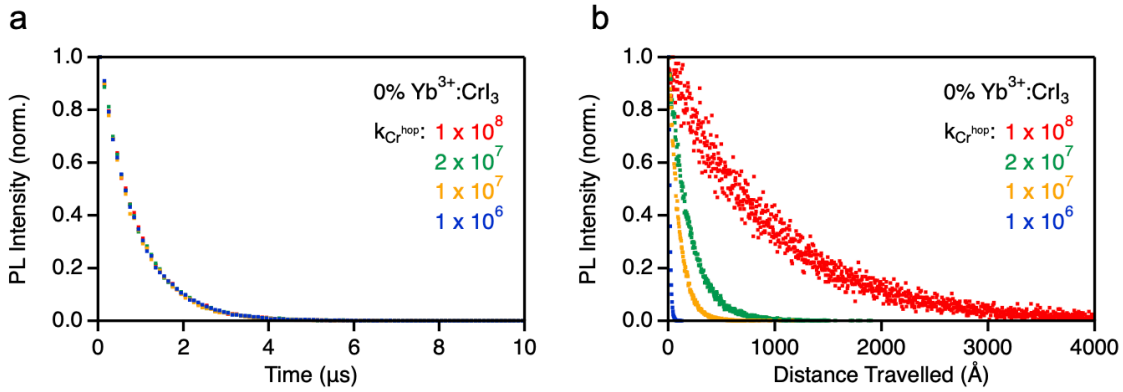

Figure 5.36 (a) Simulated PL decay curves for undoped CrI_3 at 4 K, calculated for various values of k_{Cr}^{hop}. The PL decay curves are all indistinguishable because emission events from different Cr^{3+} ions are statistically independent of one another, and the ensemble decay therefore does not depend on exciton hopping. **(b)** The same data as in panel (a), but now plotted *vs* the exciton's distance traveled. With increasing k_{Cr}^{hop}, the exciton travels further from its point of inception. This dependence allows determination of k_{Cr}^{hop} *via* simulation of PL data for different Yb^{3+} doping levels. See Chapter 5 and Figure 5.6b.

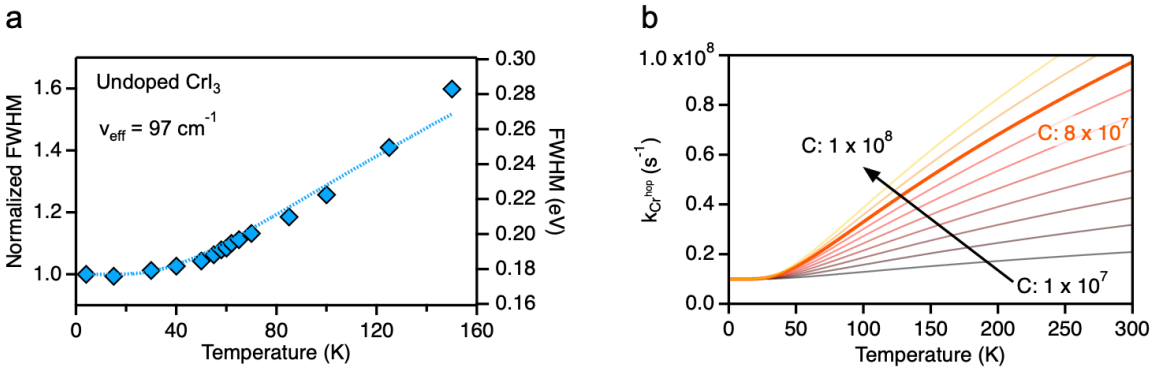

Figure 5.37 (a) Temperature dependence of the FWHM of the undoped CrI_3 PL, normalized to its low-temperature value. Following harmonic oscillator theory and assuming linear coupling to a single distortion coordinate, the PL full width at half maximum (FWHM) can be fit to eq (D.1).[4] The best-fit value for v_{eff} (dotted curve) was found to be 97 cm^{-1}. **(b)** Plot of eq (D.2) (eq (5.11) of Chapter 5) for various values of the scaling parameter *C*. The bolded orange line ($C = 8 \times 10^7\ s^{-1}$) corresponds to the value that best reproduces the experimental data (Figure 5.7).

$$FWHM(T) = FWHM(0)\left[\coth\left(\frac{\upsilon_{eff}}{2k_BT}\right)\right]^{1/2} \tag{D.1}$$

$$k_{Cr}^{hop}(T) = C\left[\left[\coth\left(\frac{\upsilon_{eff}}{2k_BT}\right)\right]^{\frac{1}{2}} - 1\right] + k_{Cr}^{hop}(0) \tag{D.2}$$

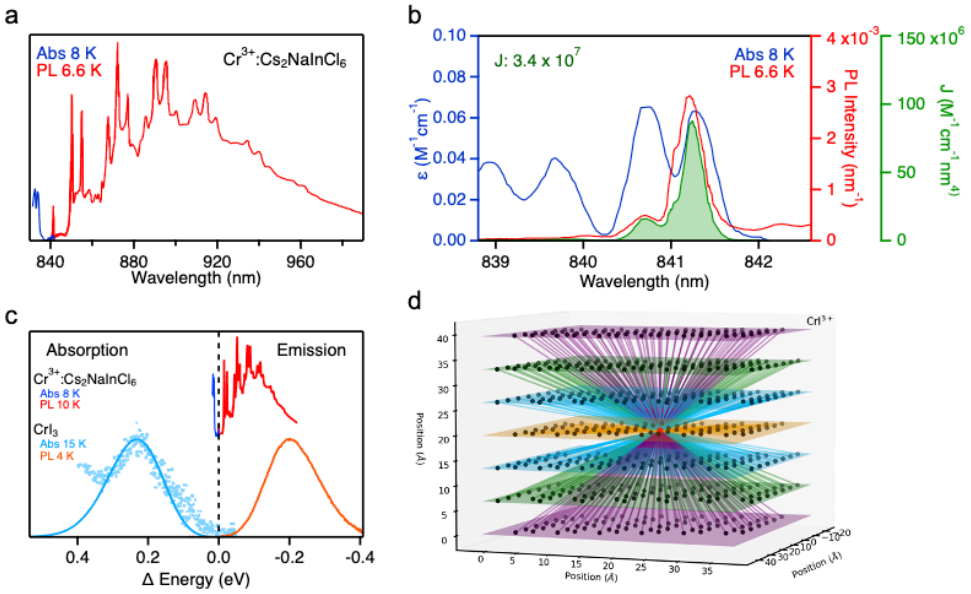

Figure 5.38 (a) Low-temperature PL (red) and absorption (blue) spectra of Cr^{3+}:$Cs_2NaInCl_6$, digitized from Güdel and Snellgrove.[5] **(b)** The overlap region of the absorption (blue) and PL (red) spectra of Cr^{3+}:$Cs_2NaInCl_6$, and the calculated spectral overlap (green). **(c)** Comparison of the low-temperature spectral overlap in Cr^{3+}:$Cs_2NaInCl_6$ and CrI_3. For CrI_3, the absorption is digitized from Seyler *et al.* and the PL is from this work.[6] **(d)** Depiction of the positions of 557 Cr^{3+} ions within a 7-layer CrI_3 crystal of 32 unit cells. Atomic positions were determined from the low-temperature rhombohedral R-3H crystal structure (a = b = 6.867 Å, c = 19.807 Å, ICSD Coll. Code 251655).[7] The colored lines represent the distances from a central Cr^{3+} ion (red) to all other Cr^{3+} ions. These distances were used calculate the FRET rate constants shown in Table D.2 as described in Section D.3.

Table D.2 Calculated ET rate constants.

Energy transfer process	Rate constant (s^{-1})
Intra-layer Dexter NN (3.69 Å)	1.00×10^7
Intra-layer FRET NN (3.69 Å)	7.73×10^4
Intra-layer FRET	1.41×10^5
1st Inter-layer FRET NN (6.87 Å)	1.87×10^3
1st Inter-layer FRET	1.32×10^4
2nd Inter-layer FRET	7.73×10^2
3rd Inter-layer FRET	1.25×10^2
Total 1st - 3rd Inter-layer FRET	1.41×10^4
Total Intra- + Inter-layer FRET	1.56×10^5

D.3 Calculation of Cr^{3+}-Cr^{3+} Energy Transfer and FRET Rate Constants

For k_{Cr}^{hop}, two possible mechanisms of energy transfer are considered: through-space multipolar Förster resonant energy transfer (FRET) and through-bond Dexter energy transfer (DET), both of which may be present. The rate constants for each process are given by eq (D.3) and (D.4), respectively.

$$k_{FRET} = 0.02108 \frac{\theta^2 Q_D J}{n^4} \left(\frac{1}{r}\right)^6 \frac{1}{\tau_D} \tag{D.3}$$

$$k_{DET} = KJ' exp\left[\frac{-2r}{L}\right] \tag{D.4}$$

For FRET, θ^2 is the donor acceptor dipole orientation factor, Q_D is the quantum yield of the donor PL, J is the spectral overlap integral defined in eq (D.5), n is the refractive index of the lattice (1.94 at 1000 nm in CrI_3),[8] τ_D is the donor PL decay time (837 ns in CrI_3), and r is the distance between the donor and acceptor. For DET K is a constant describing the magnitude of the donor-acceptor electronic coupling, J' is the spectral overlap integral defined in eq (D.6), r is the separation between donor and acceptor, and L is the sum of their van der Waals radii.

$$J = \int \bar{f}_D(\lambda) \varepsilon_A(\lambda) \lambda^4 d\lambda \tag{D.5}$$

$$J' = \int \bar{f}_D(\lambda) \bar{\varepsilon_A}(\lambda) d\lambda \tag{D.6}$$

Here $\bar{f}_D(\lambda)$ represents the area-normalized donor emission spectrum, $\varepsilon_A(\lambda)$ the acceptor molar extinction coefficient, and $\bar{\varepsilon_A}(\lambda)$ the area-normalized acceptor molar extinction coefficient.

Although both DET and FRET contain a spectral overlap component, an important distinction lies in how the spectral overlap integrals (J or J') are calculated. For FRET, J is calculated as the overlap integral of the donor luminescent spectrum normalized to a unit area, and the acceptor extinction, whereas in J' both the donor luminescence spectrum and acceptor extinction spectrum are normalized by area.[9] Accordingly, the rate of dipole-dipole FRET depends on the oscillator strengths of both the donor and accepter transitions, whereas the rate of DET does not depend on these oscillator strengths and only requires the existence of such states resonant in energy.

Because all variables in eq (D.3) can be determined experimentally, we sought to estimate the contribution of FRET to Cr^{3+}-Cr^{3+} ET at low temperature. In CrI_3, strong electron-phonon coupling

and a large ~400 meV Stokes shift result in extremely low J, and all overlap results solely from the weak electronic origins (see Figure 5.4g). To estimate J(4K) and FRET(4K) in CrI_3, we used the reference compound Cr^{3+}:$Cs_2NaInCl_6$,[5] which displays Cr^{3+} emission from pseudo-octahedral $CrCl_6^3$ and has resolvable electronic origins in both its absorption and PL spectra. Figure 5.38c compares the relevant spectra for CrI_3 and Cr^{3+}:$Cs_2NaInCl_6$. Using eq (D.3) along with the high-resolution PL (red trace in Figure 5.38b) and extinction (blue trace in Figure 5.38b) spectra, J was estimated to be 3.4 x 10^7 $M^{-1}cm^{-1}nm^4$ in Cr^{3+}:$Cs_2NaInCl_6$. Because of the greater Stokes shift, this value is considered to provide an upper bound for the value of J in CrI_3.

To assess the importance of FRET in CrI_3, distances were determined from a central Cr^{3+} ion to 557 Cr^{3+} ions within a 7-layer CrI_3 crystal consisting of 32 unit cells (Figure 5.38d). These distances were then used to calculate individual FRET rate constants from that central ion to each other Cr^{3+} ion of this crystal, and the results are summarized in Table D.2. In addition to using an upper bound for J in CrI_3 (see above), these FRET calculations used favorable values of 1.0 for Q_D and 2/3 for θ^2. The results in Table D.2 thus represent upper bounds for the FRET rate constants.

As seen in Table D.2, all calculated FRET rate constants are orders of magnitude smaller than the nearest neighbor hopping rate constant of k_{Cr}^{hop} = 1.00 x 10^7 s^{-1} determined in Chapter 5. This comparison supports the conclusion that energy migration in CrI_3 proceeds through intralayer DET.

D.4 Calculation of Excitation Density

To estimate the experimental excitation densities in CrI_3, we first find the number of photons hitting the sample in each excitation pulse. The sample was excited by a 532 nm laser with energy density of 2.0 nJ/cm^2 over a spot size with a diameter of 1.0 mm. The energy of one 532 nm excitation photon is given by eq (D.7):

$$E = \frac{hc}{\lambda} = \frac{(6.63 \times 10^{-34}\, J \cdot s)(2.998 \times 10^{8}\, m/s)}{532 \times 10^{-9}\, m} = 3.74 \times 10^{-19}\, J/photon \qquad \text{(D.7)}$$

The density of photons per excitation pulse is thus:

$$\frac{2.0 \times 10^{-9}\, J/cm^2}{3.74 \times 10^{-19} J/photon} = 5.3 \times 10^9\, photons/cm^2 \quad \text{(D.8)}$$

Over the excitation spot size, this gives:

$$5.3 \times 10^9 \frac{photons}{cm^2} * \pi(0.050\ cm)^2 = 4.2 \times 10^7\, photons \quad \text{(D.9)}$$

The penetration depth (z) of the excitation pulse corresponds to the distance at which the light intensity falls to $1/e$ (~37%) of its initial value and can be found using the material's extinction (attenuation) coefficient $\kappa(\lambda)$ at the light's wavelength. Using the value of 1.19 cm^{-1} for κ at 532 nm in CrI_3,[10] z is given by eq (D.10):

$$I(z) = I_0\, e^{-4\pi\kappa(\lambda)z/\lambda_0} \rightarrow \frac{I(z)}{I_0} = \frac{37}{100} = e^{-4\pi\kappa(\lambda)z/\lambda_0} \rightarrow z = \frac{\ln(\frac{37}{100})}{-4\pi\kappa(\lambda)/\lambda_0} = 3.5 \times 10^{-6} cm \quad \text{(D.10)}$$

This penetration depth corresponds to ~50 layers of CrI_3. Given the excitation spot size, this gives a volume of:

$$V = \pi r^2 l = \pi(0.050\ cm)^2(3.5 \times 10^{-6} cm) = 2.7 \times 10^{-8} cm^3 \quad \text{(D.11)}$$

From the density of CrI_3, this volume corresponds to 1.9×10^{14} total Cr^{3+} ions:

$$4.94 \frac{g}{cm^3} * \frac{6.02 \times 10^{23}\ ions}{432.96\ g} * 2.7 \times 10^{-8} cm^3 = 1.9 \times 10^{14}\ ions \quad \text{(D.12)}$$

Within this volume, 63% of the photons are absorbed, giving:

$$\frac{1.9 \times 10^{14}\ Cr\ ions}{(0.63) * 4.2 \times 10^7\ photons} = 7.2\ \times 10^6\ Cr\ ions/exciton \quad \text{(D.13)}$$

At such low excitation densities, exciton-exciton annihilation is deemed negligible.

D.5 References

(1) Pressler, K.; Snoeren, T. J.; Walsh, K. M.; Gamelin, D. R. Magnetic Amplification at Yb^{3+} "Designer Defects" in the van der Waals Ferromagnet CrI_3. *Nano Lett.* **2023**, *23* (4), 1320-1326.

(2) Liu, Y.; Petrovic, C. Three-dimensional magnetic critical behavior in CrI_3. *Phys. Rev. B* **2018**, *97* (1), 014420.

(3) Snoeren, T. J.; Pressler, K.; Kluherz, K. T.; Walsh, K. M.; De Yoreo, J. J.; Gamelin, D. R. Luminescence and Covalency in Ytterbium-Doped CrX_3 (X = Cl, Br, I) van der Waals Compounds. *J. Am. Chem. Soc.* **2023**, *145* (31), 17427-17434.

(4) Gamelin, D. R.; Bominaar, E. L.; Mathonière, C.; Kirk, M. L.; Wieghardt, K.; Girerd, J.-J.; Solomon, E. I. Excited-State Distortions and Electron Delocalization in Mixed-Valence

Dimers: Vibronic Analysis of the Near-IR Absorption and Resonance Raman Profiles of $[Fe_2(OH)_3(tmtacn)_2]^{2+}$. *Inorg. Chem.* **1996**, *35* (15), 4323-4335.

(5) Güdel, H. U.; Snellgrove, T. R. Jahn-Teller effect in the $^4T_{2g}$ state of chromium(III) in dicesium sodium indium(III) hexachloride. *Inorg. Chem.* **1978**, *17* (6), 1617-1620.

(6) Seyler, K. L.; Zhong, D.; Klein, D. R.; Gao, S.; Zhang, X.; Huang, B.; Navarro-Moratalla, E.; Yang, L.; Cobden, D. H.; McGuire, M. A.; et al. Ligand-field helical luminescence in a 2D ferromagnetic insulator. *Nat. Physics* **2018**, *14* (3), 277-281.

(7) McGuire, M. A.; Dixit, H.; Cooper, V. R.; Sales, B. C. Coupling of Crystal Structure and Magnetism in the Layered, Ferromagnetic Insulator CrI_3. *Chem. Mater.* **2015**, *27* (2), 612-620.

(8) Huang, L.; Shang, Z.; Gao, M.; Miao, C.; Cheng, Y.; Huang, W. Optimized Parameters for Identifying the Layer Number of Few Layer Chromium Tri-iodide from a Theoretical Perspective: Implications for Two-Dimensional Spintronics. *ACS Appl. Nano Mater.* **2020**, *3* (8), 8382-8388.

(9) Claussen, J.; Hildebrandt, N.; Medintz, I. FRET - Förster Resonance Energy Transfer: From Theory to Applications. 2013; pp 397-429.

(10) Huang, B.; Clark, G.; Navarro-Moratalla, E.; Klein, D. R.; Cheng, R.; Seyler, K. L.; Zhong, D.; Schmidgall, E.; McGuire, M. A.; Cobden, D. H.; et al. Layer-Dependent Ferromagnetism in a van der Waals Crystal Down to the Monolayer Limit. *Nature* **2017**, *546* (7657), 270-273.